

## ABSTRACT

ALPERT, SCOTT MICHAEL. Evaluation of Computational Fluid Dynamics (CFD) for Modeling UV-Initiated Advanced Oxidation Processes. (Under the direction of Joel J. Ducoste.)

The use of ultraviolet-initiated (UV-initiated) advanced oxidation processes (AOP) is rapidly becoming an attractive alternative for the degradation of emerging organic contaminants that are not easily removed using conventional water treatment processes. Design and optimization of UV/H<sub>2</sub>O<sub>2</sub> systems must incorporate both reactor design (hydrodynamics, lamp orientation) and chemical kinetics (reaction mechanisms, kinetic rate constants). This research lays the groundwork for a protocol for using CFD models to simulate UV-initiated AOPs and, in doing so, provides the start for an improved design process to meet the needs of the water treatment community. In this CFD model, the combination of turbulence sub-models, fluence rate sub-models, and kinetic rate equations results in a comprehensive and flexible design tool for predicting the effluent chemical composition from a UV-initiated AOP reactor.

To validate the CFD simulation, the results of the model under various operating conditions were compared to pilot reactor trials conducted with the target contaminants methylene blue and the antimicrobial compound sulfamethoxazole. Using the standard k- $\epsilon$  turbulence closure model and the radial-line source integration (RAD-LSI) fluence rate model, the CFD model tended to under-predict the percent removal of methylene blue within the reactor. In addition, the percent difference between the pilot and the CFD results increased with increasing flow rates. Similar to the methylene blue trials, the CFD simulations for sulfamethoxazole degradation under-predicted the percent removals

measured in the pilot reactors. Additional investigation into the hydrodynamic effects and the light model validation is recommended to determine the next steps for model revision to improve agreement with experimental results.

The sensitivity to model parameters was evaluated. The multiple segment source summation (MSSS) sub-model predicted higher fluence rate values than that of the RAD-LSI sub-model. This increase in fluence rate translates to higher contaminant removal percentages predicted for both methylene blue and SMX. The turbulence sub-model selection for this reactor configuration was found to not significantly impact the predicted removal for methylene blue. As expected, the overall degradation of methylene blue was a strong function of the second-order kinetic rate constant describing the reaction between methylene blue and the hydroxyl radical. Further, the removal of methylene blue was sensitive to the concentration of dissolved organic carbon as a radical scavenger in the water matrix.

Evaluation of Computational Fluid Dynamics (CFD) for Modeling  
UV-Initiated Advanced Oxidation Processes

by  
Scott Michael Alpert

A dissertation submitted to the Graduate Faculty of  
North Carolina State University  
in partial fulfillment of the  
requirements for the Degree of  
Doctor of Philosophy

Civil Engineering

Raleigh, North Carolina

2008

APPROVED BY:

---

Joel J. Ducoste, PhD  
Chair of Advisory Committee

---

Detlef R.U. Knappe, PhD

---

David F. Ollis, PhD

---

Karl G. Linden, PhD

## DEDICATION

To Shannon, With Love.

This would not have been possible without you.

## BIOGRAPHY

Scott M. Alpert is a professional engineer in the water and wastewater industry. He currently resides in Charlotte, North Carolina.

## ACKNOWLEDGEMENTS

I would like to acknowledge and thank all of the people who have helped and supported me in the completion of this degree:

My friends at NC State, especially Tarek Aziz, Erin Gallimore, and Colleen Bowker, all of whom always listened and offered support.

The students and friends who helped with the research, including Olivier Prat, Carolina Baeza, Alfred Rossner, Colleen Bowker, Xi Zhao, Kiseok Jang, Matt Strickland, and Catherine Hoffmann.

My dissertation committee who provided great insight into the topic: Joel Ducoste, Detlef Knappe, Karl Linden, and David Ollis.

My funding sources: American Water Works Association Research Foundation, including our project manager Alice Fulmer and the Project Advisory Committee; and the Preparing the Professoriate Program at NC State.

All of my colleagues at HDR Engineering, Inc. who remained flexible during these 6+ long years.

My good friends in Raleigh: Jennifer, Ben, and Claire Heard.

My Mom Faye Alpert for her support and all of the great conversations on the drive to and from Raleigh.

My In-laws Skip and Vicki Atkinson for all their words of wisdom.

And finally, my family, Shannon, P, B, & T – I love you.

## TABLE OF CONTENTS

LIST OF TABLES.....	viii
LIST OF FIGURES.....	x
1. INTRODUCTION .....	1
1.1 Originality and Relevance .....	2
1.2 Hypotheses.....	3
2. LITERATURE REVIEW .....	5
2.1 Ultraviolet Photochemistry .....	5
2.2 Advanced Oxidation .....	10
2.3 Computational Fluid Dynamics .....	13
2.4 Turbulence Models .....	16
2.5 Mixing Models.....	21
2.6 Fluence Rate Models .....	25
2.7 Chemical Contaminants.....	31
2.7.1 Dye Decolorization.....	32
2.7.2 Sulfamethoxazole Oxidation.....	47
2.8 Advanced Oxidation Process Optimization.....	53
3. RESEARCH APPROACH AND METHODS .....	58
3.1 Development of a CFD Model for UV-initiated Advanced Oxidation .....	58
3.2 Development of the Kinetic Rate Equations.....	64
3.3 Materials and Analytical Methods.....	65
3.3.1 Materials .....	65

3.3.2	Analytical Methods.....	66
3.3.2.1	Methylene Blue Calibration Curve.....	70
3.3.2.1	Sulfamethoxazole Calibration Curve.....	71
3.4	Collimated Beam Testing of Dye Degradation.....	72
3.4.1	Kinetic Rate Constants.....	76
3.4.2	Dye Degradation Reaction Reversibility and Stability.....	80
3.5	CFD Evaluation of Turbulence and Fluence-Rate Sub-Models.....	81
3.6	CFD Model Evaluation of Design Parameters.....	82
3.7	Validation of CFD Results for Dye Degradation Using the Pilot-Scale Reactor ...	83
3.7.1	Impact of Internal Baffle Configuration on UV/AOP Performance.....	89
3.8	Advanced Oxidation of Sulfamethoxazole.....	89
3.9	Optimization of Energy and Hydrogen Peroxide Usage.....	90
3.10	Other Numerical Methods.....	91
4.	RESEARCH RESULTS AND DISCUSSION.....	98
4.1	Experimental Results – Collimated Beam Apparatus.....	98
4.1.1	Second-Order Kinetic Rate Constant for Methylene Blue and the Hydroxyl Radical.....	98
4.1.2	Effects of the Molar Ratio of Hydrogen Peroxide to Methylene Blue.....	101
4.1.3	Stability and Reversibility of the Methylene Blue Degradation Reaction.....	104
4.2	Experimental Results – Pilot Reactor.....	108
4.2.1	Methylene Blue.....	110
4.2.2	Sulfamethoxazole.....	118

4.3	Computational Fluid Dynamics .....	120
4.3.1	Grid Independence .....	120
4.3.2	Comparison of Experimental Results to CFD Model Results .....	121
4.3.2.1	Methylene Blue .....	123
4.3.2.2	Sulfamethoxazole .....	131
4.3.4	Fluence Rate Sub-model Analysis .....	136
4.3.5	Second-Order Kinetic Rate Constant Analysis .....	140
4.3.6	Turbulence Sub-model Analysis .....	141
4.3.7	Radical Scavenger Analysis .....	145
4.3.8	Micromixing .....	148
4.3.9	Cost Metrics .....	149
4.4	Other Numerical Methods .....	154
4.4.1	Reaction Mechanism Equations .....	154
4.4.2	Dose Distributions .....	155
4.5	Future Research Opportunities .....	163
5.	JOURNAL ARTICLE NUMBER 1 .....	166
6.	JOURNAL ARTICLE NUMBER 2 .....	205
7.	LIST OF REFERENCES .....	258
8.	APPENDIX .....	270
8.1	Appendix A – Sample CFD Codes for Pressure/Velocity, Light, and Kinetics ...	271
8.2	Appendix B – CFD Result Summaries .....	319
8.3	Appendix C – Sample MATLAB Code .....	361

## LIST OF TABLES

Table 2.1: Variables in Turbulence Closure Sub-models .....	20
Table 2.2: Properties of Several Organic Dyes .....	33
Table 2.3: Characteristics of Sulfamethoxazole .....	49
Table 2.4: pH Dependent Kinetic Rate Parameters (Canonica et al., 2008).....	51
Table 3.1: CFD Model Boundary Conditions .....	60
Table 3.2: Variables in CFD Codes .....	64
Table 3.3: Constants in CFD Codes.....	65
Table 4.1: Experimental Values for the Methylene Blue Kinetic Rate Constant .....	99
Table 4.2: Methylene Blue Stability Results .....	107
Table 4.3: Research Conditions Evaluated with Pilot Scale Reactor .....	110
Table 4.4: Pilot Results for Research Condition No. 1 .....	111
Table 4.5: Pilot Results for Research Condition No. 2.....	111
Table 4.6: Pilot Results for Research Condition No. 3.....	112
Table 4.7: Pilot Results for Research Condition No. 4.....	112
Table 4.8: Pilot Results for Research Condition No. 5.....	113
Table 4.9: Pilot Results for Research Condition No. 6.....	113
Table 4.10: Pilot Results for Research Condition No. 29.....	114
Table 4.11: Pilot Results for Research Condition No. 30.....	114
Table 4.12: Pilot Results for Research Condition No. 35.....	115
Table 4.13: Pilot Results for Research Condition No. 10a (SMX Direct Photolysis) .....	118
Table 4.14: Pilot Results for Research Condition No. 10b (SMX AOP & Direct Photolysis)	
.....	119
Table 4.15: Grid Independence Data .....	121
Table 4.16: Research Condition No. 1 .....	123
Table 4.17: Research Condition No. 2.....	124
Table 4.18: Research Condition No. 3.....	124
Table 4.19: Research Condition No. 4.....	125
Table 4.20: Research Condition No. 5.....	125
Table 4.21: Research Condition No. 6.....	126
Table 4.22: Research Condition No. 29.....	126
Table 4.23: Research Condition No. 30.....	127
Table 4.24: Research Condition No. 35.....	127
Table 4.25: Research Condition No. 10a – Direct Photolysis of SMX .....	132
Table 4.26: Research Condition No. 10b – SMX Advanced Oxidation and Photolysis .....	133
Table 4.27: Impact of Fluence Rate Model on CFD Results.....	139
Table 4.28: Impact of Second-Order Rate Constant $k_{MB, \cdot OH}$ on CFD Results.....	140
Table 4.29: Impact of Turbulence Sub-model on CFD Results.....	145
Table 4.30: Impact of DOC on CFD Results.....	146

Table 4.31: Annual Average Cost per Order for Research Conditions .....	150
Table 4.32: Summary of Numerical Solution Results .....	159
Table 4.33: Example of Model Effect on Regulatory Requirements.....	161
Table 4.34: Summary of Input and Output of Three Numerical Models.....	162

## LIST OF FIGURES

Figure 2.1: Relationship Among Incident, Refracted, and Reflected Light .....	9
Figure 2.2: Angle Geometry of Attenuation Factor in RAD-LSI Model .....	28
Figure 2.3: Geometry of Focus Factor in MSSS Model .....	31
Figure 2.4: Protonation States of Sulfamethoxazole (based on Boreen et al., 2004) .....	49
Figure 3.1: Chart Summary of Research Approach .....	59
Figure 3.2: Reactor Geometry within PHOENICS .....	61
Figure 3.3: CFD Grid Spacing in Y-Z Plane .....	62
Figure 3.4: CFD Grid Spacing in X-Z Plane .....	62
Figure 3.5: CFD Grid Among Internal Baffles and Wiper Mechanism .....	62
Figure 3.6: Photograph of Pilot Reactor Spectrophotometer System .....	67
Figure 3.7: Spectrophotometric Probe (a) and Probe Mounted in Pipe (b) .....	67
Figure 3.8: Photograph of HPLC Setup .....	69
Figure 3.9: Methylene Blue Calibration Curves .....	70
Figure 3.10: Sulfamethoxazole Calibration Curve .....	71
Figure 3.11: Collimated Beam Apparatus .....	73
Figure 3.12: Collimated Beam Apparatus Sample Area .....	74
Figure 3.13: KI/KIO <sub>3</sub> Actinometric Validation of Radiometer .....	75
Figure 3.14: Determination of Turbulence Model Sensitivity .....	81
Figure 3.15: Determination of Fluence Rate Model Sensitivity .....	82
Figure 3.16: Low-Pressure UV Pilot System Schematic (NTS) .....	84
Figure 3.17: Overview of Pilot Reactor System .....	85
Figure 3.18: Baffle Plate from Reactor Interior .....	85
Figure 3.19: Flow Meter for Pilot Reactor .....	86
Figure 3.20: Pilot UV Intensity Sensor .....	86
Figure 3.21: Pilot Chemical Feed System .....	87
Figure 4.1: Competition Kinetic Data Plot for Kinetic Rate Constant Determination .....	99
Figure 4.2: Removal Rates as a Function of Hydrogen Peroxide Concentration (Collimated Beam at 50 mJ cm <sup>-2</sup> and [MB] <sub>0</sub> = 0.5 mg L <sup>-1</sup> ) (a) Multiple Experiments in DI Water; (b) DI Water Results Compared to Pilot Influent Tank Water .....	103
Figure 4.3: Removal Rates as a Function of UV Dose (Collimated Beam) .....	104
Figure 4.4: Collimated Beam Baseline: Methylene Blue (MB) = 0.5 mg L <sup>-1</sup> , Hydrogen Peroxide = 0.0 mg L <sup>-1</sup> (Trace lines added for clarity) .....	105
Figure 4.5: Initial Spectrophotometer Results for Methylene Blue in Pilot .....	106
Figure 4.6: Pilot Scale Results with No UV Irradiation .....	108
Figure 4.7: Pilot Results Showing No Direct Photolysis and Confirming Response to Hydrogen Peroxide Addition .....	109
Figure 4.8: Methylene Blue Pilot Reactor Results (Five Baffles) .....	115

Figure 4.9: Methylene Blue Pilot Reactor Results (One Baffle) .....	116
Figure 4.10: Sulfamethoxazole Pilot Test Results .....	119
Figure 4.11: Velocity Distribution in Reactor with Five Baffles and Flow = 20 GPM.....	122
Figure 4.12: Fluence Rate Distribution in Reactor (Output P = 29.6 W, UVT = 92.9 %) ...	122
Figure 4.13: Comparison of Pilot and CFD Results for Five-Baffle Trials.....	128
Figure 4.14: Comparison of Pilot and CFD Results for One-Baffle Trials .....	129
Figure 4.15: Comparison of Pilot and CFD Results for SMX Trials.....	134
Figure 4.16: Graphical Results of RAD-LSI Fluence Rate Sub-model in CFD in (a) Y-Z Plane and (b) X-Z Plane.....	137
Figure 4.17: Graphical Results of MSSS Fluence Rate Sub-model in CFD in (a) Y-Z Plane and (b) X-Z Plane.....	138
Figure 4.18: Impact of Second-Order Rate Constant on Methylene Blue Removal .....	141
Figure 4.19: Velocity Profiles for k-ε Turbulence Sub-Model at 20 GPM; (a) Y-Z Plane Contours and (b) Y-Z Vectors at Inlet .....	142
Figure 4.20: Velocity Profiles for RNG k-ε Turbulence Sub-Model at 20 GPM; (a) Y-Z Plane Contours and (b) Y-Z Vectors at Inlet .....	143
Figure 4.21: Velocity Profiles for k-ω Turbulence Sub-Model at 20 GPM; (a) Y-Z Plane Contours and (b) Y-Z Vectors at Inlet .....	144
Figure 4.22: Impact of DOC on Advanced Oxidation of Methylene Blue .....	147
Figure 4.23: CFD and Pilot Cost Trends .....	151
Figure 4.24: AAC <sub>0</sub> Fractions for Energy and Chemical Costs (CFD Results).....	153
Figure 4.25: Dose-Response Curves for 100 W Output Power .....	155
Figure 4.26: UV Dose Distribution for 20 GPM and 26.5 W Output Power .....	156
Figure 4.27: UV Dose Distribution for 20 GPM and 100 W Output Power .....	157
Figure 4.28: Dose Distributions on Common Axes.....	158
Figure 4.29: Comparison of Numerical Models for Methylene Blue Removal .....	159

## 1. INTRODUCTION

The use of ultraviolet-initiated (UV-initiated) advanced oxidation processes (AOP) is rapidly becoming an attractive alternative for the degradation of harmful organic contaminants that are not easily removed using conventional water treatment processes. UV-initiated AOPs include the combinations of UV/hydrogen peroxide ( $\text{H}_2\text{O}_2$ ), UV/ozone, and UV/heterogeneous catalyst (such as titanium dioxide). The focus of this research was the UV/ $\text{H}_2\text{O}_2$  process with the goal that the methods and models developed herein can be modified for other UV-initiated AOP processes. Design and optimization of UV/ $\text{H}_2\text{O}_2$  systems include both system configuration (reactor design, pipe and fittings, lamp number, and lamp orientation) and chemical kinetics (reaction mechanisms and kinetic rate constants). While some numerical techniques have been developed for understanding UV/AOP performance, these techniques are limited in their applicability for analyzing full-scale UV/AOP systems while incorporating both reactor design and chemical kinetics. As a result, engineers and other water professionals need more appropriate numerical tools to use as part of the design process and in optimizing UV/AOP systems.

The reaction mechanisms for the degradation of organic contaminants by UV-initiated AOPs typically consist of a complex chain of fast chemical reactions. As such, the resulting intermediates and products from these processes will be highly sensitive not only to the light distribution within the reactor but also the level of turbulence and mixing. Design factors such as upstream hydraulic configurations, internal reactor layout, and lamp arrangement, may influence process performance. Thus, it is critical that a rigorous model be

developed that is sensitive to these issues for proper simulation of UV-initiated AOP performance.

### 1.1 Originality and Relevance

Researchers have previously demonstrated the importance of combining UV reactor hydraulics with dynamic fluence rate models to predict the effectiveness of the disinfection process. The authors of a recent AwwaRF study that successfully applied UV-initiated advanced oxidation for the degradation of organic contaminants recognized the dependence on non-ideal reactor characteristics (hydrodynamics and fluence rate) for the overall AOP performance (Linden et al., 2004). Sharpless and Linden (2003) concluded that development of a predictive UV/AOP model that incorporates reactor hydraulics would allow design simulations that optimize lamp placement, minimize light screening, and improve prediction of contaminant removal in different UV reactors. However, no currently published research has applied CFD models to UV-initiated advanced oxidation reactors that experience non-ideal fluence rate and reactor hydraulic conditions. The objective of this research is to begin to develop the protocol for using CFD models to simulate UV-initiated AOPs.

As utilities and other water producers begin to incorporate advanced oxidation into their treatment process, the site-specific characteristics will need to be assessed. Water quality effects, including the impact of light- and radical-scavengers, will determine not only the size of the treatment system but also the appropriate placement in the treatment scheme. The availability of dynamic and rigorous models like the ones developed in this research will streamline design and result in a more cost-effective and efficient UV/AOP system. Further,

as oxidation pathways for emerging contaminants are identified, a simulation model, such as the one described by this research, will become an important tool for the evaluation, design, and optimization of advanced oxidation systems. This research lays the groundwork for an improved design process and will provide a foundation for the future needs of the water treatment community.

Finally, utilities that integrate UV-initiated advanced oxidation into their treatment processes may also qualify for disinfection (log-kill) credit within the UV reactor. Since this will be uncharted territory for regulators, data from validated models will be critical in awarding disinfection credit within an AOP. Additional studies that combine the advanced oxidation models generated within the proposed research with UV disinfection models previously validated by others (e.g., Ducoste and Linden, 2005) will be the next logical step to achieve accurate simulation of performance of both advanced oxidation reactions and disinfection by UV reactors.

## 1.2 Hypotheses

The following four hypotheses were proposed to support the principal objective of this research:

1. The combination of turbulence sub-models<sup>1</sup>, fluence rate sub-models, micromixing sub-models, and kinetic rate equations within a CFD model will result in a comprehensive and flexible design tool for predicting the effluent chemical composition from a UV-initiated AOP reactor. [<sup>1</sup>The term “sub-model” is introduced

here to distinguish the turbulence and fluence rate models (now called sub-models) from the overall CFD simulation (model).]

2. For the modeling of organic contaminant degradation, turbulence sub-model selection will impact the effluent concentrations of the contaminant and its oxidation byproducts predicted by CFD simulations of UV-initiated AOP reactors.
3. Incorporation of micromixing sub-models will improve the predictions of CFD models of fast reactions occurring in an AOP reactor.
4. A comprehensive CFD model for UV-initiated AOP reactors will allow designers to optimize energy and chemical usage to achieve a given degradation goal for organic contaminants.

The stated hypotheses were tested with a comprehensive research approach that included both computer modeling (CFD and other numerical solutions) and experimental procedures (bench-scale collimated beam tests and pilot-scale reactor trials). It was anticipated that the data produced from this approach would help prove the stated hypotheses.

## 2. LITERATURE REVIEW

### 2.1 Ultraviolet Photochemistry

Ultraviolet photochemistry can be defined as a chemical reaction, or a series of chemical reactions, that is initiated and/or driven by the absorption of ultraviolet radiation by one or more reactants. The ability of a reactant to absorb UV radiation is defined by its molar absorption coefficient ( $\epsilon_{\lambda}$ , units of  $\text{L mole}^{-1} \text{ cm}^{-1}$ ), a value unique to the reactant molecule, or its absorbing functional group, that comprises a measure of an electronic transition probability (Ollis, 2003).

UV photochemistry is also dependent on the energy of the UV light incident on the reacting molecule. The magnitude of energy within a photon of UV light is described by Planck's equation, which can be expressed as follows (Braun et al., 1991):

$$E = h\nu = \frac{hc}{\lambda} \quad (2-1)$$

where,  $E = \text{energy, J} \cdot \text{photon}^{-1}$

$h = \text{Planck's constant, } 6.6256 \times 10^{-34} \text{ J} \cdot \text{s} \cdot \text{photon}^{-1}$

$c = \text{speed of light, } 2.9979 \times 10^8 \text{ m} \cdot \text{s}^{-1}$

$\lambda = \text{wavelength of radiation, m}$

$\nu = \text{frequency of radiation, s}^{-1}$

Multiplying the energy per photon as calculated in Equation 2-1 by Avogadro's number ( $6.023 \times 10^{23}$ ) results in the energy per einstein, where an einstein is defined as one mole of photons. The effectiveness of a photochemical reaction may then be defined by a quantum yield  $\Phi$ , which represents the moles of a given species photochemically transformed (reactant or product) per mole of photons (einstein) absorbed.

In this research, the chemical reactants were diluted in an aqueous medium. The Beer-Lambert law describes light transmission through an absorbing medium and is defined for a monochromatic light as (Braun et al., 1991),

$$T = \frac{P}{P_0} = 10^{-\epsilon lc} = e^{-\kappa lc} \quad (2-2)$$

where,  $T$  = transmittance (typically expressed as a fraction)

$P$  = transmitted power, e.g., W; or power per unit surface area, e.g.,  $W \cdot \text{cm}^{-2}$

$P_0$  = incident power, e.g., W; or power per unit surface area, e.g.,  $W \cdot \text{cm}^{-2}$

$\epsilon$  = molar absorption coefficient,  $L \cdot \text{mol}^{-1} \cdot \text{cm}^{-1}$

$l$  = thickness of solution traversed by light, cm (path length)

$c$  = molar concentration of absorbing species,  $\text{mol} \cdot L^{-1}$

$\kappa$  = Napierian molar absorption coefficient,  $L \cdot \text{mol}^{-1} \cdot \text{cm}^{-1}$  ( $\kappa=2.303\epsilon$ )

For polychromatic light, each of the terms in Equation 2-2, with the exception of path length and molar concentration, is expressed at a fixed wavelength. Absorbance may then be defined as,

$$A = -\log T = \epsilon l c \quad (\text{or } A = -\ln T = \kappa l c \text{ for Napierian variables}) \quad (2-3)$$

Absorbance follows the additive property, and if there are multiple absorbing species in the solution, then absorbance is defined as,

$$A = \sum_i \epsilon_i c_i l \quad (2-4)$$

In Equation 2-2, the term for power (P) is used somewhat generically. To be more exact, the field of photochemistry has adopted specific definitions for terms associated with power from light. Bolton (2001) differentiates these terms as described below:

Radiant Power (P, W): The total radiant power *emitted* in all directions by a light source.

Radiant Intensity (I, W • sr<sup>-1</sup>): The total radiant power *emitted* by a source in a given direction about an infinitesimal solid angle dΩ.

Irradiance (E, W • m<sup>-2</sup>): The total radiant power *incident* from all upward directions on an infinitesimal element of surface of area dS containing the point under consideration, divided by dS.

Fluence Rate ( $E'$ ,  $W \cdot m^{-2}$ ): The total radiant power incident from all directions onto an infinitesimally small sphere of cross-sectional area  $dA$ , divided by  $dA$ .

Fluence ( $H'$ ,  $J \cdot m^{-2}$ ): The total radiant energy of all wavelengths passing from all directions through an infinitesimally small of cross-sectional area  $dA$ , divided by  $dA$ . Fluence is also referred to as UV Dose.

For a constant fluence rate, the fluence (or UV dose) equals the fluence rate multiplied by the exposure time.

Although these terms are often used interchangeably, which as the definitions imply is incorrect, it is important that a reader understand what light concept is being discussed. For the remainder of this document, the terms as defined by Bolton (2001) will be used.

Since the UV light in a water treatment reactor passes through multiple media (i.e., air, quartz, and water), several of the laws of optics are applicable. Refraction describes the change in delivery angle (bending) of light as it passes through media with different refractive indices. The refraction is quantified using Snell's Law, which relates incident angle, refractive angle, and refractive indices as follows:

$$n_1 \sin \theta_1 = n_2 \sin \theta_2 \quad (2-5)$$

The definitions of  $n$  and  $\theta$  are shown in Figure 2.1.

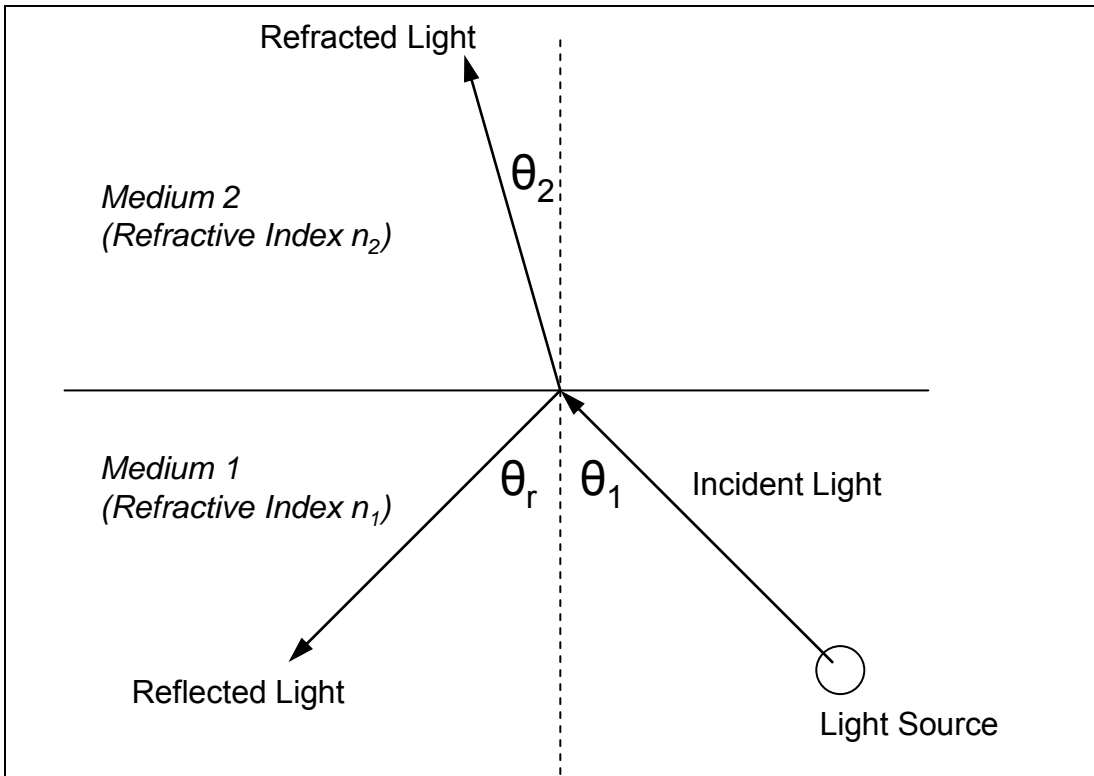


**Figure 2.1: Relationship Among Incident, Refracted, and Reflected Light**

As is shown in Figure 2.1, a portion of the incident light is reflected away from the interface between the two media. The reflectance is defined by the Fresnel Laws and can be quantified with Equation 2-6.

$$R = \frac{1}{2}(r_{||}^2 + r_{\perp}^2) \quad (2-6)$$

where  $R$  = Reflectance,

$r_{||}$  = Amplitude of radiant energy parallel to the plane of incidence, and

$r_{\perp}$  = Amplitude of radiant energy perpendicular to the plane of incidence.

The two amplitudes shown in Equation 2-6 are defined in Equations 2-7 and 2-8.

$$r_{II} = \frac{n_2 \cos \theta_1 - n_1 \cos \theta_2}{n_1 \cos \theta_2 + n_2 \cos \theta_1} \quad (2-7)$$

$$r_{\perp} = \frac{n_1 \cos \theta_1 - n_2 \cos \theta_2}{n_1 \cos \theta_1 + n_2 \cos \theta_2} \quad (2-8)$$

Both Snell's Law and Fresnel's Law will be used in the description of the fluence rate models in Section 2.6.

## 2.2 Advanced Oxidation

Advanced oxidation is the use of a powerful oxidizing agent (e.g., the hydroxyl radical  $\bullet\text{OH}$ ) to oxidize chemical compounds (Bolton, 2001). These compounds are primarily organic pollutants and can be oxidized in water, in air, or on the surface of solids. The term "advanced" describes the process of artificially creating the oxidant radicals to accelerate a reaction that could naturally occur in the environment if given time. In the UV/H<sub>2</sub>O<sub>2</sub> AOP, the hydrogen peroxide molecule produces two hydroxyl radicals when exposed to the UV light. The oxidation potential of the hydroxyl radical is 2.7 V, which makes it one of the most powerful oxidants available. The radical reacts quickly with organic compounds but is non-specific in its target. As such, evaluations of an AOP system should account for any radical scavengers within the water to be treated.

A significant amount of experimental research has been completed to evaluate the degradation of an organic species (parent compound) by UV-initiated advanced oxidation reactions (Sharpless and Linden, 2003; Bali et al., 2003; Devlin and Harris, 1984; Scheck and Frimmel, 1995). In other research studies, investigators have performed more detailed experiments to ascertain the reaction pathways involved in the degradation of the parent compound to its intermediate and final products (Stefan et al., 1996; Stefan et al., 2000; Alnaizy and Akgerman, 2000). The determination of these reaction pathways provides a more detailed picture of the photoreactive process and allows the development of numerical kinetic models that predict the rate of conversion of reactants to products. Detailed reaction pathways are very specific to the parent compound and chemical constituents in the water. However, once the reaction pathway is defined, researchers can combine the reaction kinetics of these UV-initiated AOPs with simulation models that describe the hydraulic and turbulent characteristics of a UV reactor system. Example advanced oxidation reaction mechanisms are described in Section 2.7.

UV-initiated advanced oxidation research has been performed using both low- and medium-pressure UV lamps. Sharpless and Linden (2003), in their study of direct photolysis and UV/H<sub>2</sub>O<sub>2</sub> advanced oxidation for the degradation of NDMA in a synthetic water, concluded that low-pressure and medium-pressure lamps have similar photonic efficiencies based on the calculated direct photolysis rate constants. Although Sharpless and Linden (2003) were able to develop an NDMA degradation kinetic model that predicted the results of a collimated beam study, the model equations assumed ideal mixing and could not account for the fluence rate distribution and hydrodynamic effects within a flow-through reactor.

One of the recommendations by Sharpless and Linden (2003) was that a detailed hydraulic model coupled with an irradiance distribution profile be developed to examine the effect of optical path length and multiple-lamp reactors for UV/H<sub>2</sub>O<sub>2</sub> systems. This research attempts to complete this coupling of hydrodynamics and fluence rate distribution for advanced oxidation reactions in low-pressure UV reactors.

Crittenden et al. (1999) developed a rigorous kinetic model to describe UV-initiated advanced oxidation that does not require the pseudo-steady-state assumption for radical species and can account for the impact of changing pH on the species present in a completely-mixed batch reactor. The Crittenden et al. model more accurately predicted the experimental results from an earlier study that used the pseudo-steady-state and constant pH assumption. Zalazar et al. (2004) used a one-dimensional radiation model for UV light distribution and a reaction mass balance with the pseudo-steady-state approximation for the radical species to examine the characteristics of a batch reactor that apply to scale-up of advanced oxidation processes. Similar numerical approaches to advanced oxidation modeling by direct application of continuity of mass and momentum equations with kinetic rate models and radiative transfer equations have been undertaken by other researchers (Labas et al., 2002; Alfano et al., 2001). Martin et al. (2002) describes in detail the numerical solution of the coupled equations for mass balance of the reactive species and radiative transfer for UV light distribution for both perfectly-mixed and continuous flow annular UV reactors. Although these numerical approaches often involve complex mathematical equations that may require iterative numerical solution of partial differential equations, the results tracked well with experimental validation.

### 2.3 Computational Fluid Dynamics

Computational Fluid Dynamics (CFD) is a technique for numerically solving the equations of fluid dynamics over both space and time, including the conservation of mass, conservation of momentum, and conservation of energy. Combined with appropriate boundary and initial conditions, these governing equations can describe both the physical and chemical changes within a reactor. A CFD model for UV systems also includes the spatial variations of fluence rate within the UV reactor.

Limited studies have been performed with CFD to simulate UV/AOPs. Pareek et al. (2003) used CFD combined with a discrete-ordinate radiation transport equation for light intensity and modified k- $\epsilon$  turbulence equations to model a heterogeneous, multi-phase photocatalytic reactor system for the photodegradation of a spent Bayer liquor. However, the applied radiation model did not incorporate refraction and was performed in a simple bench scale reactor. Mohseni and Taghipour (2004) used CFD to evaluate the heterogeneous photocatalytic oxidation of gas-phase vinyl chloride (VC) by the UV initiation of a TiO<sub>2</sub>-coated surface; however, this research did not incorporate a fluence rate model and only described the flux of VC toward the TiO<sub>2</sub>-coated surface. No research has been performed that investigates the sensitivity of both the turbulence model selection and the use of more rigorous fluence rate models on UV/AOP simulations. Moreover, none of the previous studies utilized the model to investigate whether the simulations were able to predict changes in the reactant degradation or formation of products due to changes in water quality and reactor configurations.

As mentioned previously, the equations of fluid dynamics include the conservation of mass, conservation of momentum, and conservation of energy. For an incompressible fluid, the equation for the conservation mass, or the continuity equation, can be written as,

$$\frac{\partial u_x}{\partial x} + \frac{\partial u_y}{\partial y} + \frac{\partial u_z}{\partial z} = 0 \quad (2-9)$$

In equation 2-9,  $u_x$ ,  $u_y$ , and  $u_z$  are the velocity components in the x, y, and z directions, respectively. The conservation of momentum equations for turbulent flow are expressed for incompressible flow and no free surface (no gravity term) as the Reynolds-averaged Navier-Stokes equation (Clark, 1996):

$$\rho \frac{\partial \bar{U}_i}{\partial t} + \rho \bar{U}_k \frac{\partial \bar{U}_i}{\partial x_k} = -\frac{\partial \bar{p}}{\partial x_i} + \mu \frac{\partial^2 \bar{U}_i}{\partial x_j \partial x_j} - \rho \frac{\partial}{\partial x_j} (\overline{u'_i u'_j}) \quad (2-10)$$

where  $\rho$  is the fluid density,  $\bar{U}_i$  is the average velocity in the  $i$ -th direction,  $t$  is time,  $\bar{p}$  is the average pressure,  $\mu$  is the absolute viscosity, and  $u'_i$  is the fluctuating component of velocity in the  $i$ -th direction. In Equation 2-10, the first term on the left-hand side of the equation represents the local acceleration, the second term on the left represents non-linear convective acceleration, the first term on the right represents pressure gradients, the second term on the right represents viscous forces, and the last term on the right-hand side of the equation represents derivatives of the Reynolds stresses between fluctuating velocity components.

The last term on the right side of Equation 2-10, representing the Reynolds stresses, creates a closure problem for turbulence since it introduces additional unknowns that outnumber the equations available for solution. Thus, in order to numerically solve turbulence problems, new equations or models must be established such as the two-equation models described in Section 2.4.

The reactive turbulent convective-diffusion equations for species transport are shown in the equations below (Liu and Ducoste, 2006):

$$\frac{\partial C_i}{\partial t} + U_j \frac{\partial C_i}{\partial x_j} = \frac{\partial}{\partial x_j} \left( (D + D_T) \frac{\partial C_i}{\partial x_j} \right) + R_i \quad (2-11)$$

where  $C_i$  is the average concentration of species  $i$ ,  $U$  is the mean velocity,  $D$  is the molecular diffusivity coefficient,  $R_i$  is the reaction term for species  $i$ , and  $D_T$  is the turbulent diffusivity that is defined as,

$$D_T = \frac{\nu_T}{Sc_T}. \quad (2-12)$$

In Equation 2-12,  $\nu_T$  is the turbulent eddy viscosity and  $Sc_T$  is the turbulent Schmidt number, which, as seen upon rearrangement of Equation 2-12, may be defined as the ratio of the eddy diffusivity of momentum (eddy viscosity) to the eddy mass diffusivity. The  $D_T \left( \frac{\partial C_i}{\partial x_j} \right)$  term in Equation 2-11 models the effects of the turbulent fluctuations of the concentration and

velocity. In this research, the reactions describing the advanced oxidation process were used in the turbulent convective-diffusion equation to describe the reactive transport of each species throughout the flow domain.

## 2.4 Turbulence Models

Typically, full-scale UV photoreactors will operate in a turbulent flow regime, and thus, simulations of a UV process must incorporate the impact of turbulent mixing on any chemical reactions that occur within these UV photoreactors. Although the standard  $k$ - $\epsilon$  turbulence model is often used for the examination of hydraulics within a flow-through reactor, the incorporation of other turbulent models may provide better characterization of the turbulent behavior within an advanced oxidation reactor. One of the outcomes of this study is to provide better guidance to researchers and engineers on numerical models for UV system analysis. Liu et al. (2007) were able to evaluate the accuracy of the turbulence model with experimental fluid mechanics measurements and were able to assess the impact of the turbulence model selection on UV disinfection performance. While their results showed a slight sensitivity of the microbial log inactivation to the turbulence model selection, the analysis revealed that the sensitivity of effluent microbial inactivation to the turbulence model selection was a function of the UV operating conditions and the UV response kinetics of the target microorganisms. A similar sensitivity study needs to be completed for UV-initiated AOPs since the proper characterization of the turbulent mixing intensity may be critical for fast competitive chemical reactions typically associated with UV/AOPs. In this study, the turbulent flow in the UV reactor is simulated using three two-equation turbulence

models: 1) standard k-ε, 2) RNG k-ε, and 3) k-ω. The goal of using multiple sub-models is to determine the CFD model sensitivity to the turbulence sub-model selection. While other more complicated turbulence models exist, such as the Reynolds Stress Model or Large Eddy Simulation model, the three two-equation models selected for this research provide reasonable and stable results without being numerically intensive.

The standard k-ε model used in this study was proposed by Launder and Sharma (1974) (as cited in Wilcox 2004) to solve the turbulence stress closure problem. This model, as described by Wilcox (2004), is shown below (reference Table 2.1 for definition of variables):

$$v_T = \frac{C_\mu k^2}{\varepsilon} \quad (2-13)$$

$$\frac{\partial k}{\partial t} + U_j \frac{\partial k}{\partial x_j} = \tau_{ij} \frac{\partial U_i}{\partial x_j} - \varepsilon + \frac{\partial}{\partial x_j} \left[ \left( \nu + \frac{v_T}{\sigma_k} \right) \frac{\partial k}{\partial x_j} \right] \quad (2-14)$$

$$\frac{\partial \varepsilon}{\partial t} + U_j \frac{\partial \varepsilon}{\partial x_j} = C_{\varepsilon 1} \frac{\varepsilon}{k} \tau_{ij} \frac{\partial U_i}{\partial x_j} - C_{\varepsilon 2} \frac{\varepsilon^2}{k} + \frac{\partial}{\partial x_j} \left[ \left( \nu + \frac{v_T}{\sigma_\varepsilon} \right) \frac{\partial \varepsilon}{\partial x_j} \right] \quad (2-15)$$

$$C_{\varepsilon 1}=1.44, \quad C_{\varepsilon 2}=1.92, \quad C_\mu=0.09, \quad \sigma_k=1.0, \quad \sigma_\varepsilon=1.3 \quad (2-16)$$

$$\omega = \frac{\varepsilon}{C_\mu k} \quad l = \frac{C_\mu k^{3/2}}{\varepsilon} \quad (2-17)$$

The second closure model used in this study, the Renormalized Group (RNG) k- $\varepsilon$  model, was developed by Yakhot and Orszag (1986) using techniques from the renormalization group theory. In the RNG k- $\varepsilon$  model,  $\nu_T$ ,  $k$ , and  $\varepsilon$  are still defined as in the standard k- $\varepsilon$  model. However, the RNG k- $\varepsilon$  model uses modified coefficients and empirical constants to reduce the higher level of dissipation that is predicted using the standard k- $\varepsilon$  model. Thus, equations 2-13, 2-14, and 2-15 are still applicable. The closure coefficients are replaced by the following (Wilcox, 2004):

$$C_{\varepsilon 2} = \tilde{C}_{\varepsilon 2} + \frac{C_\mu \lambda^3 \left(1 - \frac{\lambda}{\lambda_0}\right)}{1 + \beta \lambda^3} \quad (2-18)$$

$$\lambda = \frac{k}{\varepsilon} \sqrt{2S_{ij}S_{ji}} \quad (2-19)$$

$$C_{\varepsilon 1}=1.42, \quad \tilde{C}_{\varepsilon 2}=1.68, \quad C_\mu=0.085, \quad \sigma_k=0.72, \quad \sigma_\varepsilon=0.72, \quad \beta=0.012, \quad \lambda_0=4.38 \quad (2-20)$$

The third two-equation turbulence model used in this study, the k- $\omega$  model, was first developed by Wilcox (1988) (as cited in Wilcox 2004) and uses transport equations for  $k$  and the Reynolds Mean Stress (RMS) fluctuating vorticity  $\omega$ . In a later version developed by

Wilcox in 1998, in which changes were made to the values of  $\alpha$ ,  $\beta_0$ , and the dissipation terms ( $\beta^*$  and  $\beta$ ) and the functions  $f_\beta$  and  $f_{\beta^*}$  were added, the  $k-\omega$  (98) model was found to predict the experimental spreading rates reasonably well for all free shear flows, including far wake, mixing layer, and jet flows. The  $k-\omega$  (98) model is described below (Wilcox, 2004):

$$\nu_T = \frac{k}{\omega} \quad (2-21)$$

$$\frac{\partial k}{\partial t} + U_j \frac{\partial k}{\partial x_j} = \tau_{ij} \frac{\partial U_i}{\partial x_j} - \beta^* k \omega + \frac{\partial}{\partial x_j} \left[ (\nu + \sigma^* \nu_T) \frac{\partial k}{\partial x_j} \right] \quad (2-22)$$

$$\frac{\partial \omega}{\partial t} + U_j \frac{\partial \omega}{\partial x_j} = \alpha \frac{\omega}{k} \tau_{ij} \frac{\partial U_i}{\partial x_j} - \beta \omega^2 + \frac{\partial}{\partial x_j} \left[ (\nu + \sigma \nu_T) \frac{\partial \omega}{\partial x_j} \right] \quad (2-23)$$

$$\alpha=13/25, \beta=\beta_0 f_\beta, \beta^* = \beta_0^* f_{\beta^*}, \sigma=0.5, \sigma^*=0.5, \beta_0=9/125, \beta_0^* = 0.09 \quad (2-24)$$

$$f_\beta = \frac{1+70\chi_\omega}{1+80\chi_\omega}, \text{ where } \chi_\omega = \left| \frac{\Omega_{ij}\Omega_{jk}S_{ki}}{(\beta_0^*\omega)^3} \right| \quad (2-25)$$

$$f_{\beta^*} = \left\{ \begin{array}{ll} 1 & \chi_k \leq 0 \\ \frac{1+680\chi_k^2}{1+400\chi_k^2} & \chi_k > 0 \end{array} \right\}, \text{ where } \chi_k = \frac{1}{\omega^3} \frac{\partial k}{\partial x_j} \frac{\partial \omega}{\partial x_j} \quad (2-26)$$

$$\varepsilon = \beta^* \omega k \qquad l = \frac{k^{1/2}}{\omega} \qquad (2-27)$$

$$\Omega_{ij} = \frac{1}{2} \left( \frac{\partial U_i}{\partial x_j} - \frac{\partial U_j}{\partial x_i} \right) \qquad (2-28)$$

$$S_{ij} = \frac{1}{2} \left( \frac{\partial U_i}{\partial x_j} + \frac{\partial U_j}{\partial x_i} \right) \qquad (2-29)$$

Variables that have not been previously defined but that are used in the three turbulence models are defined in Table 2.1.

**Table 2.1: Variables in Turbulence Closure Sub-models**

Symbol	Definition
$\nu_T$	kinematic eddy viscosity
$k$	turbulent kinetic energy
$\varepsilon$	turbulent energy dissipation
$\tau_{ij}$	Reynolds stress tensor
$\nu$	kinematic molecular viscosity
$\omega$	specific dissipation rate (dissipation per unit turbulence kinetic energy)
$l$	turbulence length scale
$S_{ij}$	mean strain rate tensor
$\Omega_{ij}$	mean rotation tensor

These three models were chosen based on their general universality for modeling of uncomplicated turbulent flows. The standard k- $\varepsilon$  model is the most popular of the two-equation models and performs relatively well for most types of flows. The RNG k- $\varepsilon$  tries to

solve the  $k$ - $\epsilon$  singularity problem at wall boundaries (where  $k$  approaches zero) and reduces the higher level of dissipation that is predicted using the Standard  $k$ - $\epsilon$  model. However, the RNG  $k$ - $\epsilon$  is not as accurate in predicting free-shear (no wall) flows. The  $k$ - $\omega$  has been proven relatively accurate for boundary layer (i.e., wall bounded) flows and, with the 1998 revisions, also works well for free-shear flows.

## 2.5 Mixing Models

Contaminant oxidation, like all basic chemical reactions, requires spatial adjacency between (or among) the reacting molecules, which in this case, are initially the hydroxyl radical and the organic compound. In a typical system, the concentration of hydroxyl radicals will be much less than that of the target contaminant. Further, the reactions for radical formation and many of the oxidation reactions can be considered fast reactions. Thus, the physical process of mixing within the advanced oxidation reactor will be an important factor in determining the level of contaminant degradation. Researchers have shown that turbulent heterogeneity requires more attention than Magnussen and Hjertager's minimum reaction kinetics approach when dealing with turbulent chemical reactions (Baldyga and Bourne, 1999; Spalding, 1998; Marchisio and Barresi, 2003). For this reason, the incorporation of mixing models in the CFD code should improve the accuracy in predicting effluent concentrations of the advanced oxidation products.

Accurately defining and modeling turbulent mixing within reactors is complex and, as such, is the subject of on-going research, particularly in the area of turbulent mixing with chemical reactions. To begin the definition, mixing can be segregated into three scales:

macromixing, mesomixing, and micromixing (Baldyga and Pohorecki, 1995; Baldyga and Bourne, 1992). Macromixing, or bulk blending, is the mixing process on the dimensional scale of the reactor as a whole and determines the environment for mesomixing and micromixing (Baldyga and Pohorecki, 1995). Mesomixing constitutes the localized reaction zone, which is a coarse scale relative to the micromixing, but is finer than the macroscale. Further, mesomixing represents the inertial-convective disintegration of large eddies (Baldyga and Pohorecki, 1995). Finally, micromixing is the scale of mixing that occurs within small eddies and signifies the viscous-convective deformation and engulfment process of fluid elements, which is the key physical process for mixing-sensitive chemical reactions (Rohani and Baldyga, 1987). Larger scale mixing such as macro- and mesoscale can be calculated using CFD codes directly. However, a specialized micromixing sub-model must be separately coded within CFD to simulate the mixing at this molecular scale, which is typically smaller than the CFD grid size.

Although micromixing will have a direct impact on chemical reactions since these reactions occur on a molecular scale, both macromixing and mesomixing may also be significant processes relative to the chemical reaction processes due to the inhomogeneity related to turbulence (Baldyga and Pohorecki, 1995). Baldyga and Bourne (1992) suggest that mixing on the various scales is important for proper modeling of chemical reactions, including evaluating the relative importance of each by calculating the ratio of time constants. The importance of using micromixing and mesomixing models for simulating mixing-sensitive chemical reactions has been shown through comparison of experimental and calculated product concentrations for various reactor types and reactions (Baldyga and

Bourne, 1992; Rohani and Baldyga, 1987; Baldyga and Rohani, 1987). Although Baldyga and Rohani (1987) identify limitations of various micromixing models (e.g., the effects of turbulent circulation near inlet streams), it is clear that the inclusion of a micromixing model in a CFD simulation of UV-initiated AOPs must be investigated for accurate prediction of reaction results.

Several micromixing models have been developed, each intending to simulate the elementary process(es), i.e., eddy disintegration, engulfment, deformation, and/or molecular diffusion, which best describes mixing under the conditions presented. Baldyga and Bourne (1990) compare a simplified engulfment micromixing model (Baldyga and Bourne, 1989) with the interaction-by-exchange-with-the-mean (IEM) model, which differ by a static (IEM) versus growing (engulfment) localized reaction zone. Micromixing models also can be modified to capture the impact of the fragmentary and intermittent nature of turbulence on local chemical reactions (Baldyga and Pohorecki, 1995).

Equation 2-11, as presented previously, is considered the basis for the single fluid model (SFM) approach because the *average* concentration of each chemical species is defined by a scalar variable that is then convected and diffused by turbulent motion. In Equation 2-11, the chemical kinetic reaction rate for species *i* in reaction *k* is expressed as (Liu and Ducoste, 2006):

$$R_{ki} = KM_i \prod_{j \text{ reactant}} \frac{\rho X_j}{M_j} \quad (2-30)$$

where  $M_i$  is the molecular weight of product species  $i$ ,  $\rho$  is the fluid density,  $X_j$  is the mass concentration of reactant species  $j$ ,  $M_j$  is the molecular weight of reactant species  $j$ , and  $K$  is the reaction kinetic rate constant.

For turbulent chemical reaction conditions, a turbulent mixing rate must also be included in the reaction process (Baldyga and Bourne, 1992; Bakker et al., 2001). Several models have been proposed to describe the turbulent effects on heat/mass transfer and chemical reaction, including the eddy-break-up model, the eddy dissipation concept, and two-fluid (or multi-fluid) models. For the single fluid model approach in this study, the turbulent mixing rate was based on the eddy-dissipation concept (Forney and Nafia, 1998; Hjertager et al., 2002). The method for calculating the overall reaction rate in the SFM approach was based on Magnussen and Hjertager's model (Bakker et al., 2001) where the overall reaction rate term  $R_i$  is calculated as the minimum between the chemical kinetic reaction rate,  $R_{ki}$ , and the turbulent mixing rate,  $R_{mi}$ , as follows (Liu and Ducoste, 2006):

$$R_i = -\nu_i \min(R_{ki}, R_{mi}) \quad (2-31)$$

where  $\nu_i$  is defined as the stoichiometry of species  $i$  and is positive for reactants and negative for products. The turbulent mixing rate is described by the following:

$$R_{mi} = \left( M_i A_{mn} \frac{\varepsilon}{k} \right) \bullet \min \left( \left( \frac{\rho X_j}{\nu_j M_j} \right)_{j \text{ reactant}} \right) \quad (2-32)$$

where  $v_j$  is defined as the stoichiometry of species  $j$ ,  $A_{mn}$  is an empirical constant that varies between 1 and 5 with a nominal value of 2.5 (Hjertager et al., 2002),  $\varepsilon$  is the dissipation of turbulent kinetic energy, and  $k$  is the turbulent kinetic energy. The interpretation of Magnussen and Hjertager's model and Equation 2-32 is that (i) in regions of low mixing intensity and for fast reactions, the overall reaction rate is limited by the mixing rate, and (ii) in regions of high mixing intensity, the chemical kinetic rate is the limiting factor.

## 2.6 Fluence Rate Models

In Section 2.1, the UV fluence rate (incident radiant power) was shown to vary with distance from the lamp and as a function of the absorptive characteristics of the media through which the light passes. In advanced oxidation reactions, both the organic contaminant and  $H_2O_2$  absorb UV light, reducing the transmitted fluence rate, and consequently, changing the effectiveness of hydroxyl radical production throughout the UV reactor. Other factors, such as reflection, refraction, shadowing, and lamp effects, also influence the spatial distribution of light within a UV reactor. Several models have been developed to characterize the spatial distribution of the UV fluence rate within a reactor. These models include the Multiple Point Source Summation (MPSS) model (Jacob and Dranoff, 1970), which was later improved to incorporate reflection, refraction, and absorption (Bolton, 2000); the Line Source Integration (LSI) model (Blatchley, 1997); the Multi-Segment Source Summation (MSSS) model (as described in Liu et al., 2004); the modified LSI model (RAD-LSI) that incorporates fluence corrections close to, and far away from, the lamp (Liu et al., 2004); and Discrete Ordinate (DO) methods (Fiveland, 1984;

Stamnes et al., 1988; Liou and Wu, 1996). Liu et al. (2004) directly evaluated the performance of these models with experimental measurements of the fluence rate at different points within a UV reactor, the results being a compilation of the strengths and weaknesses of the each model's ability to predict the fluence rate. Ducoste and coworkers further showed that the microbial log inactivation and the shape of the fluence distribution were sensitive to the fluence rate model selection (Ducoste et al., 2005; Liu et al., 2006). Their results suggest the need to evaluate the influence of the fluence rate model selection on any photoreactive process such as UV-initiated advanced oxidation processes.

The RAD-LSI and MSSS models were chosen to simulate the fluence rate in this study and to determine the influence of this selection on the predicted effluent concentrations from a UV/AOP process. These two models were selected based on their performance in predicting the UV light distribution in Liu et al. (2004) and the ease of incorporation into a CFD model simulation. The RAD-LSI is a modified version of the line source integration model (Blatchley, 1997) that was enhanced to account for the physics of reflection, refraction, and absorption and provides better prediction of the fluence rate near the lamp surface using the radial model component (Liu et al., 2004). The RAD-LSI model is represented by Equations 2-33 and 2-34:

$$E'(r, h) = \min \left\{ \frac{P_\lambda}{2\pi Lr}, \frac{P_\lambda}{4\pi Lr} \left[ \arctan \left( \frac{L/2+h}{r} \right) + \arctan \left( \frac{L/2-h}{r} \right) \right] \right\} \times (\text{atten factor}) \quad (2-33)$$

$$(\text{atten factor}) = \sum_{k=1}^n (1 - R_{1,k})(1 - R_{2,k}) \frac{\frac{P/n}{4\pi(d_{1,k} + d_{2,k} + d_{3,k})^2} T_w^{d_{3,k}/0.01} T_q^{d_{2,k}/0.01}}{\sum_{k=1}^n \frac{P/n}{4\pi(r_k^2 + h_k^2)}} \quad (2-34)$$

The variables used in Equations 2-33 and 2-34 are defined as follows:

- $E(r,h)$  is the fluence rate at a point in the reactor with normal (perpendicular) distance  $r$  to the lamp axis and longitudinal distance  $h$  to the lamp center.
- $P_\lambda$  is the radiant power at wavelength  $\lambda$  uniformly emitted in all directions by the point source.
- $L$  is the total length of the lamp.
- $R_1$  is the reflectance factor for the air/quartz interface (see Equation 2-6).
- $R_2$  is the reflectance factor for the quartz/water interface (see Equation 2-6).
- $T_w$  is the 10-mm path length transmittance of the water.
- $T_q$  is the 10-mm path length transmittance of the quartz.
- $d_1$  is the path length in the air (see Figure 2.2).
- $d_2$  is the path length in the quartz (see Figure 2.2).
- $d_3$  is the path length in the water (see Figure 2.2).
- $n$  is the number of points used to describe the lamp (e.g., in an N-point MPSS model).

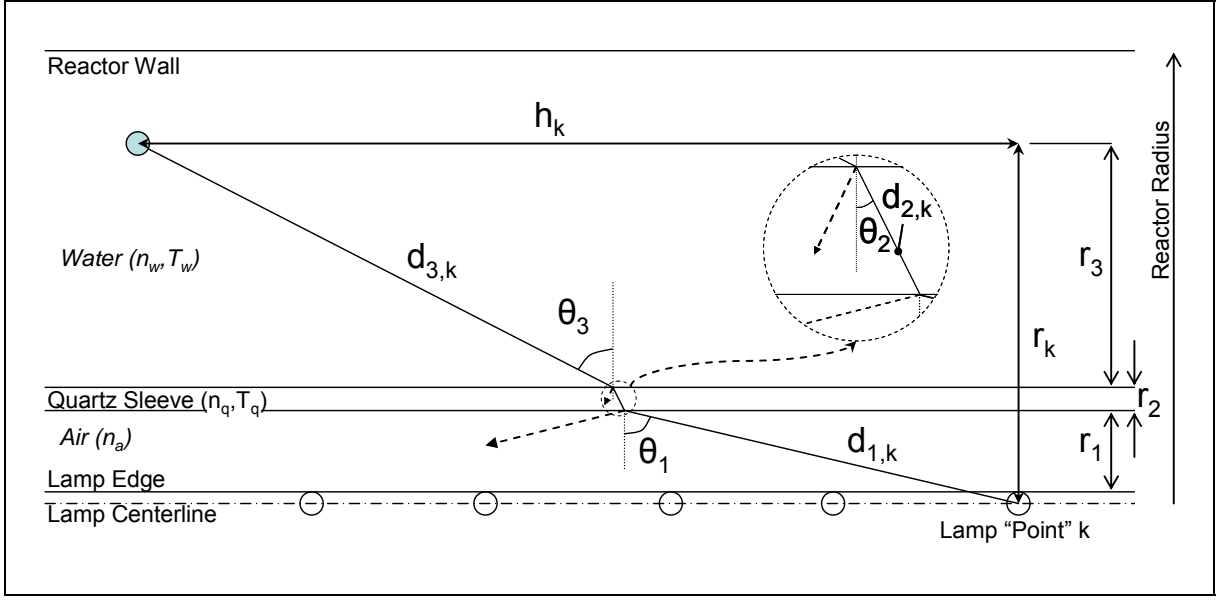


**Figure 2.2:** Angle Geometry of Attenuation Factor in RAD-LSI Model

In Figure 2.2, the normal distance between the lamp centerline to the inner edge of the quartz sleeve is defined as  $r_1$ , the thickness of the quartz sleeve is  $r_2$ , and the normal distance from the outer edge of the quartz sleeve to the point of interest is  $r_3$ . Using these terms and the incident angles shown in Figure 2.2, the distance  $h_k$  can be defined as shown in Equation 2-35.

$$h_k = r_{1,k} \tan \theta_1 + r_{2,k} \tan \theta_2 + r_{3,k} \tan \theta_3 \quad (2-35)$$

From Snell's Law, all of the angles in Equation 2-35 can be expressed in terms of a single angle as shown in Equations 2-36 and 2-37.

$$\theta_2 = \sin^{-1}\left(\frac{n_a}{n_q} \sin \theta_1\right) \quad (2-36)$$

$$\theta_3 = \sin^{-1}\left(\frac{n_a}{n_w} \sin \theta_1\right) \quad (2-37)$$

In equations 2-36 and 2-37,  $n_a$ ,  $n_q$ , and  $n_w$  are the refractive indices for air, quartz, and water, respectively. The path lengths  $d_1$ ,  $d_2$ , and  $d_3$  in the RAD-LSI equations are determined using trigonometry and previously defined variables as shown in equations 2-38, 2-39, and 2-40.

$$d_1 = \frac{r_1}{\cos \theta_1} \quad (2-38)$$

$$d_2 = \frac{r_2}{\cos \theta_2} \quad (2-39)$$

$$d_3 = \frac{r_3}{\cos \theta_3} \quad (2-40)$$

Although the RAD-LSI is an improved version of the LSI model, it is still based in part on the multiple point source summation method (MPSS), which models a lamp with a series of point sources. As discussed by Liu et al. (2004), the MPSS model with reflection, refraction, and absorption did not completely correct for the over-prediction of the fluence rate near the lamp surface and in regions near the lamp ends. This over-prediction was

corrected by modeling the lamp as a series of differential cylindrical segments, where light is emitted normal to the cylinder surface and decreases with the cosine of the angle between the unit normal and the direction vectors (Liu et al., 2004). This fluence rate modeling approach is called the multiple segment source summation (MSSS). The MSSS fluence rate at a specific point in space caused by the UV light emitted from a segment source is described as (Liu et al., 2004):

$$I_A = (1 - R_1)(1 - R_2) \frac{P/n}{4\pi(d_1 + d_2 + d_3)^2} T_w^{d_3/0.01} T_q^{d_2/0.01} (focus) \left(\frac{4}{\pi}\right) \cos\theta_1 \quad (2-41)$$

The focus factor in Equation 2.41 is defined as the ratio of surface areas for the conical frustums with axes on the lamp centerline and slant heights of  $S_w$  and  $S_{w/o}$  shown in Figure 2.3. This ratio is defined numerically in Equation 2-42.

$$(focus) = \frac{(d_1 + d_2 + d_3)^2 \Delta\theta \cos\theta_1}{r(h'' - h') \cos\theta_3} \quad (2-42)$$

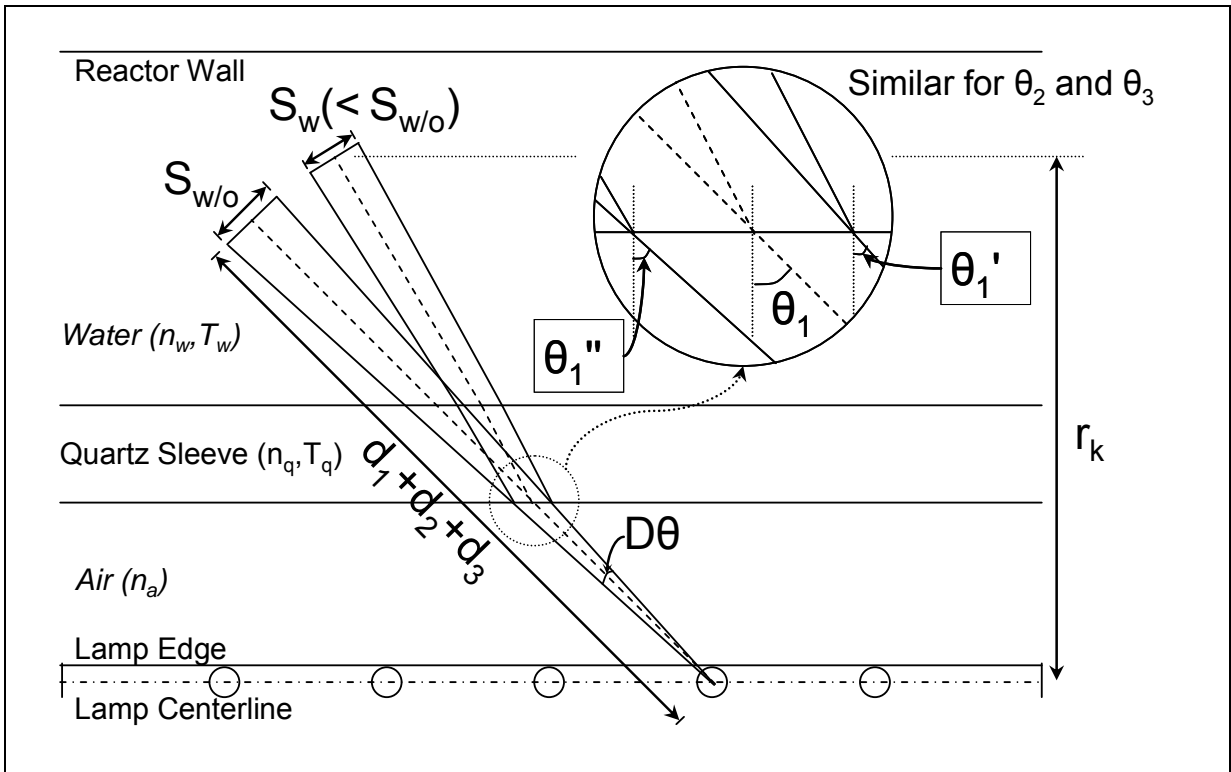


**Figure 2.3: Geometry of Focus Factor in MSSS Model**

## 2.7 Chemical Contaminants

In this research, two types of organic contaminants were studied. The first was an organic dye (methylene blue) for which the decolorization from reaction with the hydroxyl radical was quantified to evaluate the sensitivity of the micromixing, turbulence, and fluence rate sub-model selection in CFD. The second contaminant was an antimicrobial compound that can undergo both direct photolysis and advanced oxidation and is more characteristic of the advanced oxidation processes readily encountered in water and wastewater treatment.

### 2.7.1 Dye Decolorization

Many organic dyes are decolorized (bleached) upon reaction with the hydroxyl radical. These dyes are good candidates for evaluation in an advanced oxidation study since the decolorization can be i) analyzed with a spectrophotometer, and ii) described by an apparent pseudo-first-order reaction rate constant. In addition, typically these dyes do not undergo direct photolysis and are not reactive with hydrogen peroxide alone. The mechanism of decolorization varies among the types of organic dyes, but, in general, these dyes contain aromatic ring structures that are subject to attack by the hydroxyl radical. The advanced oxidation of several different dyes has been studied by others, several of which are identified in Table 2.2. As can be seen in Table 2.2, the second-order rate constants for the reaction of the dye with the hydroxyl radical are unpublished for most dyes. Since this rate constant is necessary to model the reaction mechanism in a system where the concentration of hydroxyl radicals may vary spatially, the second-order rate constant for the dye selected for this study was determined using competition kinetics as described in the experimental approach.

**Table 2.2: Properties of Several Organic Dyes**

Dye Name/ Formula/ Description	Molecular Weight	CAS Registry Number	Wavelength of Maximum Absorbance	Second-Order Rate Constant	Ref
CI Acid Orange 7 (AO7) / $C_{16}H_{11}N_2NaO_4S$ / Monoazo anionic dye-acid class	350.32	633-96-5	485 nm	NA	(1)
Methylene Blue / $C_{16}H_{18}ClN_3S$ / Azindyes	319.85	61-73-4	662 nm / 470 nm	$k = 1.2 \times 10^{10}$ $k = 2.1 \times 10^{10}$ ( $L mol^{-1} s^{-1}$ )	(2, 8)
CI Reactive Red 141 / Reactive azo dye	1781	NA	544 nm	NA	(3)
CI Reactive Black 5 / Reactive diazo dye	NA	NA	583 nm	NA	(4)
Malachite Green (MG) / $C_{23}H_{26}N_2$ / Triarylmethane dye (cationic)	330.47	129-73-7	617 nm	NA	(5)
Acid Orange 52 (AO52; Methyl Orange) / $C_{14}H_{14}N_3NaO_3S$ / Hydrosoluble aminoazobenzenes	327.33	547-58-0	463 nm	NA	(6)
Xylenol Orange / $C_{31}H_{28}N_2Na_4O_{13}S$ (sodium salt) / Sulfonephyhalein dye	760.59	3618-43-7	580 nm	$k/k_{reference} = 25$ $k = 2.4 \times 10^{10}$ ( $L mol^{-1} s^{-1}$ ), $k_{reference} = 9.7 \times 10^8$ ( $L mol^{-1} s^{-1}$ ), pH = 11	(7)

NA = Not Available

References: (1) Behnajady and Modirshahla (2006); Behnajady et al. (2004)  
 (2) Banat et al. (2005)  
 (3) Gultekin and Ince (2004)  
 (4) El-Dein et al. (2001)  
 (5) Modirshahla and Behnajady (2006)  
 (6) Galindo et al. (2000)  
 (7) Gupta and Hart (1971)  
 (8) Radiation Chemistry Data Center (RCDC), Notre Dame Radiation Laboratory, Online database

The system of kinetic rate equations describing the degradation of methylene blue by advanced oxidation begins with the reaction mechanism for the production of the hydroxyl radical from hydrogen peroxide. The photolysis of hydrogen peroxide is shown in Equation 2-43 and is followed by the reaction rate term shown in Equation 2-44.



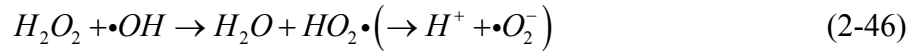
$$r_{UV} = 2\Phi_{H_2O_2} E'_{CFD} \varepsilon_{H_2O_2} [H_2O_2] \quad (2-44)$$

In Equation 2-44,  $\Phi_{H_2O_2}$  is the quantum yield for the photolysis of hydrogen peroxide (moles  $H_2O_2$  per mole photons, or moles  $H_2O_2$  per einstein) and  $\varepsilon_{H_2O_2}$  is the molar absorptivity of hydrogen peroxide ( $L \text{ mol}^{-1} \text{ cm}^{-1}$ ). The square brackets [] represent the molar concentration of the species enclosed in the brackets. The term  $E'_{CFD}$  is the irradiance (UV@254 nm) at each individual grid cell centerpoint in the CFD domain. Since the light distribution models result in an irradiance term in units of  $W \text{ m}^{-2}$ , a unit conversion is necessary for the  $r_{UV}$  term. Noting that the variable  $C_3$  is used within the CFD code to represent the irradiance at each grid location, the term  $E'_{CFD}$  can be defined as shown in Equation 2-45.

$$E'_{CFD} = \frac{C_3 \left( \frac{W}{m^2} \right) \times 100 \left( \frac{cm}{m} \right)}{U_{254} \left( \frac{J}{Einstein} \right) \times 1000 \left( \frac{L}{m^3} \right)} \quad (2-45)$$

Using this definition,  $r_{UV}$  has units of moles  $L^{-1} s^{-1}$ .

Since the hydroxyl radical is very reactive, it will begin to immediately react with other species in solution. The reaction between hydrogen peroxide and the hydroxyl radical is described by Equations 2-46 through 2-50.



$$k_1 = 2.7 \times 10^7 \text{ M}^{-1} \text{ s}^{-1} \quad (\text{Buxton et al., 1988}) \quad (2-47)$$

$$\frac{d[H_2O_2]}{dt} = -k_1 [H_2O_2] [\bullet OH] \quad (2-48)$$

$$\frac{d[\bullet OH]}{dt} = -k_1 [H_2O_2] [\bullet OH] \quad (2-49)$$

$$\frac{d[\bullet O_2^-]}{dt} = k_1 [H_2O_2] [\bullet OH] \quad (2-50)$$

Hydrogen peroxide reacts with the superoxide radical according to Equations (2-51) through (2-55).



$$k_2 = 0.13 \text{ M}^{-1} \text{ s}^{-1} \quad (\text{Weinstein et al., 1979}) \quad (2-52)$$

$$\frac{d[H_2O_2]}{dt} = -k_2 [H_2O_2] [\bullet O_2^-] \quad (2-53)$$

$$\frac{d[\bullet O_2^-]}{dt} = -k_2 [H_2O_2][\bullet O_2^-] \quad (2-54)$$

$$\frac{d[\bullet OH]}{dt} = k_2 [H_2O_2][\bullet O_2^-] \quad (2-55)$$

The hydroxyl radical will recombine with itself to form hydrogen peroxide as shown in Equations 2-56 through 2-59.



$$k_3 = 5.5 \times 10^9 \text{ M}^{-1} \text{ s}^{-1} \text{ (Buxton et al., 1988)} \quad (2-57)$$

$$\frac{d[\bullet OH]}{dt} = -k_3 [\bullet OH][\bullet OH] \quad (2-58)$$

$$\frac{d[H_2O_2]}{dt} = k_3 [\bullet OH][\bullet OH] \quad (2-59)$$

The two radical species,  $\bullet OH$  and  $\bullet O_2^-$ , will also combine with each other according to Equations 2-60 through 2-63.

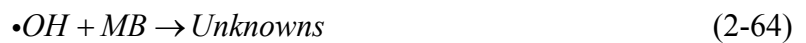


$$k_4 = 7.0 \times 10^9 \text{ M}^{-1} \text{ s}^{-1} \text{ (Beck, 1969 as cited in Crittenden, et. al, 1999)} \quad (2-61)$$

$$\frac{d[\bullet OH]}{dt} = -k_4 [\bullet OH][\bullet O_2^-] \quad (2-62)$$

$$\frac{d[\bullet O_2^-]}{dt} = -k_4 [\bullet OH][\bullet O_2^-] \quad (2-63)$$

Methylene blue (MB) degrades through reaction with the hydroxyl radical to form products not currently under investigation by this research, and thus, will be labeled as unknown in Equations 2-64 through 2-67. For the reaction rate constant defined in Equation 2-65, the reader may reference the competition kinetics process described in Section 3.4.1.



$$k_{MB, \bullet OH} = 6.9 \times 10^9 \text{ M}^{-1} \text{ s}^{-1} \quad (2-65)$$

$$\frac{d[\bullet OH]}{dt} = -k_{MB, \bullet OH} [\bullet OH][MB] \quad (2-66)$$

$$\frac{d[MB]}{dt} = -k_{MB,\cdot OH} [\cdot OH][MB] \quad (2-67)$$

Several hydroxyl radical scavengers can also be expected in the background water matrix. These scavengers will consume radicals according to Equations 2-68 through 2-83.

Dissolved Organic Carbon (DOC):



$$k_{DOC,\cdot OH} = 2.5 \times 10^4 \left( \frac{mg}{L} \right)^{-1} s^{-1} \quad (\text{Larson and Zepp, 1988}) \quad (2-69)$$

$$\frac{d[\cdot OH]}{dt} = -k_{DOC,\cdot OH} [\cdot OH](DOC) \quad (2-70)$$

Alkalinity (which at neutral pH is dominated by the bicarbonate ion):



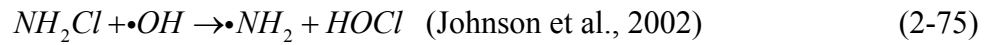
$$k_{HCO_3^-, \cdot OH} = 8.5 \times 10^6 M^{-1} s^{-1} \quad (\text{Buxton et al., 1988}) \quad (2-72)$$

$$\frac{d[\cdot OH]}{dt} = -k_{HCO_3^-, \cdot OH} [HCO_3^-][\cdot OH] \quad (2-73)$$

Monochloramine:



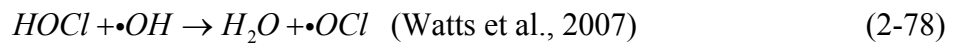
Or alternatively,



$$k_{NH_2Cl, \cdot OH} = (2.8 \pm 0.2) \times 10^9 \text{ M}^{-1} \text{ s}^{-1} \quad (\text{Johnson et al., 2002}) \quad (2-76)$$

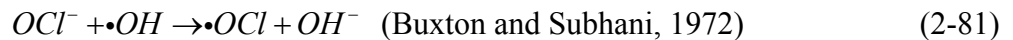
$$\frac{d[\cdot OH]}{dt} = -k_{NH_2Cl, \cdot OH} [NH_2Cl][\cdot OH] \quad (2-77)$$

Free chlorine:



$$k_{HOCl, \cdot OH} = 8.5 \times 10^4 \text{ M}^{-1} \text{ s}^{-1} \quad (\text{Watts et al., 2007}) \quad (2-79)$$

$$\frac{d[\cdot OH]}{dt} = -k_{HOCl, \cdot OH} [HOCl][\cdot OH] \quad (2-80)$$



$$k_{OCl^-, \cdot OH} = 8.8 \times 10^9 M^{-1} s^{-1} \quad (2-82)$$

(Buxton and Subhani, 1972 as cited in Feng et al., 2007)

$$\frac{d[\cdot OH]}{dt} = -k_{OCl^-, \cdot OH} [OCl^-] [\cdot OH] \quad (2-83)$$

To improve convergence within the CFD code, two modifications to the reaction equations have been made (and are included in this section for completeness). The first is that the four species being tracked were normalized to initial conditions. The second is that, since the lifetimes of the two radical species are very short, pseudo-steady-state conditions for the two radicals were assumed. For the normalization of the species concentrations, the following variables have been defined.

$$C_5 = \frac{[H_2O_2]}{[H_2O_2]_0} \Rightarrow [H_2O_2] = C_5 [H_2O_2]_0 \quad (2-84)$$

In Equation 2-84 and those following, the subscript “0” indicates the initial concentration of the species entering the UV reactor.

$$C_6 = \frac{[MB]}{[MB]_0} \Rightarrow [MB] = C_6 [MB]_0 \quad (2-85)$$

$$C_7 = \frac{[\cdot OH]}{[H_2O_2]_0} \Rightarrow [\cdot OH] = C_7 [H_2O_2]_0 \quad (2-86)$$

$$C_8 = \frac{[\cdot O_2^-]}{[H_2O_2]_0} \Rightarrow [\cdot O_2^-] = C_8 [H_2O_2]_0 \quad (2-87)$$

An example of the substitution of these variables into the kinetic rate equations is shown in Equations 2-88 and 2-89 for previously presented Equation 2-48.

$$\frac{d[H_2O_2]}{dt} = -k_1 [H_2O_2] [\cdot OH] \quad (2-48)$$

$$[H_2O_2]_0 \frac{dC_5}{dt} = -k_1 C_5 [H_2O_2]_0 C_7 [H_2O_2]_0 \quad (2-88)$$

$$\frac{dC_5}{dt} = -k_1 C_5 [H_2O_2]_0 C_7 \quad (2-89)$$

The derivation of the pseudo-steady-state equations for the hydroxyl radical begins with a composite equation (Equation 2-90) describing all reactions that produce or consume the radical.

$$\begin{aligned}
\frac{d[\bullet OH]}{dt} = & 2\Phi_{H_2O_2} \varepsilon_{H_2O_2} [H_2O_2] E'_{CFD} - k_1 [H_2O_2] [\bullet OH] \\
& + k_2 [H_2O_2] [\bullet O_2^-] - k_3 [\bullet OH] [\bullet OH] - k_4 [\bullet OH] [\bullet O_2^-] \\
& - k_{MB, \bullet OH} [\bullet OH] [MB] - k_{DOC, \bullet OH} [\bullet OH] (DOC) \\
& - k_{HCO_3^-, \bullet OH} [\bullet OH] [HCO_3^-] - k_{NH_2Cl, \bullet OH} [\bullet OH] [NH_2Cl] \\
& - k_{OCl^-, \bullet OH} [\bullet OH] [OCl^-] - k_{HOCl, \bullet OH} [\bullet OH] [HOCl]
\end{aligned} \tag{2-90}$$

Setting the change in radical concentration equal to zero, Equation 2-90 can be rearranged and written for the pseudo-steady-state hydroxyl radical concentration  $[\bullet OH]_{SS}$  as shown in Equation 2-91.

$$\begin{aligned}
0 = & -k_3 [\bullet OH]_{SS}^2 + [\bullet OH]_{SS} \left\{ -k_1 [H_2O_2] - k_4 [\bullet O_2^-] \right. \\
& - k_{MB, \bullet OH} [MB] - k_{DOC, \bullet OH} (DOC) - k_{HCO_3^-} [HCO_3^-] \\
& \left. - k_{NH_2Cl} [NH_2Cl] - k_{OCl^-} [OCl^-] - k_{HOCl} [HOCl] \right\} \\
& + k_2 [H_2O_2] [\bullet O_2^-] + 2\Phi_{H_2O_2} \varepsilon_{H_2O_2} [H_2O_2] E'_{CFD}
\end{aligned} \tag{2-91}$$

Since this is a quadratic equation, it can be solved using the following equations:

$$A = -k_3 \tag{2-92}$$

$$B = \left( \begin{array}{l} -k_1 [H_2O_2] - k_4 [\bullet O_2^-] - k_{MB, \bullet OH} [MB] - k_{DOC, \bullet OH} (DOC) \\ -k_{HCO_3^-} [HCO_3^-] - k_{NH_2Cl} [NH_2Cl] - k_{OCl^-} [OCl^-] - k_{HOCl} [HOCl] \end{array} \right) \tag{2-93}$$

$$C = k_2 [H_2O_2][\bullet O_2^-] + 2\Phi_{H_2O_2} \varepsilon_{H_2O_2} [H_2O_2] E'_{CFD} \quad (2-94)$$

And

$$[\bullet OH]_{SS} = \frac{-B \pm \sqrt{B^2 - 4AC}}{2A} \quad (2-95)$$

As an example of how Equations 2-92 through 2-95 are written into numerical code, Equation 2-96 displays the steady-state hydroxyl radical concentration in a linear format.

$$\begin{aligned} [\bullet OH]_{SS} = & -(((((-k_1*[H_2O_2])-(k_4*[\bullet O_2^-])-(k_{MB}*[MB])-(k_{DOC}*(DOC))-(k_{HCO_3^-}*[HCO_3^-])- \\ & (k_{NH_2Cl}*[NH_2Cl])-(k_{OCl^-}*[OCl^-])-(k_{HOCl}*[HOCl])))))-(((((-k_1*[H_2O_2])-(k_4*[\bullet O_2^-])- \\ & (k_{MB}*[MB])-(k_{DOC}*(DOC))-(k_{HCO_3^-}*[HCO_3^-])-(k_{NH_2Cl}*[NH_2Cl])-(k_{OCl^-}*[OCl^-])- \\ & (k_{HOCl}*[HOCl]))))^2-(4((-k_3))(((k_2*[H_2O_2]*[\bullet O_2^-])+(2*\Phi_{H_2O_2}* \\ & \varepsilon_{H_2O_2}*[H_2O_2]*E_{CFD}))))))^{0.5})/(2((-k_3))) \end{aligned} \quad (2-96)$$

This equation may also be normalized as discussed before. Substituting the variables defined in Equations 2-84 through 2-87 into Equation 2-90 results in Equation 2-97.

$$\begin{aligned}
[H_2O_2]_0 \frac{dC_7}{dt} = & 2\Phi_{H_2O_2} \varepsilon_{H_2O_2} C_5 [H_2O_2]_0 E'_{CFD} - k_1 C_5 [H_2O_2]_0 C_7 [H_2O_2]_0 \\
& + k_2 C_5 [H_2O_2]_0 C_8 [H_2O_2]_0 - k_3 C_7 [H_2O_2]_0 C_7 [H_2O_2]_0 \\
& - k_4 C_7 [H_2O_2]_0 C_8 [H_2O_2]_0 - k_{MB, \cdot OH} C_7 [H_2O_2]_0 C_6 [MB]_0 \\
& - k_{DOC, \cdot OH} C_7 [H_2O_2]_0 (DOC) - k_{HCO_3^-, \cdot OH} C_7 [H_2O_2]_0 [HCO_3^-] \\
& - k_{NH_2Cl, \cdot OH} C_7 [H_2O_2]_0 [NH_2Cl] - k_{OCl^-, \cdot OH} C_7 [H_2O_2]_0 [OCl^-] \\
& - k_{HOCl, \cdot OH} C_7 [H_2O_2]_0 [HOCl]
\end{aligned} \tag{2-97}$$

Dividing through by the initial concentration of hydrogen peroxide  $[H_2O_2]_0$  results in Equation 2-98.

$$\begin{aligned}
\frac{dC_7}{dt} = & 2\Phi_{H_2O_2} \varepsilon_{H_2O_2} C_5 E'_{CFD} - k_1 C_5 C_7 [H_2O_2]_0 + k_2 C_5 C_8 [H_2O_2]_0 \\
& - k_3 C_7 C_7 [H_2O_2]_0 - k_4 C_7 C_8 [H_2O_2]_0 - k_{MB, \cdot OH} C_7 C_6 [MB]_0 \\
& - k_{DOC, \cdot OH} C_7 (DOC) - k_{HCO_3^-, \cdot OH} C_7 [HCO_3^-] \\
& - k_{NH_2Cl, \cdot OH} C_7 [NH_2Cl] - k_{OCl^-, \cdot OH} C_7 [OCl^-] - k_{HOCl, \cdot OH} C_7 [HOCl]
\end{aligned} \tag{2-98}$$

For the pseudo-steady-state assumption, the time rate change of  $C_7$  is set equal to zero, and the equation solved for  $C_7$ , which can then be identified as  $C_{7,SS}$  as shown in Equation 2-99. In anticipation of performing the same pseudo-steady-state analysis for the superoxide radical, the term  $C_8$  will now be identified as  $C_{8,SS}$ .

$$\begin{aligned}
0 = & -k_3 [H_2O_2]_0 (C_{7,SS})^2 + C_{7,SS} \left\{ -k_1 C_5 [H_2O_2]_0 - k_4 C_{8,SS} [H_2O_2]_0 \right. \\
& - k_{MB, \cdot OH} C_6 [MB]_0 - k_{DOC, \cdot OH} (DOC) - k_{HCO_3^-, \cdot OH} [HCO_3^-] \\
& \left. - k_{NH_2Cl, \cdot OH} [NH_2Cl] - k_{OCl^-, \cdot OH} [OCl^-] - k_{HOCl, \cdot OH} [HOCl] \right\} \\
& + 2\Phi_{H_2O_2} \varepsilon_{H_2O_2} C_5 E'_{CFD} + k_2 C_5 C_{8,SS} [H_2O_2]_0
\end{aligned} \tag{2-99}$$

Since this is a quadratic equation, it can be solved by letting,

$$A = -k_3 [H_2O_2]_0 \tag{2-100}$$

$$\begin{aligned}
B = & -k_1 C_5 [H_2O_2]_0 - k_4 C_{8,SS} [H_2O_2]_0 - k_{MB, \cdot OH} C_6 [MB]_0 \\
& - k_{DOC, \cdot OH} (DOC) - k_{HCO_3^-, \cdot OH} [HCO_3^-] - k_{NH_2Cl, \cdot OH} [NH_2Cl] \\
& - k_{OCl^-, \cdot OH} [OCl^-] - k_{HOCl, \cdot OH} [HOCl]
\end{aligned} \tag{2-101}$$

$$C = 2\Phi_{H_2O_2} \varepsilon_{H_2O_2} C_5 E'_{CFD} + k_2 C_5 C_{8,SS} [H_2O_2]_0 \tag{2-102}$$

And

$$C_{7,SS} = \frac{-B \pm \sqrt{B^2 - 4AC}}{2A} \tag{2-103}$$

A similar process can be followed for the superoxide radical.

$$\frac{d[\cdot O_2^-]}{dt} = k_1 [H_2O_2][\cdot OH] - k_2 [H_2O_2][\cdot O_2^-] - k_4 [\cdot OH][\cdot O_2^-] \quad (2-104)$$

Again, substituting the variables defined in Equations 2-84 through 2-87 into Equation 2-104 results in Equation 2-105.

$$[H_2O_2]_0 \frac{dC_8}{dt} = k_1 C_5 [H_2O_2]_0 C_7 [H_2O_2]_0 - k_2 C_5 [H_2O_2]_0 C_8 [H_2O_2]_0 - k_4 C_7 [H_2O_2]_0 C_8 [H_2O_2]_0 \quad (2-105)$$

Equation 2-106 results from dividing through by the initial concentration of hydrogen peroxide  $[H_2O_2]_0$ .

$$\frac{dC_8}{dt} = k_1 C_5 C_7 [H_2O_2]_0 - k_2 C_5 C_8 [H_2O_2]_0 - k_4 C_7 C_8 [H_2O_2]_0 \quad (2-106)$$

Setting Equation 2-106 equal to zero, solving for  $C_8$  (now called  $C_{8,SS}$ ), and substituting in the variable  $C_{7,SS}$  for  $C_7$  results in Equation 2-107.

$$C_{8,SS} = \frac{k_1 C_5 C_{7,SS}}{k_2 C_5 + k_4 C_{7,SS}} \quad (2-107)$$

Finally, equations for the time rate of change of hydrogen peroxide and methylene blue (or other target contaminant) can be derived and are shown in Equations 2-108 and 2-109, respectively.

$$\begin{aligned} \frac{d[H_2O_2]}{dt} = & -\Phi_{H_2O_2} E'_{CFD} \epsilon_{H_2O_2} [H_2O_2] - k_1 [H_2O_2] [\bullet OH] \\ & -k_2 [H_2O_2] [\bullet O_2^-] + k_3 [\bullet OH] [\bullet OH] \end{aligned} \quad (2-108)$$

$$\frac{d[MB]}{dt} = -k_{MB} [MB] [\bullet OH] - \Phi_{MB} E'_{CFD} \epsilon_{MB} [MB] \quad (2-109)$$

The second term on the right-hand-side of Equation 2-109 represents the direct photolysis component (if any) for the degradation of the organic contaminant. For methylene blue, the direct photolysis component is negligible and  $\Phi_{MB}$  was set equal to zero. Substituting the normalized variables and simplifying results in Equations 2-110 and 2-111.

$$\begin{aligned} \frac{dC_5}{dt} = & -\Phi_{H_2O_2} E'_{CFD} \epsilon_{H_2O_2} C_5 - k_1 C_5 C_{7,SS} [H_2O_2]_0 \\ & -k_2 C_5 C_{8,SS} [H_2O_2]_0 + k_3 C_{7,SS} C_{7,SS} [H_2O_2]_0 \end{aligned} \quad (2-110)$$

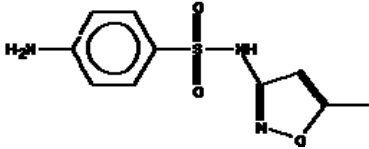
$$\frac{dC_6}{dt} = -k_{MB} C_6 C_{7,SS} [H_2O_2]_0 - \Phi_{MB} E'_{CFD} \epsilon_{MB} C_6 \quad (2-111)$$

### 2.7.2 Sulfamethoxazole Oxidation

The pharmaceutical compound sulfamethoxazole (SMX) was the second organic contaminant investigated in this research. SMX is a sulfa-based antibiotic in the category of sulfonamides typically prescribed for treatment and prevention of infections in both humans and animals (Boreen et al., 2004). Pharmaceuticals such as SMX are currently a concern in

water treatment as their prevalence in wastewater effluent and surface waters has been identified. In a survey of 139 stream sampling sites considered susceptible to human, industrial, and agricultural contamination, Kolpin et al. (2002) identified SMX in up to 19% of the samples at concentrations as high as 1.9  $\mu\text{g/L}$ . Even though concentrations of these pharmaceuticals are relatively low ( $\mu\text{g/L}$  to  $\text{ng/L}$ ), their presence may still result in undesirable effects on the aquatic species (Canonica et al., 2008), including the potential for the development of bacterial resistance to these antibiotics (Kolpin et al., 2002). Research on the ecological and human effects of the presence of these antibiotics in water at concentrations is ongoing. However, such anomalies as feminization of aquatic species have been linked potentially to the presence of pharmaceuticals and endocrine disruptors in the water (Reference, for example, Schwarzenbach et al., 2006). As such, research into appropriate removal and destruction mechanisms for pharmaceuticals such as SMX within water treatment is needed for what is almost certainly to be future regulations and control of these emerging contaminants. Relevant characteristics of sulfamethoxazole are shown in Table 2.3.

**Table 2.3: Characteristics of Sulfamethoxazole**

Common Names <sup>1</sup>	Sulfamethoxazole, Sulfanilamide, n <sup>1</sup> -(5-methyl-3-isoxazolyl)-, Benzenesulfonamide, 4-amino-N-(5-methyl-3-isoxazolyl)-
Formula <sup>1</sup>	C <sub>10</sub> H <sub>11</sub> N <sub>3</sub> O <sub>3</sub> S
Molecular Weight <sup>1</sup>	253.279
Structure <sup>1</sup>	
pK <sub>a,1</sub> <sup>2</sup>	1.6 ± 0.2
pK <sub>a,2</sub> <sup>2</sup>	5.7 ± 0.2
Maximum Absorption Wavelength (neutral state) <sup>3</sup>	268 nm
Maximum Absorption Wavelength (anionic state) <sup>4</sup>	257 nm

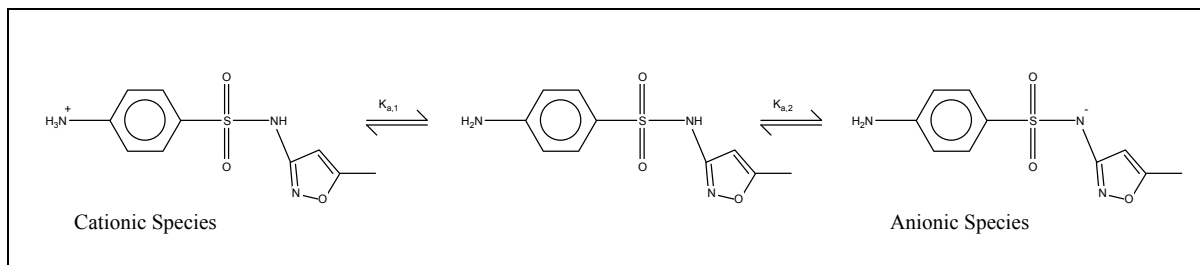
<sup>1</sup> <http://webbook.nist.gov/cgi/cbook.cgi?Name=sulfamethoxazole&Units=SI>

<sup>2</sup> Boreen et al., 2004

<sup>3</sup> Zhou and Moore, 1997

<sup>4</sup> Moore and Zhou, 1994

SMX is an acidic compound (Zhou and Moore, 1997) and the ionic species of SMX have different rates of degradation by direct photolysis; that is, the quantum yield for the direct photolysis of SMX is a function of the protonation state (cationic, neutral, anionic) of the compound (Boreen et al., 2004). These protonation states are shown in Figure 2.4.

**Figure 2.4: Protonation States of Sulfamethoxazole (based on Boreen et al., 2004)**

The anionic species that predominates above the pH value of 5.7 degrades much more slowly than the degradation rate of the neutral species (Boreen et al., 2004). Canonica et al. (2008) present data that identifies the pH dependence of the apparent fluence-based rate constant and molar absorption coefficient for the direct photolysis of sulfamethoxazole. Correlating this dependence to a specific pH (e.g., pH 7.6 as encountered for the pilot study of the current project), the Equations 2-112 through 2-114 may be developed. The photolysis reaction is independent of temperature (Moore and Zhou, 1994). The kinetic rate equation for the direct photolysis of SMX is shown in Equation 2-112.

$$\frac{d[SMX]}{dt} = -\Phi^{app} \varepsilon^{app} E'_{CFD} [SMX] \quad (2-112)$$

In Equation 2-112, the subscript “app” is used to represent composite terms for all ionic species existing for SMX at a given pH (Cannonica et al., 2008). The quantum yield and molar absorptivity then can be divided into the ionic species, and, ignoring the cationic species only relevant at very low pH values, Equation 2-113 is formed based on Canonica et al. (2008).

$$\frac{d[SMX]}{dt} = -\{\varepsilon_1 \Phi_1 + (\varepsilon_2 \Phi_2 - \varepsilon_1 \Phi_1) \alpha_2\} E'_{CFD} [SMX] \left( \frac{1}{U_{254}} \right) \quad (2-113)$$

In Equation 2-113, the subscripts “1” and “2” represent the neutral and anionic species of sulfamethoxazole, respectively. The factor of  $(U_{254})^{-1}$  is a unit conversion between those of the parameters of Canonica et al. (2008) as described in Table 2.4 and those matching the CFD modeling described previously. The parameter  $\alpha_2$  is the fraction of anionic SMX species present and is a function of pH as shown in Equation 2-114.

$$\alpha_2 = \frac{1}{1 + 10^{(pK_{a,2} - pH)}} \quad (2-114)$$

**Table 2.4: pH Dependent Kinetic Rate Parameters (Cannonica et al., 2008)**

Parameter	Value
$\varepsilon_1$	$1189 \pm 23 \text{ m}^2 \text{ mol}^{-1}$
$\Phi_1$	$0.212 \pm 0.018 \text{ mol einstein}^{-1}$
$\varepsilon_2$	$1676 \pm 38 \text{ m}^2 \text{ mol}^{-1}$
$\Phi_2$	$0.046 \pm 0.021 \text{ mol einstein}^{-1}$

Using Equation 2-113 at a pH of 7.85 results in values of  $\varepsilon_{\text{app}} = 16,720 \text{ M}^{-1} \text{ cm}^{-1}$  and  $\Phi_{\text{app}} = 0.0203 \text{ mol einstein}^{-1}$ , which compare favorably to that of  $\varepsilon = 16,580 \text{ M}^{-1} \text{ cm}^{-1}$  and  $\Phi = 0.0297 \text{ mol einstein}^{-1}$  determined experimentally by Baeza and Knappe (2005).

For SMX, the primary mode of degradation is direct photolysis with only a small fraction contributed by advanced oxidation (Cannonica et al., 2008; Baeza and Knappe, 2005; Boreen et al., 2004). However, a second order rate constant between SMX and the hydroxyl radical has been developed by others. Boreen et al. (2004) used Fenton’s reagent and a known radical competitor to calculate a rate constant  $k_{\text{SMX},\text{OH}}$  for the neutral form of SMX

equal to  $(5.8 \pm 0.2) \times 10^9 \text{ M}^{-1} \text{ s}^{-1}$ . Huber et al. (2003) found a similar rate constant of  $(5.5 \pm 0.7) \times 10^9 \text{ M}^{-1} \text{ s}^{-1}$ .

Since the UV and radical dosages encountered in most water treatment processes will be insufficient to completely mineralize SMX, the products of the reactions should be considered. Although it is not the focus of the current project, other investigators have proposed reaction mechanisms and products. In their research, Boreen et al. (2004) determined that up to 35% of SMX became sulfanilic acid under their experimental conditions. This product is consistent with the potential direct photolysis cleavage sites for SMX as presented by Boreen et al. (2004) through references to studies by Weiss et al. and Motten and Chignell. Zhou and Moore (1997) propose that the most important of these photodegradation pathways is the rearrangement of the isoxazole ring following the photolytic rupture of the N-O bond. Hu et al. (2007) studied sulfonamide oxidation using titanium dioxide photocatalysis and proposed that SMX advanced oxidation is initiated by hydroxyl radical attack on either the aromatic/heterocyclic rings or on the sulfonamide bond. Although degradation of target parent compounds may be sufficient to minimize the pharmaceutical effects (Huber et al., 2003) and the stable photoproducts may not be highly toxic compared to the parent compound (Zhou and Moore, 1997), the toxicological consequences of the byproducts in natural water systems and/or in drinking water should be studied further.

As with methylene blue, a normalized differential equation can be developed to describe the rate of change in SMX concentration using CFD. Similar to Equation 2-85, the variable  $C_6$  is now the normalized concentration of SMX as shown in Equation 2-115.

$$C_6 = \frac{[SMX]}{[SMX]_0} \Rightarrow [SMX] = C_6 [SMX]_0 \quad (2-115)$$

Given the units defined in Table 2.3, the unit conversion described for  $E'_{CFD}$  in Equation 2-45 is not required. Substituting Equation 2-115 into Equation 2-113, the normalized equation in CFD describing the direct photolysis of SMX in the CFD code is shown in Equation 2-116.

$$\frac{dC_6}{dt} = -\{\varepsilon_1\Phi_1 + (\varepsilon_2\Phi_2 - \varepsilon_1\Phi_1)\alpha_2\}C_3C_6\left(\frac{1}{U_{254}}\right) \quad (2-116)$$

For completion, the advanced oxidation portion of the degradation can be added to Equation 2-116 resulting in Equation 2-117.

$$\frac{dC_6}{dt} = -\{\varepsilon_1\Phi_1 + (\varepsilon_2\Phi_2 - \varepsilon_1\Phi_1)\alpha_2\}C_3C_6\left(\frac{1}{U_{254}}\right) - k_{SMX, \cdot OH}C_6C_{7,SS}[H_2O_2]_0 \quad (2-117)$$

## 2.8 Advanced Oxidation Process Optimization

Optimization of design parameters requires criteria or metrics that represent the cost and effectiveness of the advanced oxidation system. These metrics should be sensitive to changes in the model parameters, should relate to full-scale system evaluation criteria, and

should be based on common system foundations or outcomes. For many engineering systems, metrics such as capital costs and life-cycle operation and maintenance costs are used to compare treatment systems. For UV reactors, the main cost driver beyond initial capital investment will be energy consumption. Similarly, the effectiveness of an advanced oxidation system can be evaluated based on the overall resource consumption, including energy and chemicals (e.g., hydrogen peroxide), required to achieve some level of chemical conversion or contaminant degradation. Further, the fluence rate distribution in the UV reactor is influenced by the constituents in the water that will absorb UV. Both the organic contaminant and H<sub>2</sub>O<sub>2</sub> will reduce the fluence rate distribution and consequently, reduce the production of hydroxyl radicals throughout the reactor.

Bolton et al. (2001) proposed two figures-of-merit for UV systems performing direct photolysis or advanced oxidation reactions. When the concentration of the target contaminant is high (as defined as kinetics being near zero-order with respect to the contaminant), the electric energy per mass ( $E_{EM}$ ) is defined as the electric energy required to bring about the degradation of a unit mass of the contaminant and may be calculated for a flow through reactor as (Bolton et al., 2001):

$$E_{EM} = \frac{P}{FM(c_i - c_f)} \quad (2-118)$$

$P$  is the rated power (in kW) of the UV system,  $M$  is the molecular weight ( $\text{g mol}^{-1}$ ) of  $c$ ,  $F$  is the water flow rate ( $\text{m}^3 \text{h}^{-1}$ ),  $c_i$  is the influent molar concentration of the contaminant, and  $c_f$  is the effluent molar concentration of the contaminant.

When the concentration of the target contaminant is low (as defined as kinetics being near first-order with respect to the contaminant), the electric energy per order ( $E_{EO}$ ) is defined as the electric energy required to degrade the contaminant by one order of magnitude in a unit volume of water and may be calculated for a flow through reactor as (Bolton et al., 2001):

$$E_{EO} = \frac{P}{F \log_{10} \left( \frac{c_i}{c_f} \right)} \quad (2-119)$$

The variables in Equation 2.119 have the same meaning as defined previously.

By combining capital investment for advanced oxidation reactors, the annual cost of added chemicals or catalysts, and these Figures-of-Merit representing the change in energy consumption for contaminant degradation, the optimization of a UV-initiated advanced oxidation reactor can be achieved. Studies have shown that the  $E_{EO}$  can help assess the electrical energy efficiency of a specific AOP (Cater et al., 2000; Muller and Jekel, 2001; Muller et al., 2001; Stefan and Bolton, 2002).

For this research, a modified  $E_{EO}$  term was used to compare the results of the numerical and pilot-scale trials. This modified metric represents both the energy of the UV

lamp and the hydrogen peroxide dose, resulting in an average annual cost of these two resources. Equation 1-120 describes this new unit metric termed the Annual Average Cost per Order ( $AAC_0$ ) for a change in contaminant concentration from the inlet ( $c_{con,0}$ ) to the outlet ( $c_{con}$ ) of the reactor operating at a flow rate  $Q$ .

$$AAC_0 = \frac{C_{\$,Energy} + C_{\$,H_2O_2}}{\log_{10}\left(\frac{c_{con,0}}{c_{con}}\right)} \times Q \quad (2-120)$$

In Equation 2-120, the cost of energy  $C_{\$,Energy}$  may be expressed as a function of lamp power and a unit power cost  $\left(\frac{\$}{kW-hr}\right)$  as in Equation 2-121. The cost of hydrogen peroxide  $C_{\$,H_2O_2}$  is based on the concentration of chemical added to the system  $c_{H_2O_2}$ , the system flow rate  $Q$ , the characteristics of the chemical being fed (dilution fraction and density), and the unit cost of the chemical, as shown in Equation 2-122.

$$C_{\$,Energy} = \left( P(kW) \times 8760 \frac{hrs}{yr} \times \frac{\$}{kW-hr} \right) \quad (2-121)$$

$$C_{\$,H_2O_2} = \left( \frac{c_{H_2O_2} \left(\frac{mg}{L}\right) \times Q(MGD) \times 8.34 \frac{lb-L}{MG-mg}}{(Dilution\ Fraction)_{H_2O_2} \times Density_{H_2O_2} \left(\frac{lb}{gal}\right)} \times \frac{\$}{gal\ H_2O_2} \times \frac{365\ days}{yr} \right) \quad (2-122)$$

Equation 2-122 may also be written in terms of pounds of hydrogen peroxide fed per day by removing the dilution fraction and liquid density terms and replacing the unit chemical cost by a comparable term for  $\frac{\$}{lb_{H_2O_2}}$ . The result of Equations 2-120 through 2-122 is the Annual

Average Cost per Order with units of  $\frac{\$/yr}{order - MGD}$ . Of course, the time and flow rate terms could be adapted to any units the user chooses.

### 3. RESEARCH APPROACH AND METHODS

The overall goal of this study is to enhance the UV-initiated advanced oxidation design process, including prediction of performance through innovative numerical techniques that assess fluence rate distribution, hydraulic characterization, and photochemical reactions. Successful completion of this goal requires a well-defined research approach, which is described in this section, and shown schematically in Figure 3.1.

#### 3.1 Development of a CFD Model for UV-initiated Advanced Oxidation

The first step in this research was to complete an initial CFD model that could simulate UV-initiated advanced oxidation reactions within a flow-through reactor. A three-dimensional solid model of the UV reactor used in the pilot experiments was created in AutoCAD 2004 (Autodesk, Inc., San Rafael, CA). This model included geometric elements for the reactor, inlet and outlet piping, the UV lamp/quartz sleeve assembly with wiper mechanism, five internal baffle plates, and the inlet and outlet planes. All dimensions were measured directly on the pilot reactor and translated as full-scale into the AutoCAD model. Each of the elements was then saved as an ASCII-type stereolithographic file (extension .stl) and imported into the CFD software. Since the internal baffles were each modeled separately, they could be easily removed to evaluate the baffle configuration on the overall results.

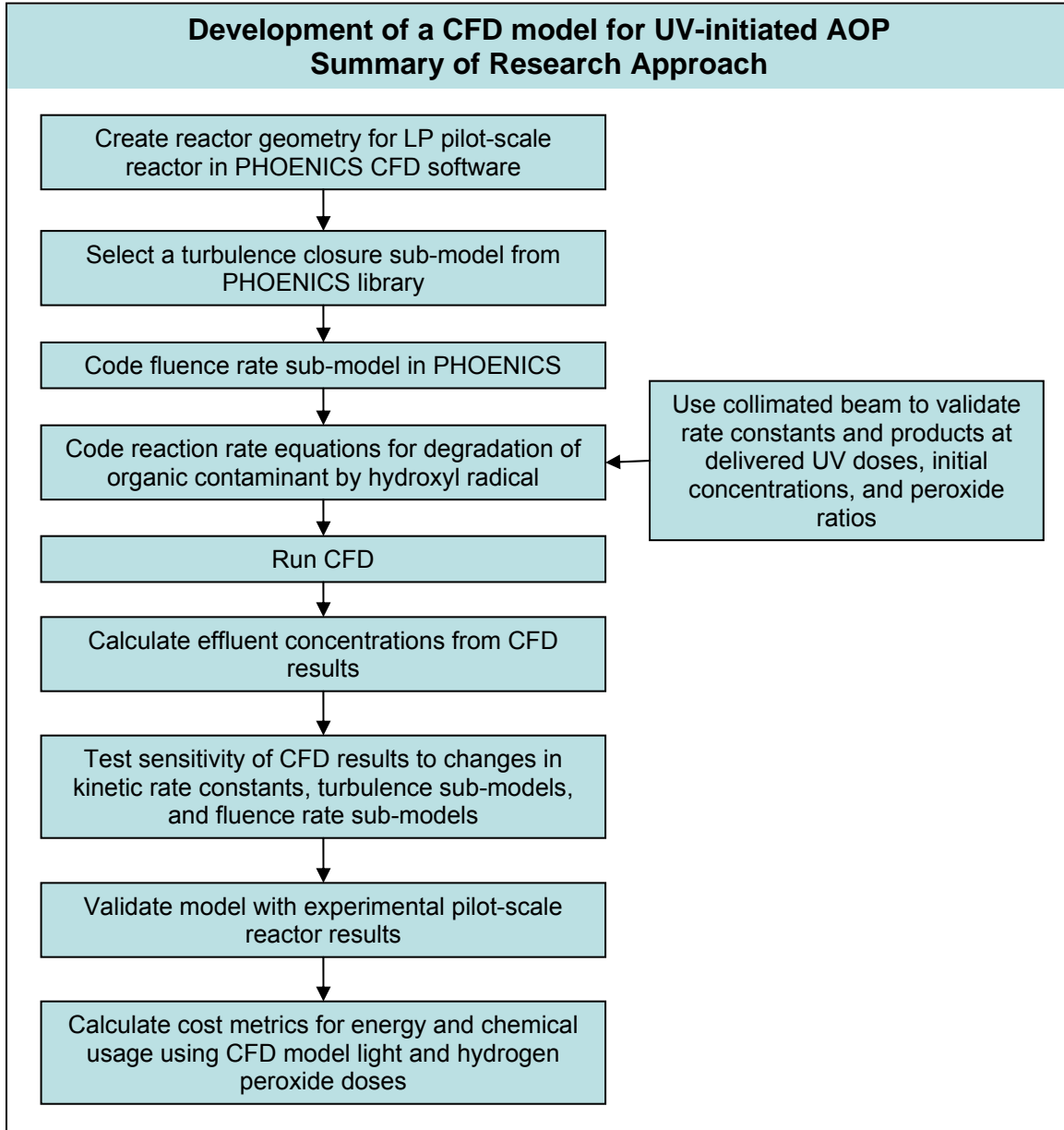


**Figure 3.1: Chart Summary of Research Approach**

PHOENICS (CHAM, Ltd, Wimbledon, England) is the CFD software that was used in this project. The PHOENICS software allows changes to the source code to incorporate numerical descriptions of physics and chemistry that are specific to a given problem. In this

research, the simulation of a photoreacting chemical species required the solution of the continuity equation, Reynolds-averaged Navier Stokes (RANS) equations, and scalar convective-diffusion transport equations (Reference Section 2.3).

Once the geometry was imported, appropriate boundary conditions for inlet and outlet velocities, pressures, and turbulence conditions were selected. Table 3.1 displays the boundary conditions that correspond to the experimental conditions evaluated in this study.

**Table 3.1: CFD Model Boundary Conditions**

Condition	Value
Inlet Velocity (normal to inlet plane)	0.128 – 0.384 m s <sup>-1</sup> (10 – 30 gal min <sup>-1</sup> ) All tangential velocities set to zero.
Outlet Velocity	No external velocity restriction <sup>(1)</sup>
Outlet (External) Pressure	100,000 Pa (Zero Gauge)
Inlet Turbulence Condition (I)	5% <sup>(2)</sup>
Inlet Methylene Blue (MB) Concentration	1.563 x 10 <sup>-6</sup> M
Inlet Hydrogen Peroxide Concentration	(150 – 267 * Inlet [MB]) M

<sup>(1)</sup> For the outlet, the gradients of all variables are zero in the flow direction with the exception of pressure.

<sup>(2)</sup> The turbulent kinetic energy and energy dissipation rate inlet conditions are defined as  $k_{inlet} = (I \times U)^2$  and  $\varepsilon_{inlet} = (k_{inlet})^{1.5} (0.1 \times D)^{-1}$  where  $U$  is the normal average inlet velocity and  $D$  is the pipe diameter.

Since PHOENICS uses a structured rectangular grid, the next step consisted of manually setting grid spacing in all three dimensions. Grid cells were created by selecting the number of intervals in the x-, y-, and z-directions for each region within the solution domain resulting in a total of 859,154 cells. For this simulation, finer grid cells were created within the reactor and in areas within which sharp changes in velocity, pressure, and/or chemistry were expected. Graphical representations of the geometry within CFD and the grid spacing are shown in Figures 3.2 through 3.5.

Numerical convergence, and, further, accuracy of results, is a function of the grid density. At a certain level of refinement, however, the change in results is negligible. One of the first tasks in CFD modeling is finding the appropriate grid dimensions such that the result is essentially grid independent (or more specifically, the change in results with ever finer grids is within selected criteria). Model run times and computer memory requirements are also functions of grid density. As the total number of grid cells increases, the more computer memory is required for PHOENICS to complete the model run. Thus, the extent of the system geometry and the grid refinement must be correlated to reflect available hardware while maintaining accuracy and simulating the important characteristics of the system. For the CFD models completed in this study, the results were considered converged when the net sum of the differences between the inlet and outlet volume fractions (i.e., conservation of mass) was on the order of  $10^{-3}$  or below.

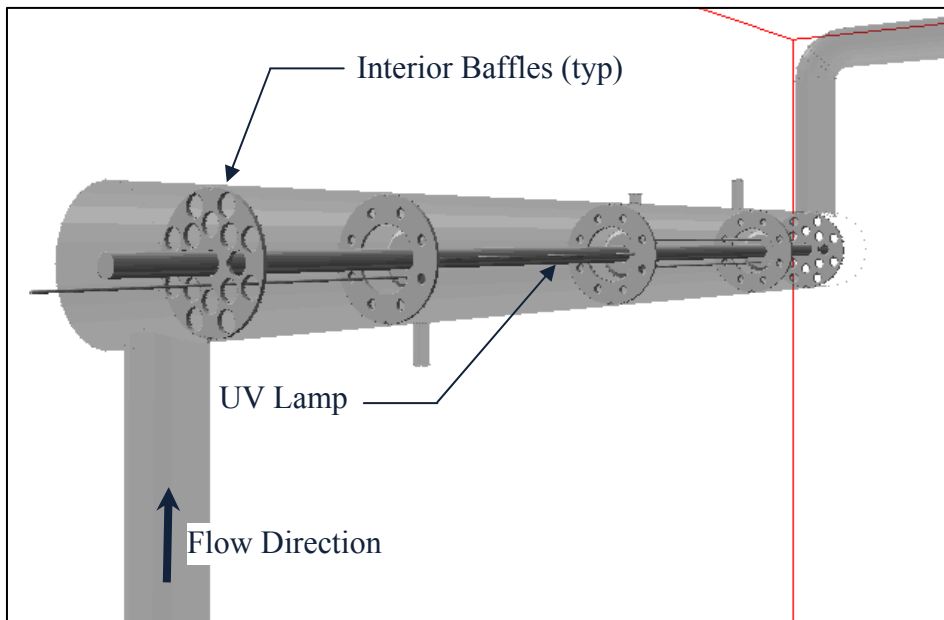


**Figure 3.2: Reactor Geometry within PHOENICS**

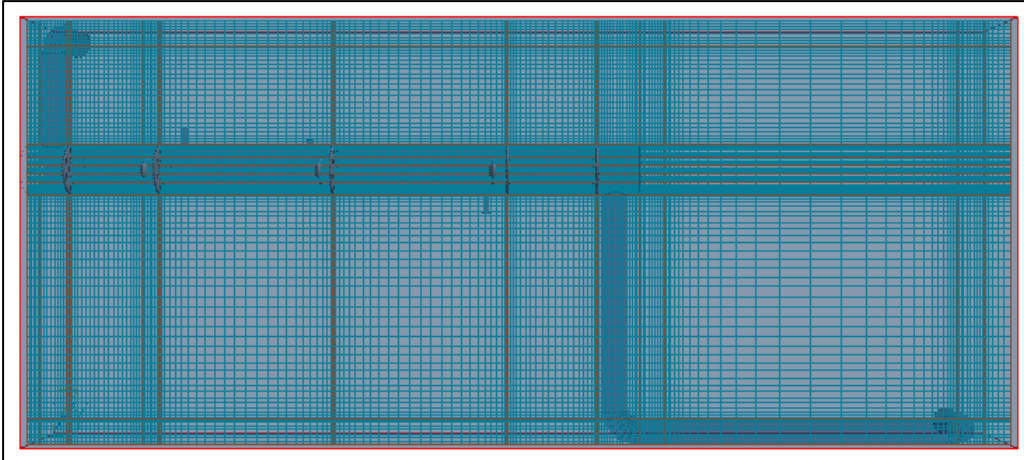


**Figure 3.3: CFD Grid Spacing in Y-Z Plane**

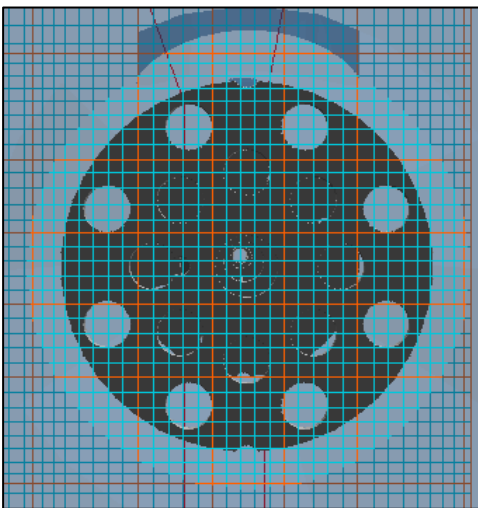


**Figure 3.4: CFD Grid Spacing in X-Z Plane**

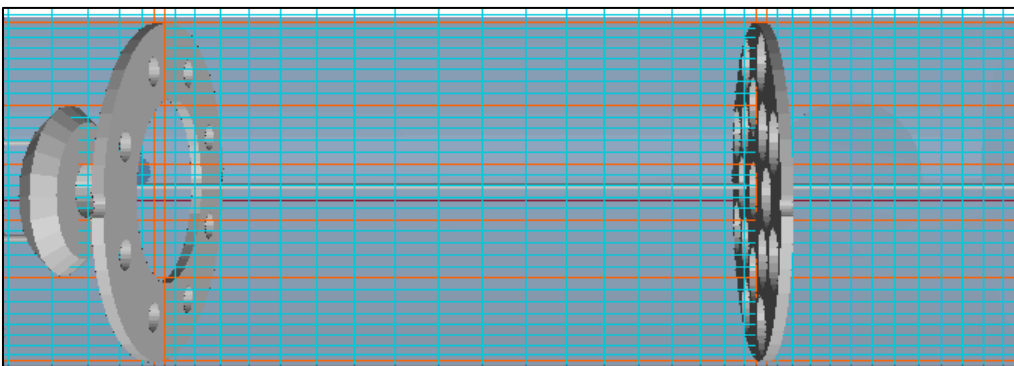


**Figure 3.5: CFD Grid Among Internal Baffles and Wiper Mechanism**

In this study, three two-equation closure models for turbulence were evaluated to simulate flow in the UV reactor. The equations for each of these models ( $k$ - $\epsilon$ , RNG  $k$ - $\epsilon$ , and  $k$ - $\omega$ ) are included within the PHOENICS library and were selected through a user interface menu. A description of the turbulence sub-models is provided in Section 2.4. Although it was intended to use a previously-written modification to the  $k$ - $\omega$  code to convert the 1988 version of the model as included in the PHOENICS library to the 1998 version of the model, the 1998 code would not converge satisfactorily. Thus, results presented for turbulence sub-model sensitivity represent the 1988 version of the  $k$ - $\omega$  model.

The spatial variation of light inside the reactor (i.e., the fluence rate characterization) was simulated using the RAD-LSI model (Liu et al., 2004) and the MSSS model, both as described in Section 2.6. The codes for these two models had been previously written by others and were modified as appropriate for the lamp characteristics and orientation being evaluated in this research. After several iterations of evaluating the length-wise fluence rate patterns, it was determined that the lamp in the reactor was best described by 30 points ( $n=30$ ) in the attenuation factor of the RAD-LSI fluence rate sub-model. The MSSS model divided the lamp into 1000 segments.

The CFD codes (consisting of the PHOENICS q1 text file and the PHOENICS Ground FORTRAN file) were developed as a series of three separate models for each design condition. The first model created the pressure and velocity vector distribution within the system and included the turbulence model and its corresponding equation parameters ( $k$ ,  $\epsilon$ , etc.). The second model used the output of the first and added the fluence rate distribution

throughout the reactor. The third model incorporated the output of the second and solved all of the appropriate kinetic rate equations describing the reactions occurring in the reactor. An example of each of these codes is included as Appendix A.

### 3.2 Development of the Kinetic Rate Equations

After the basic CFD model was created, the next step was the coding of the kinetic rate equations describing the production of hydroxyl radicals from hydrogen peroxide photolysis followed by the destruction of an organic contaminant by reaction with these radicals. The equations are described in detail in Section 2.7. Table 3.2 identifies the variables (C#) utilized within the CFD codes. Many of the constants used in the codes are shown in Table 3.3 and all are defined within the PHOENICS codes as real ground values, or RG(#) (see Appendix A for complete list of constants in the codes).

**Table 3.2: Variables in CFD Codes**

Variable/ Constant	Definition	Units
C1	Initial hydrogen peroxide concentration, $\{[H_2O_2]_0\}$	M
C2	Initial contaminant concentration, {e.g., $[MB]_0$ }	M
C3	Fluence rate	$W\ m^{-2}$
C5	Normalized hydrogen peroxide concentration, $\{[H_2O_2] [H_2O_2]_0^{-1}\}$	Unitless
C6	Normalized contaminant concentration, {e.g., $[MB] [MB]_0^{-1}$ }	Unitless
OHSS or $C_{7,SS}$	Normalized pseudo-steady-state hydroxyl radical concentration, $\{[\bullet OH] [H_2O_2]_0^{-1}\}$	Unitless
O2SS or $C_{8,SS}$	Normalized pseudo-steady-state superoxide radical concentration, $\{[\bullet O_2^-] [H_2O_2]_0^{-1}\}$	Unitless
C9	Normalized non-reacting hydrogen peroxide tracer concentration, $\{[H_2O_2] [H_2O_2]_0^{-1}\}$	Unitless
C10	Normalized non-reacting contaminant tracer concentration, {e.g., $[MB] [MB]_0^{-1}$ }	Unitless

**Table 3.3: Constants in CFD Codes**

Symbol	Definition	Value	Units
$\Phi_{\text{H}_2\text{O}_2}$	Quantum Yield of Peroxide (254 nm)	0.5	mol Einstein <sup>-1</sup>
$k_1$	Kinetic Rate Constant <sup>1</sup>	$2.7 \times 10^7$	M <sup>-1</sup> s <sup>-1</sup>
$k_2$	Kinetic Rate Constant	$1.3 \times 10^{-1}$	M <sup>-1</sup> s <sup>-1</sup>
$k_3$	Kinetic Rate Constant	$5.5 \times 10^9$	M <sup>-1</sup> s <sup>-1</sup>
$k_4$	Kinetic Rate Constant	$7.0 \times 10^9$	M <sup>-1</sup> s <sup>-1</sup>
$k_{\text{MB,OH}}$ (theoretical)	Kinetic Rate Constant	$6.9 \times 10^{10}$	M <sup>-1</sup> s <sup>-1</sup>
$\epsilon_{\text{H}_2\text{O}_2}$	Molar Absorptivity of Peroxide	19.6	M <sup>-1</sup> cm <sup>-1</sup>
$\epsilon_{\text{MB}}$	Theoretical Molar Absorptivity of Contaminant	19	M <sup>-1</sup> cm <sup>-1</sup>
$\Phi_{\text{MB}}$	Direct Photolysis Quantum Yield for Methylene Blue	0 <sup>(2)</sup>	mol Einstein <sup>-1</sup>
$a_{\text{B}}$	Background Absorbance	0 <sup>(3)</sup>	cm <sup>-1</sup>
$\Phi_{\text{SMX}}, \epsilon_{\text{SMX}}$	Constants for Sulfamethoxazole	(4)	-

<sup>1</sup> References for kinetic rate constants are cited in Section 2.7.

<sup>2</sup> Direct photolysis of methylene blue is negligible at the conditions encountered in this study.

<sup>3</sup> Background absorbance is incorporated into the UVT variable.

<sup>4</sup> Parameters related to sulfamethoxazole are a function of pH and are described in Section 2.7.2.

### 3.3 Materials and Analytical Methods

For the bench-scale (collimated beam apparatus) and pilot-scale reactor trials, various materials and methods were employed to evaluate experimental conditions and contaminant degradation. These materials and methods are described below.

#### 3.3.1 Materials

Dry methylene blue (Alfa Aesar, Acros Organics) and hydrogen peroxide solution (30% w/v, Fisher Scientific, Pittsburgh, PA) were used as purchased without further purification. For both collimated-beam and pilot reactor testing, the methylene blue and hydrogen peroxide were diluted separately with dechlorinated ultra-filtered deionized water (Dracor High Purity Water Systems) (herein referred to as DI water). Reagents used for

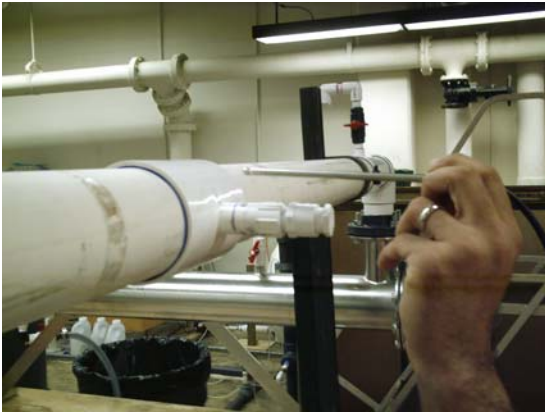
analyses, including potassium iodide, potassium iodate, sodium hydroxide, ammonium molybdate tetrahydrate, and potassium hydrogen phthalate, were acquired as ACS-grade or similar solids from Fisher Scientific (Pittsburgh, PA). Pilot influent water was pumped from a 10,000-gallon concrete reservoir filled with GAC-filtered (NORIT GAC400) municipal tap water from Raleigh, NC.

### 3.3.2 Analytical Methods

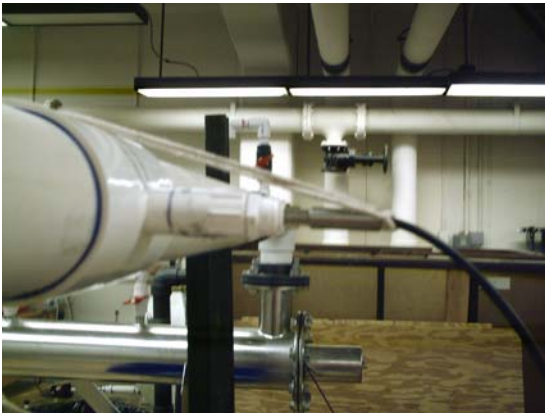
As mentioned previously, many organic dyes, such as methylene blue, are decolorized upon oxidation by the hydroxyl radical. Thus, the concentration of the dye can be monitored by measuring solution absorbance at the wavelength of maximum absorbance (i.e., 661 nm for methylene blue). In this research, methylene blue concentration at the pilot reactor effluent was measured using a UV/Vis spectrophotometer (Cary 50, Varian, Inc., Walnut Creek, CA) coupled to a fiber optic spectrophotometric probe (C Technologies, Inc., Bridgewater, NJ) inserted into the reactor effluent pipe. For bench-scale experiments using the collimated beam apparatus, the probe was replaced with a conventional 1-cm pathlength quartz cuvette. The spectrophotometer and fiber optic probe are shown in Figures 3.6 and 3.7.



**Figure 3.6: Photograph of Pilot Reactor Spectrophotometer System**



(a)



(b)

**Figure 3.7: Spectrophotometric Probe (a) and Probe Mounted in Pipe (b)**

Total chlorine concentration of the pilot reactor influent was tested using a Hach Pocket Colorimeter. Total alkalinity was measured using Standard Methods (19<sup>th</sup> Edition, 1995) Method 2320. Hydrogen peroxide residual concentrations were measured using the method described by Klassen et al. (1994).

Sulfamethoxazole (SIGMA Chemical Co., St. Louis, MO) was used as purchased without further purification. Concentrations of sulfamethoxazole (SMX) were quantified by high performance liquid chromatography. The analytical equipment consisted of a Waters (Milford, MA) 1525 Binary HPLC Pump, a Waters 717+ Autosampler, a C18-AQ HPLC column (5 micron, 4.6 x 250 mm, Alltima HP, Grace), and a Waters 2487 Dual Wavelength Absorbance Detector. The HPLC setup is shown in Figure 3.8. The analytical method for SMX utilized a mobile phase (eluent) consisting of 24% v/v acetonitrile and 76% v/v 25 mM ammonium acetate buffer (pH 5) operated in an isocratic mode at a flow rate of 1.0 mL min<sup>-1</sup>. The UV detector was set at 266 nm. Chromatograms were processed using the Waters software Breeze Version 3.0. All aqueous samples containing hydrogen peroxide were quenched with sodium thiosulfate solution immediately after sampling. All samples were filtered through 0.22- $\mu$ m membrane filters prior to HPLC injection.

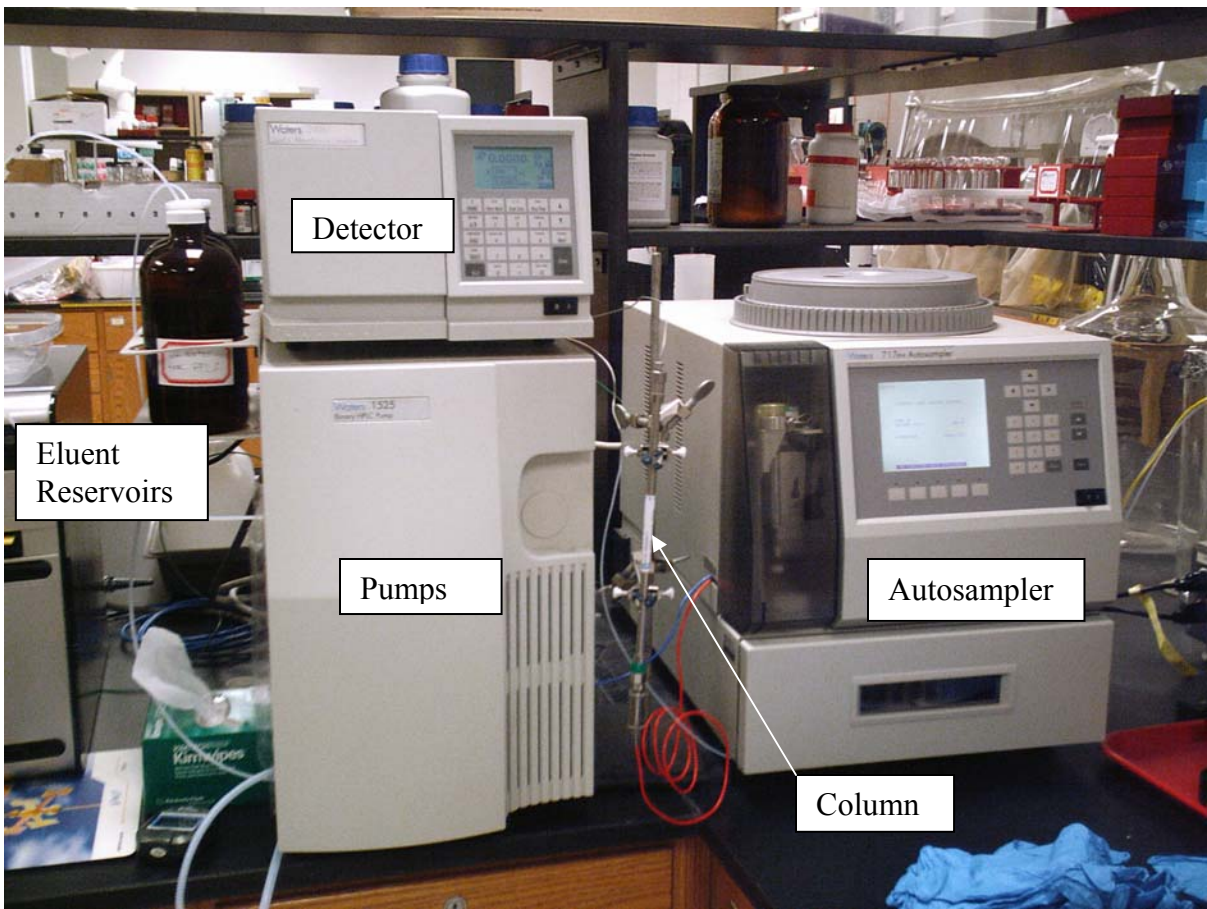


**Figure 3.8: Photograph of HPLC Setup**

Total organic carbon (TOC) was measured by the Town of Cary (NC) water quality laboratory using a Tekmar-Dohrmann Phoenix 8000 analyzer. The pH of the water matrix for each pilot run was measured using a Thermo Orion Model 410 pH meter calibrated weekly using a two-point standard. UV transmittance at 254 nm (UVT<sub>254</sub>) was measured in a 1-cm pathlength quartz cuvette using the Varian Cary 50 spectrophotometer zeroed with DI water.

### 3.3.2.1 Methylene Blue Calibration Curve

The correlation between absorbance at a wavelength of 661 nm and methylene blue concentration was determined from the preparation of a calibration curve using known concentrations of methylene blue. New calibration curves were prepared approximately every other month during the experimental phase of the research. Spike checks of the curve validity were performed intermittently. The set of calibration curves, including the linear regression results, are shown in Figure 3.9.

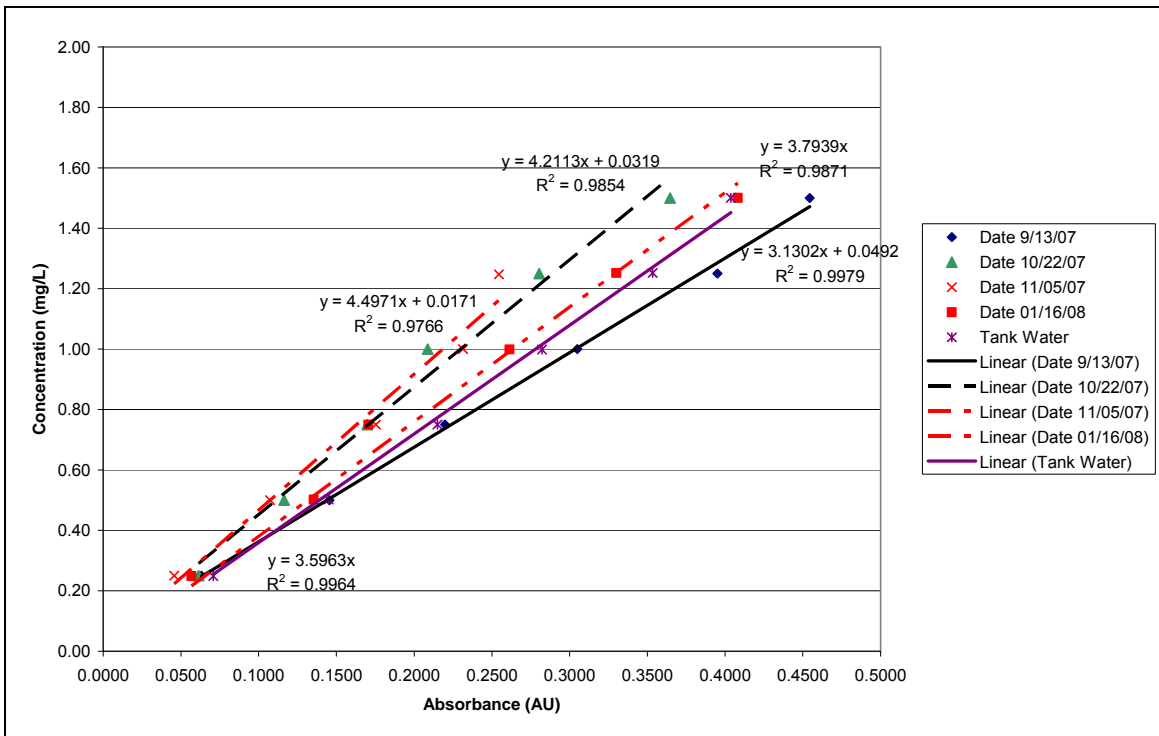


**Figure 3.9: Methylene Blue Calibration Curves**

### 3.3.2.1 Sulfamethoxazole Calibration Curve

A calibration curve correlating the area under the chromatographic peak and mass concentration was determined for SMX. Initial data on the measurement of SMX using the HPLC method described earlier was provided by others (Rossner, 2008). Standards of known SMX concentrations were included with the pilot reactor experiment samples and those standards were found to match well with the data from Rossner. The calibration curve for SMX is shown in Figure 3.10.

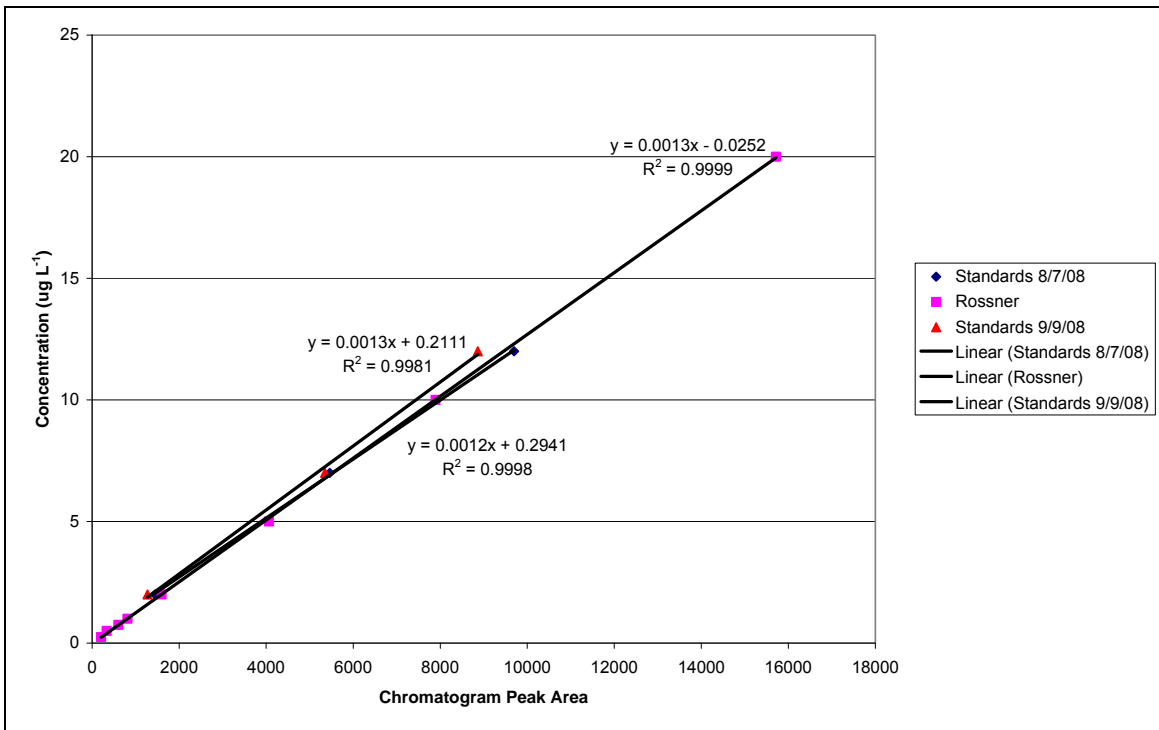
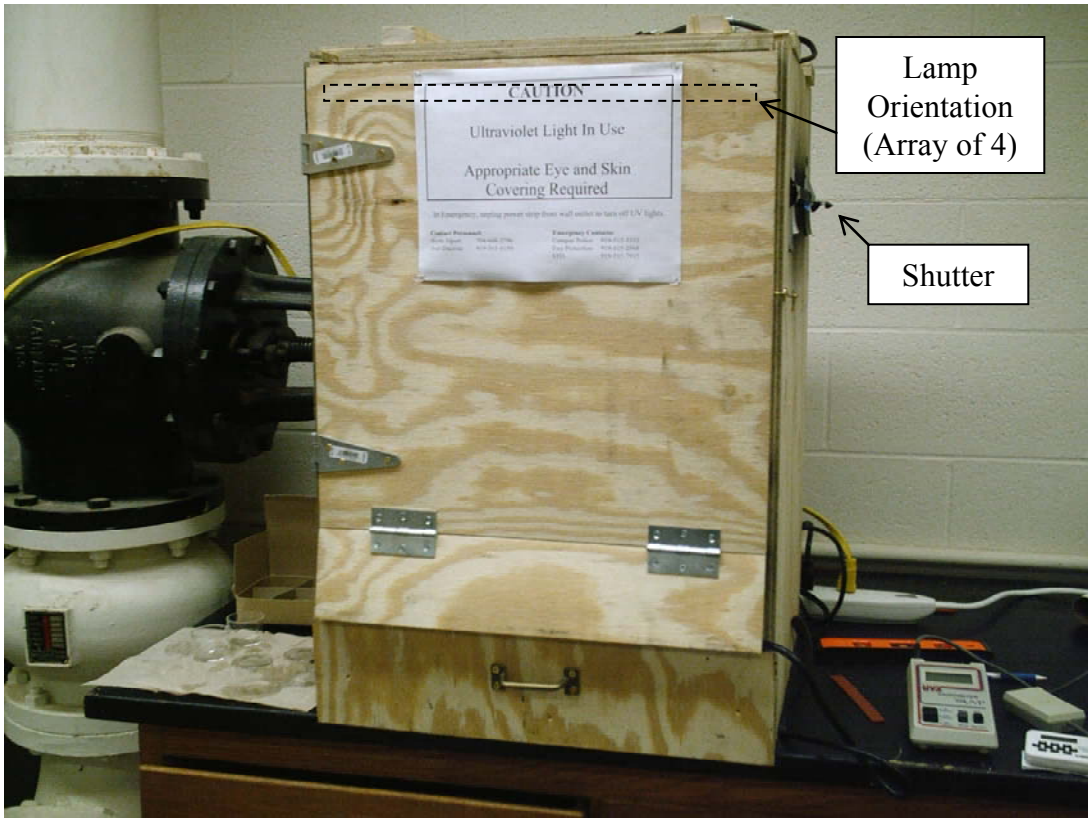


Figure 3.10: Sulfamethoxazole Calibration Curve

### 3.4 Collimated Beam Testing of Dye Degradation

A low-pressure collimated beam apparatus was used to evaluate the dose-response and second-order rate constant of methylene blue. The collimated beam apparatus, constructed as part of this research, is shown in Figures 3.11 and 3.12. Light is provided by four 18" 15W T8 UV lamps mounted horizontally (left to right end-to-end as seen from front) in a fixture that rests on the top of the unit. Pseudo-collimation is achieved through two parallel wooden plates with 4"-diameter apertures and approximately 3" separation. A drawer at the base of the unit holds the elevated platform, magnetic stir plate, and sample. A thin plate above the highest aperture plate and extending beyond the unit walls serves as the shutter. All interior surfaces are painted flat black to minimize light reflection. The reaction vessel is a shallow cylindrical container (crystallization dish) where mixing is enhanced by magnetic stirring to achieve UV dose uniformity.



**Figure 3.11: Collimated Beam Apparatus**

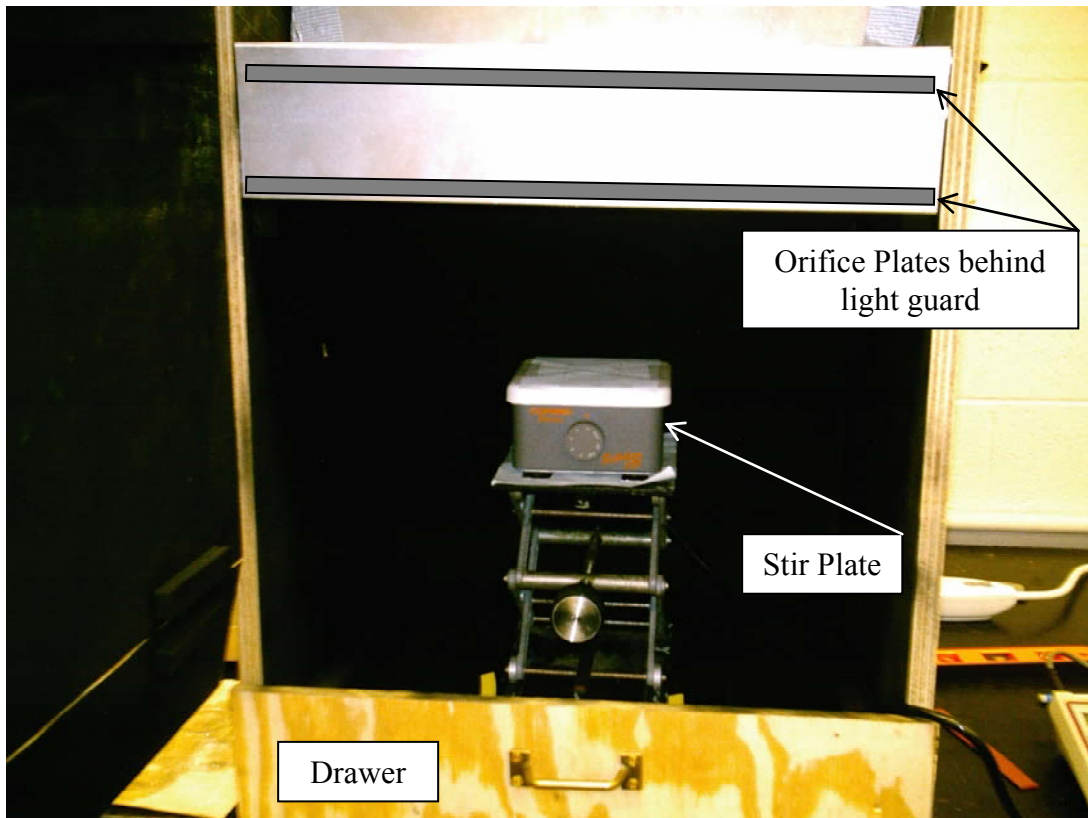


**Figure 3.12: Collimated Beam Apparatus Sample Area**

A radiometer (UVP Model UVX Digital Radiometer, Upland, CA) was used to measure the UV irradiance at 254 nm at the water surface elevations. Chemical actinometry using the KI/KIO<sub>3</sub> reaction (Rahn, 1997; Rahn et al., 2006) was used periodically to verify the radiometer readings. The actinometry calculations for the collimated beam experiments included appropriate correction factors as defined by Bolton and Linden (2003). The use of these correction factors is demonstrated in Figure 3.13, which shows the results of a radiometer validation experiment using the KI/KIO<sub>3</sub> actinometer.

**KI/KIO<sub>3</sub> Actinometer LP Collimated Beam Testing**

Date: 3/12/2008  
 Analyst: Scott Alpert/Colleen Bowker  
 Lamp warm-up time (min): 35.000

Radiometer: UVP Model UVX Digital Radiometer

**Actinometry:**

0.6M iodide and 0.1M iodate in a 0.01M borax buffer

Important Parameters

T (Sample) = 24 deg-C	Quantum Yield = 0.68224 mole/E
$\lambda$ = 254 nm	Conversion to Einstein = 4.71E+08 mJ/Einstein
d = 5 cm	Surface Area = 19.63 cm <sup>2</sup>
v = 0.010 L	Reflection Factor = 0.975
Abs (254nm) = 0.001	Extinction coefficient( $\epsilon$ ) = 26400 L/mol-cm
Sample Depth = 0.509 cm	Abs (352nm) Blank = 0
Averaging Factor = 0.999	Abs (352nm) Blank + 0 dose = 0
Petri Factor = 0.97	Pathlength = 1 cm

Sample Number	Measured Fluence Rate - Before Exposure (mW/cm <sup>2</sup> )	Measured Fluence Rate - After Exposure (mW/cm <sup>2</sup> )	Exposure Time (sec)	Abs(352)	Fluence Determined by Actinometry (mJ/cm <sup>2</sup> )	Fluence Determined by Radiometer (mJ/cm <sup>2</sup> )
1	0.9900	0.9800	0	0.048	0.00	0.00
2	0.9900	0.9800	0	0.048	0.00	0.00
3	0.9800	0.9800	0	0.043	0.00	0.00
4	0.9800	0.9800	10	0.820	10.53	9.54
5	0.9800	0.9900	10	0.825	10.60	9.59
6	0.9800	0.9900	15	1.189	15.63	14.38
7	0.9800	0.9900	15	1.273	16.72	14.38
8	0.9900	0.9900	20	1.599	21.17	19.27
9	0.9800	0.9800	20	1.586	21.06	19.08
10	0.9800	0.9800	30	2.342	31.30	28.61
11	0.9900	0.9900	30	2.438	32.62	28.90

**Averaged Data**

Measured Fluence Rate - Before Exposure (mW/cm <sup>2</sup> )	Exposure Time (sec)	Abs(352)	Fluence Determined by Actinometry (mJ/cm <sup>2</sup> )	Fluence Determined by Radiometer (mJ/cm <sup>2</sup> )	Difference (%) (Radiometer-Actinometer)
0.9833	0	0.046	0.00	0.00	-
0.9825	10	0.822	10.07	9.56	-5.27%
0.9850	15	1.231	15.37	14.38	-6.89%
0.9850	20	1.593	20.06	19.17	-4.64%
0.9850	30	2.390	30.40	28.76	-5.71%

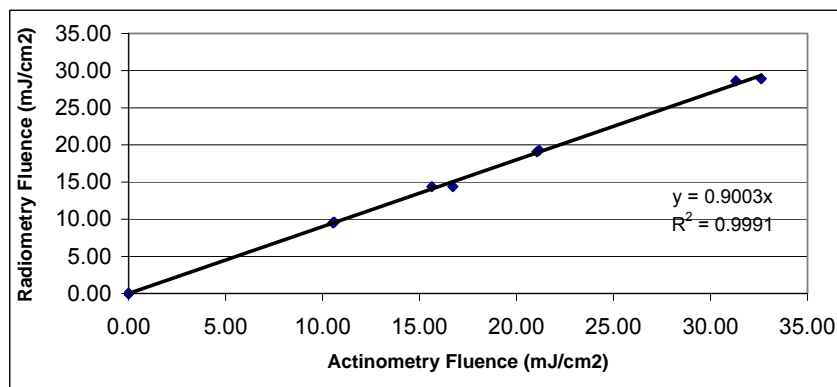


**Figure 3.13: KI/KIO<sub>3</sub> Actinometric Validation of Radiometer**

### 3.4.1 Kinetic Rate Constants

The calculation of second-order rate constants for advanced oxidation reactions involving hydroxyl radicals requires knowledge of the radical concentration within the system. Since hydroxyl radicals are difficult to measure directly, experiments using competition kinetics may be performed. In competition kinetics, the reaction of a compound with a known second-order rate constant is used to determine the concentration of hydroxyl radicals in the system. This radical concentration may then be used to calculate the second-order rate constant of the target compound.

To determine the second order rate constant for methylene blue, a competition kinetics method described by Rosenfeldt and Linden (2004) was used and is summarized herein. In this method, known concentrations of isopropyl alcohol (IPA) were used as a radical competitor within UV-exposed crystallization dishes containing a solution of methylene blue and hydrogen peroxide. By varying the initial concentration of IPA and measuring the methylene blue concentration before and after exposure, a graph of the inverse of the pseudo-first-order rate constant  $(k'_{MB})^{-1}$  (s) as a function of the initial IPA concentration (M) was prepared. The slope and y-intercept of a linear regression of this data was then used to determine the second-order rate constant for the reaction between methylene blue and the hydroxyl radical  $(k''_{MB})$ . A derivation of this process is summarized in Equations 3-1 through 3-16 (Rosenfeldt and Linden, 2004).

$$\frac{d[MB]}{dt} = -k'_{MB} [MB] \quad (3-1)$$

$$k'_{MB} = k''_{MB} [\bullet OH] \quad (3-2)$$

$$\ln \frac{[MB]}{[MB]_0} = -k'_{MB} t \quad (3-3)$$

$$\frac{1}{k'_{MB}} = -\frac{t}{\ln \frac{[MB]}{[MB]_0}} \quad (3-4)$$

Although Equation 3-4 appears to be for a single time point, a regression of many points for a single experiment could be used to calculate the inverse of the first order rate constant. If the pseudo-steady-state approximation is used for the radical concentration, the derivation can be continued as follows:

$$k'_{MB} = k''_{MB} [\bullet OH]_{SS} \quad (3-5)$$

$$[\bullet OH]_{SS} = \frac{R_{\bullet OH}^{Form}}{\sum k''_{S, \bullet OH} [S]} \quad (3-6)$$

In Equation 3-6,  $R_{\bullet OH}^{Form}$  represents the rate of hydroxyl radical formation and S represents the hydroxyl radical scavengers.

$$k'_{MB} = k''_{MB} \frac{R_{\cdot OH}^{Form}}{\sum k''_{S,\cdot OH} [S]} \quad (3-7)$$

Substitution of the major radical scavengers for these experiments in DI water into Equation 3-7 results in Equation 3-8.

$$k'_{MB} = \frac{k''_{MB} R_{\cdot OH}^{Form}}{k''_{IPA} [IPA] + k''_{H_2O_2} [H_2O_2] + k''_{MB} [MB]} \quad (3-8)$$

Rearrangement of the equation then reveals Equation 3-9.

$$\frac{1}{k'_{MB}} = \left( \frac{k''_{IPA}}{k''_{MB} R_{\cdot OH}^{Form}} \right) [IPA] + \left( \frac{k''_{H_2O_2} [H_2O_2]}{k''_{MB} R_{\cdot OH}^{Form}} + \frac{[MB]}{R_{\cdot OH}^{Form}} \right) \quad (3-9)$$

From this linear equation, the slope (m) and intercept (b) can be written.

$$m = \left( \frac{k''_{IPA}}{k''_{MB} R_{\cdot OH}^{Form}} \right) \quad (3-10)$$

$$b = \left( \frac{k''_{H_2O_2} [H_2O_2]}{k''_{MB} R_{\cdot OH}^{Form}} + \frac{[MB]}{R_{\cdot OH}^{Form}} \right) \quad (3-11)$$

Rearranging Equation 3-10 results in Equation 3-12.

$$R_{\cdot OH}^{Form} = \left( \frac{k_{IPA}''}{k_{MB}''m} \right) \quad (3-12)$$

Substitution of Equation 3-12 into Equation 3-11 results in Equation 3-13.

$$b = \left( \frac{k_{H_2O_2}'' [H_2O_2] m}{k_{IPA}''} + \frac{m [MB] k_{MB}''}{k_{IPA}''} \right) \quad (3-13)$$

Rearranging Equation 3-13 and solving for  $k_{MB}''$  results in Equation 3-14.

$$k_{MB}'' = \frac{bk_{IPA}'' - k_{H_2O_2}'' [H_2O_2] m}{[MB]} \quad (3-14)$$

$$k_{IPA}'' = 1.9 \times 10^9 \text{ M}^{-1} \text{ s}^{-1} \text{ (Rosenfeldt and Linden, 2004)} \quad (3-15)$$

$$k_{H_2O_2}'' = 2.7 \times 10^7 \text{ M}^{-1} \text{ s}^{-1} \text{ (Buxton et al., 1988)} \quad (3-16)$$

Since  $k_{IPA}''$  and  $k_{H_2O_2}''$  are known, the second order rate constant for methylene blue can be determined using Equation 3-14 and the initial concentrations of hydrogen peroxide and methylene blue. Note, however, that by substituting the initial concentrations of  $H_2O_2$  and methylene blue for the instantaneous concentrations described by Equation 3-14, error can be introduced if the concentration of either compound changes significantly during the reaction. For the conditions investigated, hydrogen peroxide is expected to change by no more than 1-2% between initial and final concentrations; however, the methylene blue

degradation could be significant depending on the UV dose. Thus, the error introduced in the calculation of the second-order rate constant must be considered in evaluating the accuracy of the results.

### 3.4.2 Dye Degradation Reaction Reversibility and Stability

It was not expected that the decolorization of the organic dye would be significantly reversible under the time and concentration conditions to be encountered in this experiment. However, since the concentration of the dye can be monitored easily using a spectrophotometer, testing was performed to check this assumption. For the molar ratios being studied, hydrogen peroxide and dye were combined in a crystallization dish and placed under the collimated beam. Following exposure, the spectrophotometric probe was placed in the dish and the instrument was programmed to monitor the absorbance over a period of 20 minutes. By evaluating the change in absorbance, it should become apparent whether there is significant reversibility in the decolorization or delayed production of any intermediates that interfere with the absorbance at a specific wavelength.

In order to check the stability of the methylene blue degradation reaction, a bench-scale test was conducted to determine if methylene blue and its oxidative derivatives continue to react at a significant rate after pilot effluent samples were collected. Sodium thiosulfate, which has negligible absorbance at 661 nm, was used as a quenching agent to neutralize the residual hydrogen peroxide in the test samples (Liu et al., 2003).

### 3.5 CFD Evaluation of Turbulence and Fluence-Rate Sub-Models

With the kinetic rate equations for the methylene blue advanced oxidation reactions coded into the CFD software, the model was executed with three different turbulence sub-models (Figure 3.14) and two different fluence rate sub-models (Figure 3.15), all of which have been described in detail in Section 2. The CFD results were evaluated to determine the effect, if any, of these sub-models on the effluent concentrations of the methylene blue.

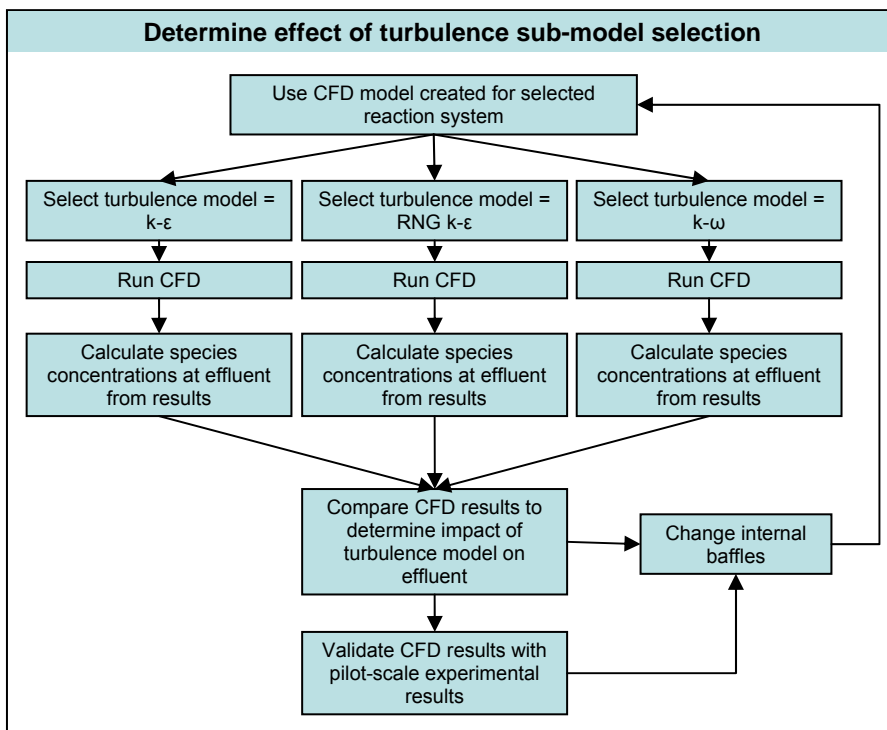


**Figure 3.14: Determination of Turbulence Model Sensitivity**

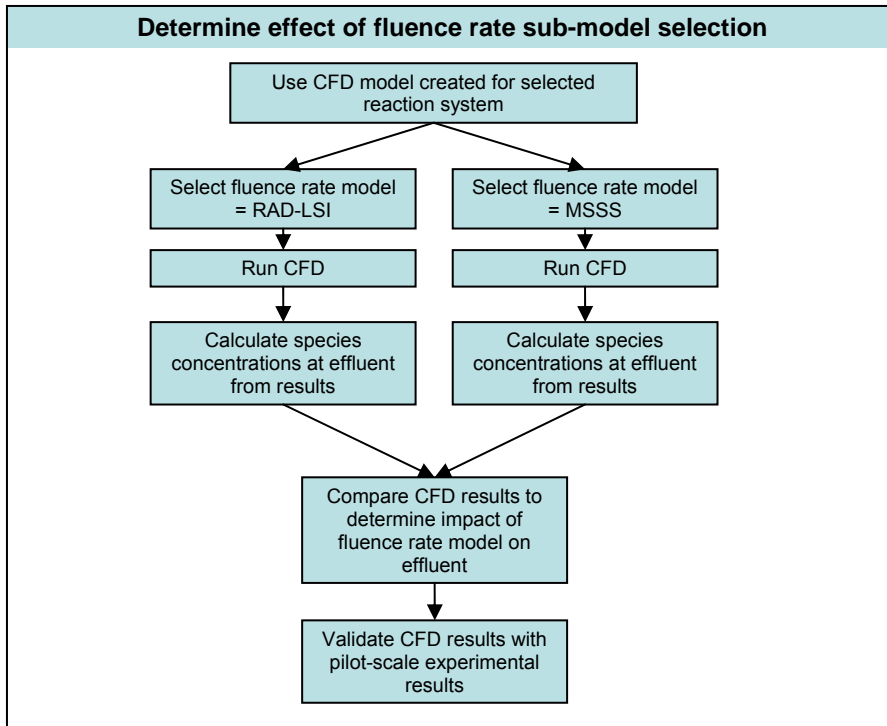


**Figure 3.15: Determination of Fluence Rate Model Sensitivity**

### 3.6 CFD Model Evaluation of Design Parameters

The CFD model was executed with several combinations of output lamp power, UV transmittance, influent hydrogen peroxide concentrations, and radical scavenger concentrations to determine the impact on the methylene blue advanced oxidation reaction. Although it is a characteristic of the target contaminant and not an adjustable design parameter, the second-order rate constant was also evaluated to determine the effect of its value on the contaminant degradation within a given set of design parameters.

As discussed in the description of competition kinetics for rate constant validation, the reaction between the hydroxyl radical and methylene blue can be described as pseudo-

first-order if the plot of  $\ln\left(\frac{[MB]}{[MB]_0}\right)$  versus time is linear and the concentration of hydroxyl radicals is assumed to be constant. In this case, the pseudo-first-order reaction rate constant  $k'_{MB}$  is equal to the second-order reaction rate constant  $k''_{MB}$  multiplied by the concentration of hydroxyl radicals  $[\bullet OH]$ . Thus, by changing the conditions which influence the concentration of hydroxyl radicals within the system, the pseudo-first-order reaction rate constant can be changed. Similarly, for a constant hydroxyl radical concentration, second-order rate constants known for other contaminants can be applied to change the pseudo-first-order reaction rate constant. In addition, the change in light intensity, UVT, radical scavenger concentrations, and hydrogen peroxide concentrations effectively change the concentration of hydroxyl radicals available for contaminant degradation.

### 3.7 Validation of CFD Results for Dye Degradation Using the Pilot-Scale Reactor

The objective of this step is to validate the CFD results with pilot scale experiments under the same reaction conditions. A pilot reactor system that matches that modeled in CFD was constructed. A schematic of the low-pressure UV pilot scale system is presented in Figure 3.16.

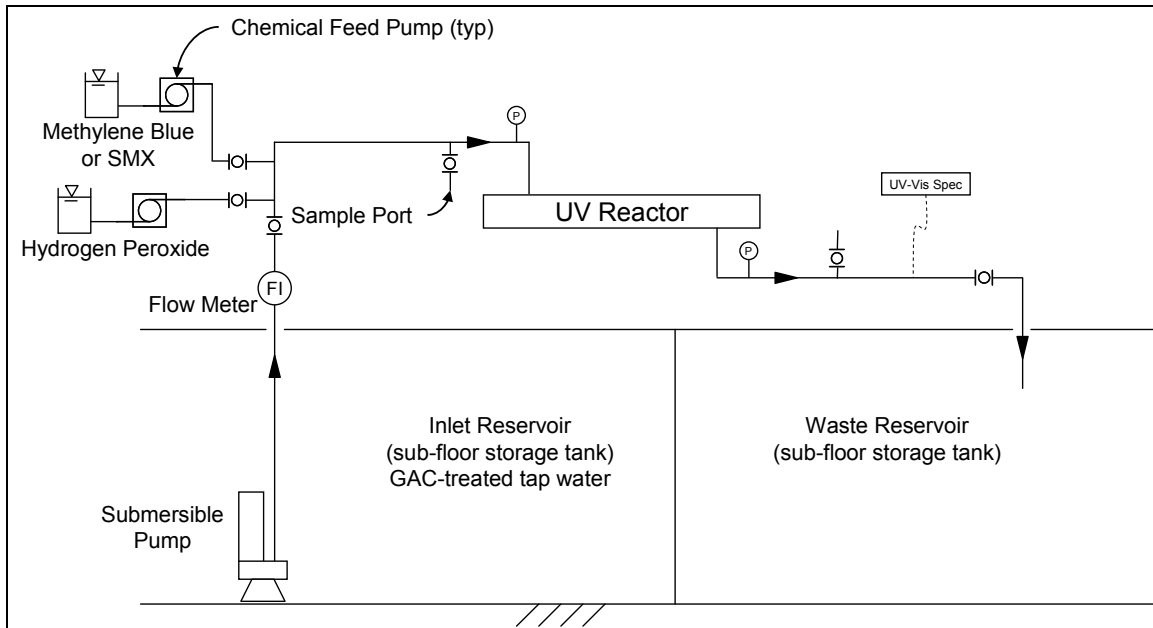


**Figure 3.16: Low-Pressure UV Pilot System Schematic (NTS)**

A 6"-diameter cylindrical stainless steel UV reactor was provided by Degremont's North American Research and Development Center (DENARD). A single low-pressure high-output UV lamp (Ondeo Degremont, No. 61645-G01, 52W nameplate output at 254 nm) was installed axially along the 6'-long reactor. Five removable perforated baffle plates were installed symmetrically about the center of the reactor. Sampling valves were installed within three feet of the influent and effluent of the reactor. One ball valve located upstream and one located downstream of the reactor were used to throttle flow between 5 and 50 gallons per minute. Two diffuser mechanisms were installed upstream of the reactor through which a contaminant (methylene blue or sulfamethoxazole) and hydrogen peroxide solutions were injected into the system. Flow rates of the contaminant and hydrogen peroxide solutions were controlled by peristaltic pumps. The diffusers were located immediately downstream of the flow regulating valve, the turbulence from which provided additional

mixing of the chemicals prior to the reactor influent. Photographs of the system are shown in Figures 3.17 through 3.21.



**Figure 3.17: Overview of Pilot Reactor System**

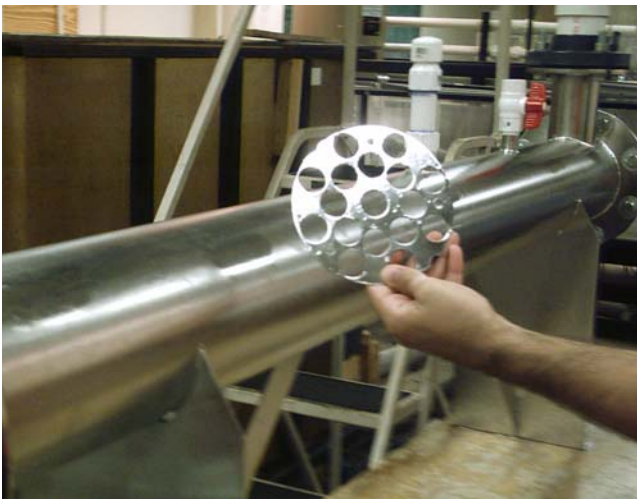


**Figure 3.18: Baffle Plate from Reactor Interior**

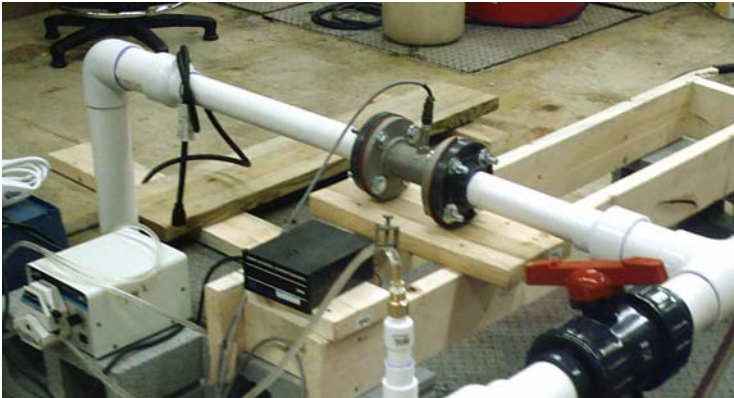


**Figure 3.19: Flow Meter for Pilot Reactor**



**Figure 3.20: Pilot UV Intensity Sensor**

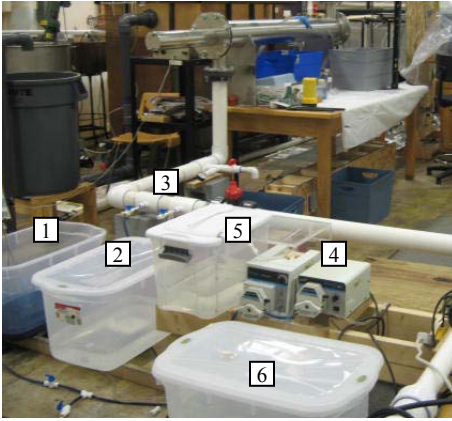


**Figure 3.21: Pilot Chemical Feed System**

(1) Methylene Blue Feed Tank, (2) Hydrogen Peroxide Feed Tank, (3) Chemical Injection Points, (4) Chemical Feed Peristaltic Pumps, (5) Sulfamethoxazole Feed Tank, and (6) Wash Feed Tank

Before each trial, a water sample was taken from the inlet reservoir and tested for total chlorine and total alkalinity. The hydrogen peroxide peristaltic pump then was turned on and allowed to achieve a steady-state (greater than 5 detention times) before a sample was withdrawn from the influent sampling valve and immediately tested to confirm proper hydrogen peroxide concentration. If the concentration was higher or lower than the trial target, the peristaltic pump was adjusted accordingly and another sample was withdrawn and tested. The peroxide pump was then stopped.

After lamp warm-up (greater than 1 hour), the contaminant peristaltic pump was started. For methylene blue, the effluent concentration was monitored real-time with the spectrophotometer and adjustments were made as necessary to achieve the desired concentration of  $0.5 \text{ mg L}^{-1}$ . Once a steady-state was achieved, a grab sample (GS1) was taken from the influent sampling valve. For sulfamethoxazole, the calibrated flow rate from the peristaltic pump and the injected batch concentration were used to estimate the influent

sulfamethoxazole concentration, which was later confirmed with analysis of the influent grab samples. The hydrogen peroxide peristaltic pump was then turned on at the preset flow rate. Once a new steady-state was reached, grab samples were taken from the influent (GS2) and effluent (GS3). For the methylene blue, each steady-state condition was confirmed by the absorption trends on the spectrophotometer. Steady-state conditions for sulfamethoxazole were estimated with multiples of calculated detention times. Steady-state conditions were monitored/timed after each change in contaminant and hydrogen peroxide flow (on/off or adjustment). Following each trial run and the stoppage of both contaminant and hydrogen peroxide, the reactor and system piping were rinsed. Rinsing of the reactor consisted of the injection of a dilute solution of laboratory glassware soap into the influent piping followed by ten or more minutes of clean water rinsing to flush any residual contaminant or hydrogen peroxide from the reactor.

Within two hours of sampling, the hydrogen peroxide concentration of sample GS2 was measured using GS1 as a blank. For methylene blue, the concentrations tracked with the probe were checked by measuring the absorbance of samples GS2 and GS3 using a 1-cm pathlength quartz cuvette in the Varian spectrophotometer at a wavelength of 661 nm. UV transmittance values at 254 nm of GS2 and GS3 were determined using DI water to zero the spectrophotometer.

For several methylene blue trials, the fiber optic probe radial position was changed during the trial from the centerline of the effluent pipe to a near-wall position of the effluent pipe. No significant changes were noticed, and as such, the assumption of a pseudo-perfectly-mixed effluent at the sample point is valid.

### 3.7.1 Impact of Internal Baffle Configuration on UV/AOP Performance

Similar to the CFD models, the pilot system was used to measure methylene blue degradation with five internal baffles and with one internal baffle in the UV reactor. Tests were performed at the same operating conditions with and without the baffles. Experimental measurements in the reactor effluent were compared to the numerical modeling results.

### 3.8 Advanced Oxidation of Sulfamethoxazole

Since the goal of this research is to evaluate CFD models for practical use by engineers for design and analysis of UV-initiated advanced oxidation, the steps for CFD modeling and pilot-scale validation were repeated with the antibiotic sulfamethoxazole (SMX) as the target contaminant instead of the dye methylene blue. Both direct photolysis and advanced oxidation was evaluated. For the pilot experiments, the SMX peristaltic pump was started after lamp warm-up and flow stabilization at 10 GPM. Four minutes (greater than four theoretical residence times) later, two grab samples each were collected from the reactor influent and effluent sampling taps. The hydrogen peroxide peristaltic pump, from which the final hydrogen peroxide concentration (post-injection) was previously measured, was then started. Again after four minutes, two grab samples each were collected from the reactor influent and effluent sampling taps. These latter samples with hydrogen peroxide were immediately quenched with sodium thiosulfate. Aliquots from each of the grab samples were passed through 0.22  $\mu\text{m}$  syringe filters and added to HPLC vials. HPLC analysis was started within three hours of the last sample collection.

### 3.9 Optimization of Energy and Hydrogen Peroxide Usage

Since the CFD model was used to predict effluent concentrations of the target contaminants with changes in the hydrogen peroxide concentrations and with changing UV fluence rate conditions, the model results were evaluated to determine the average annual costs of the lamp energy and hydrogen peroxide dosages per log order contaminant degradation. This metric was calculated for both the CFD model results and the experimental results (Figure 3.22).

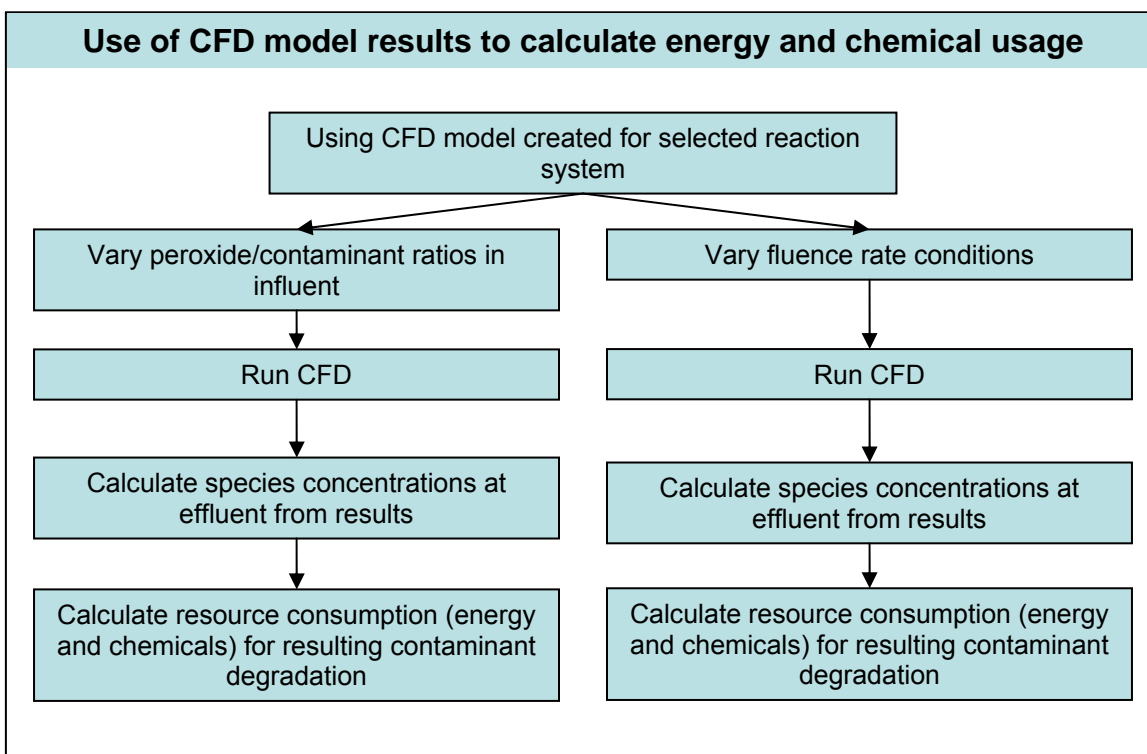


**Figure 3.22: Schematic of Tasks for Calculation of Resource Consumption**

### 3.10 Other Numerical Methods

Two numerical modeling approaches for simulating UV-initiated advanced oxidation processes were compared to the process described earlier that utilizes CFD in an Eulerian mode to simulate the reaction and transport of each species as part of the turbulent convective-diffusion equations. The first, herein referred to as the ideal hydraulics approach, was the numerical solution by MATLAB (The MathWorks, Inc., Natick, MA) of the system of ordinary differential equations (ODEs) describing the reaction mechanism for hydroxyl radical production and methylene blue destruction. The second model (CFD/Lagrangian) combined a UV dose distribution produced by a Lagrangian particle track in CFD with a dose-response curve (i.e., UV fluence versus contaminant removal) generated with MATLAB.

For the ideal hydraulics approach, the reaction rate equations developed as part of the CFD/Eulerian solution were coded into MATLAB and solved using the built-in ODE solvers that are included with the software. The irradiance value required in the equations was calculated as a volumetric average generated by discretizing the reactor in the radial and length-wise directions and using the lamp output power, UV transmittance, and a simplified RAD-LSI equation. The results consisted of the effluent concentrations of the modeled species described as a function of time. The effluent concentrations were considered as those corresponding to the theoretical hydraulic residence time calculated using the reactor volume and flow rate (i.e., a plug-flow assumption). Other hydraulic profiles could be used as appropriate; however, the simplest case was assumed here.

For the CFD/Lagrangian approach, UV dose distributions specific to the reactor operating conditions were created and used to evaluate methylene blue degradation. The dose distributions were combined with UV dose-response data for comparable reaction conditions (including hydrogen peroxide dose) to calculate overall methylene blue removal in the reactor. The UV dose-response data was generated by solving the kinetic rate equations in MATLAB for a molar ratio of hydrogen peroxide to methylene blue. The numerical value of  $\frac{C}{C_0} \left( = \frac{[MB]}{[MB]_0} \right)$  for each UV dose was imported into Microsoft® Office Excel 2003 and later used with a VLOOKUP command to find the removal associated with each discrete value within the dose distribution.

The dose distribution was developed by modifying the RAD-LSI fluence rate distribution model from the CFD/Eulerian approach for one of the research conditions (Q = 20 GPM, P = 26.5 W output at 254 nm) to incorporate the PHOENICS particle track solver GENTRA. Although only one lamp power was used in the pilot reactor, a dose distribution curve for a second theoretical output lamp power (100W) was also generated to examine the results at higher methylene blue removal rates. The CFD particle track models, also known as Lagrangian models, used within PHOENICS are discussed in detail in Ducoste et al. (2005), which is summarized herein.

The Lagrangian approach centers on equations that describe the evolution of position within a flow field. According to Ducoste et al. (2005), particle position is determined by solving Equation 3-17 where  $X_p$  is the particle position and  $U_p$  is the instantaneous particle velocity.

$$\frac{dX_p}{dt} = U_p \quad (3-17)$$

In this equation,  $U_p$  is equal to the mean velocity component plus a turbulent fluctuating velocity component. The velocity of a particle of mass  $m_p$  is determined from the particle momentum equation, which, for acceleration due to gravity  $g$  and neglecting buoyancy effects, is shown in Equation 3-18 (Ducoste et al., 2005). The drag function  $D_p$  used in Equation 3-18 is described in Equation 3-19.

$$m_p \frac{du_p}{dt} = D_p (u - u_p) + m_p g \quad (3-18)$$

$$D_p = 0.5 \rho A_p C_D |u - u_p| \quad (3-19)$$

In Equation 3-19,  $A_p$  is the particle projected area defined in Equation 3-20,  $C_D$  is the drag coefficient defined in Equation 3-21 (Ducoste et al., 2005), and  $Re$  is the particle Reynolds number.

$$A_p = \frac{\pi d_p^2}{4} \quad (3-20)$$

$$C_D = \frac{24}{Re} (1 + 0.15 Re^{0.687}) + \frac{0.42}{1 + (4.25 \times 10^4 Re^{-1.16})} \quad (3-21)$$

The particle momentum equation is based on the carrier phase instantaneous velocity  $u$  that is the sum of the mean and fluctuating components. The mean velocity is determined using the hydrodynamic and turbulence models described previously. The turbulent fluctuating velocity is calculated by assuming that each instantaneous velocity component follows a Gaussian distribution with a mean of zero and a standard deviation  $\sigma = \sqrt{\frac{2k}{3}}$  (Ducoste et al., 2005). A random number generator based on this distribution, mean, and standard deviation is then used to determine the sign and magnitude of the fluctuating velocity component. Particle motion can also be calculated using other methods such as the random-walk algorithm.

In the Lagrangian particle-track method, random fluctuations are caused by particle interactions with turbulent eddies in the flow field (Shirokar et al., 1996). The interaction time between a particle and a turbulent eddy is determined by the condition that either the particle moves sufficiently slow relative to the carrier phase to remain within the eddy throughout the eddy's lifetime ( $t_{eddy}$ ) or the velocity difference between the carrier phase and particle is sufficient to traverse the eddy in a transit time ( $t_{tr}$ ) that is shorter than the eddy lifetime. The overall interaction time scale is then determined as defined by Equations 3-22 through 3-25 (Ducoste et al., 2005).

$$t_{in} = \text{minimum}(t_{eddy}, t_{tr}, t_{user}) \quad (3-22)$$

$$t_{eddy} = \sqrt{\frac{3}{2}} C_{\mu}^{0.75} \frac{k}{\varepsilon} \quad (3-23)$$

$$t_{tr} = \frac{C_{\mu}^{0.75} k^{1.5}}{|u - u_p|} \quad (3-24)$$

$t_{user}$  = user defined minimum computational cell crossing time

$$= (\text{minimum time steps per cell}) \times \left( \frac{\text{minimum cell dimension}}{\text{maximum velocity component through cell}} \right) \quad (3-25)$$

A new random number will be generated to compute the carrier phase instantaneous velocity in the particle momentum equation only when the particle has traversed the eddy or has spent more time than the eddy lifetime.

The UV fluence as seen by each particle is calculated by integrating the fluence rate over the particle track time history using Equation 3-26 (Ducoste et al., 2005) in which *Fluence (P)* is the UV dose for a particle *P* (J m<sup>-2</sup> or mJ cm<sup>-2</sup>) and *I(t)* is the UV fluence rate (W m<sup>-2</sup> or mW cm<sup>-2</sup>).

$$Fluence(P) = \int_0^T I(t)dt \cong \sum I \Delta t \quad (3-26)$$

In a Lagrangian particle-track simulation, a spatial homogeneous concentration of particles is released at the UV system influent. Sufficient number of particles should be incorporated (e.g., greater than 1500 particles) to assure a stable particle fluence distribution. Similar to establishing a grid-independent CFD solution, the predicted fluence distribution should not be a function of the number of particles released at the inlet. Significantly higher

particle concentrations may be necessary for reactor designs that have major recirculation zones within the reactor. Particles released at the influent may be trapped within these recirculation zones and may not reach the reactor outlet. Particles should be released at least 10 pipe diameters ahead of the UV reactor inlet to allow for adequate mixing with the flow stream. A reduction in the number of pipe diameters upstream for releasing the particles can be achieved if an accurate description of the velocity and turbulent profile at the specific inlet location is provided. For the 26W and 100W distributions, the total number of particles in the reactor effluent equaled 4,648 and 4,652, respectively.

Particles can take any one of an infinite number of paths through a UV reactor. Thus, the delivered UV fluence will be comprised of a range of values that are a function of the particle paths and spatial variations in UV fluence rate throughout the reactor resulting from water quality conditions affecting UV absorbance, lamp placement and spacing in the reactor, lamp power, and other non-idealities in a treatment system. For the Lagrangian method, the fluence distribution was computed by separating the fluence value from each particle path into discrete bins each representing a smaller finite range of fluence values. The results were then reported as a frequency function that represents the fraction of the total number of particles released in the reactor influent.

With the UV dose distributions available, a segregated flow approach that matched up the individual dose values with corresponding methylene blue removal values was used to calculate the overall removal percentage predicted by the dose distributions. The probability  $p_i$  of any given dose  $i$  was calculated using the number of particles recorded in the distribution receiving dose  $i$  ( $x_i$ ) as shown in Equation 3-27.

$$p_i = \frac{x_i}{\sum x_i} \quad (3-27)$$

The fraction of methylene blue remaining associated with each UV dose  $\left(\frac{C}{C_0}\right)_i$  was determined using the dose response curves previously determined with MATLAB. The total fraction expected at the reactor effluent was then calculated using Equation 3-28.

$$\left(\frac{C}{C_0}\right)_{Final} = \sum_i \left\{ p_i \times \left(\frac{C}{C_0}\right)_i \right\} \quad (3-28)$$

The total contaminant percent removal was reported as shown in Equation 3-29.

$$\text{Total Percent Removal} = \left( 1 - \left(\frac{C}{C_0}\right)_{Final} \right) \times 100\% \quad (3-29)$$

## 4. RESEARCH RESULTS AND DISCUSSION

In this section, the results of the collimated beam and pilot research experiments are compiled and presented along with the numerical results from CFD and MATLAB. Validation trends are also discussed.

### 4.1 Experimental Results – Collimated Beam Apparatus

As discussed in Section 3, the collimated beam apparatus was utilized to conduct bench-scale experiments with varying irradiances and hydrogen peroxide concentrations, and to experimentally determine the second-order kinetic rate constant for the reaction between methylene blue and the hydroxyl radical. The results of these experiments are presented below.

#### 4.1.1 Second-Order Kinetic Rate Constant for Methylene Blue and the Hydroxyl Radical

A key parameter in predicting the overall degradation of an organic contaminant using advanced oxidation is the rate constant describing the speed of the reaction between the contaminant and the hydroxyl radical. The second-order rate constant for the reaction between the contaminant and the hydroxyl radical is unique. To determine the kinetic rate constant for methylene blue and the hydroxyl radical, a competition kinetics method, as described in Section 3, was included with this research. The competition kinetics experiments used isopropyl alcohol (IPA) as the radical competitor and produced the results shown in Figure 4.1. Based on this data set, the rate constants were calculated for the four separate trials and are reported in Table 4.1.

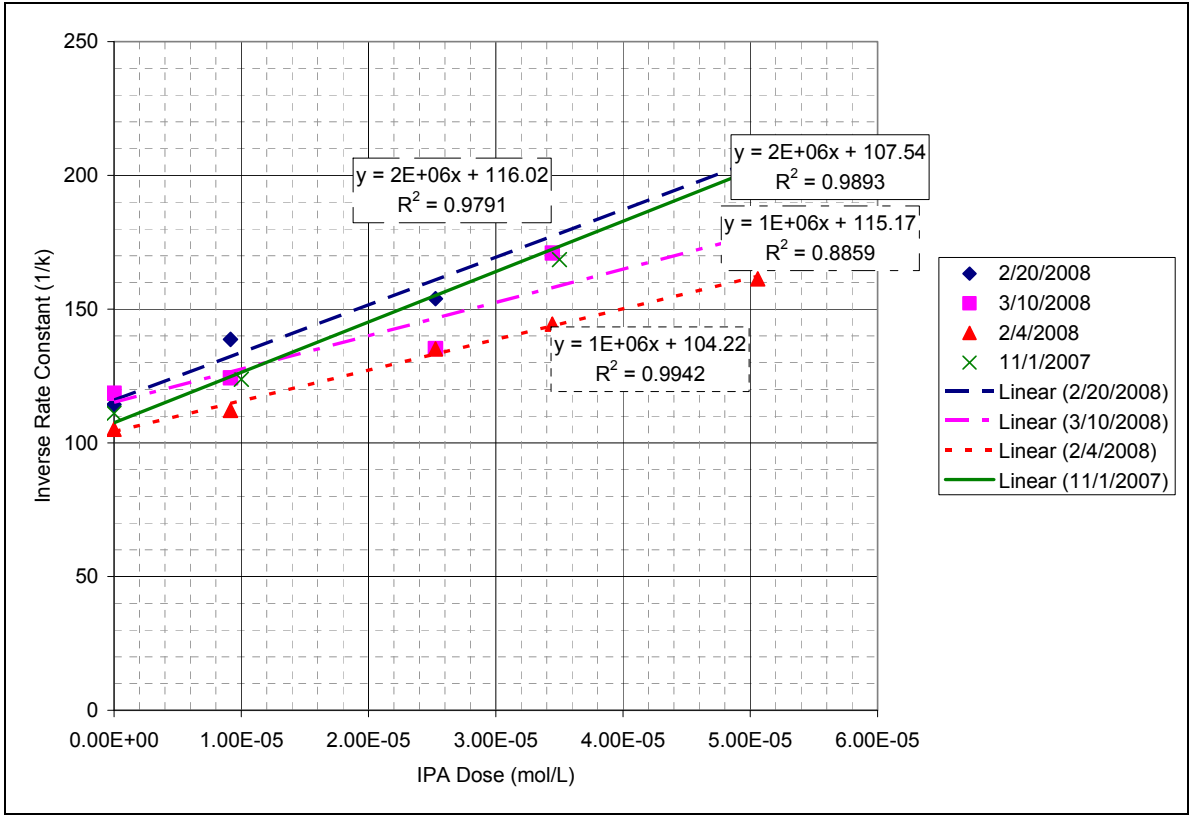


**Figure 4.1: Competition Kinetic Data Plot for Kinetic Rate Constant Determination**

**Table 4.1: Experimental Values for the Methylene Blue Kinetic Rate Constant**

Date of Experiments	Second-order Rate Constant for Methylene Blue with the Hydroxyl Radical ( $M^{-1} s^{-1}$ )
3/10/2008	8.72E+10
2/20/2008	5.93E+10
2/4/2008	8.52E+10
11/1/2007	4.40E+10
Average	6.89E+10
95% Confidence Interval	+/- 2.05E+10

Based on Table 4.1, the kinetic rate constant for methylene blue equals  $6.89 \times 10^{10} M^{-1} s^{-1}$  with a 95% confidence interval of  $2.05 \times 10^{10} M^{-1} s^{-1}$ . Since the variation in the rate constant calculations may be considered significant, as represented by the 95%

confidence interval, the sensitivity of the overall degradation of methylene blue in the system to the value of the rate constant was determined using CFD and is presented in Section 4.3.5. Values of the rate constant for the reaction between the methylene blue cation and the hydroxyl radical have also been posted to the Radiation Chemistry Data Center (RCDC), a database of radical reactions maintained by the Notre Dame Radiation Laboratory. The first value cited in the RCDC online database reports a directly-measured absolute value of the second order rate constant equal to  $1.2 \times 10^{10} M^{-1}s^{-1}$  as determined with pulse radiolysis and vis-UV absorption analyses. A second constant equal to  $2.1 \times 10^{10} M^{-1}s^{-1}$  is also cited in the RCDC online database as a relative value measured by a steady state method (competition kinetics) using gamma radiolysis and vis-UV absorption.

In addition, it should be noted that the calculated values for the rate constant are high enough to be in the range for which reactions may become diffusion-limited. A diffusion limited reaction is one in which the reaction rate is limited by the ability of diffusion to transfer one reactant to the second reactant. One way to quantify the degree of diffusion limited conditions is to model the Damkohler number. The Damkohler (second) number represents the ratio of the characteristic reaction time scale to the characteristic diffusion time scale. The Damkohler number is described in Equation 4-1.

$$D_A^{II} \propto \frac{k}{D_{AB}} = \frac{\tau_d}{\tau_r} \quad (4-1)$$

In Equation 4-1,  $k$  is the reaction rate constant and  $D_{AB}$  is the diffusion coefficient of  $A$  in  $B$ . As  $D_A''$  increases, the system moves from reaction-limited to diffusion-limited conditions. For  $D_A''$  greater than unity, the diffusion rate is slower than the reaction rate. Thus, if the latter case is true for the advanced oxidation reaction under consideration, the overall rate of reaction would need to be based on the diffusion time scale. Ultimately, this would result in a decrease in degradation of the target compound as compared to that predicted with no consideration of the diffusion limitations.

#### 4.1.2 Effects of the Molar Ratio of Hydrogen Peroxide to Methylene Blue

As part of the experiments conducted for the competition kinetics and radical formation rate determination, several different molar ratios of hydrogen peroxide to methylene blue were used. By selecting key data points, it is possible to evaluate the effect of the molar ratio on the overall contaminant degradation. Figure 4.2(a) shows methylene blue removal (oxidation) as a function of hydrogen peroxide concentration in the collimated beam experiments at a UV dose of  $50 \text{ mJ cm}^{-2}$ . As expected, the removal increases as the hydrogen peroxide concentration is increased. The curve should begin to flatten at higher concentrations since hydrogen peroxide itself will become a significant radical scavenger and UV absorber. Figure 4.2(b) displays the results of a similar experiment in which the water from the pilot influent tank is compared to DI water for methylene blue removal as a function of hydrogen peroxide concentration. In Figure 4.3, the methylene blue removal rate as a function of UV dose is shown for several hydrogen peroxide concentrations. Again, the removal rate increases as the UV dose is increased. This trend can be predicted since the

hydroxyl radical concentration is directly proportional to UV fluence as shown previously in Equation 2-44.

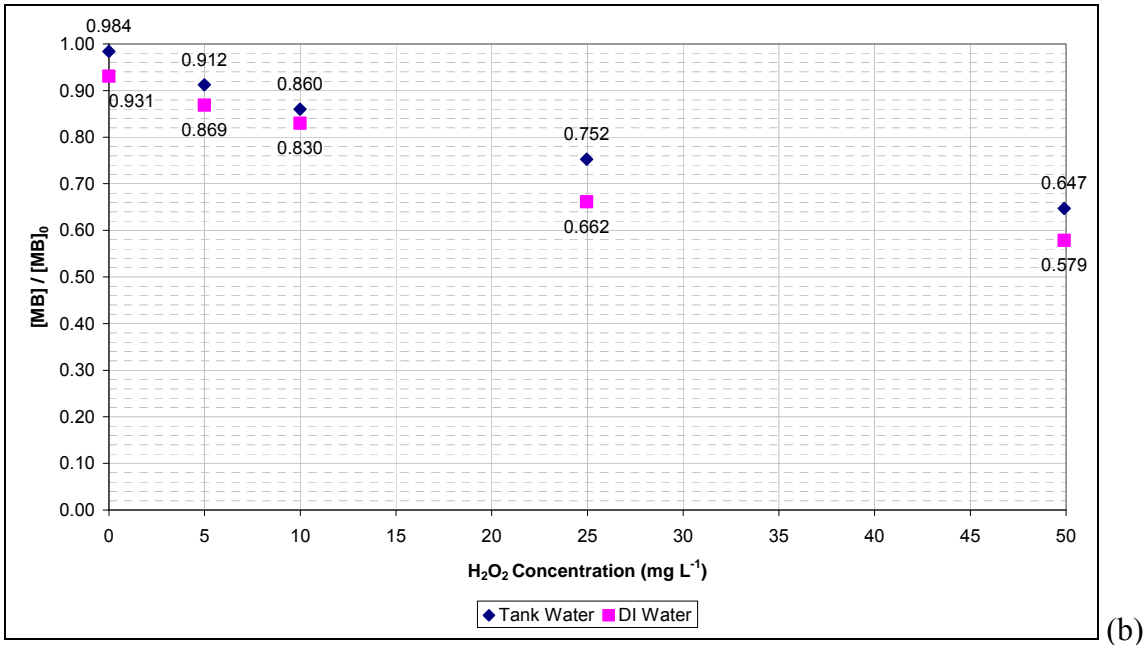
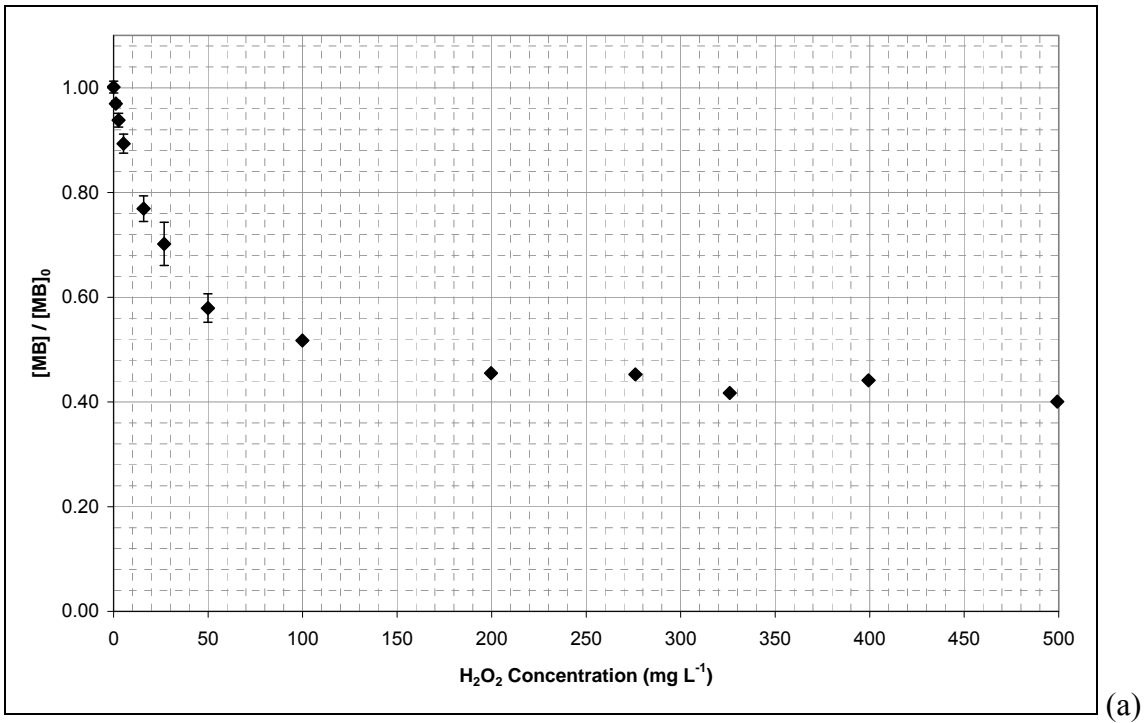


**Figure 4.2: Removal Rates as a Function of Hydrogen Peroxide Concentration (Collimated Beam at  $50\ mJ\ cm^{-2}$  and  $[MB]_0 = 0.5\ mg\ L^{-1}$ ) (a) Multiple Experiments in DI Water; (b) DI Water Results Compared to Pilot Influent Tank Water**

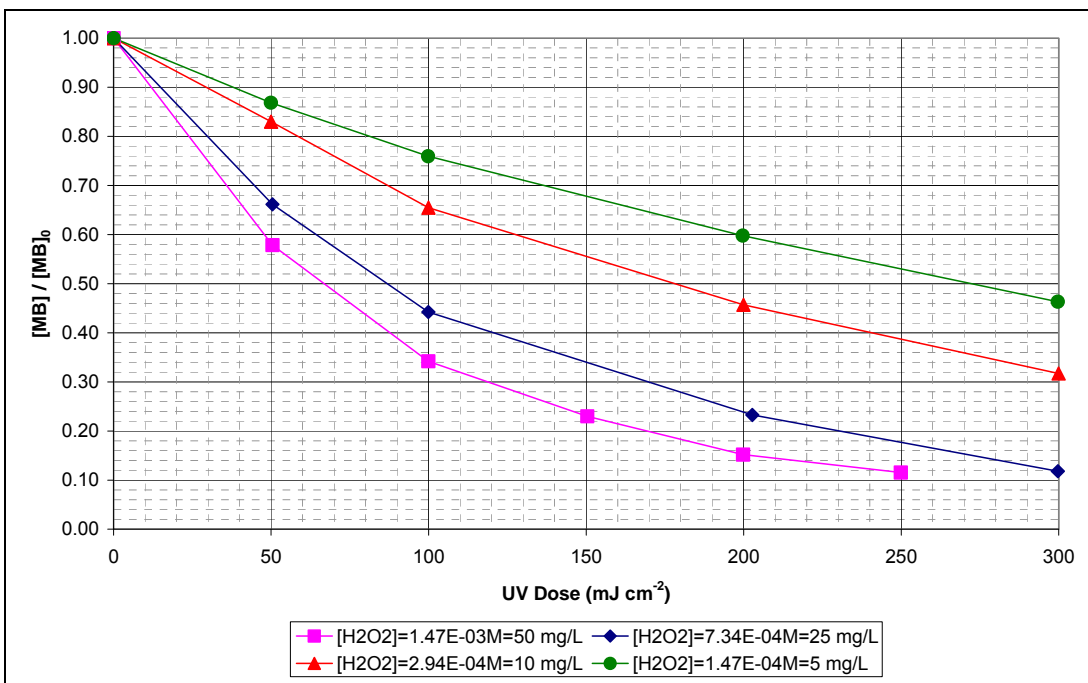


**Figure 4.3: Removal Rates as a Function of UV Dose (Collimated Beam)**

#### 4.1.3 Stability and Reversibility of the Methylene Blue Degradation Reaction

Removal percentages of the methylene blue responded as expected to changing UV doses and hydrogen peroxide concentrations. Initially, there were two potential issues related to the stability of the methylene blue solutions. The first was exhibited by the initial inability to produce a clean absolute baseline in the collimated beam experiments. Figure 4.4 shows the results of irradiating a methylene blue solution under the collimated beam without any hydrogen peroxide addition.

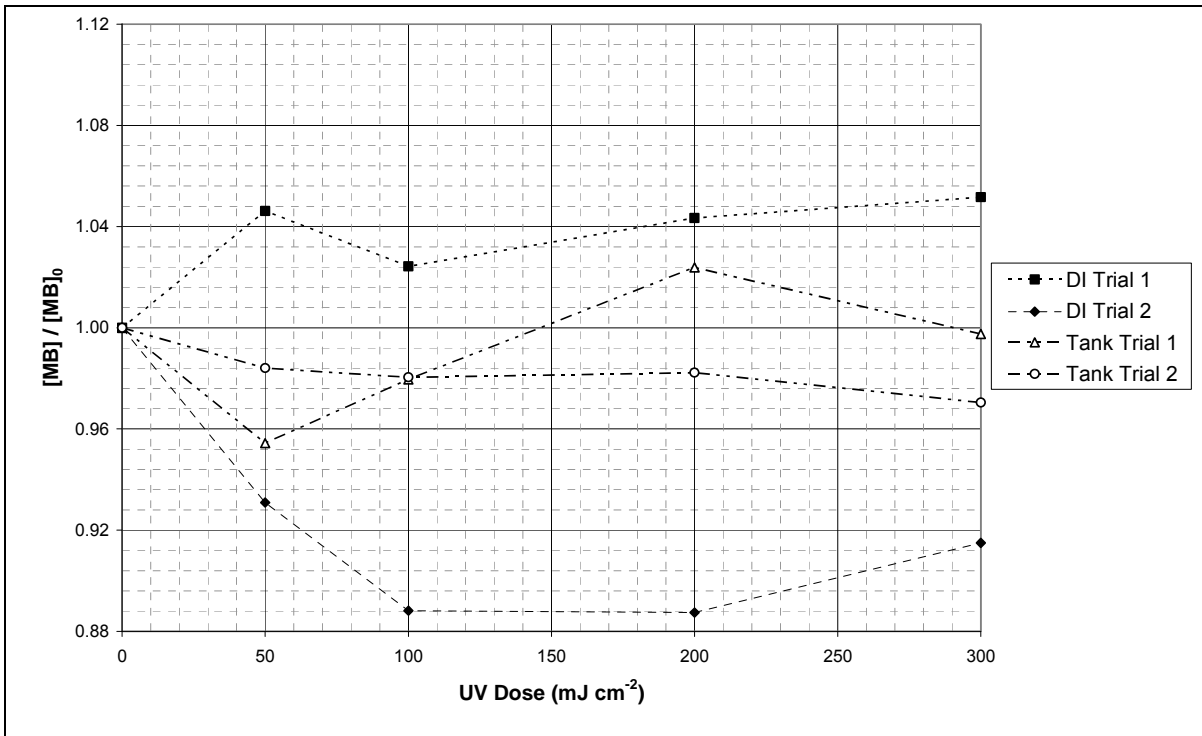


**Figure 4.4: Collimated Beam Baseline: Methylene Blue (MB) = 0.5 mg L<sup>-1</sup>, Hydrogen Peroxide = 0.0 mg L<sup>-1</sup> (Trace lines added for clarity)**

The second issue was the steadily increasing absorption of methylene blue solution in the early pilot trials, as shown in Figure 4.5.

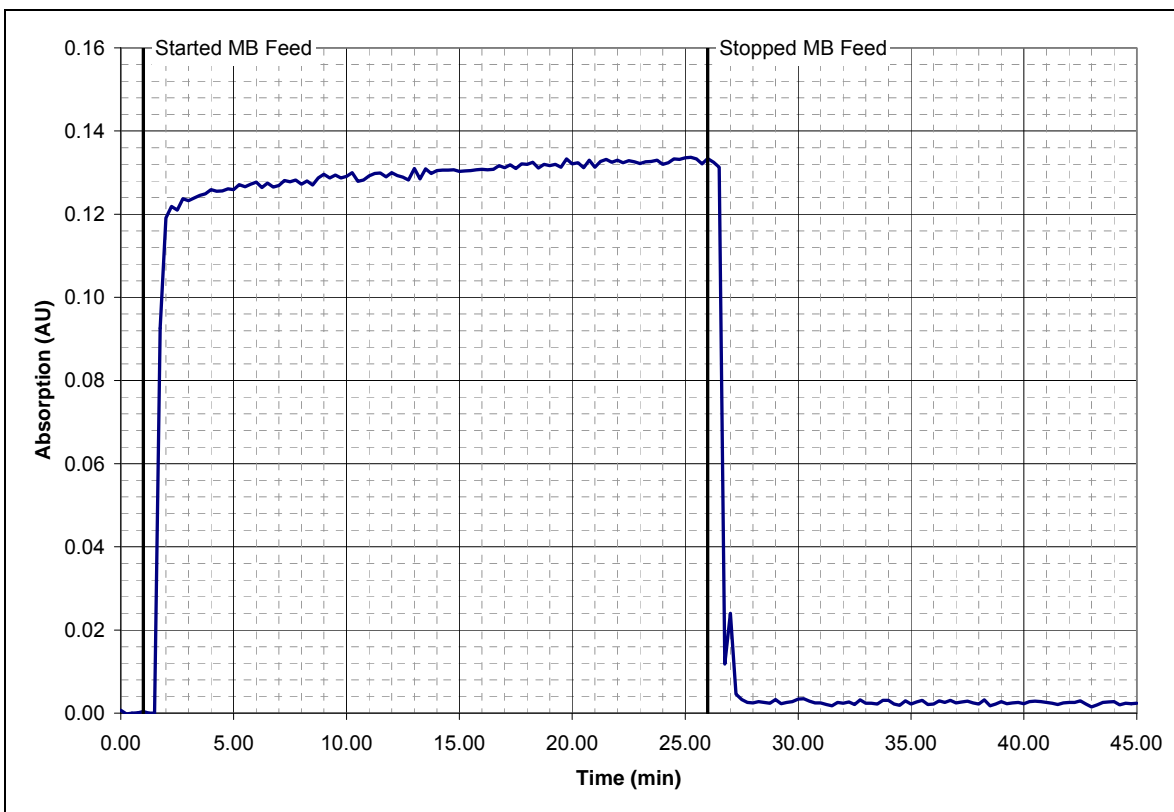


**Figure 4.5:** Initial Spectrophotometer Results for Methylene Blue in Pilot

Both of these issues appeared to be related to incomplete mixing of the methylene blue in solution. Complete mixing of the methylene blue was difficult to judge visually, especially at concentrations of  $1 \text{ mg L}^{-1}$  and above. Various tests with the batch mixing of the high concentration methylene blue stock used for the pilot feed revealed residual solid methylene blue that remained after initial mixing and that continued to dissolve. If the methylene blue was allowed to mix overnight using a lab-scale mixer set at about 50% speed, the slope of the absorption curve was minimized. Thus, this procedure was adapted for all pilot tests.

Also tested was the potential for any significant continuation of the reaction (or other source of absorption change) following sampling from the pilot reactor. Even though all

pilot samples were analyzed immediately after the trial, the objective was to check possible errors associated with a delay in testing and/or dark reactions at the concentrations under investigation. Four 10 mL samples were prepared, each containing 0.33 mg L<sup>-1</sup> methylene blue and 10.6 mg L<sup>-1</sup> hydrogen peroxide in DI water. Sample 1 served as a blank for the experiment. Samples 2-4 were exposed to 300 mJ cm<sup>-2</sup> of low-pressure UV light in the collimated beam apparatus. After exposure, the methylene blue concentration of each sample was measured using the spectrophotometer. Samples 2 and 4 were then each dosed with 0.56 mL of sodium thiosulfate solution, while Samples 1 and 3 were each treated with an equal volume of deionized water. After 20 minutes, the methylene blue concentration of each sample was tested again. Table 4.2 shows the results of this exercise.

**Table 4.2: Methylene Blue Stability Results**

Sample	Initial Concentration (mg L <sup>-1</sup> )	Concentration After UV Exposure (mg L <sup>-1</sup> )	Calculated Concentration After Dilution (mg L <sup>-1</sup> )	Concentration, After 20 Minutes (mg L <sup>-1</sup> )
1 (Blank)	0.33	0.33	0.31	0.31
2 (Quench)	0.33	0.14	0.13	0.13
3 (No Quench)	0.33	0.14	0.13	0.11
4 (Quench)	0.33	0.12	0.11	0.12

As shown in Table 4.2, the decrease in methylene blue concentration of the quenched samples is small. For the unquenched Sample No. 3, the decrease was 17.3%; however, it is proposed that this decrease is magnified because of the small concentrations being measured. If the blank is considered, the overall reduction in methylene blue following the 20-minute hold was small.

## 4.2 Experimental Results – Pilot Reactor

The first preliminary test with the pilot-scale reactor evaluated any apparent reaction between methylene blue and hydrogen peroxide with the UV lamp turned off. The results of this test are shown in Figure 4.6. As can be seen in this figure between  $t = 10$  minutes and  $t = 14$  minutes, no change in absorbance (or concentration) was detected without UV irradiation. The peak following the start of the wash cycle ( $t = 17$  minutes) represents the flushing of methylene blue from the feed tubing since the soapy water feed shares inlet tubing with both the methylene blue and the hydrogen peroxide.

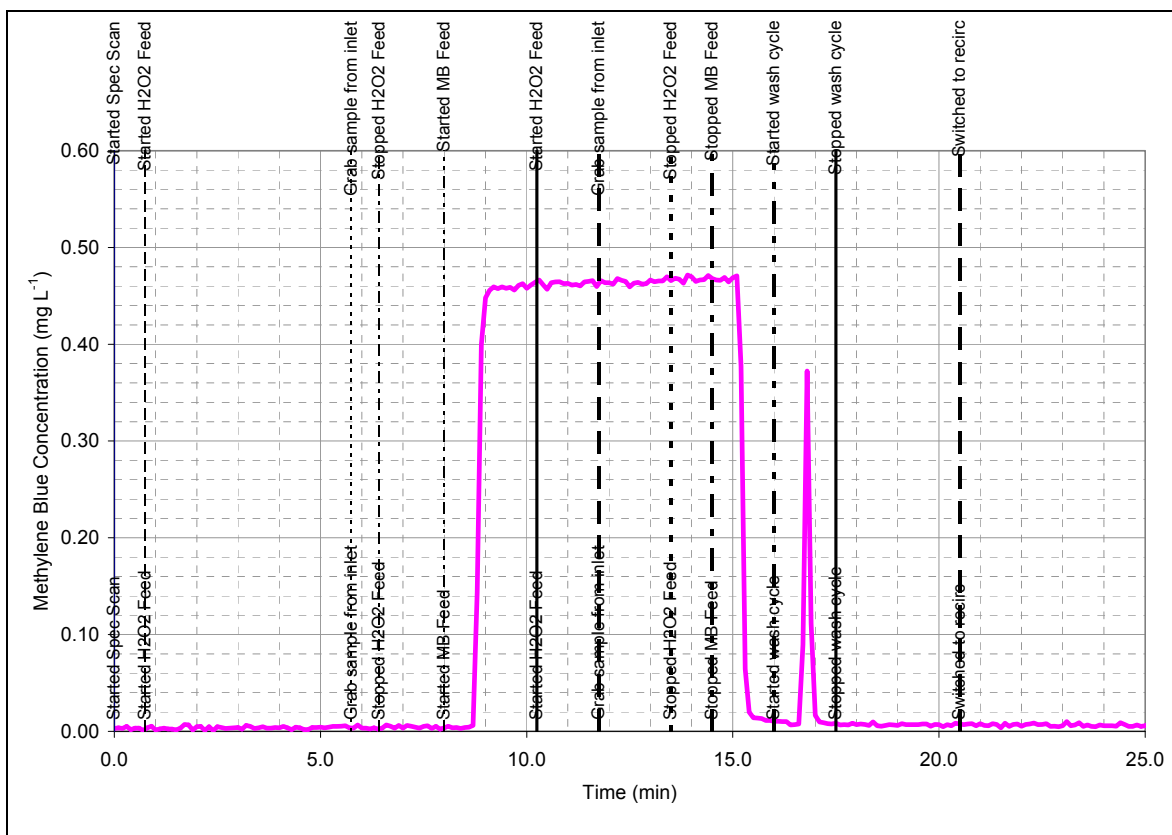
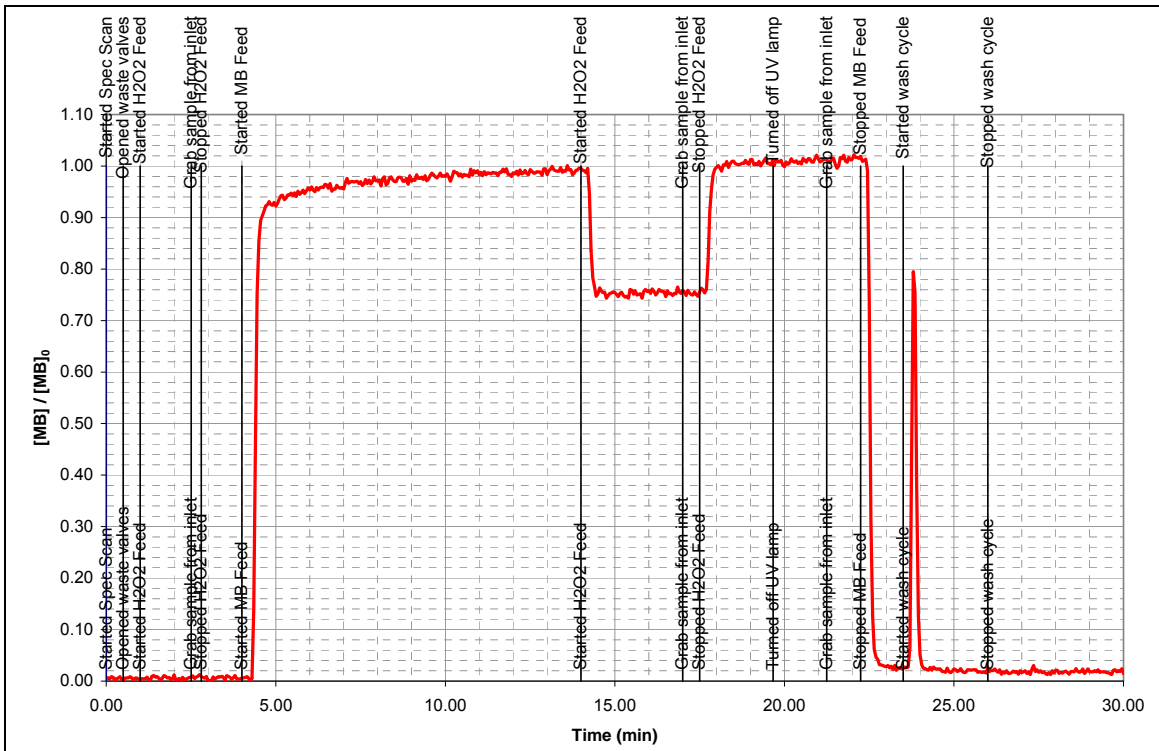


Figure 4.6: Pilot Scale Results with No UV Irradiation

The next preliminary test outlined the response of the spectrophotometer to the starting and stopping of the methylene blue and hydrogen peroxide pumps with the UV lamp on. In this test, the potential for change in absorbance (concentration) of methylene blue by direct photolysis was also investigated. The results of this test, which showed no significant direct photolysis of methylene blue ( $t = 19.5$  minutes), are shown in Figure 4.7.



**Figure 4.7: Pilot Results Showing No Direct Photolysis and Confirming Response to Hydrogen Peroxide Addition**

Once the pilot scale procedure was established, a series of tests investigating the change in percent removal of methylene blue with changing flow rates, hydrogen peroxide doses, and baffle arrangements was initiated. Four flow rates (5, 10, 20, and 30 GPM) were selected to evaluate the hydraulic residence time and turbulent mixing conditions in the

reactor. The molar ratio between hydrogen peroxide and methylene blue was varied between 150 and 250 to evaluate the peroxide dose effect on methylene blue removal. The research conditions evaluated with the pilot scale reactor are described in Table 4.3. A discussion of the results of each design condition follows.

**Table 4.3: Research Conditions Evaluated with Pilot Scale Reactor**

Research Condition <sup>1</sup>	Target Flow Rate (GPM)	Organic Contaminant	Contaminant Concentration (mg L <sup>-1</sup> )	Target H <sub>2</sub> O <sub>2</sub> :MB Molar Ratio	Target H <sub>2</sub> O <sub>2</sub> Concentration (mg L <sup>-1</sup> )	Number of Baffles in Reactor
1	10	Methylene Blue	0.50	150	7.98	5
2	10	Methylene Blue	0.50	150	7.98	1
3	20	Methylene Blue	0.50	150	7.98	5
4	20	Methylene Blue	0.50	150	7.98	1
5	20	Methylene Blue	0.50	200	10.63	5
6	20	Methylene Blue	0.50	200	10.63	1
29	20	Methylene Blue	0.50	250	13.29	5
30	30	Methylene Blue	0.50	150	7.98	5
35	5	Methylene Blue	0.50	150	7.98	5
10a	10	Sulfamethoxazole	0.01	N/A	0	5
10b	10	Sulfamethoxazole	0.01	N/A	10	5

<sup>1</sup> Numbering scheme coordinated with CFD models.

#### 4.2.1 Methylene Blue

A majority of the pilot-scale reactor trials were performed with methylene blue as the target organic contaminant. Tables 4.4 through 4.12 summarize the results of each of the methylene blue pilot trials. Comparisons of the percent removal values are shown in Figure 4.8 and Figure 4.9.

**Table 4.4: Pilot Results for Research Condition No. 1**

Category	Trial 1 (6/18/2008)	Trial 2 (6/30/2008)	Trial 3 (7/1/2008)	Average	Standard Deviation	Count	Confidence Interval (alpha = 0.05)
Methylene Blue Concentration (mg L <sup>-1</sup> )	0.51	0.49	0.51	0.50	0.01	3	0.01
H <sub>2</sub> O <sub>2</sub> :MB Molar Ratio	152	150	149	150.33	1.53	3	1.73
H <sub>2</sub> O <sub>2</sub> Concentration (mg L <sup>-1</sup> )	8.2	7.8	8.0	8.0	0.2	3	0.2
Percent Removal (%)	71.6	79.6	78.2	76.5	4.3	3	4.8
UVT <sub>254</sub> Influent (%)	95.1	95.4	92.4	94.3	1.7	3	1.9
UVT <sub>254</sub> Effluent (%)	94.1	94.8	94.3	94.4	0.4	3	0.4
UVT <sub>254</sub> Average (%)				94.4	1.1	6	0.9
pH	7.25	7.25	7.21	7.24	0.02	3	0.03
Alkalinity (mg L <sup>-1</sup> as CaCO <sub>3</sub> )	22.5	23.4	23.0	23.0	0.5	3	0.5
Total Chlorine Residual (mg L <sup>-1</sup> as Cl <sub>2</sub> )	0	N/A	0.09	0.05	0.06	2	0.09
UV Sensor Reading (W m <sup>-2</sup> ) Tank Water Only	N/A	28.7	27.6	28.2	0.8	2	1.1
UV Sensor Reading (W m <sup>-2</sup> ) With MB and H2O2	7.8	18.2	17.9	18.1	0.2	2	0.3

Flow Rate = 10 GPM, Number of Baffles in Reactor = 5

**Table 4.5: Pilot Results for Research Condition No. 2**

Category	Trial 1 (7/18/2008)	Trial 2 (7/21/2008)	Trial 3 (7/18/2008)	Average	Standard Deviation	Count	Confidence Interval (alpha = 0.05)
Methylene Blue Concentration (mg L <sup>-1</sup> )	0.50	0.49	0.50	0.50	0.01	3	0.01
H <sub>2</sub> O <sub>2</sub> :MB Molar Ratio	149	150	149	149.33	0.58	3	0.65
H <sub>2</sub> O <sub>2</sub> Concentration (mg L <sup>-1</sup> )	7.9	7.9	7.9	7.9	0	3	0
Percent Removal (%)	81.0	78.8	80.0	79.9	1.1	3	1.2
UVT <sub>254</sub> Influent (%)	92.5	92.8	92	92.4	0.4	3	0.5
UVT <sub>254</sub> Effluent (%)	92.9	93.2	92.2	92.8	0.5	3	0.6
UVT <sub>254</sub> Average (%)				92.6	0.5	6	0.4
pH	7.25	7.26	7.25	7.25	0.01	3	0.01
Alkalinity (mg L <sup>-1</sup> as CaCO <sub>3</sub> )	20.4	21.7	20.4	20.8	0.8	3	0.8
Total Chlorine Residual (mg L <sup>-1</sup> as Cl <sub>2</sub> )	0.02	0.07	0.03	0.04	0.03	3	0.03
UV Sensor Reading (W m <sup>-2</sup> ) Tank Water Only	26.7	27.6	27	27.1	0.5	3	0.5
UV Sensor Reading (W m <sup>-2</sup> ) With MB and H2O2	16.9	17.6	17.3	17.3	0.4	3	0.4

Flow Rate = 10 GPM, Number of Baffles in Reactor = 1

**Table 4.6: Pilot Results for Research Condition No. 3**

Category	Trial 1 (7/26/2008)	Trial 2 (7/28/2008)	Trial 3 (7/29/2008)	Average	Standard Deviation	Count	Confidence Interval (alpha = 0.05)
Methylene Blue Concentration (mg L <sup>-1</sup> )	0.50	0.50	0.50	0.50	0.00	3	0.00
H <sub>2</sub> O <sub>2</sub> :MB Molar Ratio	149	149	152	150.00	1.73	3	1.96
H <sub>2</sub> O <sub>2</sub> Concentration (mg L <sup>-1</sup> )	7.9	7.9	8.1	8.0	0.1	3	0.1
Percent Removal (%)	58.0	57.0	58.0	57.7	0.6	3	0.7
UVT <sub>254</sub> Influent (%)	93.1	92.1	92.6	92.6	0.5	3	0.6
UVT <sub>254</sub> Effluent (%)	93.2	92.4	92.7	92.8	0.4	3	0.5
UVT <sub>254</sub> Average (%)				92.7	0.4	6	0.3
pH	7.26	7.34	7.30	7.30	0.04	3	0.05
Alkalinity (mg L <sup>-1</sup> as CaCO <sub>3</sub> )	22.1	23.4	22.5	22.7	0.7	3	0.8
Total Chlorine Residual (mg L <sup>-1</sup> as Cl <sub>2</sub> )	0.03	0.08	0.05	0.05	0.03	3.00	0.03
UV Sensor Reading (W m <sup>-2</sup> ) Tank Water Only	27.0	27.2	27.5	27.2	0.3	3	0.3
UV Sensor Reading (W m <sup>-2</sup> ) With MB and H2O2	16.6	16.7	17.2	16.8	0.3	3	0.4

Flow Rate = 20 GPM, Number of Baffles in Reactor = 5

**Table 4.7: Pilot Results for Research Condition No. 4**

Category	Trial 1 (7/16/2008)	Trial 2 (7/22/2008)	Trial 3 (7/16/2008)	Average	Standard Deviation	Count	Confidence Interval (alpha = 0.05)
Methylene Blue Concentration (mg L <sup>-1</sup> )	0.50	0.49	0.49	0.49	0.01	3	0.01
H <sub>2</sub> O <sub>2</sub> :MB Molar Ratio	148	152	148	149.33	2.31	3	2.61
H <sub>2</sub> O <sub>2</sub> Concentration (mg L <sup>-1</sup> )	7.9	8.0	7.8	7.9	0.1	3	0.1
Percent Removal (%)	60.0	59.6	59.6	59.7	0.2	3	0.3
UVT <sub>254</sub> Influent (%)	93.0	93.0	93.3	93.1	0.2	3	0.2
UVT <sub>254</sub> Effluent (%)	93.2	93.5	93.7	93.5	0.3	3	0.3
UVT <sub>254</sub> Average (%)				93.3	0.3	6	0.2
pH	7.24	7.25	7.24	7.24	0.01	3	0.01
Alkalinity (mg L <sup>-1</sup> as CaCO <sub>3</sub> )	20.8	21.7	20.8	21.1	0.5	3	0.6
Total Chlorine Residual (mg L <sup>-1</sup> as Cl <sub>2</sub> )	0.02	0.08	0.02	0.04	0.03	3	0.04
UV Sensor Reading (W m <sup>-2</sup> ) Tank Water Only	28.2	27.4	28.1	27.9	0.4	3	0.5
UV Sensor Reading (W m <sup>-2</sup> ) With MB and H2O2	17.8	18.1	17.8	17.9	0.2	3	0.2

Flow Rate = 20 GPM, Number of Baffles in Reactor = 1

**Table 4.8: Pilot Results for Research Condition No. 5**

Category	Trial 1 (7/24/2008)	Trial 2 (7/24/2008)	Trial 3 (6/17/2008)	Average	Standard Deviation	Count	Confidence Interval (alpha = 0.05)
Methylene Blue Concentration (mg L <sup>-1</sup> )	0.50	0.50	0.51	0.50	0.01	3	0.01
H <sub>2</sub> O <sub>2</sub> :MB Molar Ratio	198	203	198	199.67	2.89	3	3.27
H <sub>2</sub> O <sub>2</sub> Concentration (mg L <sup>-1</sup> )	10.5	10.8	10.6	10.6	0.2	3	0.2
Percent Removal (%)	65.0	65.0	62.4	64.1	1.5	3	1.7
UVT <sub>254</sub> Influent (%)	92.0	92.3	95.0	93.1	1.7	3	1.9
UVT <sub>254</sub> Effluent (%)	92.3	92.3	93.5	92.7	0.7	3	0.8
UVT <sub>254</sub> Average (%)				92.9	1.2	6	0.9
pH	7.24	7.24	7.22	7.23	0.01	3	0.01
Alkalinity (mg L <sup>-1</sup> as CaCO <sub>3</sub> )	21.7	21.7	22.5	22.0	0.5	3	0.5
Total Chlorine Residual (mg L <sup>-1</sup> as Cl <sub>2</sub> )	0.00	0.00	0.01	0.00	0.01	3	0.01
UV Sensor Reading (W m <sup>-2</sup> ) Tank Water Only	27.3	27.4	N/A	27.4	0.1	2	0.1
UV Sensor Reading (W m <sup>-2</sup> ) With MB and H2O2	16.8	17.0	9.8	16.9	0.1	2	0.2

Flow Rate = 20 GPM, Number of Baffles in Reactor = 5

**Table 4.9: Pilot Results for Research Condition No. 6**

Category	Trial 1 (7/15/2008)	Trial 2 (7/10/2008)	Trial 3 (7/22/2008)	Average	Standard Deviation	Count	Confidence Interval (alpha = 0.05)
Methylene Blue Concentration (mg L <sup>-1</sup> )	0.49	0.49	0.51	0.50	0.01	3	0.01
H <sub>2</sub> O <sub>2</sub> :MB Molar Ratio	201	202	198	200.33	2.08	3	2.36
H <sub>2</sub> O <sub>2</sub> Concentration (mg L <sup>-1</sup> )	10.6	10.6	10.6	10.6	0.0	3	0.0
Percent Removal (%)	68.7	64.6	65.3	66.2	2.2	3	2.5
UVT <sub>254</sub> Influent (%)	92.5	92.2	92.4	92.4	0.2	3	0.2
UVT <sub>254</sub> Effluent (%)	92.7	93.6	93.0	93.1	0.5	3	0.5
UVT <sub>254</sub> Average (%)				92.7	0.5	6	0.4
pH	7.24	7.25	7.25	7.25	0.01	3	0.01
Alkalinity (mg L <sup>-1</sup> as CaCO <sub>3</sub> )	21.3	22.5	21.7	21.8	0.6	3	0.7
Total Chlorine Residual (mg L <sup>-1</sup> as Cl <sub>2</sub> )	0.00	0.04	0.08	0.04	0.04	3	0.05
UV Sensor Reading (W m <sup>-2</sup> ) Tank Water Only	28.3	29.7	27.3	28.4	1.2	3	1.4
UV Sensor Reading (W m <sup>-2</sup> ) With MB and H2O2	17.6	18.1	17.0	17.6	0.6	3	0.6

Flow Rate = 20 GPM, Number of Baffles in Reactor = 1

**Table 4.10: Pilot Results for Research Condition No. 29**

Category	Trial 1 (9/11/2008)
Methylene Blue Concentration (mg L <sup>-1</sup> )	0.50
H <sub>2</sub> O <sub>2</sub> :MB Molar Ratio	266.4
H <sub>2</sub> O <sub>2</sub> Concentration (mg L <sup>-1</sup> )	14.2
Percent Removal (%)	72.0
UVT <sub>254</sub> Influent (%)	91.9
UVT <sub>254</sub> Effluent (%)	91.8
UVT <sub>254</sub> Average (%)	
pH	7.6
Alkalinity (mg L <sup>-1</sup> as CaCO <sub>3</sub> )	23.8
Total Chlorine Residual (mg L <sup>-1</sup> as Cl <sub>2</sub> )	0.16
UV Sensor Reading (W m <sup>-2</sup> ) Tank Water Only	26.8
UV Sensor Reading (W m <sup>-2</sup> ) With MB and H <sub>2</sub> O <sub>2</sub>	15.7

Flow Rate = 20 GPM, Number of Baffles in Reactor = 5  
Only 1 pilot trial completed for this condition.

**Table 4.11: Pilot Results for Research Condition No. 30**

Category	Trial 1 (10/9/2008)	Trial 2 (10/14/08)	Trial 3 (N/A)	Average	Standard Deviation	Count	Confidence Interval (alpha = 0.05)
Methylene Blue Concentration (mg L <sup>-1</sup> )	0.49	0.51		0.50	0.01	2	0.01
H <sub>2</sub> O <sub>2</sub> :MB Molar Ratio	144.2	144.2		144.20	0.00	2	0.00
H <sub>2</sub> O <sub>2</sub> Concentration (mg L <sup>-1</sup> )	7.5	7.8		7.6	0.2	2	0.2
Percent Removal (%)	38.8	38.6		38.7	0.1	2	0.2
UVT <sub>254</sub> Influent (%)	97.1	92.1		92.1	N/A	1	N/A
UVT <sub>254</sub> Effluent (%)	96.4	91.7		91.7	N/A	1	N/A
UVT <sub>254</sub> Average (%)				91.9	0.3	2	0.4
pH	7.64	7.34		7.49	0.21	2	0.29
Alkalinity (mg L <sup>-1</sup> as CaCO <sub>3</sub> )	29.8	26.4		28.1	2.4	2	3.3
Total Chlorine Residual (mg L <sup>-1</sup> as Cl <sub>2</sub> )	0.16	0.13		0.15	0.02	2	0.03
UV Sensor Reading (W m <sup>-2</sup> ) Tank Water Only	25.0	24.6		24.8	0.3	2	0.4
UV Sensor Reading (W m <sup>-2</sup> ) With MB and H <sub>2</sub> O <sub>2</sub>	15.9	15.8		15.9	0.1	2	0.1

Flow Rate = 30 GPM, Number of Baffles in Reactor = 5

**Table 4.12: Pilot Results for Research Condition No. 35**

Category	Trial 1 (6/12/2008)
Methylene Blue Concentration (mg L <sup>-1</sup> )	0.51
H <sub>2</sub> O <sub>2</sub> :MB Molar Ratio	139.2
H <sub>2</sub> O <sub>2</sub> Concentration (mg L <sup>-1</sup> )	7.5
Percent Removal (%)	92.2
UVT <sub>254</sub> Influent (%)	94.8
UVT <sub>254</sub> Effluent (%)	95.0
UVT <sub>254</sub> Average (%)	
pH	7.18
Alkalinity (mg L <sup>-1</sup> as CaCO <sub>3</sub> )	22.5
Total Chlorine Residual (mg L <sup>-1</sup> as Cl <sub>2</sub> )	0
UV Sensor Reading (W m <sup>-2</sup> ), Tank Water Only	N/M <sup>1</sup>
UV Sensor Reading (W m <sup>-2</sup> ), With MB and H <sub>2</sub> O <sub>2</sub>	N/M <sup>1</sup>

Flow Rate = 5 GPM, Number of Baffles in Reactor = 5

Only 1 pilot trial completed for this condition.

<sup>1</sup> Trial occurred prior to UV sensor installation. CFD lamp power based on later trials.

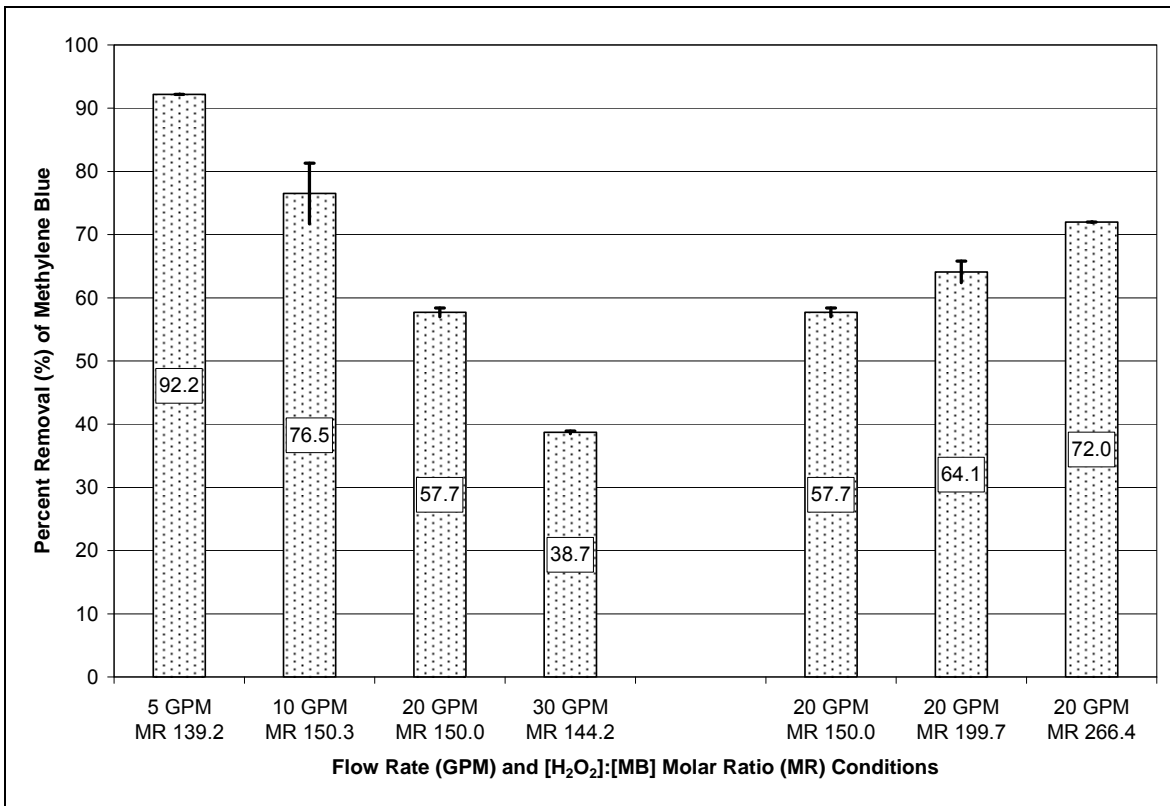


**Figure 4.8: Methylene Blue Pilot Reactor Results (Five Baffles)**

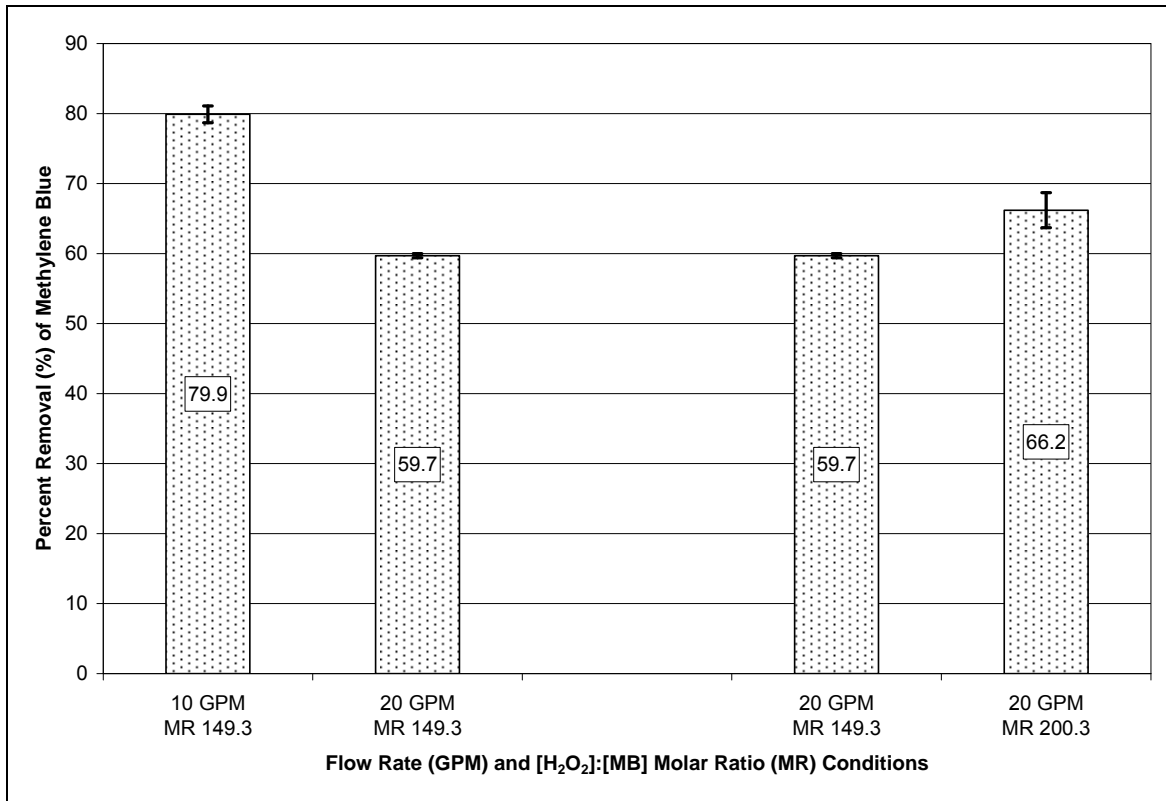


**Figure 4.9: Methylene Blue Pilot Reactor Results (One Baffle)**

The results of the methylene blue pilot trials followed expected trends. As the flow rate through the reactor was increased, the percent removal of methylene blue decreased. With higher flow rates, the delivered UV dose (i.e., fluence rate multiplied by contact time) decreases and, thus, the hydroxyl radical concentration and the corresponding methylene blue removal would decrease. Under similar hydrogen peroxide concentrations, doubling the flow from 10 GPM to 20 GPM decreased the methylene blue percent removal from 76.5% to 57.7%, a difference of 18.8%. Increasing the flow rate from 20 GPM to 30 GPM further reduces to the percent removal from 57.7% to 38.7%, a difference of 19.0%.

As the hydrogen peroxide concentration added to the reactor increased, the percent removal of methylene blue also increased. Higher influent hydrogen peroxide doses would

correspond to higher concentrations of hydroxyl radical in the reactor. Increasing the hydrogen peroxide dose from a molar ratio of 150 ( $7.9 \text{ mg L}^{-1}$ ) to  $\sim 200$  ( $10.6 \text{ mg L}^{-1}$ ) improved the removal from 57.7% to 64.1%, a difference of 6.4%. At a molar ratio of 267 ( $14.2 \text{ mg L}^{-1}$ ), the percent removal increased to 72.0%, another 7.9% increase over the molar ratio 200 condition. However, as noticed in the collimated beam studies, the percent removal of methylene blue should eventually plateau (and possibly decline) with increasing concentrations of hydrogen peroxide.

For the one-baffle trials, trends similar to the five-baffle cases were observed. As flow rate increased from 10 GPM to 20 GPM, the percent removal value decreased by a margin of 20.2% from 79.9% to 59.7%. The percent removal of methylene blue increased from 59.7% to 66.2% as the hydrogen peroxide increased from a molar ratio of 149 to 200 at 20 GPM, a difference of 6.5%. Another observation of comparing the one-baffle and five-baffle trials is that the one-baffle cases produced slightly higher methylene blue removals than similar conditions with five baffles in the reactor (79.9% with one baffle versus 76.5% with five baffles at 10 GPM and a molar ratio near 150; 59.7% with one baffle versus 57.7% with five baffles at 20 GPM and a molar ratio of approximately 150). One potential explanation for this difference is that the higher velocities through the orifices in the baffle plates force the reactor farther from ideal plug flow conditions. In addition, the baffles block axial spread of the UV light and likely reduce the total delivered UV dose.

Finally, the pilot results revealed that the change in UVT from influent to effluent was small (less than 1% for most cases). As such, the separation of the fluence rate and

kinetic codes in CFD does not introduce significant error that would be caused by change in the fluence rate distribution as a result of the chemical reactions in the system.

#### 4.2.2 Sulfamethoxazole

Three pilot trials were conducted with the antibiotic sulfamethoxazole (SMX) at a target initial concentration of  $10 \mu\text{g L}^{-1}$ . For each trial, both direct photolysis and advanced oxidation of SMX through the pilot reactor was measured. The results of the analyses are shown in Tables 4.13 and 4.14, and graphically in Figure 4.10. The first row of each of these tables shows the influent SMX concentration as the average of the two influent grab samples. The average effluent concentrations were used to calculate the percent removal values shown in the tables.

**Table 4.13: Pilot Results for Research Condition No. 10a (SMX Direct Photolysis)**

Category	Trial 1 (8/7/2008)	Trial 2 (9/9/2008)	Trial 3 (9/10/2008)	Average	Standard Deviation	Count	Confidence Interval (alpha = 0.05)
Sulfamethoxazole Concentration ( $\mu\text{g L}^{-1}$ )	8.75	10.45	9.09	9.43	0.90	3	1.02
$\text{H}_2\text{O}_2$ Concentration ( $\text{mg L}^{-1}$ )	0.0	0.0	0.0	0.0	0.0	3	0.0
Percent Removal (%)	78.1	80.7	78.8	79.3	0.0	3	0.0
UVT <sub>254</sub> Influent (%)	98.9	97.8	98.0	98.2	0.6	3	0.7
UVT <sub>254</sub> Effluent (%)	98.7	98.1	98.2	98.3	0.3	3	0.4
UVT <sub>254</sub> Average (%)				98.3	0.4	6	0.3
pH	7.39	7.25	7.63	7.63 <sup>(1)</sup>	N/A	1	N/A
Alkalinity ( $\text{mg L}^{-1}$ as $\text{CaCO}_3$ )	19.5	ND	ND	19.5 <sup>(2)</sup>	N/A	1	N/A
Total Chlorine Residual ( $\text{mg L}^{-1}$ as $\text{Cl}_2$ )	0.01	0.16	0.16	0.11	0.09	3	0.10
UV Sensor Reading ( $\text{W m}^{-2}$ )	25.0	26.2	26.5	26.3	0.8	3	0.9

Flow Rate = 10 GPM, Number of Baffles in Reactor = 5

(1) The pH readings for Trials 1 and 2 would not stabilize. A new pH meter was used for Trial 3.

(2) Alkalinity of tank water measured only once during SMX trials.

**Table 4.14: Pilot Results for Research Condition No. 10b (SMX AOP & Direct Photolysis)**

Category	Trial 1 (8/7/2008) <sup>(1)</sup>	Trial 2 (9/9/2008)	Trial 3 (9/10/2008)	Average	Standard Deviation	Count	Confidence Interval (alpha = 0.05)
Sulfamethoxazole Concentration ( $\mu\text{g L}^{-1}$ )	8.71	10.47	9.37	9.92 <sup>(4)</sup>	0.78	2	1.08
H <sub>2</sub> O <sub>2</sub> Concentration ( $\text{mg L}^{-1}$ )	9.4	NA <sup>(2)</sup>	10.2	10.2	N/A	1	N/A
Percent Removal (%)	73.4	95.1	100 <sup>(3)</sup>	95.1 - 100	N/A	2	N/A
UVT <sub>254</sub> Influent (%)	81.5	82.5	82.9	82.7	0.3	2	0.4
UVT <sub>254</sub> Effluent (%)	82.4	83.8	83.4	83.6	0.3	2	0.4
UVT <sub>254</sub> Average (%)				83.2	0.6	4	0.6
pH	7.47	7.35	7.74	7.74 <sup>(5)</sup>	N/A	1	N/A
UV Sensor Reading ( $\text{W m}^{-2}$ ) With SMX and H <sub>2</sub> O <sub>2</sub>	22.8	23.8	23.9	23.8	0.1	2	0.2

Flow Rate = 10 GPM, Number of Baffles in Reactor = 5

Alkalinity and Total Chlorine measurements same as direct photolysis since both direct photolysis and advanced oxidation performed in same trial.

- (1) Trial 1 data was eliminated since percent removal value appears to be an outlier.
- (2) Hydrogen peroxide concentration for this trial not recorded. Same bulk solution and feed rate as Trial 3.
- (3) HPLC analysis detected no SMX in effluent.
- (4) Averages represent Trials 2 and 3. Percent Removal reported as a range since Trial 3 produced 100% removal.
- (5) The pH readings for Trials 1 and 2 would not stabilize. A new pH meter was used for Trial 3.

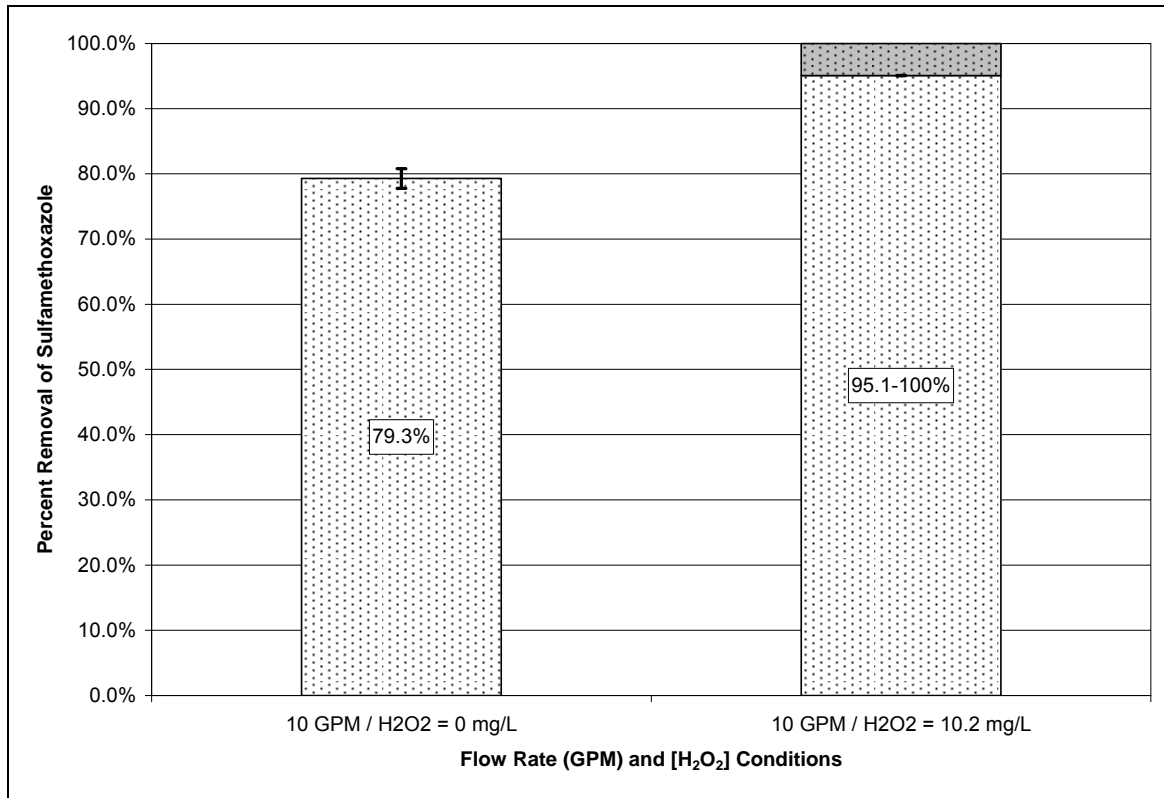


**Figure 4.10: Sulfamethoxazole Pilot Test Results**

Only one flow rate and hydrogen peroxide condition was completed with the pilot reactor using SMX as the target compound. As seen in Figure 4.10, direct photolysis removed 79.3% of the influent SMX. Following the introduction of hydrogen peroxide to the system, the percent removal increased to 95.1%. The fraction of the latter removal that is caused by advanced oxidation only is unknown since the direct photolysis would be expected to decrease as hydrogen peroxide is added and the UVT decreases.

### 4.3 Computational Fluid Dynamics

#### 4.3.1 Grid Independence

To determine grid independence in this study, several grid densities were created that maintained fine grid spacing within the reactor in areas of expected high gradients and that were symmetrical about the UV lamp inside the reactor. Based on preliminary results, two grid systems that differed in the number of cells in each direction by approximately 10% were selected for evaluation of grid independence. These two grid systems are described in Table 4.15. For reference, the system with the higher grid density (greater number of cells) was called “LP3D Grid Hi” and the other grid density was named “LP3D Grid Avg.” Since the change in velocity, methylene blue concentration, and hydrogen peroxide concentration differed by no more than 1%, the grid density developed in “LP3D Grid Avg” was sufficient to achieve grid independence while minimizing run time and memory requirements. As such, this grid density was used for the CFD models in this research.

**Table 4.15: Grid Independence Data**

Number of Cells	LP3D Grid Hi	LP3D Grid Avg	Difference
x	48	43	10.42%
y	194	185	4.64%
z	124	108	12.90%
Total	1,154,688	859,140	25.60%
Velocity ( $\text{m s}^{-1}$ ) at (x,y,z) = (0.014372, 0.079605, 1.224519)	0.687169	0.657912	4.26%
Average Velocity ( $\text{m s}^{-1}$ ) across entire domain	0.635699	0.639553	0.61%
Normalized Methylene Blue Concentration ( $C/C_0$ ) at (x,y,z) = (0.014372, 0.079605, 1.224519)	0.698752	0.706758	1.15%
Average Normalized Methylene Blue Concentration across entire domain	0.849220	0.849814	0.07%
Average Normalized Methylene Blue Concentration across slice at $i=2$ (approximate spectrophotometric probe location)	0.696683	0.696680	0.00%
Normalized Hydrogen Peroxide Concentration ( $C/C_0$ ) at (x,y,z) = (0.014372, 0.079605, 1.224519)	0.998428	0.998482	0.01%
Average Normalized Hydrogen Peroxide Concentration across entire domain	0.999215	0.999221	0.00%

#### 4.3.2 Comparison of Experimental Results to CFD Model Results

Each of the research conditions previously described for the pilot reactor was modeled with CFD. The results of these model runs are presented with the corresponding pilot data in this section. Summary sheets for each model are included in Appendix B. As described in Section 3, each CFD model actually consists of three CFD codes. Typical results from the pressure and velocity code are shown in Figure 4.11 for a five-baffle system operating at 20 GPM. Most noticeable in Figure 4.11 are the areas of high velocity for the flow through the circular orifices in each of the baffle plates. Figure 4.12 displays the

fluence rate distribution ( $C3$  in  $W\ m^{-2}$ ) produced by the RAD-LSI sub-model for a lamp with a 29.6-watt output at 254 nm at a UV transmittance of 92.9%.

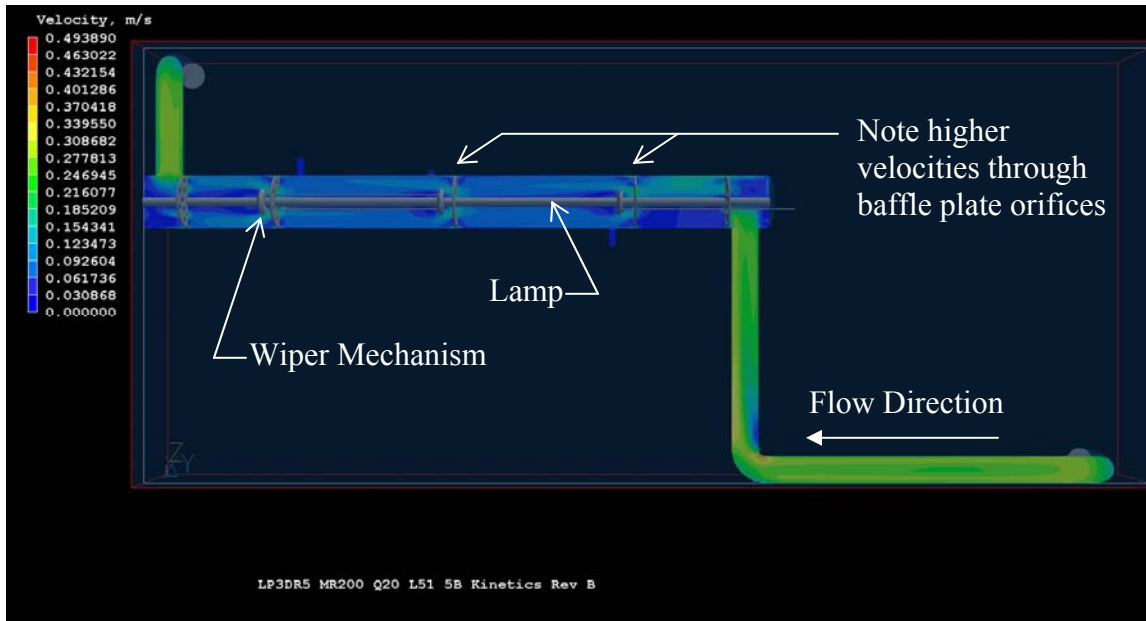


Figure 4.11: Velocity Distribution in Reactor with Five Baffles and Flow = 20 GPM

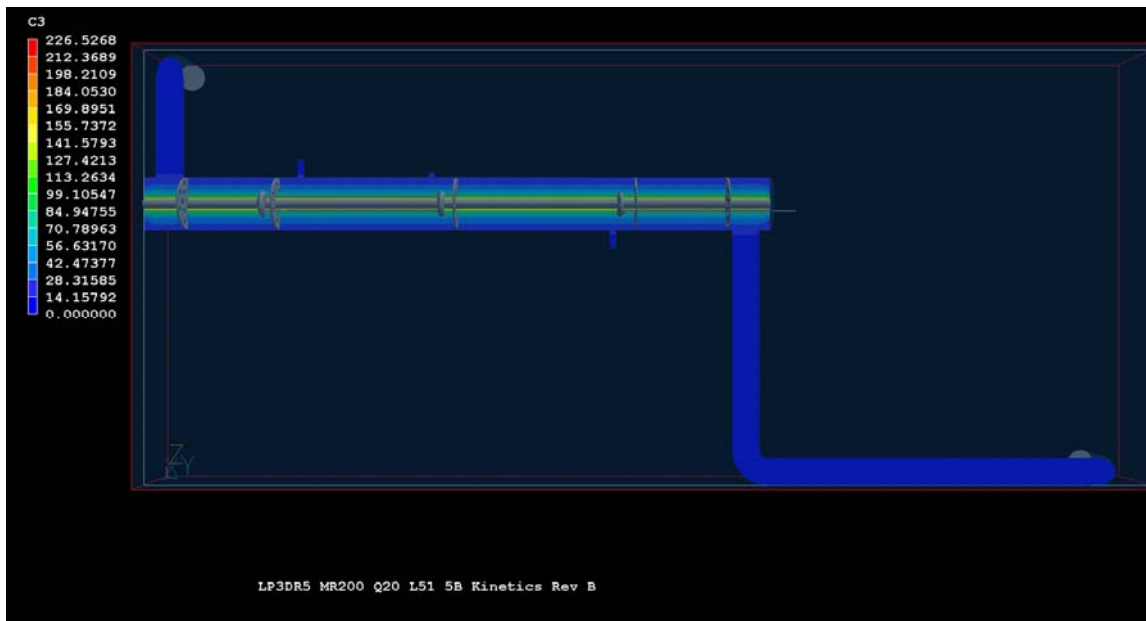


Figure 4.12: Fluence Rate Distribution in Reactor (Output P = 29.6 W, UVT = 92.9 %)

#### 4.3.2.1 Methylene Blue

During this research, nine (9) combinations of flow rate and hydrogen peroxide concentration were evaluated using methylene blue in the pilot-scale reactor and the CFD model. The resulting data for these combinations are shown in Tables 4.16 through 4.24. The pilot and CFD data are compared in Figures 4.13 and 4.14.

**Table 4.16: Research Condition No. 1**

Parameter	Goal	Actual – Experimental <sup>1</sup>	CFD Model
Flow Rate (gal min <sup>-1</sup> )	10	10	10
Target Compound	Methylene Blue		
Compound Concentration (mg L <sup>-1</sup> )	0.50	0.50 ± 0.01	0.50
Molar Ratio of H <sub>2</sub> O <sub>2</sub> to Compound	150	150.3 ± 1.7	150.3
H <sub>2</sub> O <sub>2</sub> Concentration (mg L <sup>-1</sup> )	7.98	8.0 ± 0.2	7.99
Power output at lamp surface (W)		N/A <sup>2</sup>	26.5
Fluence Rate at Sensor (W m <sup>-2</sup> )		18.1 ± 0.3	18.0
UVT <sub>254</sub> (%)		94.4 ± 0.9 <sup>3</sup>	94.9
pH		7.24 ± 0.03	7.24
DOC (mg L <sup>-1</sup> )		0.57 <sup>4</sup>	0.57
Alkalinity (mg L <sup>-1</sup> as CaCO <sub>3</sub> )		23.0 ± 0.5	23.0
Total Chlorine Residual (mg L <sup>-1</sup> as Cl <sub>2</sub> )		0.05 ± 0.09	0.05
Number of Baffles in Reactor	5	5	5
Turbulence Sub-model			k-ε
Fluence Rate Sub-model			RAD-LSI
k <sub>MB,OH</sub> (M <sup>-1</sup> s <sup>-1</sup> )			6.9 x 10 <sup>10</sup>
Fraction of Initial Compound Remaining		0.235	0.219
Compound Percent Removal (%)		76.5 ± 4.8	78.1

<sup>1</sup> 95% confidence intervals calculated using Microsoft Excel. Sample size = 3 trials (with exception of “total chlorine residual” and “fluence rate at sensor”, each of which has sample size = 2, and UVT, which has a sample size of 6). <sup>2</sup> Light output not measured at surface of lamps. <sup>3</sup> UVT is the average of influent and effluent samples. <sup>4</sup> TOC was measured once for influent water and the result used as DOC for all models.

**Table 4.17: Research Condition No. 2**

Parameter	Goal	Actual – Experimental <sup>1</sup>	CFD Model
Flow Rate (gal min <sup>-1</sup> )	10	10	10
Target Compound	Methylene Blue		
Compound Concentration (mg L <sup>-1</sup> )	0.50	0.50 ± 0.01	0.50
Molar Ratio of H <sub>2</sub> O <sub>2</sub> to Compound	150	149.3 ± 0.7	149.3
H <sub>2</sub> O <sub>2</sub> Concentration (mg L <sup>-1</sup> )	7.98	7.9 ± 0.0	7.94
Power output at lamp surface (W)		N/A <sup>2</sup>	26.5
Fluence Rate at Sensor (W m <sup>-2</sup> )		17.3 ± 0.4	17.3
UVT <sub>254</sub> (%)		92.6 ± 0.4 <sup>3</sup>	94.6
pH		7.25 ± 0.01	7.25
DOC (mg L <sup>-1</sup> )		0.57 <sup>4</sup>	0.57
Alkalinity (mg L <sup>-1</sup> as CaCO <sub>3</sub> )		20.8 ± 0.8	20.8
Total Chlorine Residual (mg L <sup>-1</sup> as Cl <sub>2</sub> )		0.04 ± 0.03	0.04
Number of Baffles in Reactor	1	1	1
Turbulence Sub-model			k-ε
Fluence Rate Sub-model			RAD-LSI
k <sub>MB,OH</sub> (M <sup>-1</sup> s <sup>-1</sup> )			6.9 x 10 <sup>10</sup>
Fraction of Initial Compound Remaining		0.201	0.227
Compound Percent Removal (%)		79.9 ± 1.3	77.3

<sup>1</sup> 95% confidence intervals calculated using Microsoft Excel. Sample size = 3 trials (with exception of UVT, which has a sample size of 6). <sup>2</sup> Light output not measured at surface of lamps. <sup>3</sup> UVT is the average of influent and effluent samples. <sup>4</sup> TOC was measured once for influent water and the result used as DOC for all models.

**Table 4.18: Research Condition No. 3**

Parameter	Goal	Actual – Experimental <sup>1</sup>	CFD Model
Flow Rate (gal min <sup>-1</sup> )	20	20	20
Target Compound	Methylene Blue		
Compound Concentration (mg L <sup>-1</sup> )	0.50	0.50 ± 0.00	0.50
Molar Ratio of H <sub>2</sub> O <sub>2</sub> to Compound	150	150.0 ± 2.0	150
H <sub>2</sub> O <sub>2</sub> Concentration (mg L <sup>-1</sup> )	7.98	8.0 ± 0.1	7.97
Power output at lamp surface (W)		N/A <sup>2</sup>	29.9
Fluence Rate at Sensor (W m <sup>-2</sup> )		16.8 ± 0.4	16.8
UVT <sub>254</sub> (%)		92.7 ± 0.3 <sup>3</sup>	92.7
pH		7.30 ± 0.05	7.30
DOC (mg L <sup>-1</sup> )		0.57 <sup>4</sup>	0.57
Alkalinity (mg L <sup>-1</sup> as CaCO <sub>3</sub> )		22.7 ± 0.8	22.7
Total Chlorine Residual (mg L <sup>-1</sup> as Cl <sub>2</sub> )		0.05 ± 0.03	0.05
Number of Baffles in Reactor	5	5	5
Turbulence Sub-model			k-ε
Fluence Rate Sub-model			RAD-LSI
k <sub>MB,OH</sub> (M <sup>-1</sup> s <sup>-1</sup> )			6.9 x 10 <sup>10</sup>
Fraction of Initial Compound Remaining		0.423	0.529
Compound Percent Removal (%)		57.7 ± 0.7	47.1

<sup>1</sup> 95% confidence intervals calculated using Microsoft Excel. Sample size = 3 trials (with exception of UVT, which has a sample size of 6). <sup>2</sup> Light output not measured at surface of lamps. <sup>3</sup> UVT is the average of influent and effluent samples. <sup>4</sup> TOC was measured once for influent water and the result used as DOC for all models.

**Table 4.19: Research Condition No. 4**

Parameter	Goal	Actual – Experimental <sup>1</sup>	CFD Model
Flow Rate (gal min <sup>-1</sup> )	20	20	20
Target Compound	Methylene Blue		
Compound Concentration (mg L <sup>-1</sup> )	0.50	0.49 ± 0.01	0.49
Molar Ratio of H <sub>2</sub> O <sub>2</sub> to Compound	150	149.3 ± 2.6	149.3
H <sub>2</sub> O <sub>2</sub> Concentration (mg L <sup>-1</sup> )	7.98	7.8 ± 0.1	7.78
Power output at lamp surface (W)		N/A <sup>2</sup>	26.5
Fluence Rate at Sensor (W m <sup>-2</sup> )		17.9 ± 0.2	17.8
UVT <sub>254</sub> (%)		93.3 ± 0.2 <sup>3</sup>	94.9
pH		7.24 ± 0.01	7.24
DOC (mg L <sup>-1</sup> )		0.57 <sup>4</sup>	0.57
Alkalinity (mg L <sup>-1</sup> as CaCO <sub>3</sub> )		21.1 ± 0.6	21.1
Total Chlorine Residual (mg L <sup>-1</sup> as Cl <sub>2</sub> )		0.04 ± 0.04	0.04
Number of Baffles in Reactor	1	1	1
Turbulence Sub-model			k-ε
Fluence Rate Sub-model			RAD-LSI
k <sub>MB,OH</sub> (M <sup>-1</sup> s <sup>-1</sup> )			6.9 x 10 <sup>10</sup>
Fraction of Initial Compound Remaining		0.403	0.540
Compound Percent Removal (%)		59.7 ± 0.3	46.0

<sup>1</sup> 95% confidence intervals calculated using Microsoft Excel. Sample size = 3 trials (with exception of UVT, which has a sample size of 6). <sup>2</sup> Light output not measured at surface of lamps. <sup>3</sup> UVT is the average of influent and effluent samples. <sup>4</sup> TOC was measured once for influent water and the result used as DOC for all models.

**Table 4.20: Research Condition No. 5**

Parameter	Goal	Actual – Experimental <sup>1</sup>	CFD Model
Flow Rate (gal min <sup>-1</sup> )	20	20	20
Target Compound	Methylene Blue		
Compound Concentration (mg L <sup>-1</sup> )	0.50	0.50 ± 0.01	0.50
Molar Ratio of H <sub>2</sub> O <sub>2</sub> to Compound	200	199.7 ± 3.3	199.7
H <sub>2</sub> O <sub>2</sub> Concentration (mg L <sup>-1</sup> )	10.6	10.6 ± 0.2	10.6
Power output at lamp surface (W)		N/A <sup>2</sup>	29.6
Fluence Rate at Sensor (W m <sup>-2</sup> )		16.9 ± 0.2	16.9
UVT <sub>254</sub> (%)		92.9 ± 0.9 <sup>3</sup>	92.9
pH		7.23 ± 0.01	7.23
DOC (mg L <sup>-1</sup> )		0.57 <sup>4</sup>	0.57
Alkalinity (mg L <sup>-1</sup> as CaCO <sub>3</sub> )		22.0 ± 0.5	22.2
Total Chlorine Residual (mg L <sup>-1</sup> as Cl <sub>2</sub> )		0.01 ± 0.01	0.013
Number of Baffles in Reactor	5	5	5
Turbulence Sub-model			k-ε
Fluence Rate Sub-model			RAD-LSI
k <sub>MB,OH</sub> (M <sup>-1</sup> s <sup>-1</sup> )			6.9 x 10 <sup>10</sup>
Fraction of Initial Compound Remaining		0.359	0.414
Compound Percent Removal (%)		64.1 ± 1.7	58.6

<sup>1</sup> 95% confidence intervals calculated using Microsoft Excel. Sample size = 3 trials (with exception of “fluence rate at sensor”, which has sample size = 2 and UVT, which has a sample size of 6). <sup>2</sup> Light output not measured at surface of lamps. <sup>3</sup> UVT is the average of influent and effluent samples. <sup>4</sup> TOC was measured once for influent water and the result used as DOC for all models.

**Table 4.21: Research Condition No. 6**

Parameter	Goal	Actual – Experimental <sup>1</sup>	CFD Model
Flow Rate (gal min <sup>-1</sup> )	20	20	20
Target Compound	Methylene Blue		
Compound Concentration (mg L <sup>-1</sup> )	0.50	0.50 ± 0.01	0.50
Molar Ratio of H <sub>2</sub> O <sub>2</sub> to Compound	200	200.3 ± 2.4	200.3
H <sub>2</sub> O <sub>2</sub> Concentration (mg L <sup>-1</sup> )	10.6	10.6 ± 0.0	10.6
Power output at lamp surface (W)		N/A <sup>2</sup>	26.5
Fluence Rate at Sensor (W m <sup>-2</sup> )		17.6 ± 0.6	17.8
UVT <sub>254</sub> (%)		92.7 ± 0.4 <sup>3</sup>	94.9
pH		7.25 ± 0.01	7.25
DOC (mg L <sup>-1</sup> )		0.57 <sup>4</sup>	0.57
Alkalinity (mg L <sup>-1</sup> as CaCO <sub>3</sub> )		21.8 ± 0.7	21.8
Total Chlorine Residual (mg L <sup>-1</sup> as Cl <sub>2</sub> )		0.04 ± 0.04	0.04
Number of Baffles in Reactor	1	1	1
Turbulence Sub-model			k-ε
Fluence Rate Sub-model			RAD-LSI
k <sub>MB,OH</sub> (M <sup>-1</sup> s <sup>-1</sup> )			6.9 x 10 <sup>10</sup>
Fraction of Initial Compound Remaining		0.338	0.429
Compound Percent Removal (%)		66.2 ± 2.5	57.1

<sup>1</sup> 95% confidence intervals calculated using Microsoft Excel. Sample size = 3 trials (with exception of UVT, which has a sample size of 6). <sup>2</sup> Light output not measured at surface of lamps. <sup>3</sup> UVT is the average of influent and effluent samples. <sup>4</sup> TOC was measured once for influent water and the result used as DOC for all models.

**Table 4.22: Research Condition No. 29**

Parameter	Goal	Actual – Experimental <sup>1</sup>	CFD Model
Flow Rate (gal min <sup>-1</sup> )	20	20	20
Target Compound	Methylene Blue		
Compound Concentration (mg L <sup>-1</sup> )	0.5	0.50	0.50
Molar Ratio of H <sub>2</sub> O <sub>2</sub> to Compound	250	266.4	266.4
H <sub>2</sub> O <sub>2</sub> Concentration (mg L <sup>-1</sup> )	13.29	14.16	14.16
Power output at lamp surface (W)		N/A <sup>2</sup>	26.5
Fluence Rate at Sensor (W m <sup>-2</sup> )		15.7	15.6
UVT <sub>254</sub> (%)		91.9 <sup>3</sup>	93.2
pH		7.60	7.37
DOC (mg L <sup>-1</sup> )		0.57 <sup>4</sup>	0.57
Alkalinity (mg L <sup>-1</sup> as CaCO <sub>3</sub> )		23.8	23.8
Total Chlorine Residual (mg L <sup>-1</sup> as Cl <sub>2</sub> )		0.16	0.16
Number of Baffles in Reactor	5	5	5
Turbulence Sub-model			k-ε
Fluence Rate Sub-model			RAD-LSI
k <sub>MB,OH</sub> (M <sup>-1</sup> s <sup>-1</sup> )			6.9 x 10 <sup>10</sup>
Fraction of Initial Compound Remaining		0.28	0.376
Compound Percent Removal (%)		72	62.4

<sup>1</sup> Only one pilot trial at this condition. <sup>2</sup> Light output not measured at surface of lamps. <sup>3</sup> UVT is the average of influent and effluent samples. <sup>4</sup> TOC was measured once for influent water and the result used as DOC for all models.

**Table 4.23: Research Condition No. 30**

Parameter	Goal	Actual – Experimental <sup>1</sup>	CFD Model
Flow Rate (gal min <sup>-1</sup> )	30	30	30
Target Compound	Methylene Blue		
Compound Concentration (mg L <sup>-1</sup> )	0.50	0.50 ± 0.01	0.50
Molar Ratio of H <sub>2</sub> O <sub>2</sub> to Compound	150	144.2 ± 0.00	144.2
H <sub>2</sub> O <sub>2</sub> Concentration (mg L <sup>-1</sup> )	7.98	7.64 ± 0.23	7.66
Power output at lamp surface (W)		N/A <sup>2</sup>	30.2
Fluence Rate at Sensor (W m <sup>-2</sup> )		15.9 ± 0.1	15.8
UVT <sub>254</sub> (%)		91.9 ± 0.4 <sup>3</sup>	91.9
pH		7.49 ± 0.29	7.49
DOC (mg L <sup>-1</sup> )		0.57 <sup>4</sup>	0.57
Alkalinity (mg L <sup>-1</sup> as CaCO <sub>3</sub> )		28.1 ± 3.33	28.1
Total Chlorine Residual (mg L <sup>-1</sup> as Cl <sub>2</sub> )		0.15 ± 0.03	0.14
Number of Baffles in Reactor	5	5	5
Turbulence Sub-model			k-ε
Fluence Rate Sub-model			RAD-LSI
k <sub>MB,OH</sub> (M <sup>-1</sup> s <sup>-1</sup> )			6.9 x 10 <sup>10</sup>
Fraction of Initial Compound Remaining		0.613	0.701
Compound Percent Removal (%)		38.7	29.9

<sup>1</sup> 95% confidence intervals calculated using Microsoft Excel. Sample size = 2 trials. <sup>2</sup> Light output not measured at surface of lamps. <sup>3</sup> UVT is the average of influent and effluent samples. <sup>4</sup> TOC was measured once for influent water and the result used as DOC for all models.

**Table 4.24: Research Condition No. 35**

Parameter	Goal	Actual – Experimental <sup>1</sup>	CFD Model
Flow Rate (gal min <sup>-1</sup> )	5	5	5
Target Compound	Methylene Blue		
Compound Concentration (mg L <sup>-1</sup> )	0.50	0.51	0.50
Molar Ratio of H <sub>2</sub> O <sub>2</sub> to Compound	150	139.2	139.2
H <sub>2</sub> O <sub>2</sub> Concentration (mg L <sup>-1</sup> )	7.98	7.5	7.4
Power output at lamp surface (W)		N/A <sup>2</sup>	29.6
Fluence Rate at Sensor (W m <sup>-2</sup> )		N/M <sup>5</sup>	18.2
UVT <sub>254</sub> (%)		94.9 <sup>3</sup>	93.7
pH		7.18	7.18
DOC (mg L <sup>-1</sup> )		0.57 <sup>4</sup>	0.57
Alkalinity (mg L <sup>-1</sup> as CaCO <sub>3</sub> )		22.5	22.5
Total Chlorine Residual (mg L <sup>-1</sup> as Cl <sub>2</sub> )		0.0	0.0
Number of Baffles in Reactor	5	5	5
Turbulence Sub-model			k-ε
Fluence Rate Sub-model			RAD-LSI
k <sub>MB,OH</sub> (M <sup>-1</sup> s <sup>-1</sup> )			6.9 x 10 <sup>10</sup>
Fraction of Initial Compound Remaining		0.078	0.082
Compound Percent Removal (%)		92.2	91.8

<sup>1</sup> Only one pilot trial at this condition. <sup>2</sup> Light output not measured at surface of lamps. <sup>3</sup> UVT is the average of influent and effluent samples. <sup>4</sup> TOC was measured once for influent water and the result used as DOC for all models. <sup>5</sup> Trial occurred prior to UV sensor installation. CFD lamp power based on later trials.

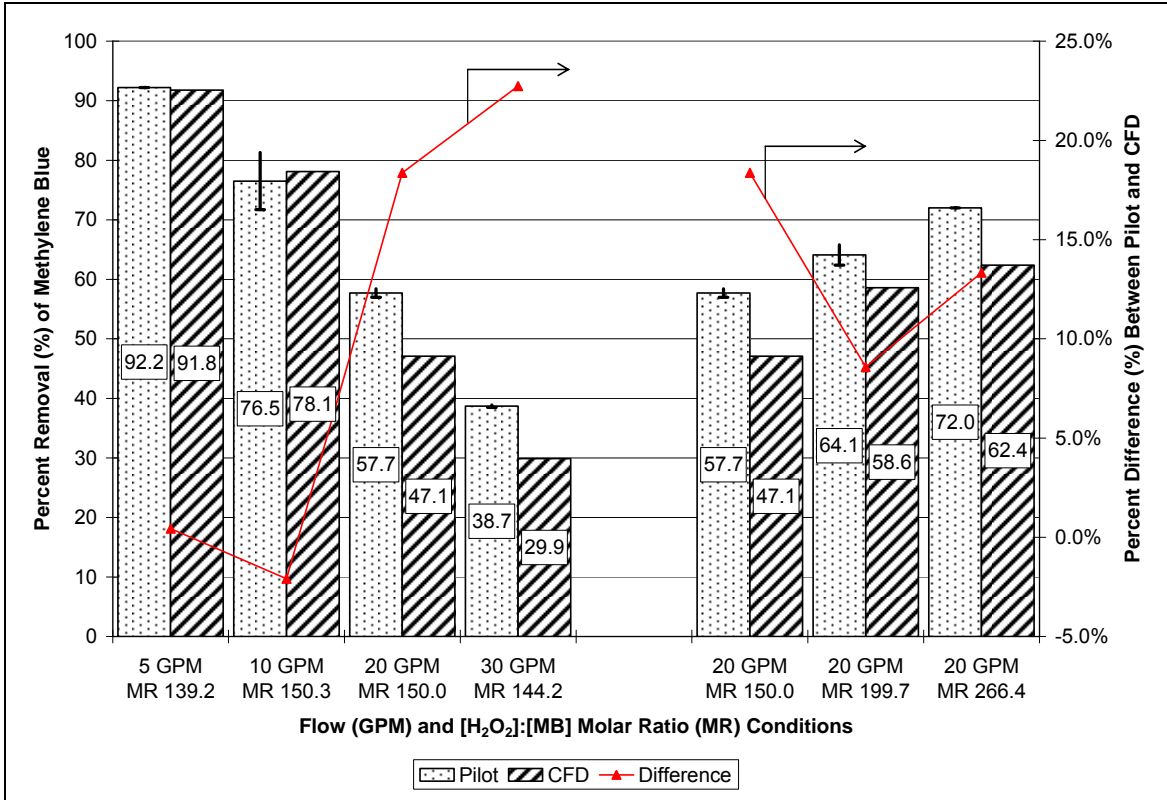


**Figure 4.13: Comparison of Pilot and CFD Results for Five-Baffle Trials**

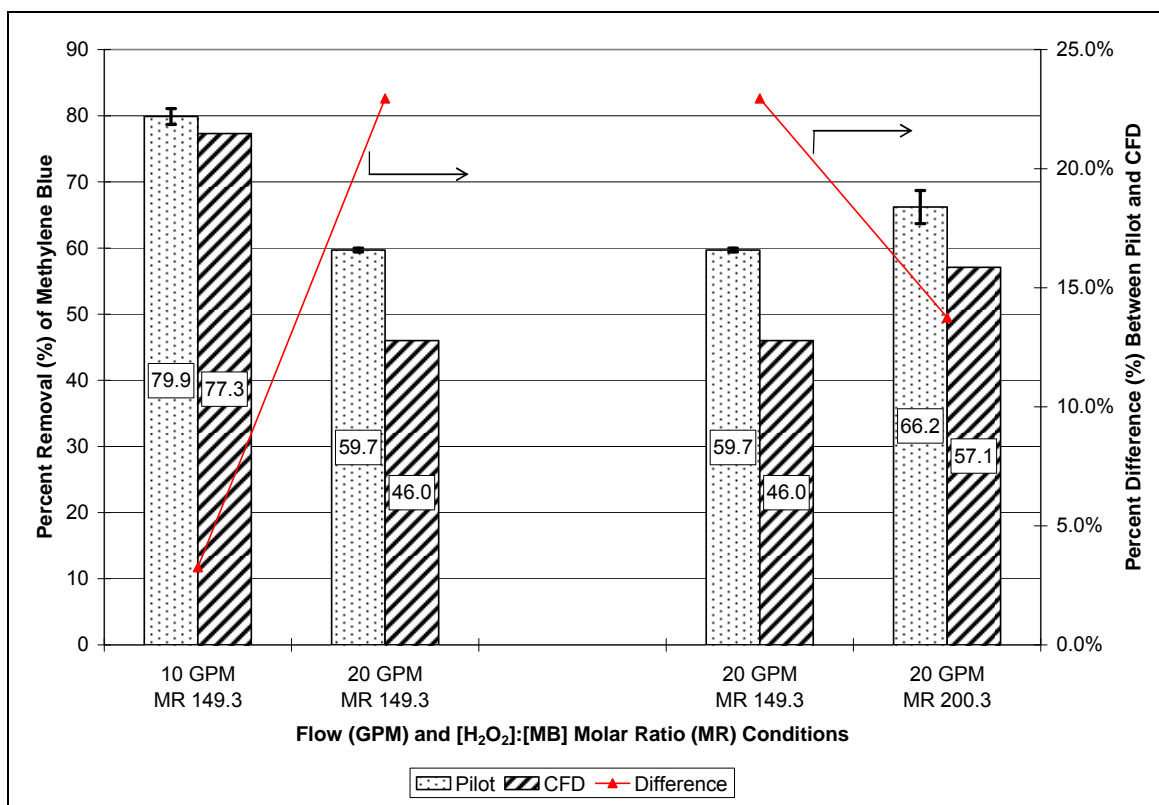


**Figure 4.14: Comparison of Pilot and CFD Results for One-Baffle Trials**

Examination of Figure 4.13 reveals several trends. First, the CFD model tends to under-predict the percent removal of methylene blue within the reactor. While the research conditions performed at 5 and 10 GPM produced relatively good agreement between pilot and CFD results, the CFD removal predicted at higher flows was significantly less than that achieved in the pilot. For the comparison of flow rate effects, the difference between pilot and CFD results was as high as 18.4%. For the trials in which hydrogen peroxide dose was varied, the difference between pilot and CFD reached 22.7%. One potential explanation is an over-prediction of radical scavenger effects in the model. More hydroxyl radicals would be available for reaction if the DOC concentration, which will later be shown to significantly impact the degradation of methylene blue, was lower in any individual pilot trial than that

modeled. Another likely cause of this under-prediction trend is the potential for additional reactions occurring in the pilot system that lead to methylene blue degradation but that are not modeled in CFD. For instance, a reaction between carbonate and/or NOM radicals and methylene blue could be occurring in the reactor. Although reactions with radicals other than the hydroxyl radical are common for organic contaminants, they are often not quantified in the literature (and, thus, may or may not be reflected in reported reaction rate constants). As for this latter potential cause, the only inconsistency is that if there were other reactions occurring in the reactor, they should have also produced under-predictions in the 5 and 10 GPM cases.

The second trend in Figure 4.13, as displayed for the data points on the left side of the figure, is that the percent difference between the pilot and the CFD results increased with increasing flow rates. It would be expected that the solution of reactions with rate constants large enough to be considered diffusion-limited would cause CFD to over-predict the percent removal if diffusion effects were not considered. However, this trend is not what is shown in Figure 4.13. Thus, it appears that there might be other hydraulic effects that are not being considered. These hydraulic differences are not reflected in the three two-equation turbulence sub-models considered (as will be presented in a later section) and thus could be related to small-scale eddy effects. Turbulence can be composed of many transient structural features that are difficult to capture with Reynolds Averaged Navier-Stokes (RANS) equations. The RANS equations in CFD have been shown to poorly capture the turbulent kinetic energy and the extent of the recirculation zones in the wake regions behind flow obstructions. Another hypothesis for the differences between the experimental and model

results at the higher flow rates in this study is that the CFD RANS models used did not adequately capture the flow characteristics downstream of the baffle plates in which enhanced mixing might improve the reaction conditions between the hydroxyl radical and methylene blue.

#### 4.3.2.2 Sulfamethoxazole

The conditions of the pilot trials testing the removal of sulfamethoxazole (SMX) were also modeled in CFD. Separate CFD models were created for the direct photolysis and the combined (direct photolysis + advanced oxidation) portions of the trials. The results of these models are presented in Tables 4.25 and 4.26, and summarized graphically in Figure 4.15. In addition, the CFD models for SMX were run with both the RAD-LSI and MSSS fluence rate sub-models. The comparison of the fluence rate sub-model results is shown in Table 4.27 presented in the next section.

**Table 4.25: Research Condition No. 10a – Direct Photolysis of SMX**

Parameter	Goal	Actual – Experimental <sup>1</sup>	CFD Model
Flow Rate (gal min <sup>-1</sup> )	10	10	10
Target Compound	SMX		
Compound Concentration (µg L <sup>-1</sup> )	10	9.43 ± 1.02	9.43
H <sub>2</sub> O <sub>2</sub> Concentration (mg L <sup>-1</sup> )	0	0	0
Power output at lamp surface (W)		N/A <sup>2</sup>	29.6
Fluence Rate at Sensor (W m <sup>-2</sup> )		26.3 ± 0.9	26.2
UVT <sub>254</sub> (%)		98.3 ± 0.3 <sup>3</sup>	98.0
pH		7.63 <sup>5</sup>	7.63
DOC (mg L <sup>-1</sup> )		0.57 <sup>4</sup>	0.57
Alkalinity (mg L <sup>-1</sup> as CaCO <sub>3</sub> )		19.5 <sup>5</sup>	19.5
Total Chlorine Residual (mg L <sup>-1</sup> as Cl <sub>2</sub> )		0.16 <sup>5</sup>	0.16
Number of Baffles in Reactor	5	5	5
Turbulence Sub-model			RNG k-ε
Fluence Rate Sub-model			RAD-LSI
k <sub>SMX,OH</sub> (M <sup>-1</sup> s <sup>-1</sup> )			5.6 x 10 <sup>9</sup>
Apparent Quantum Yield, Φ' (mol ein <sup>-1</sup> )			0.047
Apparent Absorptivity, ε' (m <sup>2</sup> mol <sup>-1</sup> )			1670
Fraction of Initial Compound Remaining		0.207	0.648
Compound Percent Removal (%)		79.3 ± 1.5	35.2

<sup>1</sup> 95% confidence intervals calculated using Microsoft Excel. Sample size = 3 trials (with exception of UVT, which has a sample size of 6). <sup>2</sup> Light output not measured at surface of lamps. <sup>3</sup> UVT is the average of influent and effluent samples. <sup>4</sup> TOC was measured once for influent water and the result used as DOC for all models. <sup>5</sup> Only one data point.

**Table 4.26: Research Condition No. 10b – SMX Advanced Oxidation and Photolysis**

Parameter	Goal	Actual – Experimental <sup>1</sup>	CFD Model
Flow Rate (gal min <sup>-1</sup> )	10	10	10
Target Compound	SMX		
Compound Concentration (µg L <sup>-1</sup> )	10	9.92 ± 1.08	10.0
H <sub>2</sub> O <sub>2</sub> Concentration (mg L <sup>-1</sup> )	10	10.2	10.13
Power output at lamp surface (W)		N/A <sup>2</sup>	29.6
Fluence Rate at Sensor (W m <sup>-2</sup> )		23.8 ± 0.2	23.9
UVT <sub>254</sub> (%)		83.2 ± 0.6 <sup>3</sup>	96.9
pH		7.74	7.74
DOC (mg L <sup>-1</sup> )		0.57 <sup>4</sup>	0.57
Alkalinity (mg L <sup>-1</sup> as CaCO <sub>3</sub> )		19.5	19.5
Total Chlorine Residual (mg L <sup>-1</sup> as Cl <sub>2</sub> )		0.16	0.16
Number of Baffles in Reactor	5	5	5
Turbulence Sub-model			RNG k-ε
Fluence Rate Sub-model			RAD-LSI
k <sub>SMX,OH</sub> (M <sup>-1</sup> s <sup>-1</sup> )			5.6 x 10 <sup>9</sup>
Apparent Quantum Yield, Φ' (mol ein <sup>-1</sup> )			0.047
Apparent Absorptivity, ε' (m <sup>2</sup> mol <sup>-1</sup> )			1672
Fraction of Initial Compound Remaining		0.000-0.049	0.439
Compound Percent Removal (%)		95.1-100	56.1

<sup>1</sup> See notes for Table 4.14. <sup>2</sup> Light output not measured at surface of lamps. <sup>3</sup> UVT is the average of influent and effluent samples. <sup>4</sup> TOC was measured once for influent water and the result used as DOC for all models.

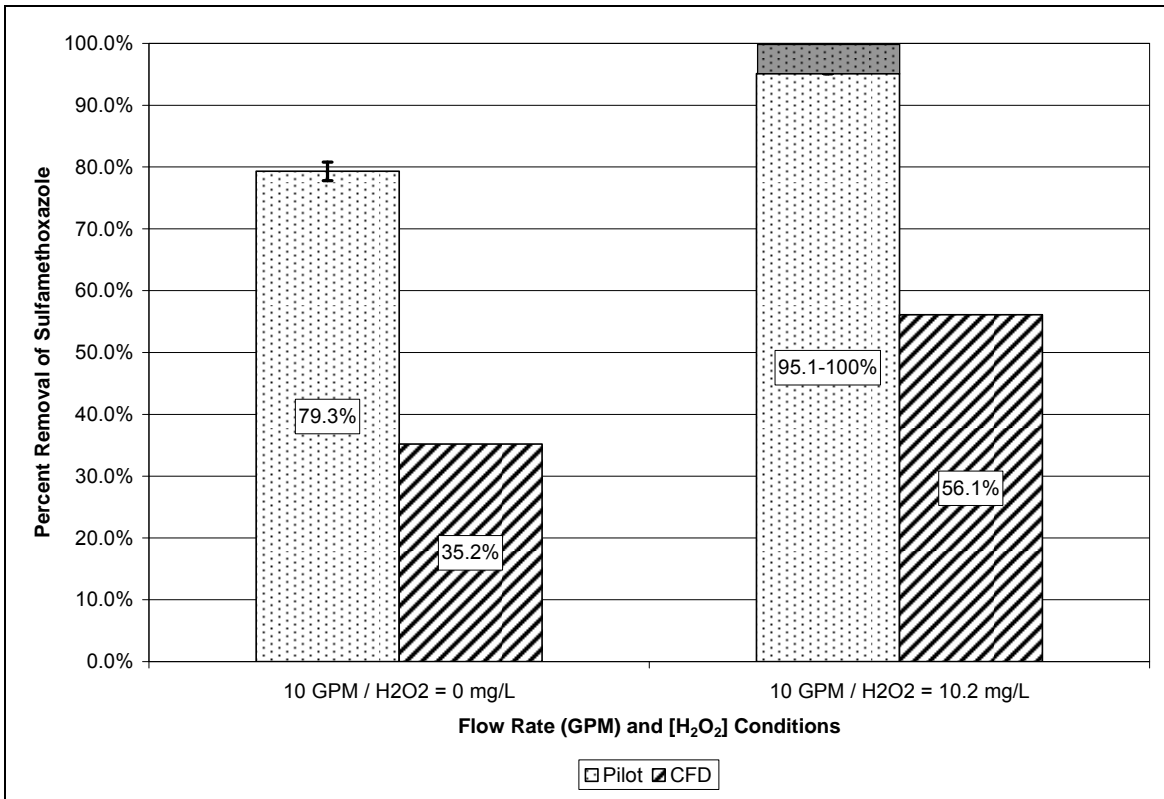


**Figure 4.15: Comparison of Pilot and CFD Results for SMX Trials**

Similar to the methylene blue trials, the CFD simulations for SMX degradation under-predict the percent removals measured in the pilot reactors. Again, one of the most likely explanations is an incomplete reaction mechanism that does not capture all of the radical reactions leading to destruction of the SMX molecule. For the advanced oxidation reaction, as discussed for the methylene blue reaction, the CFD RANS models may not have adequately captured the flow characteristics downstream of the baffle plates in which enhanced mixing might improve the reaction conditions.

Two other limitations in this research must be acknowledged in potentially contributing to the differences between the CFD and pilot results for both methylene blue and

SMX. The first limitation is that the fluence rate model, and specifically the output power of the lamp, was validated using a single point at the reactor wall where the intensity sensor was installed in the reactor. Although Liu et al. (2004) verified that the two fluence rate distribution models perform very well in predicting light profiles in an annular reactor as used in this experiment, a multi-point validation is recommended to confirm that the magnitude of the fluence rate values matches that within the pilot reactor (i.e., the lamp power input to the model matches the pilot lamp). Another validation process could involve the direct photolysis of a compound with a known fluence-based rate constant. For example, the percent removal of SMX in the direct photolysis pilot experiments could be used to back-calculate the delivered UV dose in the reactor. This “reduction-equivalent dose” could then be an iteration target for the CFD fluence rate and kinetic models (e.g., vary the CFD model input lamp power until the effluent concentration of SMX from the CFD kinetic model matches that of the pilot). Based on the SMX results presented in Figure 4.15, it would appear that the fluence rate in the CFD model is less than that delivered in the pilot. Increasing the lamp power in the CFD model for methylene blue would predict higher percent removal values; however, whether this increase would completely explain the current under-prediction (or result in an over-prediction) is yet to be determined.

The second limitation is the uncertainty in the accuracy of the value of the second-order rate constant for the reaction between methylene blue and the hydroxyl radical. The value determined experimentally with competition kinetics ( $6.9 \times 10^{10} \text{ M}^{-1} \text{ s}^{-1}$ ) is much greater than that of the value published online that was discovered late in the research ( $1.2 \times 10^{10} \text{ M}^{-1} \text{ s}^{-1}$ ). The CFD results presented in Figure 4.13 and Figure 4.14 were

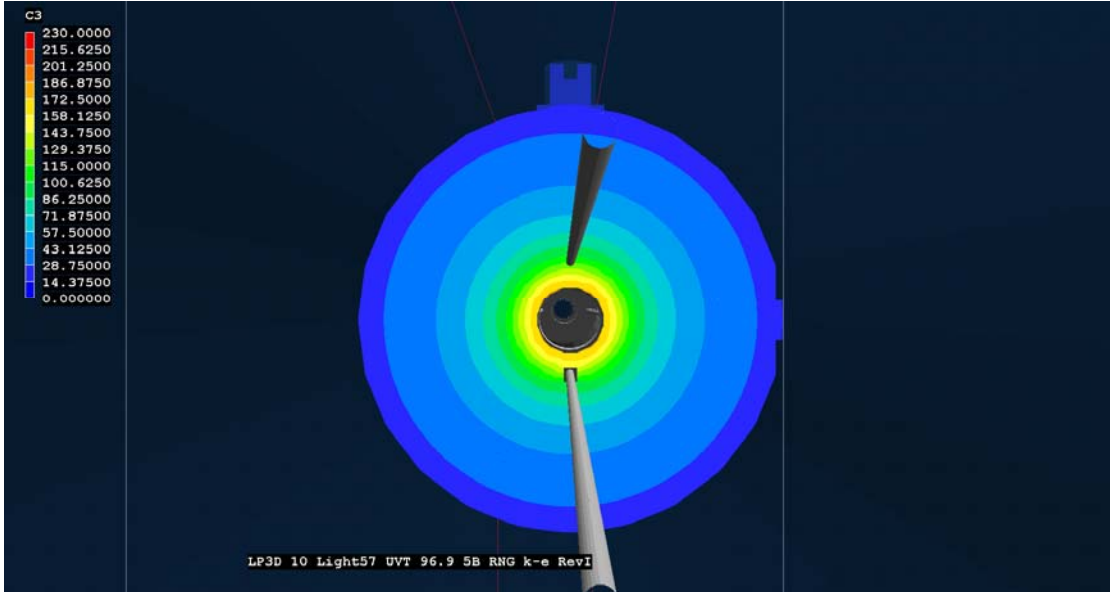
produced using the higher rate constant. Since the sensitivity analysis performed as a part of this study (and described in Section 4.3.5) showed numerically that the effluent methylene blue concentration is a strong-function of the rate constant, any variability in this constant will impact the comparison between the model and pilot results. The CFD model already under-predicts the pilot results, and, thus, further reduction in the rate constant used in the model will result in a larger gap between the model and pilot. It is possible, however, that a decrease in the rate constant combined with an increase in the fluence rate described above could improve the comparison between model and pilot results.

#### 4.3.4 Fluence Rate Sub-model Analysis

One of the objectives of this research is to evaluate the effect, if any, of the fluence rate sub-model selection on the overall degradation prediction of the advanced oxidation of an organic contaminant. As described previously, the two fluence rate models used in this evaluation are the RAD-LSI and the MSSS models. Figures 4.16 and 4.17 depict the CFD results of the RAD-LSI and MSSS fluence rate sub-models, respectively, under the same power and UVT conditions. The variable C3 is the fluence rate in units of  $W\ m^{-2}$ . The CFD “pointer” in these two figures is placed at the location of the UV sensor on the pilot reactor. These figures show that the MSSS sub-model predicted a higher fluence rate at the sensor than the RAD-LSI sub-model. This increase in fluence rate translated to higher contaminant removal percentages predicted for both methylene blue and SMX as shown in Table 4.27.

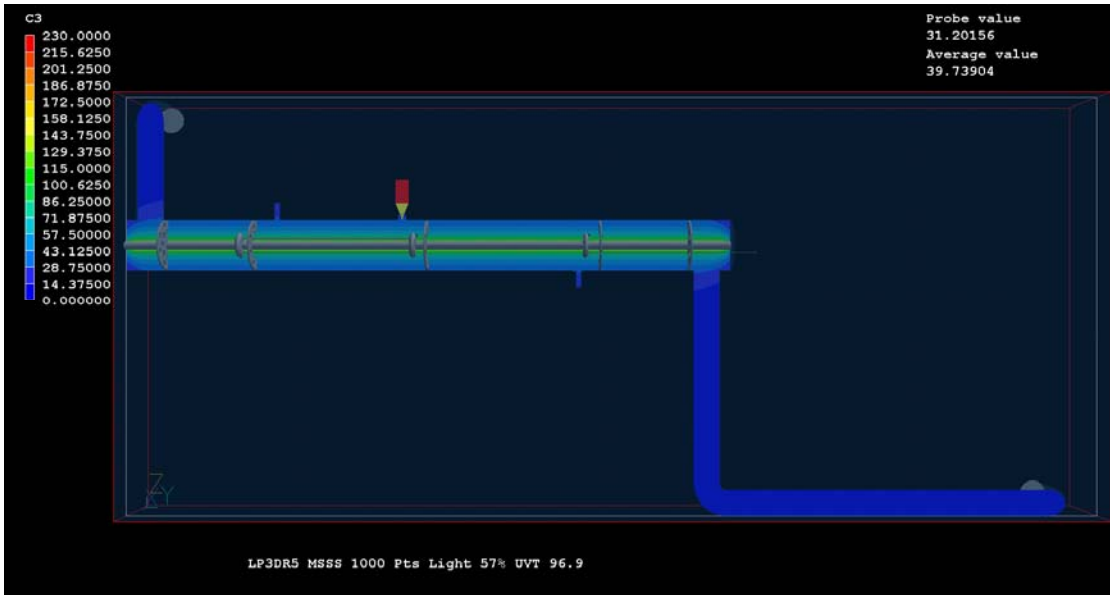


(a)

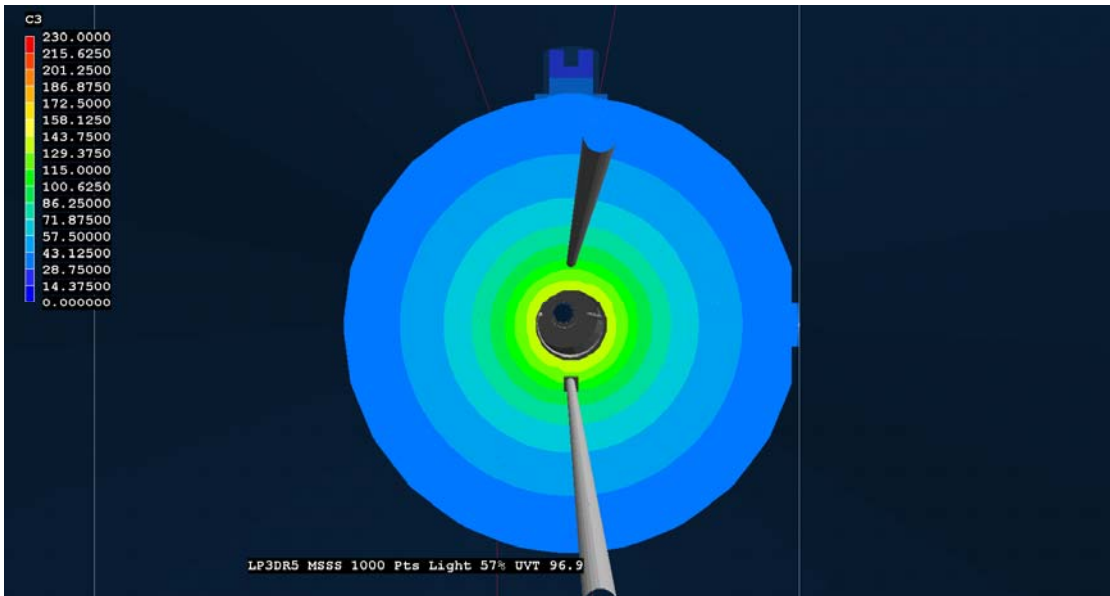


(b)

Figure 4.16: Graphical Results of RAD-LSI Fluence Rate Sub-model in CFD in (a) Y-Z Plane and (b) X-Z Plane



(a)



(b)

**Figure 4.17: Graphical Results of MSSS Fluence Rate Sub-model in CFD in (a) Y-Z Plane and (b) X-Z Plane**

**Table 4.27: Impact of Fluence Rate Model on CFD Results**

Parameter	Model 5	Model 9	Pilot	Model 10a	Model 11a	Pilot	Model 10b	Model 11b	Pilot
Flow Rate (gal min <sup>-1</sup> )	20	20	20	10	10	10	10	10	10
Target Compound Methylene Blue (MB), Sulfamethoxazole (SMX)	MB	MB	MB	SMX	SMX	SMX	SMX	SMX	SMX
Compound Concentration (mg L <sup>-1</sup> for MB, µg L <sup>-1</sup> for SMX)	0.50	0.50	0.50 ±0.01	9.4	9.4	9.4 ±1.0	10.0	10.0	9.9 ±1.1
Molar Ratio of H <sub>2</sub> O <sub>2</sub> to Compound	199.25	199.25	199.7 ±3.3	-	-	-	-	-	-
H <sub>2</sub> O <sub>2</sub> Concentration (mg L <sup>-1</sup> )	10.6	10.6	10.6 ±0.2	0	0	0	10.13	10.13	10.2
Power output at lamp surface (W)	26.5	26.5		29.6	29.6		29.6	29.6	
<b>Fluence Rate at Sensor (W m<sup>-2</sup>)</b>	<b>18.0</b>	<b>24.0</b>	16.9 ±0.2	<b>26.2</b>	<b>33.9</b>	26.3 ±0.9	<b>23.9</b>	<b>31.2</b>	23.8 ±0.2
UVT <sub>254</sub> (%)	94.9	94.9	92.9 ±0.9	98.0	98.0	98.3 ±0.3	96.9	96.9	83.2 ±0.6
pH	7.24	7.24	7.23 ±0.01	7.63	7.63	7.63	7.74	7.74	7.74
Alkalinity (mg L <sup>-1</sup> as CaCO <sub>3</sub> )	22.2	22.2	22.0 ±0.5	19.5	19.5	19.5	19.5	19.5	19.5
Total Chlorine Residual (mg L <sup>-1</sup> as Cl <sub>2</sub> )	0.013	0.013	0.01 ±0.01	0.16	0.16	0.16	0.16	0.16	0.16
Number of Baffles in Reactor	5	5	5	5	5	5	5	5	5
DOC (mg L <sup>-1</sup> )	0.57	0.57	0.57	0.57	0.57	0.57	0.57	0.57	0.57
Turbulence Sub-model	k-ε	k-ε		RNG k-ε	RNG k-ε		RNG k-ε	RNG k-ε	
<b>Fluence Rate Sub-model</b>	<b>RAD-LSI</b>	<b>MSSS</b>		<b>RAD-LSI</b>	<b>MSSS</b>		<b>RAD-LSI</b>	<b>MSSS</b>	
k <sub>R,OH</sub> (M <sup>-1</sup> s <sup>-1</sup> )	6.9 x 10 <sup>10</sup>	6.9 x 10 <sup>10</sup>		5.6 x 10 <sup>9</sup>	5.6 x 10 <sup>9</sup>		5.6 x 10 <sup>9</sup>	5.6 x 10 <sup>9</sup>	
Fraction of Initial Compound Remaining	0.440	0.386	0.359	0.648	0.618	0.207	0.439	0.399	0 - 0.049
<b>Compound Percent Removal (%)</b>	<b>56.0</b>	<b>61.4</b>	64.1 ±1.7	<b>35.2</b>	<b>38.2</b>	79.3 ±1.5	<b>56.1</b>	<b>60.1</b>	95.1-100

#### 4.3.5 Second-Order Kinetic Rate Constant Analysis

In order to evaluate the impact of the second-order kinetic rate constant for the reaction between the hydroxyl radical and methylene blue, several additional values of this constant were used in separate CFD models in addition to the average value determined experimentally by competition kinetics. These values include the limits of the 95% confidence interval that describes the experimental results for methylene blue ( $6.89 \times 10^{10} \pm 2.05 \times 10^{10} \text{ M}^{-1} \text{ s}^{-1}$ ). The results of the model runs using different rate constants are shown in Table 4.28 and Figure 4.18.

**Table 4.28: Impact of Second-Order Rate Constant  $k_{\text{MB},\text{OH}}$  on CFD Results**

Parameter	Model 15	Model 5	Model 23	Model 32	Model 33
Flow Rate (gal min <sup>-1</sup> )	20	20	20	20	20
Compound R Concentration (mg L <sup>-1</sup> )	0.50	0.50	0.50	0.50	0.50
Molar Ratio of H <sub>2</sub> O <sub>2</sub> to Compound	199.25	199.25	199.25	199.25	199.25
H <sub>2</sub> O <sub>2</sub> Concentration (mg L <sup>-1</sup> )	10.6	10.6	10.6	10.6	10.6
Power output at lamp surface (W)	26.5	26.5	26.5	26.5	26.5
Fluence Rate at Sensor (W m <sup>-2</sup> )	18.0	18.0	18.0	18.0	18.0
UVT <sub>254</sub> (%)	94.9	94.9	94.9	94.9	94.9
pH	7.24	7.24	7.24	7.24	7.24
Alkalinity (mg L <sup>-1</sup> as CaCO <sub>3</sub> )	22.2	22.2	22.2	22.2	22.2
Total Chlorine Residual (mg L <sup>-1</sup> as Cl <sub>2</sub> )	0.013	0.013	0.013	0.013	0.013
Number of Baffles in Reactor	5	5	5	5	5
DOC (mg L <sup>-1</sup> )	0.57	0.57	0.57	0.57	0.57
Turbulence Sub-model	k-ε	k-ε	k-ε	k-ε	k-ε
Fluence Rate Sub-model	RAD-LSI	RAD-LSI	RAD-LSI	RAD-LSI	RAD-LSI
$k_{\text{R,OH}}$ (M <sup>-1</sup> s <sup>-1</sup> )	<b>1.0 x 10<sup>9</sup></b>	<b>6.9 x 10<sup>10</sup></b>	<b>3.5 x 10<sup>10</sup></b>	<b>8.9 x 10<sup>10</sup></b>	<b>4.8 x 10<sup>10</sup></b>
Fraction of Initial Compound Remaining	0.966	0.440	0.553	0.389	0.486
<b>Compound Percent Removal (%)</b>	<b>3.4</b>	<b>56.0</b>	<b>44.7</b>	<b>61.1</b>	<b>51.4</b>

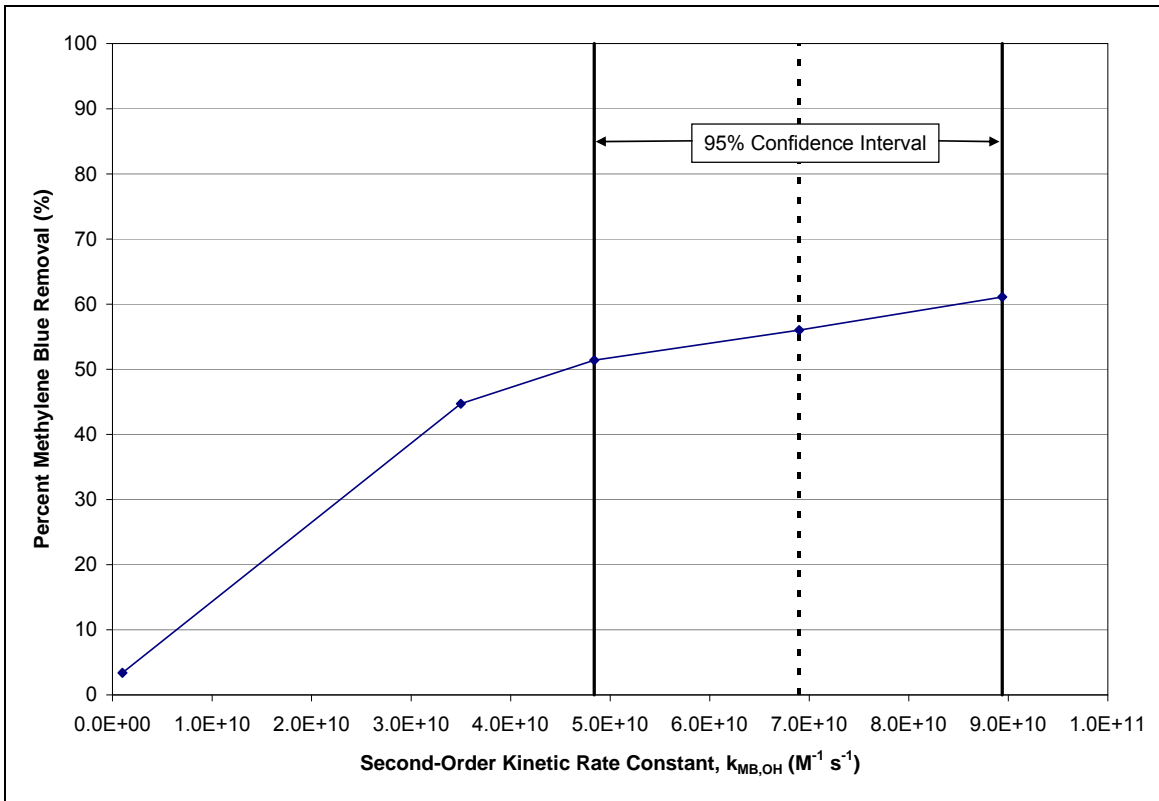


**Figure 4.18: Impact of Second-Order Rate Constant on Methylene Blue Removal**

As seen in Table 4.28, the overall degradation of methylene blue is a strong function of the kinetic rate constant. Within the range of the 95% confidence interval of the rate constants determined experimentally, the percent removal of methylene blue varied by 9.7% (i.e., 51.4% removal at the lower limit and 61.1% removal at the upper limit).

#### 4.3.6 Turbulence Sub-model Analysis

In this research, three turbulence closure sub-models were evaluated to determine the effect, if any, on the overall degradation prediction of the advanced oxidation of an organic contaminant. CFD velocity profiles for the standard  $k$ - $\epsilon$ , RNG  $k$ - $\epsilon$ , and  $k$ - $\omega$  sub-models are shown in Figures 4.19, 4.20, and 4.21, respectively. Table 4.29 shows the contaminant

degradation results of running the same experimental parameters using the three turbulence sub-models for two different flow rates.

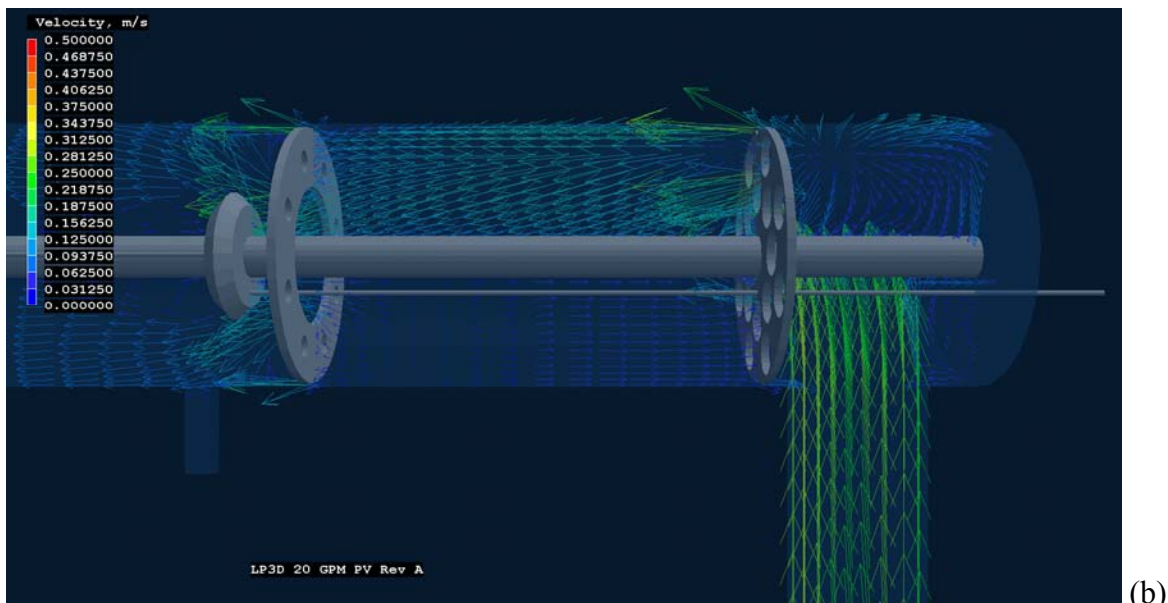
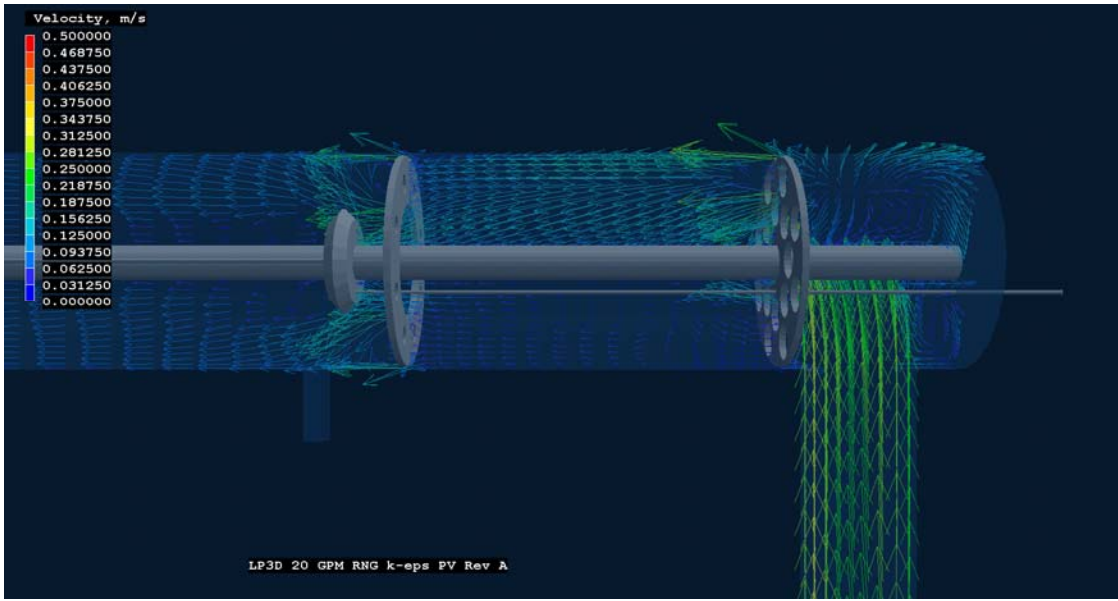


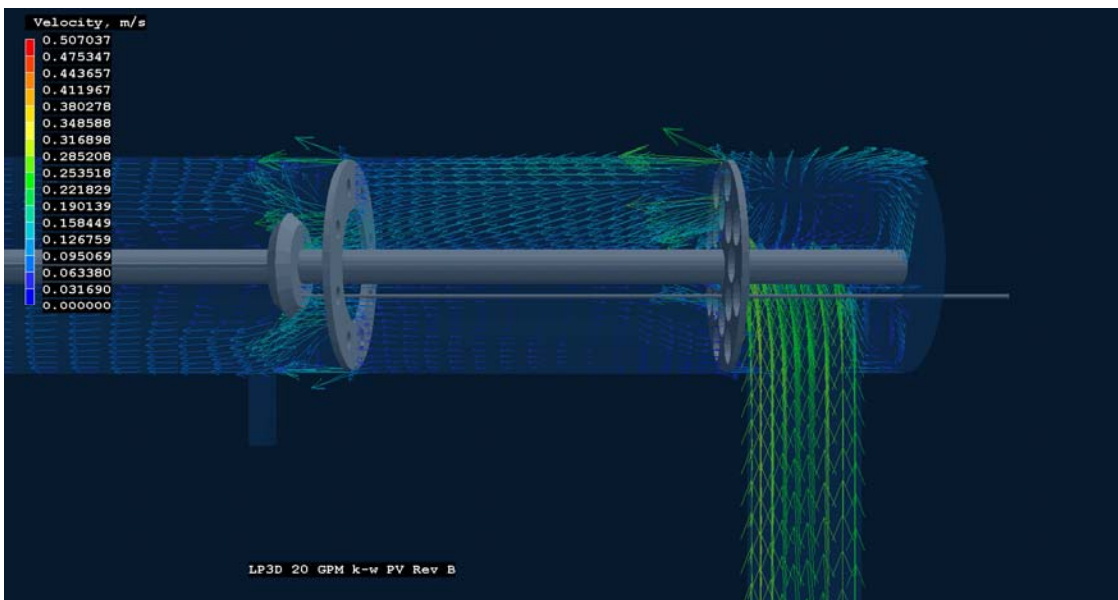
Figure 4.19: Velocity Profiles for  $k-\epsilon$  Turbulence Sub-Model at 20 GPM; (a) Y-Z Plane Contours and (b) Y-Z Vectors at Inlet



**Figure 4.20: Velocity Profiles for RNG k- $\epsilon$  Turbulence Sub-Model at 20 GPM; (a) Y-Z Plane Contours and (b) Y-Z Vectors at Inlet**



(a)



(b)

**Figure 4.21: Velocity Profiles for  $k-\omega$  Turbulence Sub-Model at 20 GPM; (a) Y-Z Plane Contours and (b) Y-Z Vectors at Inlet**

**Table 4.29: Impact of Turbulence Sub-model on CFD Results**

Parameter	Model 5	Model 7	Model 8	Model 30	Model 34
Flow Rate (gal min <sup>-1</sup> )	20	20	20	30	30
Compound R Concentration (mg L <sup>-1</sup> )	0.50	0.50	0.50	0.50	0.50
Molar Ratio of H <sub>2</sub> O <sub>2</sub> to Compound	199.25	199.25	199.25	144.2	144.2
H <sub>2</sub> O <sub>2</sub> Concentration (mg L <sup>-1</sup> )	10.6	10.6	10.6	7.66	7.66
Power output at lamp surface (W)	26.5	26.5	26.5	30.2	30.2
Fluence Rate at Sensor (W m <sup>-2</sup> )	18.0	18.0	18.0	15.8	15.8
UVT <sub>254</sub> (%)	94.9	94.9	94.9	91.9	91.9
pH	7.24	7.24	7.24	7.49	7.49
Alkalinity (mg L <sup>-1</sup> as CaCO <sub>3</sub> )	22.2	22.2	22.2	28.1	28.1
Total Chlorine Residual (mg L <sup>-1</sup> as Cl <sub>2</sub> )	0.013	0.013	0.013	0.14	0.14
Number of Baffles in Reactor	5	5	5	5	5
DOC (mg L <sup>-1</sup> )	0.57	0.57	0.57	0.57	0.57
<b>Turbulence Sub-model</b>	<b>k-ε</b>	<b>RNG k-ε</b>	<b>k-ω</b>	<b>k-ε</b>	<b>RNG k-ε</b>
Fluence Rate Sub-model	RAD-LSI	RAD-LSI	RAD-LSI	RAD-LSI	RAD-LSI
k <sub>MB,OH</sub> (M <sup>-1</sup> s <sup>-1</sup> )	6.9 x 10 <sup>10</sup>				
Fraction of Initial Compound Remaining	0.440	0.442	0.431	0.701	0.701
<b>Compound Percent Removal (%)</b>	<b>56.0</b>	<b>55.8</b>	<b>56.9</b>	<b>29.9</b>	<b>29.9</b>

The percent removal values in Table 4.29 indicate that the two-equation turbulence sub-model selection for this reactor configuration does not significantly impact the predicted removal for methylene blue. Thus, any hydraulic effects contributing to the differences between the pilot and CFD results are not being captured by these three two-equation sub-models alone.

#### 4.3.7 Radical Scavenger Analysis

The reaction mechanism for the hydroxyl radical modeled in this research incorporates several radical scavengers, including dissolved organic carbon (DOC), bicarbonate ions, and chlorine. DOC, as an indicator for natural organic matter, is likely the most important of these scavengers that will be encountered in natural systems. As such, the CFD model was used to examine the influence of changing DOC concentrations on the

overall percent removal of methylene blue. A summary of the results is provided in Table 4.30 and graphically in Figure 4.22.

**Table 4.30: Impact of DOC on CFD Results**

Parameter	Model 18	Model 28	Model 19	Model 20
Flow Rate (gal min <sup>-1</sup> )	10	10	10	10
Target Compound (MB = Methylene Blue)	MB	MB	MB	MB
Compound Concentration (mg L <sup>-1</sup> )	0.50	0.50	0.5	0.5
Molar Ratio of H <sub>2</sub> O <sub>2</sub> to Compound	150	150	150	150
H <sub>2</sub> O <sub>2</sub> Concentration (mg L <sup>-1</sup> )	7.98	7.98	7.98	7.98
Power output at lamp surface (W)	31.6	31.6	31.6	31.6
Fluence Rate at Sensor (W m <sup>-2</sup> )	21.5	21.5	21.5	21.5
UVT <sub>254</sub> (%)	94.9	94.9	94.9	94.9
pH	7.25	7.25	7.25	7.25
Alkalinity (mg L <sup>-1</sup> as CaCO <sub>3</sub> )	23	23	23	23
Total Chlorine Residual (mg L <sup>-1</sup> as Cl <sub>2</sub> )	0	0	0	0
Number of Baffles in Reactor	5	5	5	5
<b>DOC (mg L<sup>-1</sup>)</b>	<b>0.0</b>	<b>0.5</b>	<b>1.0</b>	<b>2.0</b>
Turbulence Sub-model	k-ε	k-ε	k-ε	k-ε
Fluence Rate Sub-model	RAD-LSI	RAD-LSI	RAD-LSI	RAD-LSI
k <sub>MB,OH</sub> (M <sup>-1</sup> s <sup>-1</sup> )	6.9 x 10 <sup>10</sup>			
Fraction of Initial Compound Remaining	0.059	0.133	0.197	0.300
<b>Compound Percent Removal (%)</b>	<b>94.1</b>	<b>86.7</b>	<b>80.3</b>	<b>70.0</b>

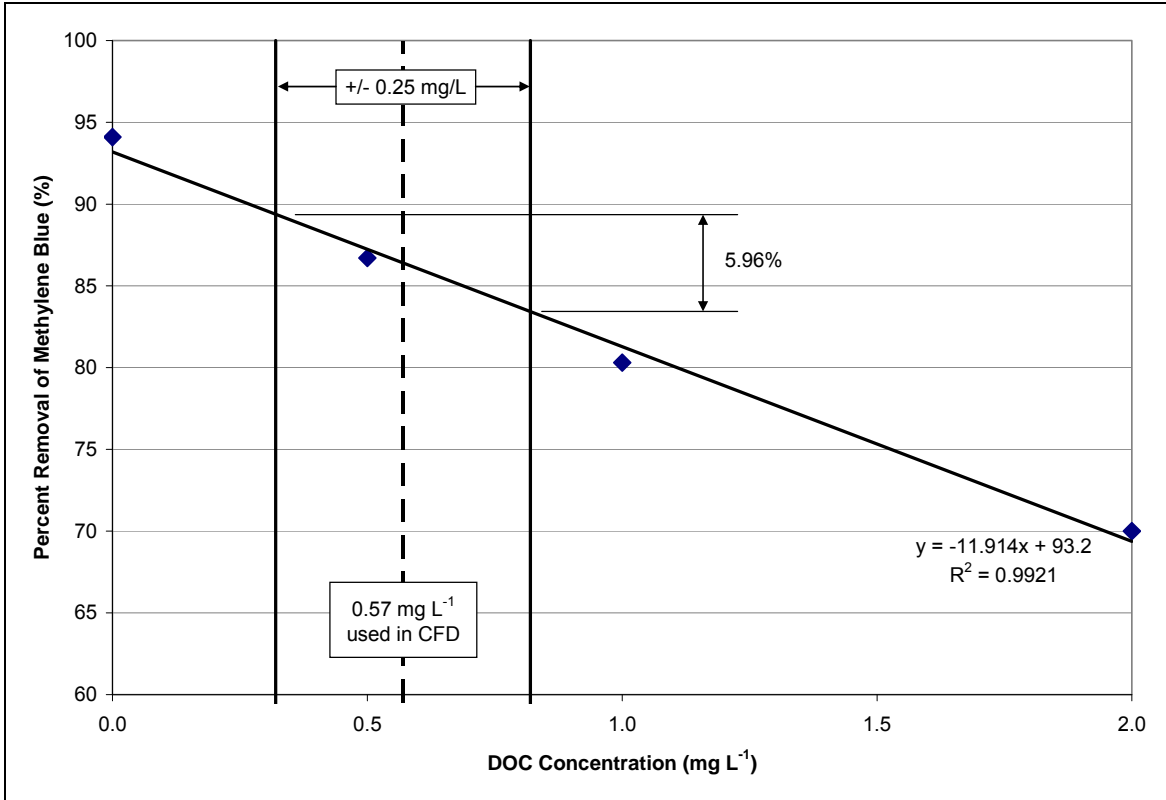


**Figure 4.22: Impact of DOC on Advanced Oxidation of Methylene Blue**

The overall removal of methylene blue is shown to be sensitive to the concentration of DOC in the water matrix. Since the DOC of the pilot influent was only measured successfully once in this research, any variance between pilot runs could explain some part of the differences between the pilot and CFD results. From Figure 4.22, the methylene blue removal can be expected to shift by approximately 6% if the DOC concentration changes by plus or minus 0.25 mg L<sup>-1</sup> from the DOC value (0.57 mg L<sup>-1</sup>) used in the CFD model throughout this study.

#### 4.3.8 Micromixing

It was hypothesized that under some operating conditions, the reaction time scales reflective of the large kinetic rate constants associated with advanced oxidation would become significantly smaller than the turbulent eddy time scale, and, thus, the inclusion of micromixing sub-models might better predict the results of the reactions within the reactor. During this research, CFD code for a Single Fluid Micromixing (SFM) model based on the eddy dissipation concept was written and tested. However, the results of the SFM model showed almost no removal (0%) of methylene blue for most operating conditions. Thus, it was initially hypothesized that the SFM model as written was not physically modeling the time scale comparison that was intended to be studied.

Upon further review of the literature associated with these micromixing models, it was determined that the existing models described only those systems that were not perfectly mixed initially (i.e., systems that contained Compound A becoming mixed in Compound B). However, these conditions are not what are typically encountered in water or wastewater advanced oxidation systems in which the contaminant and hydrogen peroxide are already well-mixed prior to entering the UV reactor. As such, the micromixing sub-models predominant in the literature reviewed for this study may not be applicable to the AOP system under investigation.

The other consideration for the application of micromixing models to advanced oxidation reactions is the mixing of the hydroxyl radical after formation. However, given the orders of magnitude differences between the concentrations of hydroxyl radical and its potential scavengers (e.g., methylene blue and hydrogen peroxide) and the large kinetic rate

constants associated with the hydroxyl radical reactions, it might be expected that the radical is consumed faster than it could be diffused and/or convected away from its production site.

That being said, there are enough differences in the CFD and pilot results presented previously, especially as flow rates increased, to indicate that there still might be phenomena occurring on the microscale that need to be considered. Future research should continue to examine the relationship between the reaction and eddy time scales. Further, the micromixing that occurs after the initial production of the hydroxyl radicals from UV exposure should be considered, especially in the areas of high shear downstream of internal baffles and at the inlet. Micromixing models may also be relevant in AOP systems when the hydrogen peroxide is injected close to the reactor inlet and, as a result, may not be well-mixed prior to entering the reactor.

#### 4.3.9 Cost Metrics

Since the evaluation of any engineering alternative is not complete without considering the economics of the system, the operations cost metric of the annual average cost per order ( $AAC_0$ ) was calculated for each of the conditions investigated in this research. For these calculations, several unit parameters common to all conditions were defined. The annual run time was assumed to be equal to 8,760 hours per year. The cost of energy was assumed equal to \$0.05 per kilowatt-hour and the cost of hydrogen peroxide at 50% dilution was assumed to be \$0.345 per pound. The results of this analysis are shown in Table 4.31 and Figure 4.23.

**Table 4.31: Annual Average Cost per Order for Research Conditions**

Research Condition	Flow Rate (GPM)	Compound	Inlet Conc. (mg L <sup>-1</sup> )	H <sub>2</sub> O <sub>2</sub> Dose (mg L <sup>-1</sup> )	Output Power (W)	Percent Removal (CFD)	AAC <sub>0</sub> (CFD) <sup>1</sup>	Percent Removal (Pilot)	AAC <sub>0</sub> (Pilot) <sup>1</sup>
<b>Modeling of Pilot Conditions</b>									
1	10	MB	0.50	8.0	26.5	0.781	<b>\$20.08</b>	0.765	<b>\$21.08</b>
2	10	MB	0.50	7.9	26.5	0.773	<b>\$20.44</b>	0.799	<b>\$18.81</b>
3	20	MB	0.50	8.0	29.9	0.471	<b>\$45.98</b>	0.577	<b>\$34.13</b>
4	20	MB	0.49	7.8	26.5	0.46	<b>\$46.13</b>	0.597	<b>\$31.74</b>
5 (Rev B)	20	MB	0.50	10.6	29.6	0.586	<b>\$43.62</b>	0.641	<b>\$37.49</b>
6	20	MB	0.50	10.6	26.5	0.571	<b>\$45.40</b>	0.662	<b>\$35.26</b>
29	20	MB	0.50	14.2	26.5	0.624	<b>\$51.79</b>	0.720	<b>\$39.78</b>
30	30	MB	0.50	7.7	30.2	0.299	<b>\$78.01</b>	0.387	<b>\$56.44</b>
<b>Effects of Turbulence Model</b>									
5 (Rev A)	20	MB	0.50	10.6	26.5	0.56	<b>\$46.56</b>		
7	20	MB	0.50	10.6	26.5	0.56	<b>\$46.88</b>		
8	20	MB	0.50	10.6	26.5	0.57	<b>\$45.44</b>		
34	30	MB	0.50	7.7	30.2	0.30	<b>\$77.96</b>		
<b>Effects of Fluence Rate Model Using Methylene Blue</b>									
5 (Rev A)	20	MB	0.50	10.6	26.5	0.56	<b>\$46.56</b>		
9	20	MB	0.50	10.6	26.5	0.61	<b>\$40.18</b>		
<b>Effects of Fluence Rate Model Using SMX</b>									
10a	10	SMX	0.0094	0.0	29.6	0.352	<b>\$6.89</b>	0.793	<b>\$1.90</b>
10b	10	SMX	0.010	10.1	29.6	0.561	<b>\$46.48</b>	0.951	<b>\$12.31</b>
11a	10	SMX	0.0094	0.0	29.6	0.382	<b>\$6.21</b>		
11b	10	SMX	0.010	10.1	29.6	0.601	<b>\$41.64</b>		
<b>Effects of DOC Concentrations</b>									
18	10	MB	0.50	8.0	31.6	0.941	<b>\$10.94</b>		
28	10	MB	0.50	8.0	31.6	0.867	<b>\$15.34</b>		
19	10	MB	0.50	8.0	31.6	0.803	<b>\$19.06</b>		
20	10	MB	0.50	8.0	31.6	0.700	<b>\$25.71</b>		
<b>Effects of Second-Order Rate Constant</b>									
15	20	MB	0.50	10.6	26.5	0.034	<b>\$1,090.72</b>		
5 (RevA)	20	MB	0.50	10.6	26.5	0.560	<b>\$46.56</b>		
23	20	MB	0.50	10.6	26.5	0.447	<b>\$64.49</b>		
32	20	MB	0.50	10.6	26.5	0.611	<b>\$40.48</b>		
33	20	MB	0.50	10.6	26.5	0.514	<b>\$52.98</b>		
<b>High Lamp Power</b>									
31	20	MB	0.50	8.0	100.0	0.974	<b>\$8.96</b>		

<sup>1</sup> AAC<sub>0</sub> units: \$/yr/GPM/order

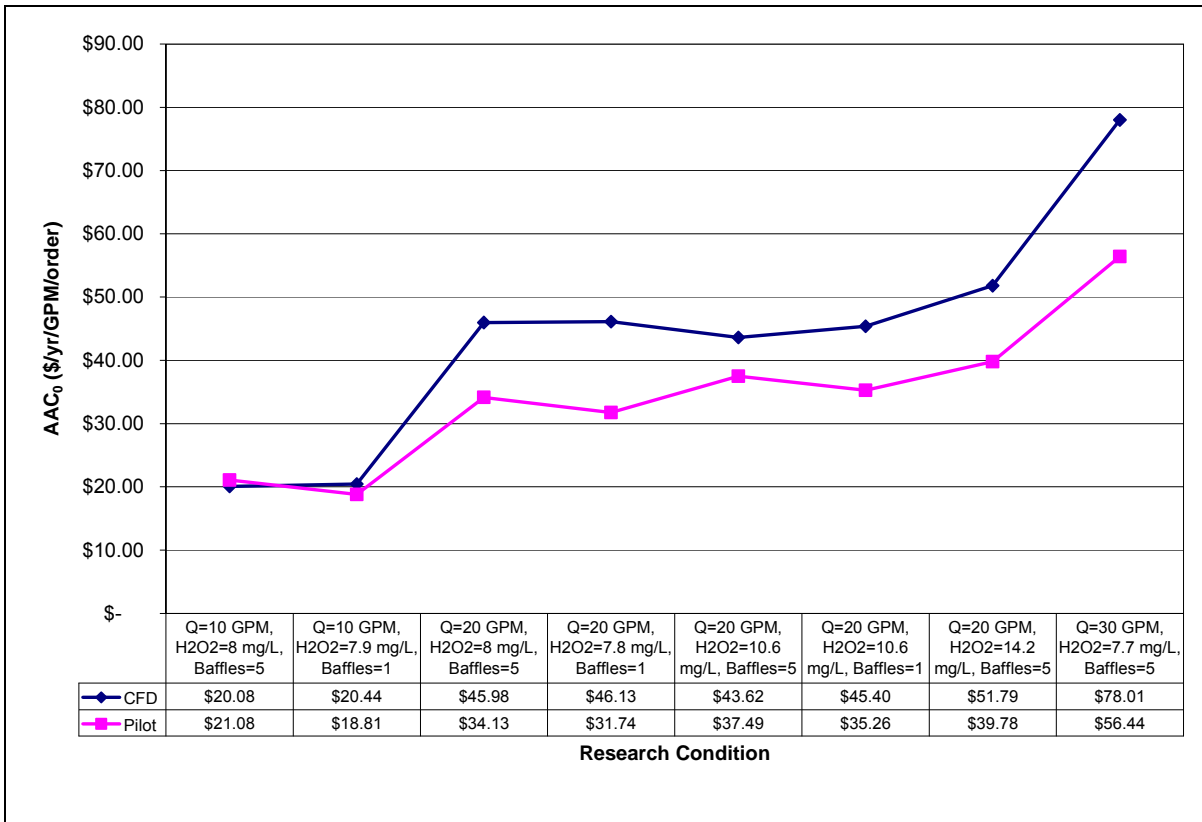


**Figure 4.23: CFD and Pilot Cost Trends**

The  $AAC_0$  values reported in Table 4.31 and Figure 4.23 reflect the differences in hydrogen peroxide dosage, energy input required for the UVT of each condition, and flow rate. For this study, the magnitude of the values is not as important as the relative comparisons among values. In this case, the interest lies in the relationship between contaminant removal and hydrogen peroxide dose. As shown in Figure 4.23, increasing the hydrogen peroxide dose from 7.8 to 10.6 mg L<sup>-1</sup> while keeping the flow rate at 20 GPM does not significantly increase the  $AAC_0$ . In fact, the CFD analysis actually shows the higher peroxide concentration to be a less expensive option. The second critical aspect of this cost analysis is that the trends shown for CFD in Figure 4.23 match that of the experimental trials.

Since one of the goals of a CFD UV/AOP model is to optimize treatment costs, the CFD model should track the estimated costs of experimental studies and full-scale operation.

Since the  $AAC_0$  metric is defined as the summation of the operational costs for energy input and chemical usage, the examination of the contribution of each cost to the total value can prove valuable. Although the component cost fractions are a function of both the unit energy cost and the bulk chemical costs, both of which vary geographically, the evaluation of the CFD results for this study can be useful. As shown in Figure 4.24, the operating conditions modeled in this study produced  $AAC_0$  values that are dominated by the hydrogen peroxide costs. If this condition were to exist on a full-scale system, optimization would center on minimizing the hydrogen peroxide concentration to reduce overall operational costs.

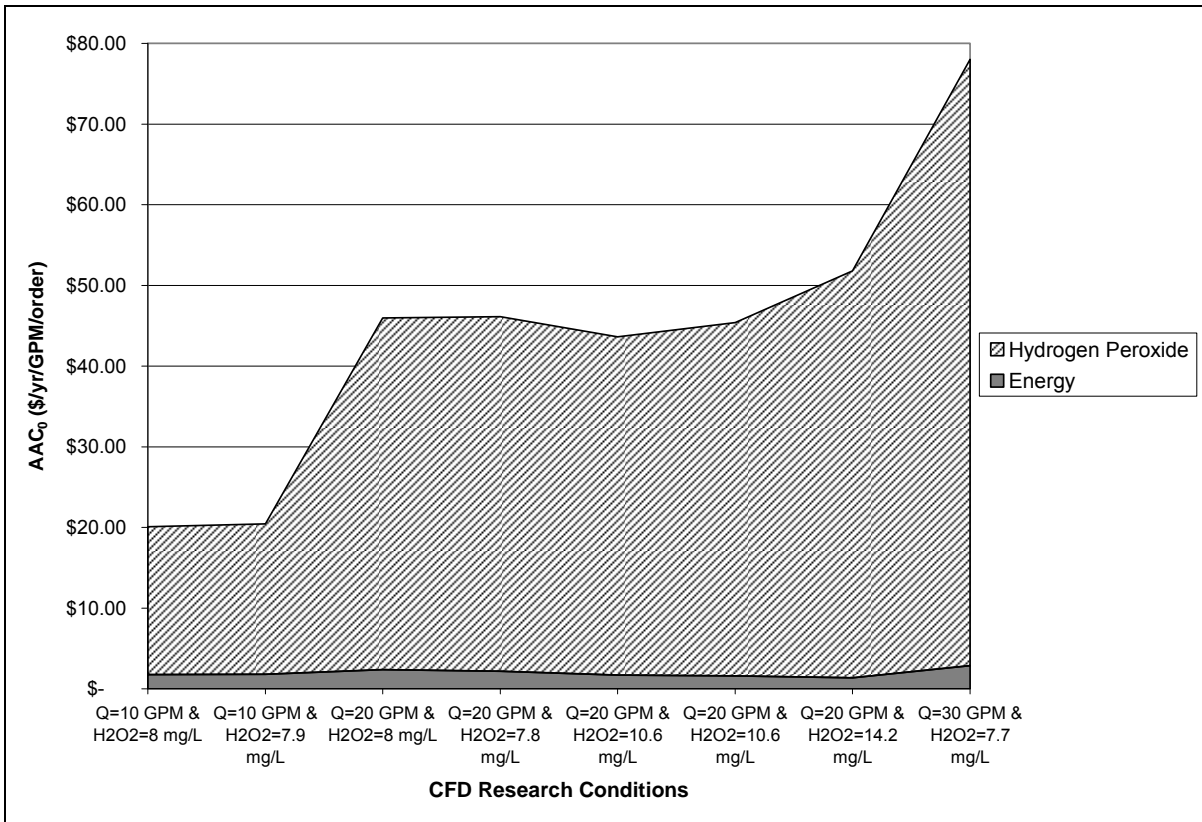


**Figure 4.24: AAC<sub>0</sub> Fractions for Energy and Chemical Costs (CFD Results)**

Although the AAC<sub>0</sub> is a useful cost metric, it must be considered with two other design criteria. The first is that goal effluent concentrations must be achieved. If the modeled effluent concentration result is not below the regulatory MCL, for example, then that condition should not be considered in the AAC<sub>0</sub> analysis. The second criterion is the capital cost of the reactors. The research conditions describe a “flow per reactor”, so more reactors may be required for a given design flow, and the relative cost of the reactors versus operating costs would need to be considered. A present worth analysis of the capital costs over the life of the system can be added into the AAC<sub>0</sub> metric to determine the true cost of the system. Finally, since the choice of fluence rate sub-model selection and value for the

second-order rate constant will influence the predicted overall removal of the contaminant, these model parameters will also be reflected in the  $AAC_0$  values.

#### 4.4 Other Numerical Methods

Both the ideal hydraulics assumption and the CFD/Lagrangian approach were used to simulate the UV-initiated advanced oxidation process for methylene blue destruction. Although CFD is a powerful tool that can lead to rigorous analyses of systems, it is also time and computer intensive. If there are better simulation alternatives that produce accurate results, they need to be considered.

##### 4.4.1 Reaction Mechanism Equations

The equations presented in Section 2.7.1 for methylene blue degradation were input into a MATLAB code and solved using the built-in ODE solvers that are included with the software. A sample code is presented in Appendix C. The irradiance used in the code was calculated as a volumetric average from the output lamp power, UVT, and a simplified RAD-LSI equation together with a discretization of the reactor in the radial and length-wise directions. The equations are solved for the theoretical hydraulic residence time calculated using the reactor volume and flow rate. The results are presented together with the dose distribution outcomes in the next section.

#### 4.4.2 Dose Distributions

The first step in evaluating the UV dose distributions was to produce dose-response data that described the degradation of methylene blue by advanced oxidation for given UV doses (fluence values) and a set of reaction conditions including hydrogen peroxide concentration. Data for a molar ratio of hydrogen peroxide to methylene blue equal to 150 is shown graphically in Figure 4.25. With the exception that each curve is for a specific hydrogen peroxide concentration, this AOP dose-response curve parallels the reduction-equivalent dose curve developed for the disinfection kinetics of a specific microorganism.

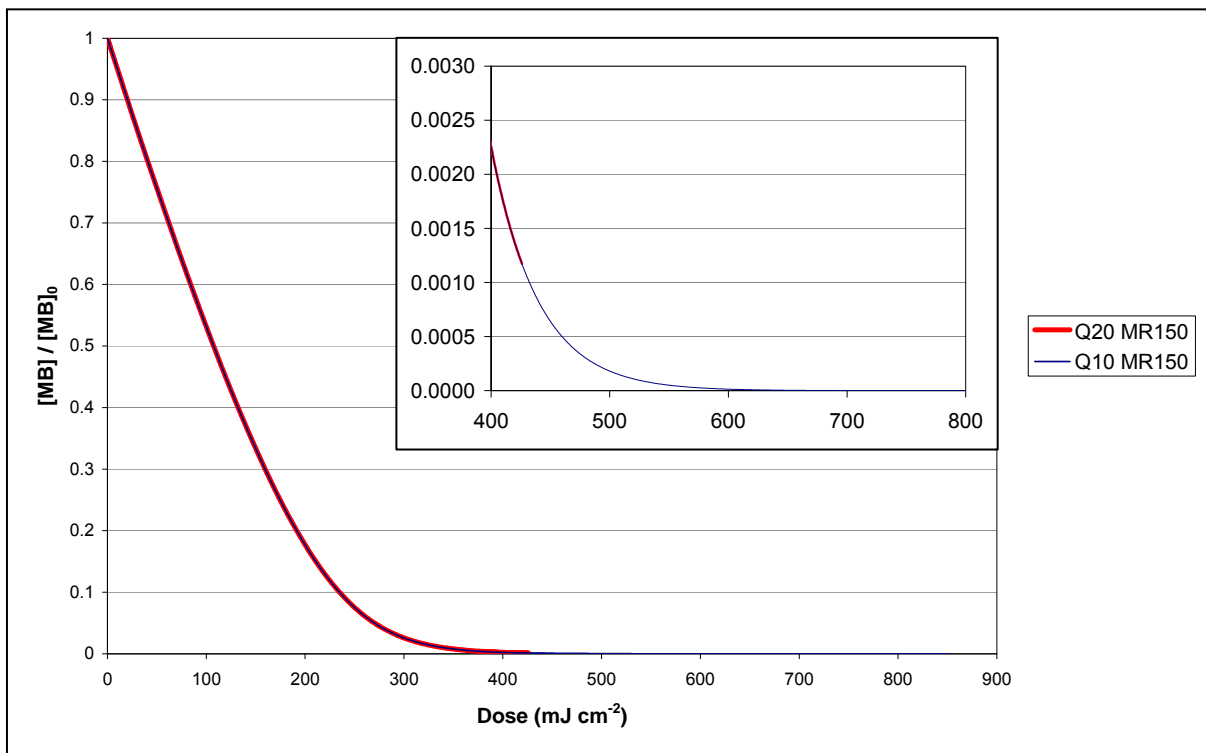


**Figure 4.25: Dose-Response Curves for 100 W Output Power**

The dose distributions for P = 26.5 W and P = 100 W output at 254 nm are shown in Figures 4.26 and 4.27, respectively. Averages and standard deviations were calculated with Microsoft® Office Excel 2003.

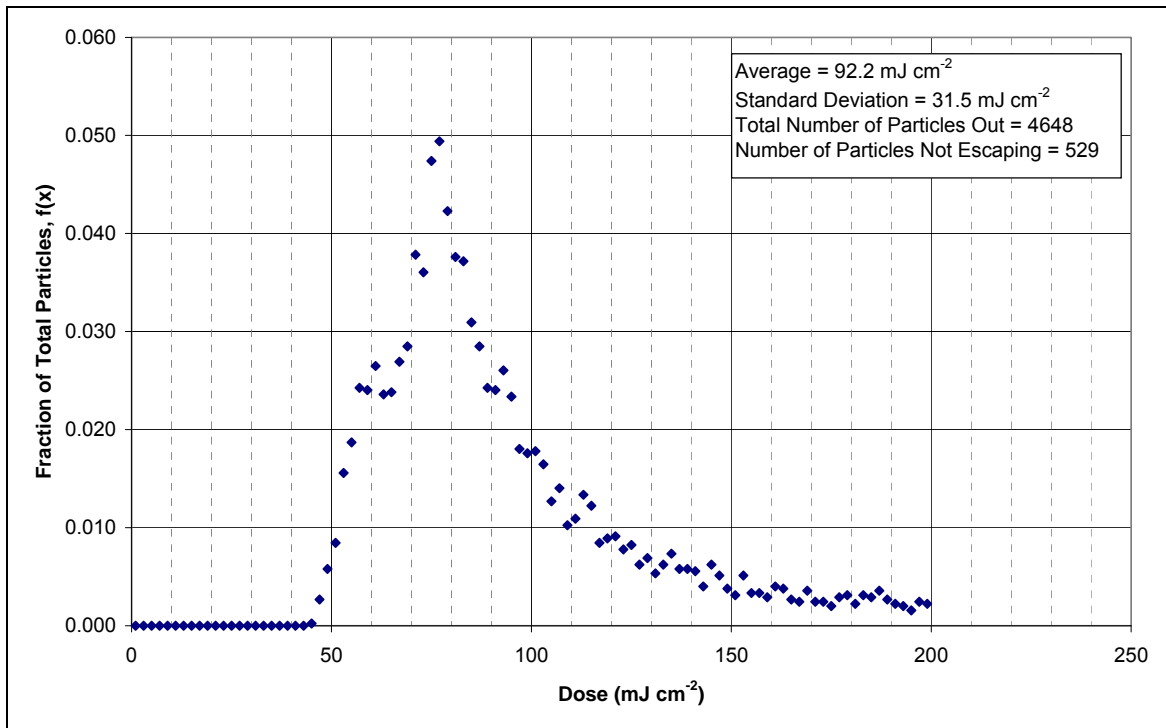


**Figure 4.26: UV Dose Distribution for 20 GPM and 26.5 W Output Power**

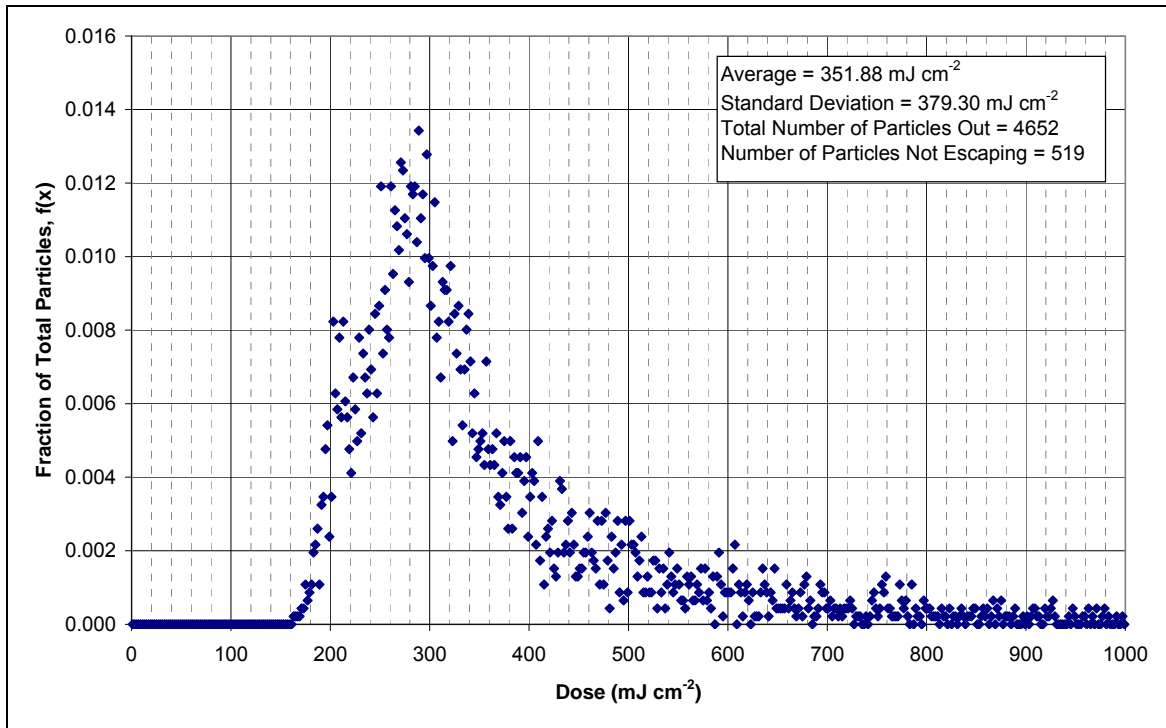


**Figure 4.27: UV Dose Distribution for 20 GPM and 100 W Output Power**

Although the distributions in Figures 4.26 and 4.27 appear to be generally of the same shape, they are found to be quite different when plotted on common axes. As shown in Figure 4.28, the dose distribution for the 100W case is much flatter than that of the 26W case. This difference is quantified in the standard deviations reported for each and may be explained by the performance of UV reactors with non-ideal hydraulics being a non-linear function of lamp power (Wright and Lawryshyn, 2000). In both cases, the delivered UV dose clearly departs from ideal plug-flow conditions and a larger variance is expected with increasing lamp power (or lower flow conditions).

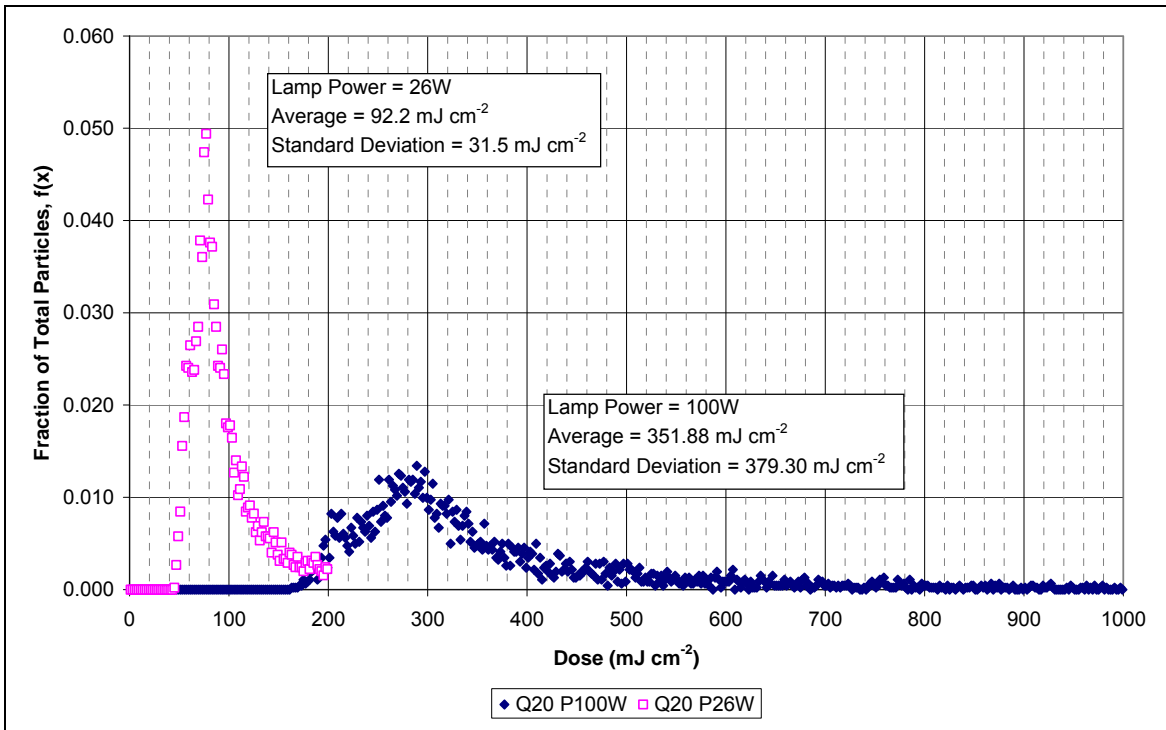


**Figure 4.28: Dose Distributions on Common Axes**

Once the UV dose distributions were available, a segregated flow approach that matched up individual doses with corresponding methylene blue removal values was used to calculate the overall removal percentage predicted by the dose distributions. The results of this analysis for the two cases are summarized in Table 4.32 and Figure 4.29, both of which include the associated CFD/Eulerian and pilot results.

**Table 4.32: Summary of Numerical Solution Results**

Numerical Solution Technique	Percent Removal at P = 26.5 W <sup>1</sup>	Percent Removal at P = 100 W <sup>1</sup>
MATLAB Ideal Hydraulics with Volumetric Average Irradiance	52.3%	99.9%
CFD/MATLAB/Lagrangian (Average Dose)	43.4%	99.3%
CFD/MATLAB/Lagrangian (Segregated Dose Summation)	42.9%	95.8%
CFD/Eulerian	45.9%	97.4%
CFD/Eulerian with Power and UVT Adjusted to Match Pilot Sensor Fluence Rate	47.1%	N/A
Pilot Results	57.7% ± 0.7%	N/A

<sup>1</sup> Lamp Output Power at 254 nm.

Flow Conditions: Q = 20 GPM, Molar Ratio (H<sub>2</sub>O<sub>2</sub>:MB) = 150, k<sub>MB,OH</sub> = 6.9E10 M<sup>-1</sup> s<sup>-1</sup>, DOC = 0.57 mg L<sup>-1</sup>, ALK = 22.7 mg L<sup>-1</sup> as CaCO<sub>3</sub>, pH = 7.3, Combined Chlorine = 0.05 mg L<sup>-1</sup> as Cl<sub>2</sub>

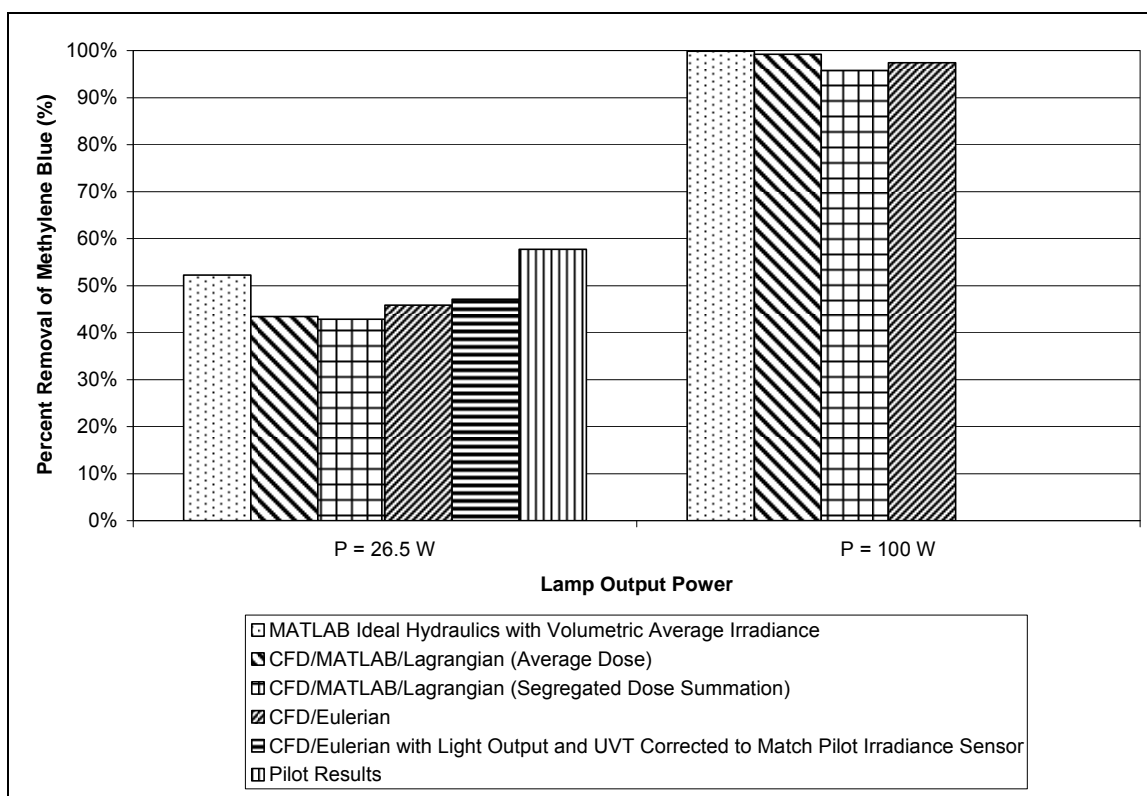


**Figure 4.29: Comparison of Numerical Models for Methylene Blue Removal**

For the  $P = 26.5 \text{ W}$  case, the dose distribution produced a result that was lower than the CFD case and farther from the result of the pilot trial. The ideal plug-flow assumption used in the MATLAB model resulted in a value closest to that achieved in the pilot reactor. Even though there is not an available LPHO lamp that produces an output power of 100 W at 254 nm, this case was evaluated to compare results that would theoretically produce a contaminant removal between 99.0 and 99.9%. Except for the value produced by the CFD/MATLAB/Lagrangian (Average Dose) approach, the trends were the same as with the 26.5 W case. CFD/Eulerian produced a value lower than that of the ideal hydraulics solution. The CFD/MATLAB/Lagrangian (Segregated Dose Summation) approach resulted in a value lower than that of CFD/Eulerian. Again, the two limitations discussed in Section 4.3.2 concerning the fluence rate validation and the second-order rate constant must be acknowledged since both would influence all three of the numerical methods.

Although the differences in results of the three modeling options would appear significant on a log-scale that would be used, for example, for microbial inactivation regulations, most limits for organic contaminants are (and likely will continue to be) based on effluent concentration requirements such as maximum contaminant limits (MCLs). As an example, the herbicide atrazine can be considered. The U.S. Environmental Protection Agency (EPA) has set an MCL of  $3 \mu\text{g L}^{-1}$  for atrazine. If a contaminated water had an initial atrazine concentration of  $10 \mu\text{g L}^{-1}$ , the treatment system would only need to provide 70% removal. Thus, the difference in the results of the three models would be insignificant, as shown in Table 4.33.

**Table 4.33: Example of Model Effect on Regulatory Requirements**

Numerical Model	Predicted Removal (%)	Influent Concentration ( $\mu\text{g L}^{-1}$ )	Effluent Concentration ( $\mu\text{g L}^{-1}$ )	Meets MCL of $3 \mu\text{g L}^{-1}$	Log Removal
MATLAB Ideal Hydraulics	99.88	10	0.01	Yes	2.92
CFD/MATLAB/Lagrangian	95.78	10	0.42	Yes	1.37
CFD/Eulerian	97.43	10	0.26	Yes	1.59

The three numerical models presented in this study (ideal hydraulics, CFD/Eulerian, and CFD/MATLAB/Lagrangian) each have their advantages as tools for designing and optimizing UV/AOP systems. Numerical solutions using ideal hydraulics are certainly the most expedient of the methods and could be appropriate for predicting species concentrations for batch reactors and simple continuous flow systems that approximate plug-flow hydraulics and one-dimensional fluence rate distributions. As shown in Table 4.33, this approach may also be valuable in initial determination of compliance with MCLs. Evaluation of more complex reactors, including the impact of reactor design characteristics such as lamp or baffle placement, may require CFD-based approaches that can incorporate hydrodynamic effects and non-uniform fluence rate distributions. The choice of numerical methods depends ultimately on the goal of the simulation and known information. Table 4.34 summarizes the input and output of each of the methods discussed in this research. The current research evaluated only one pilot reactor with a single low-pressure lamp. Further studies with more complex reactors are required to determine the differences in CFD and ideal reactor simulations.

**Table 4.34: Summary of Input and Output of Three Numerical Models**

Ideal Hydraulics		CFD/Eulerian		CFD/Lagrangian	
Input	Output	Input	Output	Input	Output
Average UV fluence rate	Effluent concentration of target contaminant	System Geometry	Effluent concentration of all tracked species	System Geometry	UV fluence (dose) distribution indicating reactor departure from ideal plug flow
Reaction mechanism with rate constants		Flow Rate	Spatial distribution of all species within reactor	Flow Rate	
Inlet contaminant and hydrogen peroxide concentrations		Inlet contaminant and hydrogen peroxide concentrations	Spatial distribution of UV light within reactor	Inlet contaminant and hydrogen peroxide concentrations	Effluent concentration of target contaminant
Theoretical hydraulic residence time of reactor		Lamp arrangement, lamp number, lamp output power at UV wavelength(s) of interest	Velocity and pressure distribution within reactor	Lamp arrangement, lamp number, lamp output power at UV wavelength(s) of interest	
		Turbulence model	Headloss across reactor	Turbulence model	
		Fluence rate model		Fluence rate model	
		Reaction mechanism with rate constants		Reaction mechanism with rate constants	
				Inlet particle number and distribution	
				UV dose – response curve for contaminant destruction at specific hydrogen peroxide concentration	

Several conclusions can be drawn from this research on numerical methods to model UV-initiated advanced oxidation systems. If reactor design (lamp locations, baffle placement, etc.) is the goal and several designs will be compared for effluent concentrations, headloss across the reactor, static velocity zones, dark zones, and optimization of reactor dimensions, then the CFD/Eulerian method is the most appropriate tool. If UV fluence (dose) of an existing reactor is known (e.g., from previous bioassay RED analysis) and the goal is to determine contaminant degradation under different hydrogen peroxide concentrations or in a batch reactor, then an ideal hydraulics solution using MATLAB to solve the kinetic rate equations should suffice. If the influence of various lamp orientations on contaminant destruction is being studied or the determination of dose distribution is desired, the CFD/MATLAB/Lagrangian method may be the best choice.

#### 4.5 Future Research Opportunities

This research has laid the groundwork for using CFD to model advanced oxidation processes. However, it has also led to several new questions that should be explored with future research. Since there were significant differences between the CFD and pilot results at higher flow rates, additional investigation into the light model validation and hydrodynamic effects is recommended to determine the next steps for model revision to improve agreement with experimental results.

In the current study, the CFD model value for the power output (at 254 nm) at the lamp centerline was adjusted to produce a value predicted by the RAD-LSI sub-model that

matches the UV sensor reading at the pilot reactor wall under the same UVT conditions. Future research should include a secondary fluence rate validation location or a measurement of the lamp power input combined with an accurate lamp efficiency rating. Further, a direct photolysis experiment, such as that begun with SMX, could be used as an indirect actinometer to validate the fluence delivered by the reactor.

Follow-up research should also include the evaluation of more advanced turbulence models. Models incorporating the Reynolds Stress Model can account for the convection and diffusion of the Reynolds-stress tensor and can more realistically incorporate history effects (Wilcox, 2004), while those using the Large Eddy Simulation can better describe instantaneous sub-grid scale flow characteristics in which chemical reactions can occur. Continuing the investigation of fluid dynamics on the advanced oxidation process should also include the influence of diffusion limitations, the reaction time scale, and the turbulent eddy time scale as discussed in the micromixing section.

The use of a UV dose distribution, or more accurately a hydroxyl-radical exposure distribution, was only initially investigated in this research. The comparison of numerical models based on the CFD Eulerian approach, the CFD Lagrangian approach, and ideal hydraulics should be continued for multi-lamp reactors operating at higher flow rates. This evaluation could also include medium-pressure lamps to supplement the analyses of low-pressure high-output lamps.

As the reaction mechanisms for additional emerging contaminants become available, especially quantification of specific byproduct formation, CFD should be considered as a tool for predicting the outcome of direct photolysis and advanced oxidation on these

environmentally-important compounds. Further the investigation of an emerging contaminant with a known second-order kinetic rate constant well below diffusion-limited conditions (i.e., below  $10^{10} \text{ M}^{-1} \text{ s}^{-1}$ ) should be considered.

Finally, utilities that integrate UV-initiated advanced oxidation into their treatment processes may also qualify for disinfection (log-kill) credit within the UV reactor. Data from validated numerical models will be critical in awarding disinfection credit within an AOP. Additional studies that combine the advanced oxidation models generated within this research with UV disinfection models is the next step to achieve accurate simulation of performance of both advanced oxidation and microbial disinfection by UV reactors.

5. JOURNAL ARTICLE NUMBER 1

Journal Target: Water Research

Paper Title: Modeling the UV/Hydrogen Peroxide Advanced Oxidation Process  
Using Computational Fluid Dynamics

Modeling the UV/Hydrogen Peroxide Advanced Oxidation Process Using Computational  
Fluid Dynamics

Author 1: Mr. Scott M. Alpert, PE  
PhD Candidate  
Department of Civil, Construction, and Environmental Engineering  
North Carolina State University  
Mann Hall, Box 7908  
Raleigh, North Carolina 27695  
Phone: 704-608-3796  
Email: [smalpert@gmail.com](mailto:smalpert@gmail.com)

Author 2: Dr. Joel J Ducoste  
Associate Professor  
Department of Civil, Construction and Environmental Engineering  
North Carolina State University  
Mann Hall 319c, Box 7908  
Raleigh, North Carolina 27695  
Phone: 919-515-8150  
Fax: 919-515-7908  
Email: [jducoste@eos.ncsu.edu](mailto:jducoste@eos.ncsu.edu)

# Modeling the UV/Hydrogen Peroxide Advanced Oxidation Process Using Computational Fluid Dynamics

## **ABSTRACT**

Design and optimization of UV/H<sub>2</sub>O<sub>2</sub> systems must incorporate both reactor design (hydrodynamics, lamp orientation) and chemical kinetics (reaction mechanisms, kinetic rate constants). In this CFD model, the combination of turbulence sub-models, fluence rate sub-models, and kinetic rate equations resulted in a comprehensive and flexible design tool for predicting the effluent chemical composition from a UV-initiated AOP reactor. A study has been performed to evaluate the performance of these comprehensive CFD/UV/AOP models for the degradation of an indicator organic contaminant. The CFD model tended to under predict the percent removal of methylene blue compared to pilot reactor trials under the same operating conditions. In addition, the percent difference between the pilot and the CFD results increases with increasing flow rates. The MSSS fluence rate sub-model predicted higher contaminant removal values than that of the RAD-LSI sub-model. The turbulence sub-model selection for this reactor configuration was found to not significantly impact the predicted removal for methylene blue. The overall degradation of methylene blue was a function of the second-order kinetic rate constant describing the reaction between methylene blue and the hydroxyl radical. In addition, the removal of methylene blue was sensitive to the concentration of dissolved organic carbon in the water matrix since DOC acts as a scavenger of hydroxyl radicals.

**KEYWORDS: Ultraviolet, Advanced Oxidation, Methylene Blue, Emerging Contaminants**

## **INTRODUCTION**

The use of ultraviolet-initiated (UV-initiated) advanced oxidation processes (AOP) is rapidly becoming an attractive alternative for the degradation of emerging organic contaminants that are not easily removed using conventional water treatment processes. Of the available UV-initiated AOPs, UV/hydrogen peroxide ( $H_2O_2$ ) is one of the more promising technologies. Design and optimization of UV/ $H_2O_2$  systems include both system configuration (reactor design, pipe and fittings, lamp number, and lamp orientation) and chemical kinetics (reaction mechanisms and kinetic rate constants). While some numerical techniques have been developed for understanding UV AOP performance, these techniques are limited in their applicability for analyzing full-scale UV/AOP systems while incorporating both reactor design and chemical kinetics (see, for example, Sharpless and Linden, 2003; Pareek et al., 2003; Crittenden et al., 1999). As a result, engineers and other water professionals need more appropriate numerical tools to use as part of the design process and in optimizing UV/AOP systems.

The reaction mechanisms for the degradation of organic contaminants by UV-initiated AOPs typically consist of a complex chain of fast chemical reactions. As such, the resulting intermediates and products from these processes may be highly sensitive not only to the light distribution within the reactor but also the level of turbulence and mixing (Baldyga and Bourne, 1999; Spalding, 1998; Marchiso and Barresi, 2003). Design factors such as

upstream hydraulic configurations, internal reactor layout, and lamp arrangement, may influence process performance (Ducoste and Linden, 2005). Water quality effects, including the impact of light- and radical-scavengers, will determine not only the size of the treatment system but also the appropriate placement in the treatment scheme (Linden et al., 2004).

Researchers have previously demonstrated the importance of combining UV reactor hydraulics with dynamic fluence rate models to predict the effectiveness of the disinfection process. The authors of a recent AwwaRF study that successfully applied UV-initiated advanced oxidation for the degradation of organic contaminants recognized the dependence on non-ideal reactor characteristics (hydrodynamics and fluence rate) for the overall AOP performance (Linden et al., 2004). Sharpless and Linden (2003) concluded that development of a predictive UV/AOP model that incorporates reactor hydraulics would allow design simulations that optimize lamp placement, minimize light screening, and improve prediction of contaminant removal in different UV reactors. Thus, an effective CFD simulation must include turbulence models, fluence rate models, and accurate reaction mechanisms describing the oxidation of the contaminant.

A significant amount of experimental research has been completed to evaluate the degradation of an organic species (parent compound) by UV-initiated advanced oxidation reactions (Sharpless and Linden, 2003; Bali et al., 2003; Devlin and Harris, 1984; Scheck and Frimmel, 1995). In other research studies, investigators have performed more detailed experiments to ascertain the reaction pathways involved in the degradation of the parent compound to its intermediate and final products (Stefan et al., 1996; Stefan et al., 2000; Alnaizy and Akgerman, 2000). The determination of these reaction pathways provides a

more detailed picture of the photoreactive process and allows the development of numerical kinetic models that predict the rate of conversion of reactants to products. Detailed reaction pathways are very specific to the parent compound and chemical constituents in the water. However, once the reaction pathway is defined, researchers can combine the reaction kinetics of these UV-initiated AOPs with simulation models that describe the hydraulic and turbulent characteristics of a UV reactor system. Although Sharpless and Linden (2003) were able to develop an NDMA degradation kinetic model, the model assumed ideal mixing for a batch reactor. As a result, the model does not account for variations in the UV fluence rate distribution or variations in fluence distributions due to fluid element paths within a flow-through reactor. One of the recommendations by Sharpless and Linden (2003) was that a detailed hydraulic model coupled with an irradiance distribution profile be developed to examine the effect of optical path length and multiple-lamp reactors for UV/H<sub>2</sub>O<sub>2</sub> systems.

Computational Fluid Dynamics (CFD) is a technique for numerically solving the equations of fluid dynamics over both space and time, including the conservation of mass, conservation of momentum, and conservation of energy. Combined with appropriate boundary and initial conditions, these governing equations can describe both the physical and chemical changes within a reactor. A CFD model for UV systems also includes the spatial variations of fluence rate within the UV reactor.

Limited studies have been performed with CFD to simulate UV/AOPs. Pareek et al. (2003) used CFD combined with a discrete-ordinate radiation transport equation for light intensity and modified k- $\epsilon$  turbulence equations to model a heterogeneous, multi-phase photocatalytic reactor system for the photodegradation of a spent Bayer liquor. However, the

applied radiation model did not incorporate refraction and was performed in a simple bench scale reactor. Mohseni and Taghipour (2004) used CFD to evaluate the heterogeneous photocatalytic oxidation of gas-phase vinyl chloride (VC) by the UV initiation of a TiO<sub>2</sub>-coated surface; however, this research did not incorporate a fluence rate model and only described the flux of VC toward the TiO<sub>2</sub>-coated surface. No research has been performed that investigates the sensitivity of both the turbulence model selection and the use of more rigorous fluence rate models on UV/AOP simulations.

Typically, full-scale UV photoreactors will operate in a turbulent flow regime, and thus, simulations of a UV process must incorporate the impact of turbulent mixing on any chemical reactions that occur within these UV photoreactors. Although the standard k-ε turbulence model is often used for the examination of hydraulics within a flow-through reactor, the incorporation of other turbulent models may provide better characterization of the turbulent behavior within an advanced oxidation reactor. One of the outcomes of this study is to provide better guidance to researchers and engineers on numerical models for UV system analysis. Liu et al. (2007) were able to evaluate the accuracy of the turbulence model with experimental fluid mechanics measurements and were able to assess the impact of the turbulence model selection on UV disinfection performance. While their results showed a slight sensitivity of the microbial log inactivation to the turbulence model selection, the analysis revealed that the sensitivity of effluent microbial inactivation to the turbulence model selection was a function of the UV operating conditions and the UV response kinetics of the target microorganisms. A similar sensitivity study needs to be completed for UV-

initiated AOPs since the proper characterization of the turbulent mixing intensity may be critical for fast competitive chemical reactions typically associated with UV/AOPs.

In this study, the turbulent flow in the UV reactor was simulated using three two-equation turbulence models (standard  $k$ - $\epsilon$ , RNG  $k$ - $\epsilon$ , and  $k$ - $\omega$ ) to assess the sensitivity of turbulence model selection on the indicator compound degradation. While other more complicated turbulence models exist, such as the Reynolds Stress Model or Large Eddy Simulation model, the three two-equation models selected for this research provide reasonable and stable results without being numerically intensive. The standard  $k$ - $\epsilon$  model used in this study was that proposed by Launder and Sharma (1974) (as cited in Wilcox 2004) to solve the turbulence stress closure problem. A second closure model, the Renormalized Group (RNG)  $k$ - $\epsilon$  model, was developed by Yakhot and Orszag (1986) using techniques from the renormalization group theory. The third model, the  $k$ - $\omega$  model, uses transport equations for  $k$  and the Reynolds Mean Stress (RMS) fluctuating vorticity  $\omega$ . These three models were chosen based on their general universality for modeling of uncomplicated turbulent flows. The standard  $k$ - $\epsilon$  model is the most popular of the two-equation closure models and performs relatively well for most types of flows. The RNG  $k$ - $\epsilon$  model tries to solve the  $k$ - $\epsilon$  singularity problem at wall boundaries (where  $k$  approaches zero) and reduces the higher level of dissipation that is predicted using the standard  $k$ - $\epsilon$  model. However, the RNG  $k$ - $\epsilon$  model is not as accurate in predicting free-shear (no wall) flows. The  $k$ - $\omega$  model has been proven relatively accurate for boundary layer (wall-bounded) flows, and, with the 1998 revisions, also works well for free-shear flows (Wilcox, 2004).

The UV fluence rate (incident radiant power) varies with distance from the lamp and as a function of the absorptive characteristics of the media through which the light passes. In advanced oxidation reactions, both the organic contaminant and  $H_2O_2$  absorb UV light, reducing the transmitted fluence rate, and consequently, changing the effectiveness of hydroxyl radical production throughout the UV reactor. Other factors, such as reflection, refraction, shadowing, and lamp effects, also influence the spatial distribution of light within a UV reactor. Several models have been developed to characterize the spatial distribution of the UV fluence rate. These models include the Multiple Point Source Summation (MPSS) model (Jacob and Dranoff, 1970; Bolton, 2000); the Line Source Integration (LSI) model (Blatchley, 1997); the Multi-Segment Source Summation (MSSS) model (Liu et al., 2004); the modified LSI model (RAD-LSI) (Liu et al., 2004); and Discrete Ordinate (DO) methods (Fiveland, 1984; Stamnes et al., 1988; Liou and Wu, 1996). Liu et al. (2004) directly evaluated the performance of these models with experimental measurements of the fluence rate at different points within a UV reactor, the results being a compilation of the strengths and weaknesses of the each model's ability to predict the fluence rate. Ducoste and coworkers further showed that the microbial log inactivation and the shape of the fluence distribution were sensitive to the fluence rate model selection (Ducoste et al., 2005; Liu et al., 2006). Their results suggest the need to evaluate the influence of the fluence rate model selection on any photoreactive process such as UV-initiated advanced oxidation processes.

In this study, the RAD-LSI and MSSS fluence rate sub-models are incorporated into the CFD UV/AOP model. The RAD-LSI is a modified version of the line source integration model (Blatchley, 1997) that was enhanced to account for the physics of reflection,

refraction, and absorption and provides better prediction of the fluence rate near the lamp surface using the radial model component (Liu et al., 2004). Although the RAD-LSI is an improved version of the LSI model, it is still based in part on the multiple point source summation method (MPSS), which models a lamp with a series of point sources. As discussed by Liu et al. (2004), the MPSS model with reflection, refraction, and absorption did not completely correct for the over-prediction of the fluence rate near the lamp surface and in regions near the lamp ends. This over-prediction was corrected by modeling the lamp as a series of differential cylindrical segments, where light is emitted normal to the cylinder surface and decreases with the cosine of the angle between the unit normal and the direction vectors (Liu et al., 2004). This fluence rate modeling approach is called the multiple segment source summation (MSSS), as described more detail in Liu et al. (2004).

Methylene blue is a dye that is used as the indicator organic contaminant in this study. Many organic dyes are decolorized (bleached) upon reaction with the hydroxyl radical. These dyes are good candidates for evaluation in an advanced oxidation study since the decolorization can be i) analyzed with a spectrophotometer, and ii) described by an apparent pseudo-first-order reaction rate constant. In addition, typically these dyes do not undergo direct photolysis and are not reactive with hydrogen peroxide alone. The mechanism of decolorization varies among the types of organic dyes, but, in general, these dyes contain aromatic ring structures that are subject to attack by the hydroxyl radical. The system of kinetic rate equations describing the production of the hydroxyl radical from hydrogen peroxide and the corresponding degradation of methylene blue is shown in Table 1. The photolysis of hydrogen peroxide is shown as Reaction System 1 in Table 1.

In Table 1,  $\Phi_{H_2O_2}$  is the quantum yield for the photolysis of hydrogen peroxide (moles  $H_2O_2$  per mole photons, or moles  $H_2O_2$  per Einstein) and  $\epsilon_{H_2O_2}$  is the molar absorptivity of hydrogen peroxide ( $L\ mol^{-1}\ cm^{-1}$ ). The square brackets  $[\ ]$  represent the molar concentration of the species enclosed in the brackets. The term  $E'_{CFD}$  is the irradiance (UV at 254 nm) at each individual grid cell centerpoint in the CFD domain. Since the light distribution models result in an irradiance term in units of  $W\ m^{-2}$ , a unit conversion is necessary for the variable  $I_{UV}$ , which is used within the CFD code to represent the irradiance at each grid location. Using this definition,  $r_{UV}$  has units of  $moles\ L^{-1}\ s^{-1}$ .

Since the hydroxyl radical is very reactive, it will begin to immediately react with other species in solution. The reaction between hydrogen peroxide and the hydroxyl radical produces the superoxide radical as described by Reaction System 2 in Table 1. Hydrogen peroxide reacts with the superoxide radical generating a hydroxyl radical according to Reaction System 3. Reaction System 4 describes the hydroxyl radical recombining with itself to form hydrogen peroxide. The two radical species,  $\bullet OH$  and  $\bullet O_2^-$ , will also combine with each other as shown in Reaction System 5. Reaction System 6 in Table 1 describes methylene blue (MB) degrading through reaction with the hydroxyl radical to form products not currently under investigation by this research. The reaction rate constant for methylene blue was determined by a competition kinetics process. Several hydroxyl radical scavengers can also be expected in the background water matrix. These scavengers, including dissolved organic carbon (DOC), alkalinity (which at neutral pH can be assumed to be dominated by

the bicarbonate ion), and chloramines (for the water used in this research), will consume radicals according to Reaction Systems 7-9 in Table 1.

To improve convergence within the CFD code, two modifications to the equations were made. The first is that the four species being tracked (methylene blue, hydrogen peroxide, the hydroxyl radical, and the superoxide radical) are normalized to initial hydrogen peroxide or methylene blue conditions. The second is that, since the lifetimes of the two radical species are very short, pseudo-steady-state conditions for the two radicals are assumed.

## **MATERIALS AND METHODS**

A three-dimensional solid model of the UV reactor used in the pilot experiments was created in AutoCAD 2004 (Autodesk, Inc., San Rafael, CA). This model included geometric elements for the reactor, inlet and outlet piping, the UV lamp/quartz sleeve assembly with wiper mechanism, five internal baffle plates, and the inlet and outlet planes. All dimensions were measured directly on the pilot reactor and translated as full-scale into the AutoCAD model. This model was then imported into the CFD software PHOENICS (CHAM, Ltd, Wimbledon, England) and appropriate boundary conditions for inlet and outlet velocities, pressures, and turbulence conditions were set. Table 2 displays the boundary conditions that correspond to the experimental conditions of this study. Since PHOENICS uses a structured rectangular grid, the grid spacing in all three dimensions was manually created and resulted in a total of 859,154 cells across the domain. The grid was verified as adequate to achieve grid dependence by ensuring average species concentrations changed by no more than 1% as

a function of grid refinement. The equations for each of the turbulence sub-models (k- $\epsilon$ , RNG k- $\epsilon$ , and k- $\omega$ ) are included within the PHOENICS library and are selected through a user interface menu. The spatial variation of light inside the reactor (i.e., the fluence rate characterization) was simulated using the RAD-LSI model (Liu et al., 2004) and the MSSS model, by incorporating codes for these two sub-models as appropriate for the lamp characteristics and orientation being evaluated in this research. The coding of the kinetic rate equations describing the production of hydroxyl radicals from hydrogen peroxide followed by the destruction of methylene blue by reaction with these radicals was added to the CFD model. The CFD model results were considered converged when the net sum of the differences between the inlet and outlet volume fractions (i.e., conservation of mass) was on the order of  $10^{-3}$  or below.

For the pilot-scale experiments, dry methylene blue (Alfa Aesar, Acros Organics) and hydrogen peroxide solution (30% w/v, Fisher Scientific, Pittsburgh, PA) were used as purchased without further purification. The methylene blue and hydrogen peroxide were diluted separately with dechlorinated ultra-filtered deionized water (Dracor High Purity Water Systems) (herein referred to as DI water). Reagents used for analyses, including potassium iodide, potassium iodate, sodium hydroxide, ammonium molybdate tetrahydrate, and potassium hydrogen phthalate, were acquired as ACS-grade or similar solids from Fisher Scientific (Pittsburgh, PA). Pilot influent water was pumped from a 10,000-gallon concrete reservoir filled with GAC-filtered (NORIT GAC400) municipal tap water from Raleigh, NC.

Methylene blue concentration at the pilot reactor effluent was correlated to absorption at 661 nm measured using a UV/Vis spectrophotometer (Cary 50, Varian, Inc., Walnut

Creek, CA) coupled to a fiber optic spectrophotometric probe (C Technologies, Inc., Bridgewater, NJ) inserted into the reactor effluent pipe. Total chlorine concentration of the pilot reactor influent was tested using a Hach Pocket Colorimeter. Total alkalinity was measured using Standard Methods (19<sup>th</sup> Edition, 1995) Method 2320. Hydrogen peroxide residual concentrations were measured using the method described by Klassen et al. (1994). Total organic carbon (TOC) was measured by the Town of Cary (NC) water quality laboratory using a Tekmar-Dohrmann Phoenix 8000 analyzer. The pH of the water matrix for each pilot run was measured using a Thermo Orion Model 410 pH meter calibrated weekly using a two-point standard. UV transmittance at 254 nm (UVT<sub>254</sub>) was measured in a 1-cm pathlength quartz cuvette using the Varian Cary 50 spectrophotometer zeroed with DI water.

To determine the second order rate constant for methylene blue, a competition kinetics method described by Rosenfeldt and Linden (2004) was used. In this method, known concentrations of isopropyl alcohol (IPA) were used as a radical scavenger within UV-exposed crystallization dishes of methylene blue and hydrogen peroxide under a collimated beam apparatus. By varying the initial concentration of IPA and measuring the methylene blue concentration before and after exposure, a graph of the inverse of the pseudo-first-order rate constant  $(k'_{MB})^{-1}$  (s) as a function of the initial IPA concentration (M) was prepared. The slope and y-intercept of a linear regression of this data was then used to determine the second-order rate constant for the reaction between methylene blue and the hydroxyl radical  $(k''_{MB})$ .

CFD results were validated with pilot scale experiments under the same reaction conditions. A schematic of the low-pressure UV pilot scale system is presented in Figure 1. A 6"-diameter cylindrical stainless steel UV reactor was provided by Degremont's North American Research and Development Center (DENARD). A single low-pressure high-output UV lamp (Ondeo Degremont, No. 61645-G01, 52W nameplate output at 254 nm) was installed axially along the 6'-long reactor. Five removable perforated baffle plates were installed symmetrically about the center of the reactor. Sampling valves were installed within three feet of the influent and effluent of the reactor. Two ball valves located upstream and downstream of the reactor were used to throttle flow between 5 and 50 gallons per minute. Two diffuser mechanisms were installed upstream of the reactor through which methylene blue and hydrogen peroxide solutions were injected into the system. Flow rates of the contaminant and hydrogen peroxide solutions were controlled by peristaltic pumps. The diffusers were located immediately downstream of the flow regulating valve, the turbulence from which provided additional mixing of the chemicals prior to the reactor influent. Similar to the CFD models, the pilot system was used to measure methylene blue degradation with five internal baffles and with one internal baffle in the UV reactor.

## **RESULTS**

The results of the competition kinetics experiments using isopropyl alcohol (IPA) as the radical scavenger produced the results shown in Figure 2. Based on this data, the second-order rate constants for the reaction between methylene blue and the hydroxyl radical were calculated for the four separate trials and are reported in Table 3. Since the variation in rate

constant values may be considered significant, as represented by the 95% confidence interval, the sensitivity of the overall degradation of methylene blue in the system being modeled was determined using CFD. In addition, it should be noted that the calculated values for the rate constant are high enough to be in the range for which reactions may become diffusion-limited. A diffusion limited reaction is one in which the reaction rate is limited by the ability of diffusion to transfer one reactant to the second reactant.

During this research, eight (8) combinations of flow rate and hydrogen peroxide dose were evaluated using methylene blue in the pilot-scale reactor and the CFD model. The pilot and CFD results for the trials in which five baffles were in the reactor are shown in Figure 3. Similar data is compared for the trials with only one baffle in the reactor in Figure 4.

The three turbulence closure sub-models were evaluated to determine the effect, if any, on the overall degradation prediction of the advanced oxidation of the methylene blue. Table 4 displays the contaminant degradation results of running the same experimental parameters using the three turbulence sub-models for two different flow rates. Table 5 displays the effects of the fluence rate sub-model selection on the overall degradation prediction of the advanced oxidation of methylene blue. As shown in Table 5, the MSSS sub-model predicts a higher fluence rate at the location of the pilot reactor sensor than the RAD-LSI sub-model, which translates to higher contaminant removal percentages predicted for methylene blue.

In order to evaluate the effect of the value of the second-order kinetic rate constant for the reaction between the hydroxyl radical and methylene blue, several additional values of this constant were used in separate CFD models in addition to the average value

determined experimentally by competition kinetics. These values include the limits of the 95% confidence interval that describes the experimental results for methylene blue ( $6.89 \times 10^{10} \pm 2.05 \times 10^{10} \text{ M}^{-1} \text{ s}^{-1}$ ). The results of the model runs using different rate constants are shown in Table 6 and Figure 5. The CFD model was also evaluated for the sensitivity of the methylene blue degradation to changes in dissolved organic carbon (DOC). A summary of the results is provided in Table 7 and graphically in Figure 6.

## DISCUSSION

Examination of Figure 3 reveals several trends. First, the CFD model tends to under predict the percent removal of methylene blue within the reactor. While the low flow conditions produced good agreement between pilot and CFD results, the CFD predicted removal was 8.6% to 22.7% less than that achieved in the pilot for the higher flows. One potential explanation for this difference could be an over-prediction of radical scavenger effects in the model. More hydroxyl radicals would be available for reaction if the DOC concentration, which will later be shown to significantly impact the degradation of methylene blue, was lower in any individual pilot trial than that modeled. Another likely cause of this under-prediction trend is that there may be additional reactions occurring in the pilot system that lead to methylene blue degradation but that were not modeled in CFD. For instance, a reaction between carbonate and/or NOM radicals and methylene blue could be occurring in the reactor. Although reactions with radicals other than the hydroxyl radical are common for organic contaminants, they are often not quantified in the literature (and reflected in known reaction rate constants). However, if additional reactions were the cause of the differences

between the pilot and the CFD results, they should have also shown up in the 5 and 10 GPM cases.

The second trend in Figure 3, as displayed for the data points on the left side of the figure, is that the percent difference between the pilot and the CFD results increased with increasing flow rates. Although it would be expected that reactions fast enough to be considered diffusion-limited would produce the opposite effect (i.e., higher velocities would cause less time for diffusion, and thus if diffusion limitations are not considered, the CFD model should over-predict the removal rate), it is apparent that there are hydraulic effects that are not being considered. These hydraulic differences are not reflected in the three two-equation turbulence models considered (as shown in Table 4) and thus could be related to small-scale eddy effects. Turbulence can be composed of many transient structural features that are difficult to capture with Reynolds Averaged Navier-Stokes (RANS) equations. The RANS equations in CFD have been shown to poorly capture the turbulent kinetic energy and the extent of the recirculation zones in the wake regions behind flow obstructions. One hypothesis for the differences between the experimental and model results at the higher flow rates in this study is the CFD RANS models used did not adequately capture the flow characteristics downstream of the baffle plates in which enhanced mixing might improve the reaction conditions between the hydroxyl radical and methylene blue. The percent removal values in Table 4 indicate that the two-equation turbulence model selection for this reactor configuration does not significantly impact the predicted removal for methylene blue.

As seen in Table 6, the overall degradation of methylene blue is a strong function of the kinetic rate constant as expected. Within the range of the 95% confidence interval of the

rate constants determined experimentally, the percent removal of methylene blue varied by 9.7% (i.e., 51.4% removal at the lower limit and 61.1% removal at the upper limit). The overall removal of methylene blue is shown also to be sensitive to the concentration of DOC in the water matrix. Since the DOC of the pilot influent was only measured successfully once in this research, any variance between pilot runs could explain some of the differences between the pilot and CFD results. In Figure 6, the value of DOC used in the CFD model ( $0.57 \text{ mg L}^{-1}$ ) is shown along with the resulting variability in removal if the DOC changed by plus or minus  $0.25 \text{ mg L}^{-1}$ .

## CONCLUSIONS

This research into the use of CFD for the evaluation of UV-initiated advanced oxidation processes for the degradation of an organic contaminant produced several results.

- Effective CFD models for AOP must incorporate rigorous turbulence sub-models, fluence rate sub-models, kinetic rate equations, and proper characterization of the background water matrix.
- In this research, the CFD model tended to under predict the percent removal of methylene blue compared to pilot reactor trials under the same operating conditions. The percent difference between the pilot and the CFD results increases with increasing flow rates.
- The MSSS fluence rate sub-model predicted higher contaminant removal values than that of the RAD-LSI sub-model under the same operating conditions.
- The turbulence sub-model selection for this reactor configuration was found to not significantly impact the predicted removal for methylene blue.

- The overall degradation of methylene blue was a strong function of the value of the second-order kinetic rate constant describing the reaction between methylene blue and the hydroxyl radical.
- The overall removal of methylene blue was shown to be sensitive to the concentration of the radical scavenger dissolved organic carbon in the water matrix.

As oxidation pathways for emerging water contaminants are identified, a simulation model, such as the one described herein, may become an important tool for the design and optimization of advanced oxidation systems. These numerical models will allow evaluation of multiple design scenarios, including number of lamps, layout of reactors, and upstream hydraulic conditions. However, there were significant differences between the CFD and pilot results at higher flow rates for the reactor studied in this research. Thus, follow-up research should include the evaluation of more advanced turbulence models, including those incorporating the Reynolds Stress Model and/or the Large Eddy Simulation. The investigation of fluid dynamics on the advanced oxidation process should also include the influence of the reaction time scale and turbulent eddy time scales. As the reaction mechanisms for additional emerging contaminants become available, especially quantification of specific byproduct formation, CFD should be considered as a tool for predicting the outcome of direct photolysis and advanced oxidation on these environmentally-important compounds.

## REFERENCES

- Alnaizy, R., & Akgerman, A. (2000). Advanced Oxidation of Phenolic Compounds. *Advances in Environmental Research*, 4(3), 233-244.
- American Public Health Association, American Water Works Association, & Water Environment Federation. (1995). *Standard Methods for the Examination of Water and Wastewater, 19th Edition* (19th ed.). Washington, DC: American Public Health Association.
- Baldyga, J., & Bourne, J. R. (1999). *Turbulent Mixing and Chemical Reactions*. Chichester, England: John Wiley & Sons Ltd.
- Bali, U., Catalkaya, E. C., & Sengul, F. (2003). Photochemical Degradation and Mineralization of Phenol: A Comparative Study. *Journal of Environmental Science and Health, Part A-Toxic/Hazardous Substances & Environmental Engineering*, A38(10), 2259-2275.
- Blatchley, E. R., III. (1997). Numerical Modelling of UV Intensity: Application to Collimated-Beam Reactors and Continuous-Flow Systems. *Water Research*, 31(9), 2205-2218.
- Bolton, J. R. (2000). Calculation of Ultraviolet Fluence Rate Distributions in an Annular Reactor: Significance of Refraction and Reflection. *Water Research*, 34(13), 3315-3324.

- Buxton, G. V., Greenstock, C. L., Helman, W. P., & Ross, A. B. (1988). Critical Review of Rate Constants for Reactions of Hydrated Electrons, Hydrogen Atoms and Hydroxyl Radicals (OH/O<sup>-</sup>) in Aqueous Solution. *J. Phys. Chem. Ref. Data*, 17(2), 513-886.
- Crittenden, J. C., Hu, S., Hand, D. W., & Green, S. A. (1999). A Kinetic Model for H<sub>2</sub>O<sub>2</sub>/UV Process in a Completely Mixed Batch Reactor. *Wat. Res.*, 33(10), 2315-2328.
- Devlin, H. R., & Harris, I. J. (1984). Mechanism of the Oxidation of Aqueous Phenol with Dissolved Oxygen. *Ind. Eng. Chem. Fundam.*, 23(4), 387-392.
- Ducoste, J., Liu, D., & Linden, K. G. (2005). Alternative Approaches to Modeling Fluence Distribution and Microbial Inactivation in Ultraviolet Reactors: Lagrangian versus Eulerian. *Journal of Environmental Engineering*, 1393-1403.
- Ducoste, J., & Linden, K. G. (2005). *Hydrodynamic Characterization of UV Reactors*. Denver: Awwa Research Foundation.
- Fiveland, W. A. (1984). Discrete-Ordinates Solutions of the Radiative Transport Equation for Rectangular Enclosures. *Journal of Heat Transfer*, 106, 699-705.
- Jacob, S. M., & Dranoff, J. S. (1970). Light Intensity Profiles in a Perfectly Mixed Photoreactor. *AIChE Journal*, 16(3), 359-363.
- Johnson, H. D., Cooper, W. J., Mezyk, S. P., & Bartels, D. M. (2002). Free Radical Reactions of Monochloramine and Hydroxylamine in Aqueous Solution. *Radiation Physics and Chemistry*, 65, 317-326.
- Klassen, N. V., Marchington, D., & McGowan, H. C. E. (1994). H<sub>2</sub>O<sub>2</sub> Determination by the I<sub>3</sub><sup>-</sup> Method and by KMnO<sub>4</sub> Titration. *Analytical Chemistry*, 66(18), 2921-2925.

- Larson, R. A., & Zepp, R. G. (1988). Reactivity of the Carbonate Radical with Aniline Derivatives. *Environmental Toxicology and Chemistry*, 7, 265-274.
- Linden, K. G., Sharpless, C. M., Andrews, S. A., Atasi, K. Z., Korategere, V., Stefan, M. I., et al. (2004). *Innovative UV Technologies to Oxidize Organic and Organoleptic Chemicals*: Awwa Research Foundation.
- Liou, B. T., & Wu, C. Y. (1996). Radiative transfer in a multi-layer medium with Fresnel interfaces. *Heat and Mass Transfer*, 32(1-2), 103-107.
- Liu, D., Ducoste, J., Jin, S., & Linden, K. G. (2004). Evaluation of Alternative Fluence Rate Distribution Models. *Journal of Water Supply: Research and Technology - AQUA*, 53(6), 391-408.
- Liu, D., Ducoste, J., Wu, C., & Linden, K. G. (2007). Numerical Simulation of UV Disinfection Reactors: Evaluation of Alternative Turbulence Models. *Applied Mathematical Modeling*, 31, 1753-1769.
- Marchisio, D. L., & Barresi, A. A. (2003). CFD Simulation of Mixing and Reaction: The Relevance of the Micro-Mixing Model. *Chemical Engineering Science*, 58, 3579-3587.
- Mohseni, M., & Taghipour, F. (2004). Experimental and CFD Analysis of Photocatalytic Gas Phase Vinyl Chloride (VC) Oxidation. *Chemical Engineering Science*, 59, 1601-1609.
- Pareek, V. K., Cox, S. J., Brungs, M. P., Young, B., & Adesina, A. A. (2003). Computational Fluid Dynamic (CFD) Simulation of a Pilot-Scale Annular Bubble Column Photocatalytic Reactor. *Chemical Engineering Science*, 58, 859-865.

- Rosenfeldt, E. J., & Linden, K. G. (2004). Degradation of Endocrine Disrupting Chemicals Bisphenol A, Ethinyl Estradiol, and Estradiol during IV Photolysis and Advanced Oxidation Processes. *Environ. Sci. Technol.*, 38(20), 5476-5483.
- Scheck, C. K., & Frimmel, F. H. (1995). Degradation of Phenol and Salicylic Acid by Ultraviolet Radiation/Hydrogen Peroxide/Oxygen. *Water Research*, 29(10), 2346-2352.
- Sharpless, C. M., & Linden, K. G. (2003). Experimental and Model Comparisons of Low- and Medium-Pressure Hg Lamps for the Direct and H<sub>2</sub>O<sub>2</sub> Assisted UV Photodegradation of N-Nitrosodimethylamine in Simulated Drinking Water. *Environ. Sci. Technol.*, 37(9), 1933-1940.
- Spalding, B. (1998). Turbulent Mixing and Chemical Reaction; The Multi-Fluid Approach. A Lecture. *Based on The International Symposium on the Physics of Heat Transfer in Boiling and Condensation*, from [http://www.simuserve.com/phoenics/d\\_polis/d\\_lecs/mfm/mfm0.htm](http://www.simuserve.com/phoenics/d_polis/d_lecs/mfm/mfm0.htm)
- Stamnes, K., Tsay, S.-C., Wiscombe, W., & Jayaweera, K. (1988). Numerically Stable Algorithm for Discrete-Ordinate-Method for Radiative Transfer in Multiple Scattering and Emitting Layered Media. *Applied Optics*, 27(12), 2502-2509.
- Stefan, M. I., Hoy, A. R., & Bolton, J. R. (1996). Kinetics and Mechanism of the Degradation and Mineralization of Acetone in Dilute Aqueous Solution Sensitized by the UV Photolysis of Hydrogen Peroxide. *Environ. Sci. Technol.*, 30, 2382-2390.

- Stefan, M. I., Mack, J., & Bolton, J. R. (2000). Degradation Pathways during the Treatment of Methyl tert-Butyl Ether by the UV/H<sub>2</sub>O<sub>2</sub> Process. *Environ. Sci. Technol.*, 34(4), 650-658.
- Weinstein, J., & Bielski, B. H. J. (1979). Kinetics of the Interaction of HO<sub>2</sub> and O<sub>2</sub><sup>-</sup> Radicals with Hydrogen Peroxide. The Haber-Weiss Reaction. *Journal of the American Chemical Society*, 101(1), 58-62.
- Wilcox, D. C. (2004). *Turbulence Modeling for CFD* (Second ed.). La Canada, California: DCW Industries, Inc.
- Yakhot, V., & Orszag, S. A. (1986). Renormalization-Group Analysis of Turbulence. *Physical Review Letters*, 57(14), 1722-1724.

**Table 1: Kinetic Rate Equations**

Reaction System	Equations	Constants (References)
1	$r_{UV} = 2\Phi_{H_2O_2} E'_{CFD} \varepsilon_{H_2O_2} [H_2O_2]$ $E'_{CFD} = \frac{I_{UV} (W m^{-2}) \times 100 (cm m^{-1})}{U_{254} (J Ein^{-1}) \times 1000 (L m^{-3})}$	$\Phi_{H_2O_2} = 0.5$ $\varepsilon_{H_2O_2} = 19.6 M^{-1} cm^{-1}$ $U_{254} = 471,528 J Ein^{-1}$
2	$\frac{d[H_2O_2]}{dt} = -k_1 [H_2O_2][\bullet OH]$ $\frac{d[\bullet OH]}{dt} = -k_1 [H_2O_2][\bullet OH]$ $\frac{d[\bullet O_2^-]}{dt} = k_1 [H_2O_2][\bullet OH]$	$k_1 = 2.7 \times 10^7 M^{-1} s^{-1}$ (Buxton et al., 1988)
3	$\frac{d[H_2O_2]}{dt} = -k_2 [H_2O_2][\bullet O_2^-]$ $\frac{d[\bullet O_2^-]}{dt} = -k_2 [H_2O_2][\bullet O_2^-]$ $\frac{d[\bullet OH]}{dt} = k_2 [H_2O_2][\bullet O_2^-]$	$k_2 = 0.13 M^{-1} s^{-1}$ (Weinstein et al., 1979)
4	$\frac{d[\bullet OH]}{dt} = -k_3 [\bullet OH][\bullet OH]$ $\frac{d[H_2O_2]}{dt} = k_3 [\bullet OH][\bullet OH]$	$k_3 = 5.5 \times 10^9 M^{-1} s^{-1}$ (Buxton et al., 1988)
5	$\frac{d[\bullet OH]}{dt} = -k_4 [\bullet OH][\bullet O_2^-]$ $\frac{d[\bullet O_2^-]}{dt} = -k_4 [\bullet OH][\bullet O_2^-]$	$k_4 = 7.0 \times 10^9 M^{-1} s^{-1}$ (Beck, 1969 as cited in Crittenden, et. al, 1999)
6	$\frac{d[\bullet OH]}{dt} = -k_{MB,\bullet OH} [\bullet OH][MB]$ $\frac{d[MB]}{dt} = -k_{MB,\bullet OH} [\bullet OH][MB]$	$k_{MB,\bullet OH} = 6.9 \times 10^9 M^{-1} s^{-1}$

**Table 1 Continued**

Reaction System	Equations	Constants (References)
7	$\frac{d[\cdot OH]}{dt} = -k_{DOC,\cdot OH} [\cdot OH](DOC)$	$k_{DOC,\cdot OH} = 2.5 \times 10^4 \left( \frac{mg}{L} \right)^{-1} s^{-1}$ (Larson and Zepp, 1988)
8	$\frac{d[\cdot OH]}{dt} = -k_{HCO_3^-, \cdot OH} [HCO_3^-][\cdot OH]$	$k_{HCO_3^-, \cdot OH} = 8.5 \times 10^6 M^{-1} s^{-1}$ (Buxton et al., 1988)
9	$\frac{d[\cdot OH]}{dt} = -k_{NH_2Cl, \cdot OH} [NH_2Cl][\cdot OH]$	$k_{NH_2Cl, \cdot OH} = (2.8 \pm 0.2) \times 10^9 M^{-1} s^{-1}$ (Johnson et al., 2002)

**Table 2: CFD Model Boundary Conditions**

Condition	Value
Inlet Velocity (normal to inlet plane)	0.128 – 0.384 m s <sup>-1</sup> (10 – 30 gal min <sup>-1</sup> ) All tangential velocities set to zero.
Outlet Velocity	No external velocity restriction <sup>(1)</sup>
Outlet (External) Pressure	100,000 Pa (Zero Gauge)
Inlet Turbulence Condition (I)	5% <sup>(2)</sup>
Inlet Methylene Blue (MB) Concentration	1.563 x 10 <sup>-6</sup> M
Inlet Hydrogen Peroxide Concentration	(150 – 267 * Inlet [MB]) M

<sup>(1)</sup> For the outlet, the gradients of all variables are zero in the flow direction with the exception of pressure.

<sup>(2)</sup> The turbulent kinetic energy and energy dissipation rate inlet conditions are defined as  $k_{inlet} = (I \times U)^2$  and  $\varepsilon_{inlet} = (k_{inlet})^{1.5} (0.1 \times D)^{-1}$  where  $U$  is the normal average inlet velocity and  $D$  is the pipe diameter.

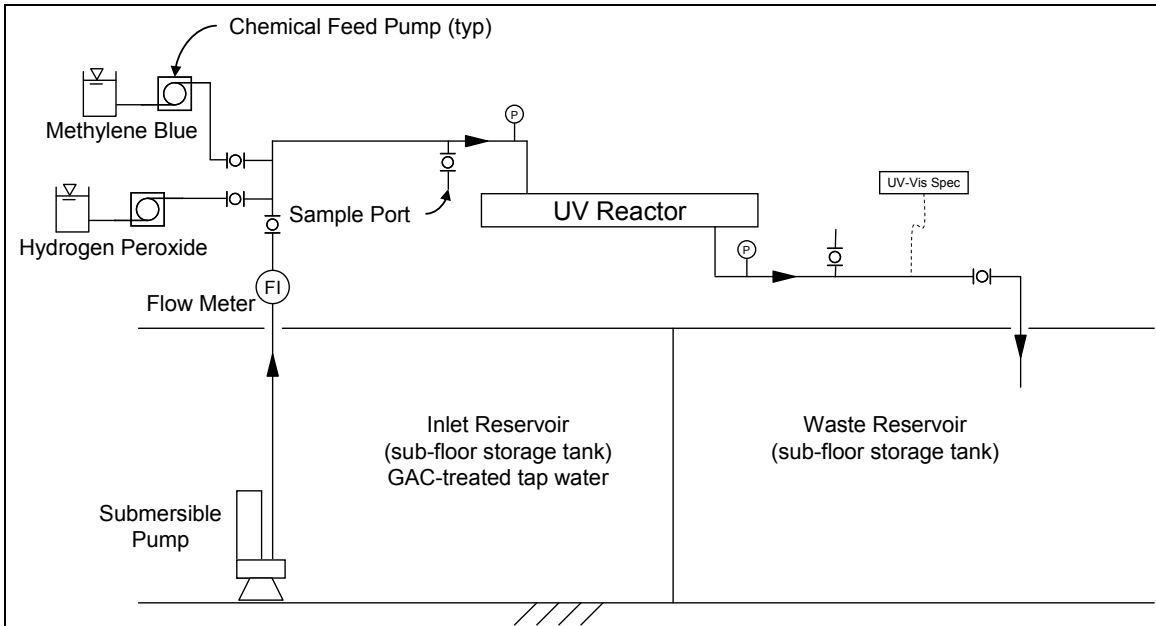


**Figure 1: Low-Pressure UV Pilot System Schematic**

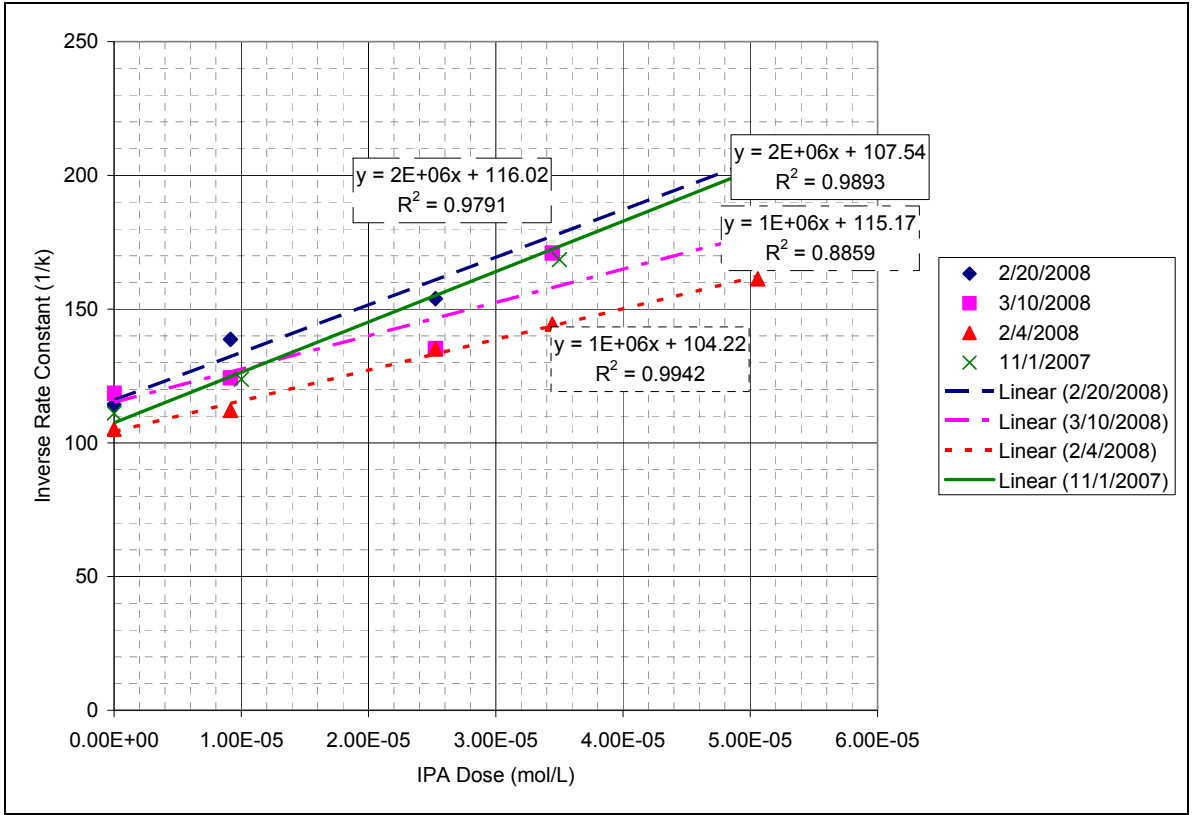


**Figure 2: Competition Kinetic Data Plot for Kinetic Rate Constant Determination**

**Table 3: Experimental Values for the Methylene Blue Kinetic Rate Constant**

Date of Experiments	Second-order Rate Constant for Methylene Blue with the Hydroxyl Radical ( $M^{-1} s^{-1}$ )
3/10/2008	8.72E+10
2/20/2008	5.93E+10
2/4/2008	8.52E+10
11/1/2007	4.40E+10
Average	6.89E+10
95% Confidence Interval	+/- 2.05E+10

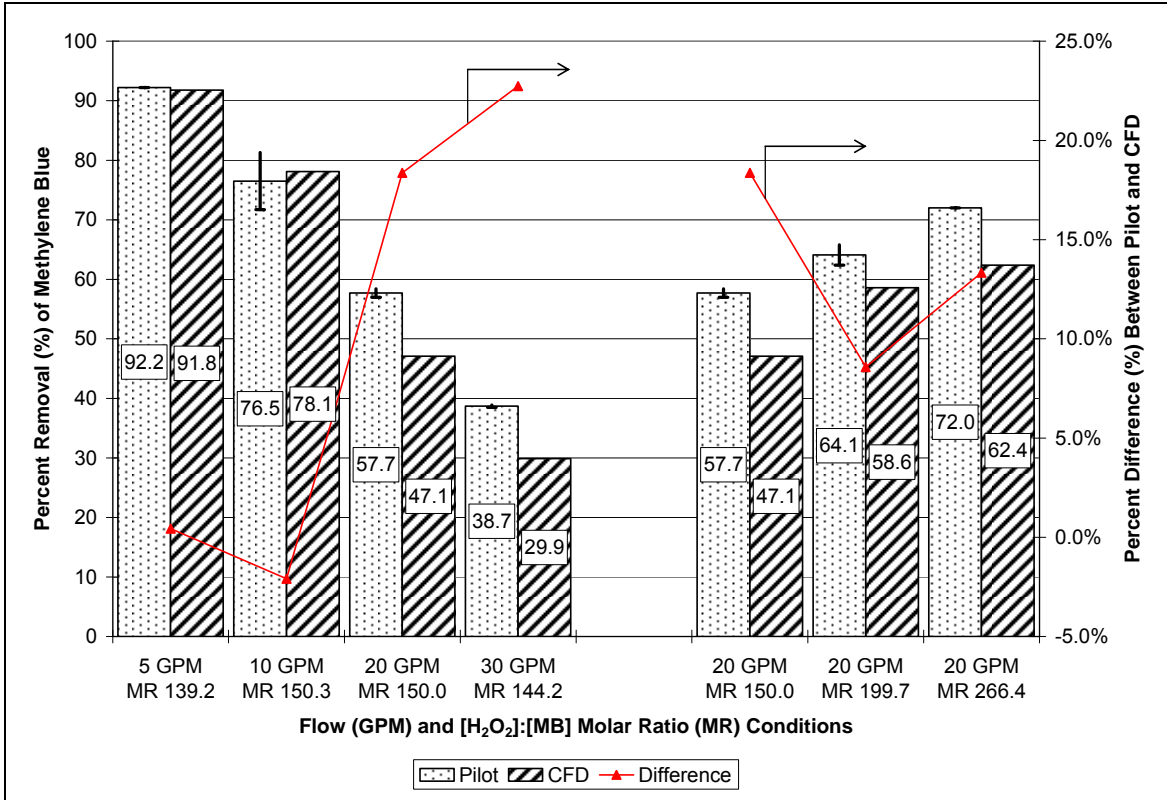


**Figure 3: Comparison of Pilot and CFD Results for Five-Baffle Trials**

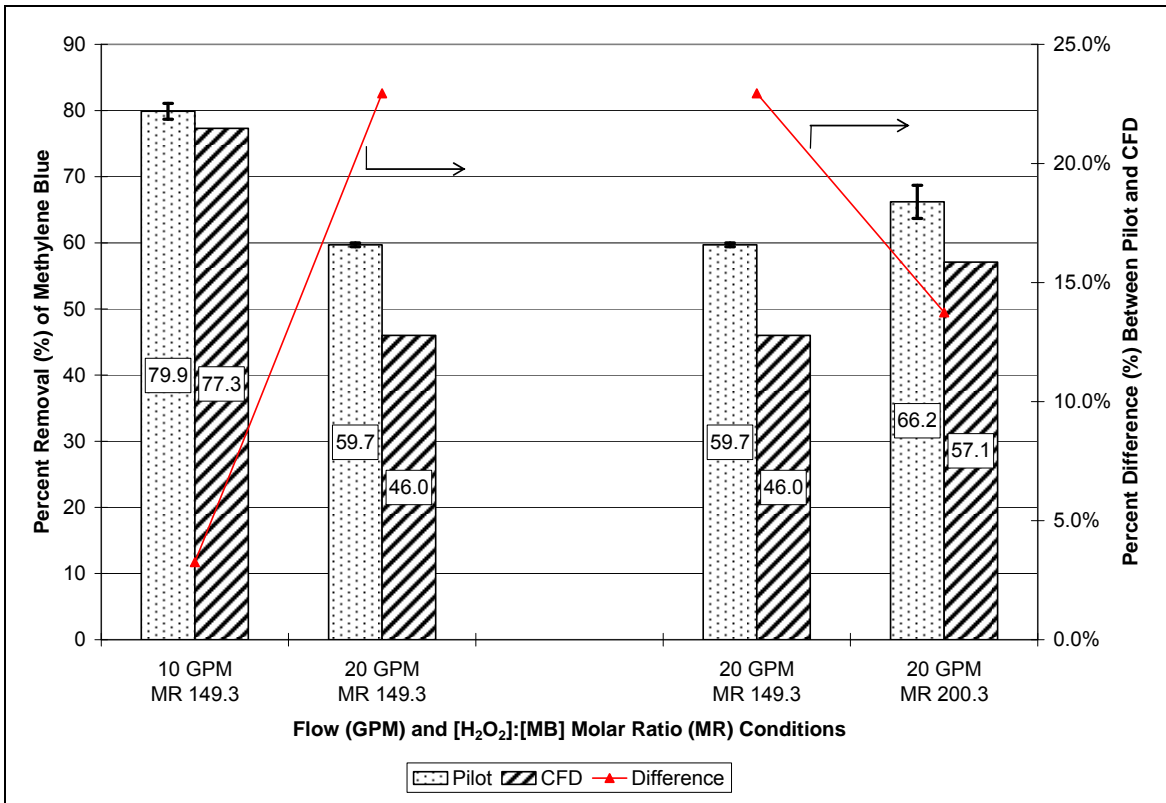


**Figure 4: Comparison of Pilot and CFD Results for One-Baffle Trials**

**Table 4: Impact of Turbulence Sub-model on CFD Results**

Parameter	Model 5	Model 7	Model 8	Model 30	Model 34
Flow Rate (gal min <sup>-1</sup> )	20	20	20	30	30
Compound R Concentration (mg L <sup>-1</sup> )	0.50	0.50	0.50	0.50	0.50
Molar Ratio of H <sub>2</sub> O <sub>2</sub> to Compound	199.25	199.25	199.25	144.2	144.2
H <sub>2</sub> O <sub>2</sub> Concentration (mg L <sup>-1</sup> )	10.6	10.6	10.6	7.66	7.66
Power output at lamp surface (W)	26.5	26.5	26.5	30.2	30.2
Fluence Rate at Sensor (W m <sup>-2</sup> )	18.0	18.0	18.0	15.8	15.8
UVI <sub>254</sub> (%)	94.9	94.9	94.9	91.9	91.9
pH	7.24	7.24	7.24	7.49	7.49
Alkalinity (mg L <sup>-1</sup> as CaCO <sub>3</sub> )	22.2	22.2	22.2	28.1	28.1
Total Chlorine Residual (mg L <sup>-1</sup> as Cl <sub>2</sub> )	0.013	0.013	0.013	0.14	0.14
Number of Baffles in Reactor	5	5	5	5	5
DOC (mg L <sup>-1</sup> )	0.57	0.57	0.57	0.57	0.57
<b>Turbulence Sub-model</b>	<b>k-ε</b>	<b>RNG k-ε</b>	<b>k-ω</b>	<b>k-ε</b>	<b>RNG k-ε</b>
Fluence Rate Sub-model	RAD-LSI	RAD-LSI	RAD-LSI	RAD-LSI	RAD-LSI
k <sub>MB,OH</sub> (M <sup>-1</sup> s <sup>-1</sup> )	6.9 x 10 <sup>10</sup>				
Fraction of Initial Compound Remaining	0.440	0.442	0.431	0.701	0.701
<b>Compound Percent Removal (%)</b>	<b>56.0</b>	<b>55.8</b>	<b>56.9</b>	<b>29.9</b>	<b>29.9</b>

**Table 5: Impact of Fluence Rate Model on CFD Results**

Parameter	Model 5	Model 9
Flow Rate (gal min <sup>-1</sup> )	20	20
Target Compound	Methylene Blue	Methylene Blue
Compound Concentration (mg L <sup>-1</sup> )	0.50	0.50
Molar Ratio of H <sub>2</sub> O <sub>2</sub> to Compound	199.25	199.25
H <sub>2</sub> O <sub>2</sub> Concentration (mg L <sup>-1</sup> )	10.6	10.6
Power output at lamp surface (W)	26.5	26.5
<b>Fluence Rate at Sensor (W m<sup>-2</sup>)</b>	<b>18.0</b>	<b>24.0</b>
UVT <sub>254</sub> (%)	94.9	94.9
pH	7.24	7.24
Alkalinity (mg L <sup>-1</sup> as CaCO <sub>3</sub> )	22.2	22.2
Total Chlorine Residual (mg L <sup>-1</sup> as Cl <sub>2</sub> )	0.013	0.013
Number of Baffles in Reactor	5	5
DOC (mg L <sup>-1</sup> )	0.57	0.57
Turbulence Sub-model	k-ε	k-ε
<b>Fluence Rate Sub-model</b>	<b>RAD-LSI</b>	<b>MSSS</b>
k <sub>MB,OH</sub> (M <sup>-1</sup> s <sup>-1</sup> )	6.9 x 10 <sup>10</sup>	6.9 x 10 <sup>10</sup>
Fraction of Initial Compound Remaining	0.440	0.386
<b>Compound Percent Removal (%)</b>	<b>56.0</b>	<b>61.4</b>

**Table 6: Impact of Second-Order Rate Constant  $k_{MB,OH}$  on CFD Results**

Parameter	Model 15	Model 5	Model 23	Model 32	Model 33
Flow Rate (gal min <sup>-1</sup> )	20	20	20	20	20
Compound R Concentration (mg L <sup>-1</sup> )	0.50	0.50	0.50	0.50	0.50
Molar Ratio of H <sub>2</sub> O <sub>2</sub> to Compound	199.25	199.25	199.25	199.25	199.25
H <sub>2</sub> O <sub>2</sub> Concentration (mg L <sup>-1</sup> )	10.6	10.6	10.6	10.6	10.6
Power output at lamp surface (W)	26.5	26.5	26.5	26.5	26.5
Fluence Rate at Sensor (W m <sup>-2</sup> )	18.0	18.0	18.0	18.0	18.0
UVT <sub>254</sub> (%)	94.9	94.9	94.9	94.9	94.9
pH	7.24	7.24	7.24	7.24	7.24
Alkalinity (mg L <sup>-1</sup> as CaCO <sub>3</sub> )	22.2	22.2	22.2	22.2	22.2
Total Chlorine Residual (mg L <sup>-1</sup> as Cl <sub>2</sub> )	0.013	0.013	0.013	0.013	0.013
Number of Baffles in Reactor	5	5	5	5	5
DOC (mg L <sup>-1</sup> )	0.57	0.57	0.57	0.57	0.57
Turbulence Sub-model	k-ε	k-ε	k-ε	k-ε	k-ε
Fluence Rate Sub-model	RAD-LSI	RAD-LSI	RAD-LSI	RAD-LSI	RAD-LSI
$k_{R,OH}$ (M <sup>-1</sup> s <sup>-1</sup> )	<b>1.0 x 10<sup>9</sup></b>	<b>6.9 x 10<sup>10</sup></b>	<b>3.5 x 10<sup>10</sup></b>	<b>8.9 x 10<sup>10</sup></b>	<b>4.8 x 10<sup>10</sup></b>
Fraction of Initial Compound Remaining	0.966	0.440	0.553	0.389	0.486
<b>Compound Percent Removal (%)</b>	<b>3.4</b>	<b>56.0</b>	<b>44.7</b>	<b>61.1</b>	<b>51.4</b>

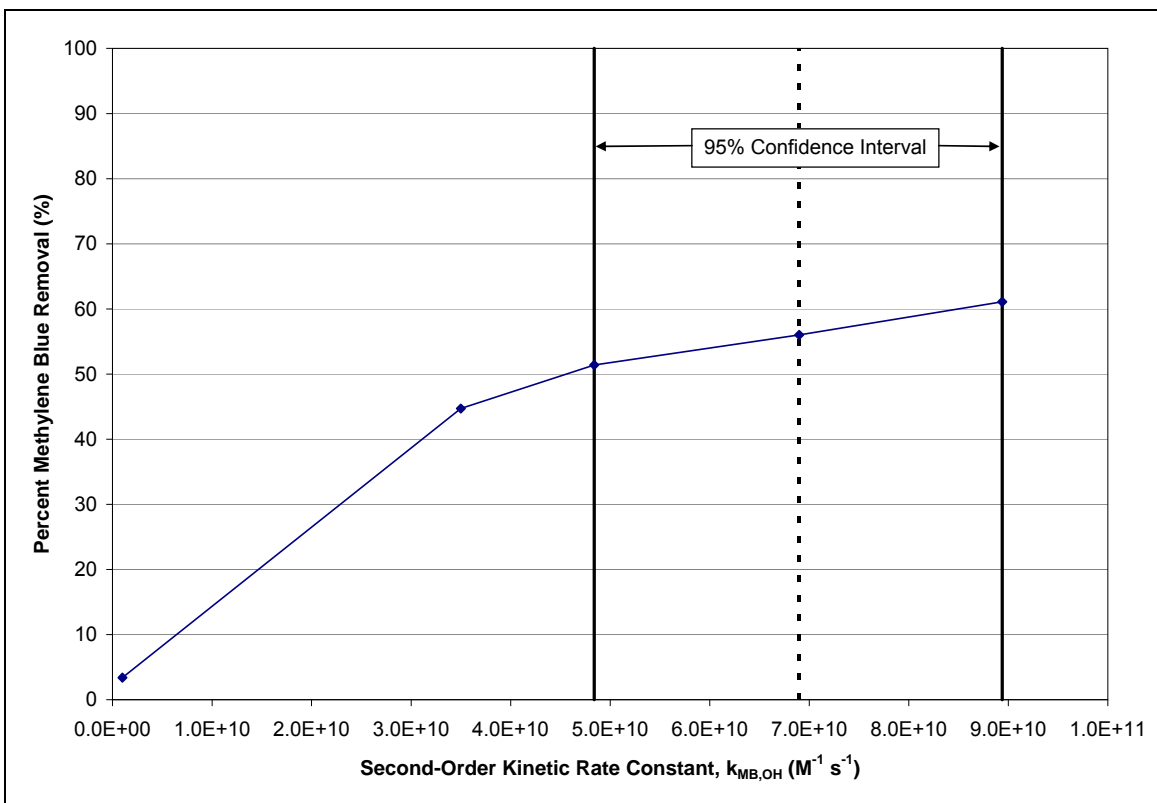


**Figure 5: Impact of Second-Order Rate Constant on Methylene Blue Removal**

**Table 7: Impact of DOC on CFD Results**

Parameter	Model 18	Model 28	Model 19	Model 20
Flow Rate (gal min <sup>-1</sup> )	10	10	10	10
Target Compound (MB = Methylene Blue)	MB	MB	MB	MB
Compound Concentration (mg L <sup>-1</sup> )	0.50	0.50	0.5	0.5
Molar Ratio of H <sub>2</sub> O <sub>2</sub> to Compound	150	150	150	150
H <sub>2</sub> O <sub>2</sub> Concentration (mg L <sup>-1</sup> )	7.98	7.98	7.98	7.98
Power output at lamp surface (W)	31.6	31.6	31.6	31.6
Fluence Rate at Sensor (W m <sup>-2</sup> )	21.5	21.5	21.5	21.5
UVT <sub>254</sub> (%)	94.9	94.9	94.9	94.9
pH	7.25	7.25	7.25	7.25
Alkalinity (mg L <sup>-1</sup> as CaCO <sub>3</sub> )	23	23	23	23
Total Chlorine Residual (mg L <sup>-1</sup> as Cl <sub>2</sub> )	0	0	0	0
Number of Baffles in Reactor	5	5	5	5
<b>DOC (mg L<sup>-1</sup>)</b>	<b>0.0</b>	<b>0.5</b>	<b>1.0</b>	<b>2.0</b>
Turbulence Sub-model	k-ε	k-ε	k-ε	k-ε
Fluence Rate Sub-model	RAD-LSI	RAD-LSI	RAD-LSI	RAD-LSI
k <sub>MB,OH</sub> (M <sup>-1</sup> s <sup>-1</sup> )	6.9 x 10 <sup>10</sup>			
Fraction of Initial Compound Remaining	0.059	0.133	0.197	0.300
<b>Compound Percent Removal (%)</b>	<b>94.1</b>	<b>86.7</b>	<b>80.3</b>	<b>70.0</b>

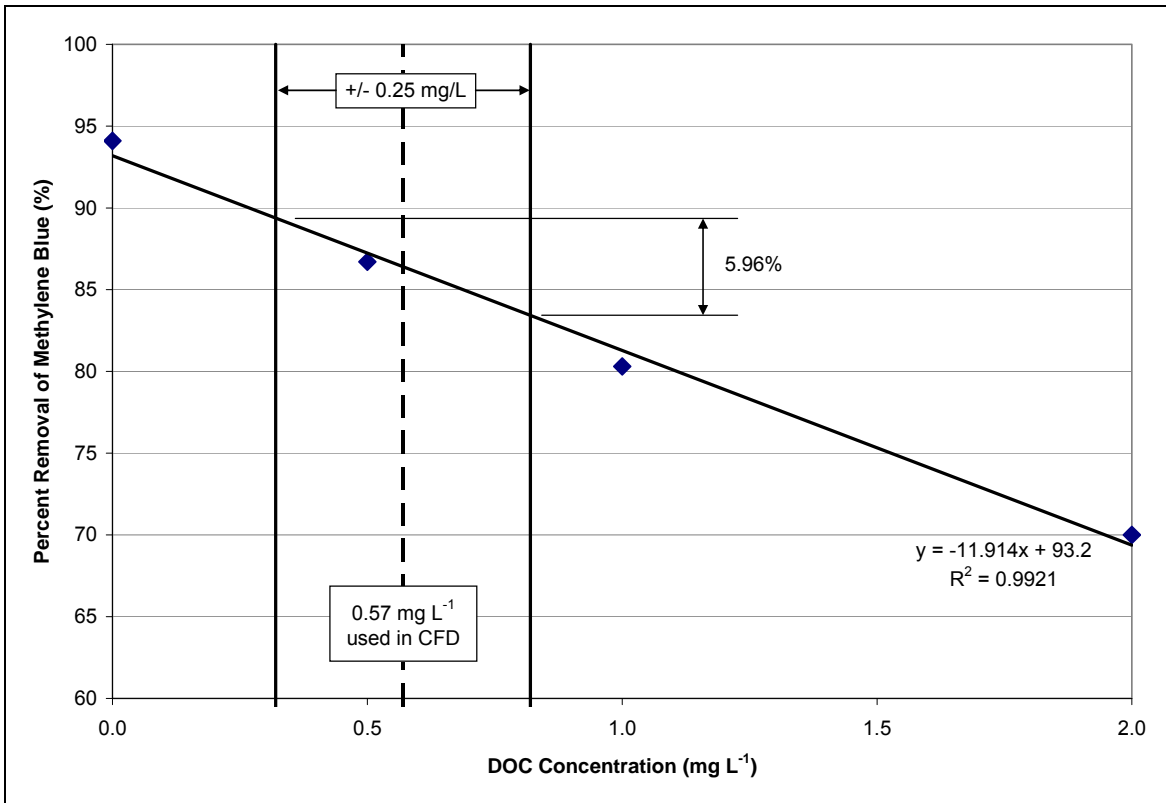


**Figure 6: Impact of DOC on Advanced Oxidation of Methylene Blue**

6. JOURNAL ARTICLE NUMBER 2

Journal Target: Journal of Environmental Engineering, ASCE

Paper Title: Selection of Appropriate Numerical Analysis Techniques for UV-  
Initiated Advanced Oxidation Processes

## **Selection of Appropriate Numerical Analysis Techniques for UV-Initiated Advanced Oxidation Processes**

Scott M. Alpert, PE <sup>(1)</sup> and Joel J. Ducoste, PhD <sup>(2)</sup>

### **ABSTRACT**

The use of ultraviolet-initiated (UV-initiated) advanced oxidation processes (AOP) is rapidly becoming an attractive alternative for the degradation of emerging organic contaminants that are not easily removed using conventional water treatment processes. Design and optimization of UV/H<sub>2</sub>O<sub>2</sub> systems typically include both system configuration (reactor design, pipe and fittings, lamp number, and lamp orientation) and chemical kinetics (reaction mechanisms and kinetic rate constants). Three numerical models were evaluated to determine which, if any, is appropriate for simulating the UV/hydrogen peroxide advanced oxidation process. Computational fluid dynamics was compared to the numerical solution of the system of ordinary differential equations describing the reaction mechanism for hydroxyl radical production and methylene blue destruction and to a UV dose distribution analysis produced by a Lagrangian particle track in CFD with a given dose-response curve. To validate the simulations, the results of the models were compared to pilot reactor trials for methylene blue. The CFD model and the UV dose distribution tended to under-predict the percent removal of methylene blue within the reactor. The solution of the differential equations assuming ideal reactor characteristics produced effluent methylene blue values closest to that of the pilot. Results suggest that numerical solutions using ideal hydraulics could be appropriate for predicting effluent results for non-complex or batch systems. Evaluation of different system designs, such as lamp or baffle placement, may require incorporation of hydrodynamic effects using CFD analysis.

**SUBJECT HEADINGS:** Numerical Models, Computational fluid dynamics technique, Fluid dynamics, Water Treatment, Oxidation

**AFFILIATIONS:**

- (1) PhD Candidate  
Department of Civil, Construction, and Environmental Engineering  
North Carolina State University  
Mann Hall, Box 7908  
Raleigh, North Carolina 27695  
Phone: 704-608-3796  
Email: [smalpert@gmail.com](mailto:smalpert@gmail.com)
  
- (2) Associate Professor  
Civil, Construction and Environmental Engineering  
North Carolina State University  
Mann Hall 319c, Box 7908  
Raleigh, North Carolina 27695  
Phone: 919-515-8150  
Fax: 919-515-7908  
Email: [jducoste@eos.ncsu.edu](mailto:jducoste@eos.ncsu.edu)

**INTRODUCTION**

The use of ultraviolet-initiated (UV-initiated) advanced oxidation processes (AOP) is becoming an attractive alternative for the degradation of emerging organic contaminants that are not easily removed using conventional water treatment processes. Of the UV-initiated AOPs available, UV/hydrogen peroxide (H<sub>2</sub>O<sub>2</sub>) is one of the more promising technologies. Design and optimization of UV/H<sub>2</sub>O<sub>2</sub> systems typically include both system configuration (reactor design, pipe and fittings, lamp number, and lamp orientation) and chemical kinetics (reaction mechanisms and kinetic rate constants). While some numerical techniques have been developed for understanding the performance of these systems, these techniques are usually based on ideal hydraulics and thus are limited in their applicability for analyzing full-

scale continuous-flow UV/AOP systems incorporating both reactor design and chemical kinetics. Literature results suggest that numerical solutions using ideal hydraulics could be appropriate for predicting species concentrations for batch reactors and simple continuous flow systems that approximate plug-flow hydraulics and one-dimensional fluence rate distributions. Evaluation of more complex reactors, including the impact of reactor design characteristics such as lamp or baffle placement, may require CFD-based approaches that incorporate hydrodynamic effects and non-uniform fluence rate distributions. As a result, engineers and other water professionals need guidance in selecting the most appropriate numerical tool to use as part of the design process and in optimizing UV/AOP systems. However, no study has been performed to quantify alternative methods for modeling UV/AOP systems.

The ideal hydraulics numerical solution uses MATLAB (The MathWorks, Inc., Natick, MA) or similar software to solve the system of differential equations representing the reaction mechanism that describes the production of radical species and the degradation of the target contaminant using an average UV fluence rate value. Collimated beam and batch reactor simulations may include a fluence rate integrated across the light path with given absorption characteristics while still assuming a perfectly-mixed reactor. Since the reaction mechanisms for the degradation of organic contaminants by UV-initiated AOPs typically consist of a complex chain of fast chemical reactions, the resulting intermediates and products from these processes may be highly sensitive not only to the light distribution within the reactor but also the level of turbulence and mixing. Design factors such as upstream hydraulic configurations, internal reactor layout, and lamp arrangement, may

influence process performance. One of the objectives of this research is determine when these hydrodynamic effects need to be incorporated into a numerical model to accurately predict the results of a UV-initiated advanced oxidation process.

A significant amount of experimental research has been completed to evaluate the degradation of an organic species (parent compound) by UV-initiated advanced oxidation reactions (Sharpless and Linden, 2003; Bali et al., 2003; Devlin and Harris, 1984; Scheck and Frimmel, 1995). In other research studies, investigators have performed more detailed experiments to ascertain the reaction pathways involved in the degradation of the parent compound to its intermediate and final products (Stefan et al., 1996; Stefan et al., 2000; Alnaizy and Akgerman, 2000). The determination of these reaction pathways provides a more detailed picture of the photoreactive process and allows the development of numerical kinetic models that predict the rate of conversion of reactants to products. Detailed reaction pathways are very specific to the parent compound and chemical constituents in the water. However, once the reaction pathway is defined, researchers can combine the reaction kinetics of these UV-initiated AOPs with simulation models that describe the hydraulic and turbulent characteristics of a UV reactor system. Although Sharpless and Linden (2003) were able to develop an NDMA degradation kinetic model that predicted the results of a collimated beam study, the model equations assumed ideal mixing and could not account for the fluence rate distribution and hydrodynamic effects within a flow-through reactor. Crittenden et al. (1999) developed a rigorous kinetic model to describe UV-initiated advanced oxidation that does not require the pseudo-steady-state assumption for radical species and can account for the impact of changing pH on the species present in a completely-mixed batch reactor. The Crittenden

et al. (1999) model more accurately predicted the experimental results from an earlier study that used the pseudo-steady-state and constant pH assumption.

Zalazar et al. (2004) used a one-dimensional radiation model for UV light distribution and a reaction mass balance with the pseudo-steady-state approximation for the radical species to examine the characteristics of a batch reactor that apply to scale-up of advanced oxidation processes. Similar numerical approaches to advanced oxidation modeling by direct application of continuity of mass and momentum equations with kinetic rate models and radiative transfer equations have been undertaken by other researchers (Labas et al., 2002; Alfano et al., 2001). Martin et al. (2002) describes in detail the numerical solution of the coupled equations for mass balance of the reactive species and radiative transfer for UV light distribution for both perfectly-mixed and continuous flow annular UV reactors. Although these numerical approaches often involve complex mathematical equations that may require iterative numerical solution of partial differential equations, the results tracked well with experimental validation.

Computational Fluid Dynamics (CFD) is a technique for numerically solving the equations of fluid dynamics over both space and time, including the conservation of mass, conservation of momentum, and conservation of energy. Combined with appropriate boundary and initial conditions, these governing equations can describe both the physical and chemical changes within a reactor. A CFD model for UV systems also includes the spatial variations of fluence rate within the UV reactor. Limited studies have been performed with CFD to simulate UV/AOPs. Pareek et al. (2003) used CFD combined with a discrete-ordinate radiation transport equation for light intensity and modified  $k$ - $\epsilon$  turbulence equations

to model a heterogeneous, multi-phase photocatalytic reactor system for the photodegradation of a spent Bayer liquor. However, the applied radiation model did not incorporate refraction and was performed in a simple bench scale reactor. Mohseni and Taghipour (2004) used CFD to evaluate the heterogeneous photocatalytic oxidation of gas-phase vinyl chloride (VC) by the UV initiation of a TiO<sub>2</sub>-coated surface; however, this research did not incorporate a fluence rate model and only described the flux of VC toward the TiO<sub>2</sub>-coated surface. No research has been performed that compares the results of CFD models to ideal hydraulics and dose distribution analyses.

Typically, full-scale UV photoreactors will operate in a turbulent flow regime, and thus, CFD simulations of a UV process must incorporate the impact of turbulent mixing on any chemical reactions that occur within these UV photoreactors. The standard k- $\epsilon$  turbulence model is often used for the examination of hydraulics within a flow-through reactor and is what is incorporated into the CFD model for this research. Alpert and Ducoste (2008) demonstrated that the choice of two-equation closure models did not significantly affect the predicted degradation of methylene blue in a UV-initiated advanced oxidation reactor.

The UV fluence rate (incident radiant power) varies with distance from the lamp and as a function of the absorptive characteristics of the media through which the light passes. In advanced oxidation reactions, both the organic contaminant and hydrogen peroxide absorb UV light, reducing the transmitted fluence rate, and consequently, changing the effectiveness of hydroxyl radical production throughout the UV reactor. Other factors, such as reflection, refraction, shadowing, and lamp effects, also influence the spatial distribution of light within

a UV reactor. In this study, the RAD-LSI fluence rate model (Liu et al., 2004) is used in the CFD UV/AOP model. The RAD-LSI is a modified version of the line source integration model (Blatchley, 1997) that was enhanced to account for the physics of reflection, refraction, and absorption and provides better prediction of the fluence rate near the lamp surface using the radial model component (Liu et al., 2004).

Methylene blue is a dye that is used as the indicator organic contaminant in this study. Many organic dyes are decolorized (bleached) upon reaction with the hydroxyl radical. These dyes are good candidates for evaluation in an advanced oxidation study since the decolorization can be i) analyzed with a spectrophotometer, and ii) described by an apparent pseudo-first-order reaction rate constant. In addition, typically these dyes do not undergo direct photolysis and are not reactive with hydrogen peroxide alone. The mechanism of decolorization varies among the types of organic dyes, but, in general, these dyes contain aromatic ring structures that are subject to attack by the hydroxyl radical. The system of kinetic rate equations describing the degradation of methylene blue begins with the reaction mechanism for the production of the hydroxyl radical from hydrogen peroxide.

Three modeling approaches were compared for simulating UV-initiated advanced oxidation processes. The first, herein referred to as the ideal hydraulics approach, is the numerical solution by MATLAB of the system of ordinary differential equations (ODEs) describing the reaction mechanism for hydroxyl radical production and methylene blue destruction. The second model (CFD/Lagrangian) combined a UV dose distribution produced by a Lagrangian particle track in CFD with a dose-response curve (i.e., UV fluence versus contaminant removal) curve generated with MATLAB. The final approach utilized

CFD in an Eulerian mode (CFD/Eulerian) that included the reaction and transport of each species as part of the turbulent convective-diffusion equations.

## **MATERIALS AND EXPERIMENTAL METHODS**

For the pilot-scale experiments, dry methylene blue (Alfa Aesar, Acros Organics) and hydrogen peroxide solution (30% w/v, Fisher Scientific, Pittsburgh, PA) were used as purchased without further purification. The methylene blue and hydrogen peroxide were diluted separately with dechlorinated ultra-filtered deionized water (Dracor High Purity Water Systems) (herein referred to as DI water). Pilot influent water was pumped from a 10,000-gallon concrete reservoir filled with GAC-filtered (NORIT GAC400) municipal tap water from Raleigh, NC.

Methylene blue concentration at the pilot reactor effluent was correlated to absorption at 661 nm measured using a UV/Vis spectrophotometer (Cary 50, Varian, Inc., Walnut Creek, CA) coupled to a fiber optic spectrophotometric probe (C Technologies, Inc., Bridgewater, NJ) inserted into the reactor effluent pipe. Total chlorine concentration of the pilot reactor influent was tested using a Hach Pocket Colorimeter. Total alkalinity was measured using Standard Methods (19<sup>th</sup> Edition, 1995) Method 2320. Hydrogen peroxide residual concentrations were measured using the method described by Klassen et al. (1994). Total organic carbon (TOC) was measured by the Town of Cary (NC) water quality laboratory using a Tekmar-Dohrmann Phoenix 8000 analyzer. The pH of the water matrix for each pilot run was measured using a Thermo Orion Model 410 pH meter calibrated weekly using a two-point standard. UV transmittance at 254 nm (UVT<sub>254</sub>) was measured in

a 1-cm pathlength quartz cuvette using the Varian Cary 50 spectrophotometer zeroed with DI water.

To determine the second order rate constant for methylene blue, a competition kinetics method described by Rosenfeldt and Linden (2004) was used. In this method, known concentrations of isopropyl alcohol (IPA) were used as a radical scavenger within UV-exposed crystallization dishes of methylene blue and hydrogen peroxide under a collimated beam apparatus.

A schematic of the low-pressure UV pilot scale system is presented in Figure 1. A 6"-diameter cylindrical stainless steel UV reactor was donated by Degremont's North American Research and Development Center (DENARD). A single low-pressure high-output UV lamp (Ondeo Degremont, No. 61645-G01, 52W nameplate output at 254 nm) was installed axially along the 6'-long reactor. Five removable perforated baffle plates were installed symmetrically about the center of the reactor. Sampling valves were installed within three feet of the influent and effluent of the reactor. Two ball valves located upstream and downstream of the reactor were used to throttle flow between 5 and 50 gallons per minute. Two diffuser mechanisms were installed upstream of the reactor through which methylene blue and hydrogen peroxide solutions were injected into the system. Flow rates of the contaminant and hydrogen peroxide solutions were controlled by peristaltic pumps. The diffusers were located immediately downstream of the flow regulating valve, the turbulence from which provided additional mixing of the chemicals prior to the reactor influent. Similar to the CFD models, the pilot system was used to measure methylene blue degradation with five internal baffles and with one internal baffle in the UV reactor.

## NUMERICAL METHODS

A three-dimensional solid model of the UV reactor used in the pilot experiments was created in AutoCAD 2004 (Autodesk, Inc., San Rafael, CA). This model included geometric elements for the reactor, inlet and outlet piping, the UV lamp/quartz sleeve assembly with wiper mechanism, five internal baffle plates, and the inlet and outlet planes. All dimensions were measured directly on the pilot reactor and translated as full-scale into the AutoCAD model. Each of the elements was then saved as an ASCII-type stereolithographic file (extension .stl) and imported into the CFD software.

The CFD software package PHOENICS (CHAM, Ltd, Wimbledon, England) was used since it allows changes to the source code to incorporate numerical descriptions of physics and chemistry that are specific to a given problem. In this research, the simulation of a photoreacting chemical species required the solution of the continuity equation, Reynolds-averaged Navier Stokes (NS) equations, and scalar convective-diffusion transport equations. For an incompressible fluid, the equation for the conservation mass, or the continuity equation, can be written as shown in Equation 1.

$$\frac{\partial u_x}{\partial x} + \frac{\partial u_y}{\partial y} + \frac{\partial u_z}{\partial z} = 0 \quad (1)$$

In Equation 1,  $u_x$ ,  $u_y$ , and  $u_z$  are the velocity components in the x, y, and z directions, respectively. The conservation of momentum equations for turbulent flow are expressed for

incompressible flow and no free surface (no gravity term) as the Reynolds-averaged Navier-Stokes equation (Clark, 1996) described in Equation 2:

$$\rho \frac{\partial \bar{U}_i}{\partial t} + \rho \bar{U}_k \frac{\partial \bar{U}_i}{\partial x_k} = -\frac{\partial \bar{p}}{\partial x_i} + \mu \frac{\partial^2 \bar{U}_i}{\partial x_j \partial x_j} - \rho \frac{\partial}{\partial x_j} (\overline{u'_i u'_j}) \quad (2)$$

where  $\rho$  is the fluid density,  $\bar{U}_i$  is the average velocity in the  $i$ -th direction,  $t$  is time,  $\bar{p}$  is the average pressure,  $\mu$  is the absolute viscosity, and  $u'_i$  is the fluctuating component of velocity in the  $i$ -th direction. The last term on the right side of Equation 2, representing the Reynolds stresses, creates the closure problem for turbulence since it introduces additional unknowns that outnumber the equations available for solution. In this study, two-equation turbulence models were included to complete the hydrodynamic evaluation.

The reactive turbulent convective-diffusion equations for species transport are shown in Equation 3 (Liu and Ducoste, 2006).

$$\frac{\partial C_i}{\partial t} + U_j \frac{\partial C_i}{\partial x_j} = \frac{\partial}{\partial x_j} \left( (D + D_T) \frac{\partial C_i}{\partial x_j} \right) + R_i \quad (3)$$

where  $C_i$  is the average concentration of species  $i$ ,  $U$  is the mean velocity,  $D$  is the molecular diffusivity coefficient,  $R_i$  is the reaction term for species  $i$ , and  $D_T$  is the turbulent diffusivity that is defined as,

$$D_T = \frac{v_T}{Sc_T}. \quad (4)$$

In Equation 4,  $Sc_T$  is the turbulent Schmidt number and  $v_T$  is the turbulent eddy viscosity.

The  $D_T \left( \frac{\partial C_i}{\partial x_j} \right)$  term in Equation 3 models the effects of the turbulent fluctuations of the concentration and velocity. In this research, the reactions describing the advanced oxidation process were used in the turbulent convective-diffusion equation to describe the reactive transport of each species throughout the flow domain.

Appropriate boundary conditions for inlet and outlet velocities, pressures, and turbulence conditions were selected to correspond to the experimental conditions evaluated in this study and are shown in Table 1. Since PHOENICS uses a structured rectangular grid, grid cells were created manually by selecting the number of intervals in the x-, y-, and z-directions for each region within the solution domain. The CFD solutions were tested for grid-independence (i.e., effluent concentrations are not a function of grid density) and the final grid contained a total of 859,154 cells. For this simulation, finer grid cells were created within the reactor and in areas within which sharp changes in velocity, pressure, and/or chemistry are expected. Graphical representations of the geometry within CFD and the grid spacing are shown in Figures 2 through 5. For the CFD models completed in this study, the results were considered converged when the net sum of the differences between the inlet and outlet volume fractions (i.e., conservation of mass) was on the order of  $10^{-3}$  or below.

The standard k-ε turbulence closure model used in this study was proposed by Launder and Sharma (1974) (as cited in Wilcox 2004) to solve the turbulence stress closure problem. The equations for this turbulence model were included within the PHOENICS library and selected through a user interface menu. This model, as described by Wilcox (2004), is shown in Equations 5 - 9 and the variables are defined in Table 2:

$$v_T = \frac{C_\mu k^2}{\varepsilon} \quad (5)$$

$$\frac{\partial k}{\partial t} + U_j \frac{\partial k}{\partial x_j} = \tau_{ij} \frac{\partial U_i}{\partial x_j} - \varepsilon + \frac{\partial}{\partial x_j} \left[ \left( \nu + \frac{v_T}{\sigma_k} \right) \frac{\partial k}{\partial x_j} \right] \quad (6)$$

$$\frac{\partial \varepsilon}{\partial t} + U_j \frac{\partial \varepsilon}{\partial x_j} = C_{\varepsilon 1} \frac{\varepsilon}{k} \tau_{ij} \frac{\partial U_i}{\partial x_j} - C_{\varepsilon 2} \frac{\varepsilon^2}{k} + \frac{\partial}{\partial x_j} \left[ \left( \nu + \frac{v_T}{\sigma_\varepsilon} \right) \frac{\partial \varepsilon}{\partial x_j} \right] \quad (7)$$

$$C_{\varepsilon 1}=1.44, \quad C_{\varepsilon 2}=1.92, \quad C_\mu=0.09, \quad \sigma_k=1.0, \quad \sigma_\varepsilon=1.3 \quad (8)$$

$$\omega = \frac{\varepsilon}{C_\mu k} \quad l = \frac{C_\mu k^{3/2}}{\varepsilon} \quad (9)$$

The spatial variation of light inside the reactor (i.e., the fluence rate characterization) was simulated using the RAD-LSI model (Liu et al., 2004). The RAD-LSI is a modified version of the line source integration model (Blatchley, 1997) that was enhanced to account

for the physics of reflection, refraction, and absorption and provides better prediction of the fluence rate near the lamp surface using the radial model component (Liu et al., 2004). The RAD-LSI model is represented by Equations 10 and 11.

$$E'(r, h) = \min \left\{ \frac{P_\lambda}{2\pi Lr}, \frac{P_\lambda}{4\pi Lr} \left[ \arctan \left( \frac{L/2 + h}{r} \right) + \arctan \left( \frac{L/2 - h}{r} \right) \right] \right\} \times (\text{atten factor}) \quad (10)$$

$$(\text{atten factor}) = \sum_{k=1}^n (1 - R_{1,k}) (1 - R_{2,k}) \frac{\frac{P/n}{4\pi(d_{1,k} + d_{2,k} + d_{3,k})^2} T_w^{d_{3,k}/0.01} T_q^{d_{2,k}/0.01}}{\sum_{k=1}^n \frac{P/n}{4\pi(r_k^2 + h_k^2)}} \quad (11)$$

In these equations,  $E'(r, h)$  is the fluence rate at a point in the reactor with normal (perpendicular) distance  $r$  to the lamp axis and longitudinal distance  $h$  to the lamp center,  $P_\lambda$  is the radiant power at wavelength  $\lambda$  uniformly emitted in all directions by the point source,  $L$  is the total length of the lamp,  $R_1$  is the reflectance factor for the air/quartz interface,  $R_2$  is the reflectance factor for the quartz/water interface,  $T_w$  is the 10-mm path length transmittance of the water,  $T_q$  is the 10-mm path length transmittance of the quartz,  $d_1$  is the path length in the air,  $d_2$  is the path length in the quartz,  $d_3$  is the path length in the water, and  $n$  is the number of points used to describe the lamp. These variables are shown graphically in Figure 6.

In Figure 6, the normal distance between the lamp centerline to the inner edge of the quartz sleeve is defined as  $r_1$ , the thickness of the quartz sleeve is  $r_2$ , and the normal distance

from the outer edge of the quartz sleeve to the point of interest is  $r_3$ . Using these terms and the incident angles shown in Figure 6, the distance  $h_k$  can be defined as shown in Equation 12 (Liu et al., 2004).

$$h_k = r_{1,k} \tan \theta_1 + r_{2,k} \tan \theta_2 + r_{3,k} \tan \theta_3 \quad (12)$$

From Snell's Law, all of the angles in Equation 2-35 can be expressed in terms of a single angle as shown in Equations 13 and 14 (Liu et al., 2004).

$$\theta_2 = \sin^{-1} \left( \frac{n_a}{n_q} \sin \theta_1 \right) \quad (13)$$

$$\theta_3 = \sin^{-1} \left( \frac{n_a}{n_w} \sin \theta_1 \right) \quad (14)$$

In equations 13 and 14,  $n_a$ ,  $n_q$ , and  $n_w$  are the refractive indices for air, quartz, and water, respectively. The path lengths  $d_1$ ,  $d_2$ , and  $d_3$  in the RAD-LSI equations are determined using trigonometry and previously defined variables as shown in Equations 15, 16, and 17.

$$d_1 = \frac{r_1}{\cos \theta_1} \quad (15)$$

$$d_2 = \frac{r_2}{\cos \theta_2} \quad (16)$$

$$d_3 = \frac{r_3}{\cos \theta_3} \quad (17)$$

The FORTRAN code for this model had been previously written by others and was modified as appropriate for the lamp characteristics and orientation being evaluated in this research.

The CFD/Eulerian codes (consisting of the PHOENICS q1 text file and the PHOENICS Ground FORTRAN file) were developed as a series of three separate models for each design condition. The first model created the pressure and velocity vector distribution within the system and included the turbulence model and its corresponding equation parameters ( $k$ ,  $\epsilon$ , etc.). The second model used the output of the first and added the fluence rate distribution throughout the reactor. The third model incorporated the output of the second and solved all of the appropriate kinetic rate equations describing the reactions occurring in the reactor.

The system of kinetic rate equations describing the production of the hydroxyl radical from hydrogen peroxide and the corresponding degradation of methylene blue is shown in Table 3. Table 4 contains additional rate equations for the scavenging of the hydroxyl radical by compounds in the background water matrix. In Tables 3 and 4,  $\Phi_{H_2O_2}$  is the quantum yield for the photolysis of hydrogen peroxide (moles  $H_2O_2$  per mole photons, or moles  $H_2O_2$  per einstein) and  $\epsilon_{H_2O_2}$  is the molar absorptivity of hydrogen peroxide ( $L \text{ mol}^{-1} \text{ cm}^{-1}$ ). The square brackets  $[\ ]$  represent the molar concentration of the species enclosed in the brackets. The term  $E'_{CFD}$  is the irradiance (UV@254 nm) at each individual grid cell centerpoint in the

CFD domain. Since the light distribution models result in an irradiance term in units of  $\text{W m}^{-2}$ , a unit conversion is necessary for the  $r_{UV}$  term. Noting that the variable  $I_{UV}$  is used within the CFD code to represent the irradiance at each grid location, the term  $E'_{CFD}$  can be defined as shown in Table 3. Using this definition,  $r_{UV}$  has units of  $\text{moles L}^{-1} \text{s}^{-1}$ .

To improve convergence within the CFD code, two modifications to the equations have been made (and are included in this section for completeness). The first is that the four species being tracked (methylene blue, hydrogen peroxide, the hydroxyl radical, and the superoxide radical) are normalized to initial conditions. The normalization of the species concentrations is shown in Table 5, in which the subscript “0” indicates the initial concentration of the species entering the UV reactor and the asterisk superscript indicates the normalized species.

The second modification is that, since the lifetimes of the two radical species are very short, pseudo-steady-state conditions for the two radicals are assumed. The derivation of the pseudo-steady-state equations for the hydroxyl radical begins with a composite equation (Equation 18) describing all reactions that produce or consume the radical, including dissolved organic carbon (DOC), alkalinity (assumed to be dominated by the bicarbonate ion), and chlorine as radical scavengers in the background water matrix. The values of the kinetic rate constants are as reported in Table 3.

$$\begin{aligned}
\frac{d[\bullet OH]}{dt} = & 2\Phi_{H_2O_2} \varepsilon_{H_2O_2} [H_2O_2] E'_{CFD} - k_1 [H_2O_2][\bullet OH] \\
& + k_2 [H_2O_2][\bullet O_2^-] - k_3 [\bullet OH][\bullet OH] - k_4 [\bullet OH][\bullet O_2^-] \\
& - k_{MB, \bullet OH} [\bullet OH][MB] - k_{DOC, \bullet OH} [\bullet OH](DOC) \\
& - k_{HCO_3^-, \bullet OH} [\bullet OH][HCO_3^-] - k_{NH_2Cl, \bullet OH} [\bullet OH][NH_2Cl] \\
& - k_{OCl^-, \bullet OH} [\bullet OH][OCl^-] - k_{HOCl, \bullet OH} [\bullet OH][HOCl]
\end{aligned} \tag{18}$$

This equation may also be normalized as discussed before. Substituting the variables defined in Table 5 into Equation 18 and dividing through by the initial concentration of hydrogen peroxide  $[H_2O_2]_0$  results in Equation 19.

$$\begin{aligned}
\frac{d[\bullet OH]^*}{dt} = & 2\Phi_{H_2O_2} \varepsilon_{H_2O_2} [H_2O_2]^* E'_{CFD} - k_1 [H_2O_2]^* [\bullet OH]^* [H_2O_2]_0 \\
& + k_2 [H_2O_2]^* [\bullet O_2^-]^* [H_2O_2]_0 - k_3 [\bullet OH]^* [\bullet OH]^* [H_2O_2]_0 \\
& - k_4 [\bullet OH]^* [\bullet O_2^-]^* [H_2O_2]_0 - k_{MB, \bullet OH} [\bullet OH]^* [MB]^* [MB]_0 \\
& - k_{DOC, \bullet OH} [\bullet OH]^* (DOC) - k_{HCO_3^-, \bullet OH} [\bullet OH]^* [HCO_3^-] \\
& - k_{NH_2Cl, \bullet OH} [\bullet OH]^* [NH_2Cl] - k_{OCl^-, \bullet OH} [\bullet OH]^* [OCl^-] \\
& - k_{HOCl, \bullet OH} [\bullet OH]^* [HOCl]
\end{aligned} \tag{19}$$

For the pseudo-steady-state assumption, the time rate change of  $[\bullet OH]^*$  is set equal to zero, and the equation solved for  $[\bullet OH]^*$ , which can then be identified as  $[\bullet OH]_{SS}^*$  as shown in Equation 20. In anticipation of performing the same pseudo-steady-state analysis for the superoxide radical, the term  $[\bullet O_2^-]^*$  will now be identified as  $[\bullet O_2^-]_{SS}^*$ .

$$\begin{aligned}
0 = & -k_3 [H_2O_2]_0 \left( [\cdot OH]_{SS}^* \right)^2 + [\cdot OH]_{SS}^* \left\{ -k_1 [H_2O_2]^* [H_2O_2]_0 - k_4 [\cdot O_2^-]_{SS}^* [H_2O_2]_0 \right. \\
& -k_{MB, \cdot OH} [MB]^* [MB]_0 - k_{DOC, \cdot OH} (DOC) - k_{HCO_3^-, \cdot OH} [HCO_3^-] - k_{NH_2Cl, \cdot OH} [NH_2Cl] \\
& -k_{OCl^-, \cdot OH} [OCl^-] - k_{HOCl, \cdot OH} [HOCl] \left. \right\} + 2\Phi_{H_2O_2} \varepsilon_{H_2O_2} [H_2O_2]^* E'_{CFD} \\
& + k_2 [H_2O_2]^* [\cdot O_2^-]_{SS}^* [H_2O_2]_0
\end{aligned} \tag{20}$$

Equation 20 can be solved using the quadratic equation where,

$$A = -k_3 [H_2O_2]_0 \tag{21}$$

$$\begin{aligned}
B = & -k_1 [H_2O_2]^* [H_2O_2]_0 - k_4 [\cdot O_2^-]_{SS}^* [H_2O_2]_0 - k_{MB, \cdot OH} [MB]^* [MB]_0 \\
& -k_{DOC, \cdot OH} (DOC) - k_{HCO_3^-, \cdot OH} [HCO_3^-] - k_{NH_2Cl, \cdot OH} [NH_2Cl] \\
& -k_{OCl^-, \cdot OH} [OCl^-] - k_{HOCl, \cdot OH} [HOCl]
\end{aligned} \tag{22}$$

$$C = 2\Phi_{H_2O_2} \varepsilon_{H_2O_2} [H_2O_2]^* E'_{CFD} + k_2 [H_2O_2]^* [\cdot O_2^-]_{SS}^* [H_2O_2]_0 \tag{23}$$

And

$$[\cdot OH]_{SS}^* = \frac{-B \pm \sqrt{B^2 - 4AC}}{2A} \tag{24}$$

In Equation 24, the variable  $[\bullet OH]_{SS}^*$  now represents the normalized pseudo-steady-state concentration of the hydroxyl radical. A similar process can be followed for the superoxide radical.

$$\frac{d[\bullet O_2^-]}{dt} = k_1 [H_2O_2][\bullet OH] - k_2 [H_2O_2][\bullet O_2^-] - k_4 [\bullet OH][\bullet O_2^-] \quad (25)$$

Again, substituting the variables defined in Table 5 into Equation 25 and dividing through by the initial concentration of hydrogen peroxide  $[H_2O_2]_0$  results in Equation 26.

$$[\bullet O_2^-]_{SS}^* = \frac{k_1 [H_2O_2]^* [\bullet OH]_{SS}^*}{k_2 [H_2O_2]^* + k_4 [\bullet OH]_{SS}^*} \quad (26)$$

Finally, equations for the time rate of change of hydrogen peroxide and methylene blue (or other target contaminant) can be derived and are shown in Equations 27 and 28, respectively.

$$\begin{aligned} \frac{d[H_2O_2]}{dt} = & -\Phi_{H_2O_2} E'_{CFD} \epsilon_{H_2O_2} [H_2O_2] - k_1 [H_2O_2][\bullet OH] \\ & - k_2 [H_2O_2][\bullet O_2^-] + k_3 [\bullet OH][\bullet OH] \end{aligned} \quad (27)$$

$$\frac{d[MB]}{dt} = -k_{MB} [MB][\bullet OH] - \Phi_{MB} E'_{CFD} \epsilon_{MB} [MB] \quad (28)$$

The second term on the right-hand-side of Equation 28 represents the direct photolysis component (if any) for the degradation of the organic contaminant, which in the case of methylene blue the variable  $\Phi_{MB}$  is set equal to zero. Substituting the normalized variables and simplifying results in Equations 29 and 30.

$$\begin{aligned} \frac{d[H_2O_2]^*}{dt} = & -\Phi_{H_2O_2} E'_{CFD} \varepsilon_{H_2O_2} [H_2O_2]^* - k_1 [H_2O_2]^* [\bullet OH]_{SS}^* [H_2O_2]_0 \\ & -k_2 [H_2O_2]^* [\bullet O_2^-]_{SS}^* [H_2O_2]_0 + k_3 [\bullet OH]_{SS}^* [\bullet OH]_{SS}^* [H_2O_2]_0 \end{aligned} \quad (29)$$

$$\frac{d[MB]^*}{dt} = -k_{MB} [MB]^* [\bullet OH]_{SS}^* [H_2O_2]_0 - \Phi_{MB} E'_{CFD} \varepsilon_{MB} [MB]^* \quad (30)$$

In addition to using the kinetic model as part of the CFD/Eulerian solution, the rate equations were coded into MATLAB and solved using the built-in ODE solvers that are included with the software. The irradiance value required in the equations was calculated as a volumetric average generated by discretizing the reactor in the radial and length-wise directions and using the lamp output power, UV transmittance, and a simplified RAD-LSI equation. The results of this ideal hydraulics approach consisted of the effluent concentrations of the modeled species described as a function of time. The effluent concentrations were considered as those corresponding to the theoretical hydraulic residence time calculated using the reactor volume and flow rate (i.e., a plug-flow assumption). Other hydraulic profiles could be used as appropriate; however, the simplest case was assumed here.

As the third numerical evaluation, UV dose distributions specific to reactor operating conditions were created and used to evaluate methylene blue degradation. This dose distribution was combined with UV dose-response data for comparable reaction conditions (including hydrogen peroxide dose) to calculate overall methylene blue removal in the reactor. The UV dose-response data was generated by solving the kinetic rate equations in MATLAB. This data is shown graphically in Figure 7 for a molar ratio of hydrogen peroxide to methylene blue equal to 150. The numerical value of  $\frac{C}{C_0} \left( = \frac{[MB]}{[MB]_0} \right)$  for each UV dose was imported into Microsoft® Office Excel 2003 and later used with a VLOOKUP command to find the removal associated with each discrete value within the dose distribution.

The fluence rate distribution CFD code previously solved for one of the research conditions (Q = 20 GPM, P = 26.5 W output at 254 nm) was modified to incorporate the PHOENICS particle track solver GENTRA. Although only one lamp was used in the pilot reactor, a dose distribution curve for a second output lamp power (100W) was also generated to examine the results at theoretically higher methylene blue removal rates. The CFD particle track models, also known as Lagrangian models, used within PHOENICS are discussed in detail in Ducoste et al. (2005), which is summarized herein.

The Lagrangian approach centers on equations that describe the evolution of position within a flow field. According to Ducoste et al. (2005), particle position is determined by solving Equation 31 where  $X_p$  is the particle position and  $U_p$  is the instantaneous particle velocity.

$$\frac{dX_p}{dt} = U_p \quad (31)$$

In this equation,  $U_p$  is equal to the mean velocity component plus a turbulent fluctuating velocity component. The velocity of a particle of mass  $m_p$  is determined from the particle momentum equation, which, for acceleration due to gravity  $g$  and neglecting buoyancy effects, is shown in Equation 32 (Ducoste et al., 2005). The drag function  $D_p$  used in Equation 32 is described in Equation 33.

$$m_p \frac{du_p}{dt} = D_p (u - u_p) + m_p g \quad (32)$$

$$D_p = 0.5 \rho A_p C_D |u - u_p| \quad (33)$$

In Equation 33,  $A_p$  is the particle projected area defined in Equation 34,  $C_D$  is the drag coefficient defined in Equation 35 (Ducoste et al., 2005), and  $Re$  is the particle Reynolds number.

$$A_p = \frac{\pi d_p^2}{4} \quad (34)$$

$$C_D = \frac{24}{Re} (1 + 0.15 Re^{0.687}) + \frac{0.42}{1 + (4.25 \times 10^4 Re^{-1.16})} \quad (35)$$

The particle momentum equation is based on the carrier phase instantaneous velocity  $u$  that is the sum of the mean and fluctuating components. The mean velocity is determined using the hydrodynamic and turbulence models described previously. The turbulent fluctuating velocity is calculated by assuming that each instantaneous velocity component follows a Gaussian distribution with a mean of zero and a standard deviation  $\sigma = \sqrt{\frac{2k}{3}}$  (Ducoste et al., 2005). A random number generator based on this distribution, mean, and standard deviation is then used to determine the sign and magnitude of the fluctuating velocity component. Particle motion can also be calculated using other methods such as the random-walk algorithm (RWA).

In the Lagrangian particle-tracking method, random fluctuations are caused by particle interactions with turbulent eddies in the flow field (Shirokar et al., 1996). The interaction time between a particle and a turbulent eddy is determined by the condition that either the particle moves sufficiently slow relative to the carrier phase to remain within the eddy throughout the eddy's lifetime ( $t_{eddy}$ ) or the velocity difference between the carrier phase and particle is sufficient to traverse the eddy in a transit time ( $t_{tr}$ ) that is shorter than the eddy lifetime. The overall interaction time scale is then determined as defined by Equations 36 – 39 (Ducoste et al., 2005).

$$t_{in} = \text{minimum}(t_{eddy}, t_{tr}, t_{user}) \quad (36)$$

$$t_{eddy} = \sqrt{\frac{3}{2}} C_{\mu}^{0.75} \frac{k}{\varepsilon} \quad (37)$$

$$t_{tr} = \frac{C_{\mu}^{0.75} k^{1.5}}{|u - u_p| \varepsilon} \quad (38)$$

$$t_{user} = \text{user defined minimum computational cell crossing time} \\ = (\text{minimum time steps per cell}) \times \left( \frac{\text{minimum cell dimension}}{\text{maximum velocity component through cell}} \right) \quad (39)$$

A new random number will be generated to compute the carrier phase instantaneous velocity in the particle momentum equation only when the particle has traversed the eddy or has spent more time than the eddy lifetime.

The UV fluence as seen by each particle is calculated by integrating the fluence rate over the particle track time history using Equation 40 (Ducoste et al., 2005) in which *Fluence* (*P*) is the UV dose for a particle *P* (J m<sup>-2</sup> or mJ cm<sup>-2</sup>) and *I*(*t*) is the UV fluence rate (W m<sup>-2</sup> or mW cm<sup>-2</sup>).

$$Fluence(P) = \int_0^T I(t)dt \cong \sum I \Delta t \quad (40)$$

In a Lagrangian particle-track simulation, a spatial homogeneous concentration of particles is released at the UV system influent. Sufficient number of particles should be incorporated (e.g., greater than 1500 particles) to assure a stable particle fluence distribution. Similar to establishing a grid-independent CFD solution, the predicted fluence distribution should not be a function of the number of particles released at the inlet. Significantly higher

particle concentrations may be necessary for reactor designs that have major recirculation zones within the reactor. Particles released at the influent may be trapped within these recirculation zones and may not reach the reactor outlet. Particles should be released at least 10 pipe diameters ahead of the UV reactor inlet to allow for adequate mixing with the flow stream. A reduction in the number of pipe diameters upstream for releasing the particles can be achieved if an accurate description of the velocity and turbulent profile at the specific inlet location is provided. For the 26W and 100W distributions, the total number of particles in the reactor effluent equaled 4,648 and 4,652, respectively.

Particles can take any one of an infinite number of paths through a UV reactor. Thus, the delivered UV fluence will be comprise a range of values that are a function of the particle paths and spatial variations in UV fluence rate throughout the reactor resulting from water quality conditions affecting UV absorbance, lamp placement and spacing in the reactor, lamp power, and other non-idealities in a treatment system. For the Lagrangian method, the fluence distribution was computed by separating the fluence value from each particle path into discrete bins each representing a smaller finite range of fluence values. The results were then reported as a frequency function that represents the fraction of the total number of particles released in the reactor influent.

With the UV dose distributions available, a segregated flow approach that matched up the individual dose values with corresponding methylene blue removal values was used to calculate the overall removal percentage predicted by the dose distributions. The probability  $p_i$  of any given dose  $i$  was calculated using the number of particles recorded in the distribution receiving dose  $i$  ( $x_i$ ) as shown in Equation 41.

$$p_i = \frac{x_i}{\sum x_i} \quad (41)$$

The fraction of methylene blue remaining associated with each UV dose  $\left(\frac{C}{C_0}\right)_i$  was determined using the dose response curves previously determined with MATLAB. The total fraction expected at the reactor effluent was then calculated using Equation 42.

$$\left(\frac{C}{C_0}\right)_{Final} = \sum_i \left\{ p_i \times \left(\frac{C}{C_0}\right)_i \right\} \quad (42)$$

The total contaminant percent removal was reported as shown in Equation 43.

$$\text{Total Percent Removal} = \left( 1 - \left(\frac{C}{C_0}\right)_{Final} \right) \times 100\% \quad (43)$$

## RESULTS AND DISCUSSION

The resulting dose distributions for the two lamp output powers are shown in Figure 8. The dose distribution for the 100W case is much flatter than that of the 26W case. This difference is quantified in the standard deviations reported for each and may be explained by the performance of UV reactors with non-ideal hydraulics being a non-linear function of lamp power (Wright and Lawryshyn, 2000). In both cases, the delivered UV dose clearly

departs from ideal plug-flow conditions and a larger variance is expected with increasing lamp power (or lower flow conditions). The results of the CFD/MATLAB/Lagrangian analyses for the two cases are summarized in Table 6 and Figure 9.

For the  $P = 26.5$  W case, the dose distribution produced a result that was lower than the CFD case and farther from the result of the pilot trial. The ideal plug-flow assumption used in the MATLAB model resulted in a value closest to that achieved in the pilot reactor. Except for the value produced by the CFD/MATLAB/Lagrangian (Average Dose) approach, the trends for the theoretical 100W lamp were the same as with the 26.5 W case. CFD produced a value lower than that of the ideal hydraulics solution. The CFD/MATLAB/Lagrangian (Segregated Dose Summation) approach resulted in a value lower than that of CFD/Eulerian.

Although the differences in results of the three modeling options would appear significant on a log-scale that would be used, for example, for microbial inactivation regulations, most limits for organic contaminants are (and likely will continue to be) based on effluent concentration criteria (i.e., maximum contaminant limits, MCLs). As an example, the herbicide atrazine can be considered. The U.S. Environmental Protection Agency (EPA) has set an MCL of  $3 \mu\text{g L}^{-1}$  for atrazine. If a contaminated water had an initial atrazine concentration of  $10 \mu\text{g L}^{-1}$ , the treatment system would only need to provide 70% removal. Thus, the difference in the results of the three models would be insignificant, as shown in Table 7.

The three numerical models presented in this study (ideal hydraulics, CFD/Eulerian, and CFD/MATLAB/Lagrangian) each have their advantages as tools for designing and

optimizing UV/AOP systems. Numerical solutions using ideal hydraulics are certainly the most expedient of the methods and could be appropriate for predicting species concentrations for batch reactors and simple continuous flow systems that approximate plug-flow hydraulics and one-dimensional fluence rate distributions. As shown in Table 7, this approach may also be valuable in initial determination of compliance with MCLs. Evaluation of more complex reactors, including the impact of reactor design characteristics such as lamp or baffle placement, may require CFD-based approaches that can incorporate hydrodynamic effects and non-uniform fluence rate distributions. The choice of numerical methods depends ultimately on the goal of the simulation and known information. Table 8 summarizes the input and output of each of the methods discussed in this research. The current research evaluated only one pilot reactor with a single low-pressure lamp. Further studies with more complex reactors are required to determine the differences in CFD and ideal reactor simulations.

## **CONCLUSIONS**

Several conclusions can be drawn from this research on numerical methods to model UV-initiated advanced oxidation systems.

- For the evaluation of UV/AOP systems, at least three numerical approaches are valid, including the solution of the kinetic rate equations assuming ideal hydraulics and average fluent rate values, CFD operating in an Eulerian mode, and CFD particle-tracking (Lagrangian) combined with a dose-response curve.

- The ideal hydraulics solution uses an ODE solver, such as MATLAB, and an average UV fluence rate to solve the equations that describe the reaction mechanism for production of the hydroxyl radical and destruction of the target contaminant.
- The CFD/Eulerian method uses a dimensionally-correct 3D (or 2D) simulation of the UV/AOP system to solve the hydrodynamics/turbulence, fluence rate distribution, and chemical kinetics of the system under a specific set of operating conditions.
- The CFD/Lagrangian method combines a CFD particle track estimation of the UV fluence distribution with a theoretical or experimentally determined dose response characterizing UV fluence, hydrogen peroxide concentration, and contaminant destruction.
- The choice of numerical methods depends on the ultimate goal of the simulation and known information. If reactor design (lamp locations, baffle placement, etc.) is the goal and several designs will be compared for effluent concentrations, headloss across the reactor, static velocity zones, dark zones, and optimization of reactor dimensions, then the CFD/Eulerian method is the most appropriate tool.
- If UV fluence (dose) of an existing reactor is known (e.g., from previous bioassay RED analysis) and the goal is to determine contaminant degradation under different hydrogen peroxide concentrations or in a batch reactor, then a

ideal hydraulics solution using MATLAB to solve the kinetic rate equations should suffice.

- If the influence of various lamp powers and lamp locations on contaminant destruction is being studied, the CFD/Lagrangian method may be the best choice.

### **ACKNOWLEDGEMENTS**

The authors would like to acknowledge the American Water Works Association Research Foundation for the funding of this project.

## REFERENCES

- Alfano, O. M., Brandi, R. J., & Cassano, A. E. (2001). Degradation Kinetics of 2,4-D in Water Employing Hydrogen Peroxide and UV Radiation. *Chemical Engineering Journal*, 82, 209-218.
- Alnaizy, R., & Akgerman, A. (2000). Advanced Oxidation of Phenolic Compounds. *Advances in Environmental Research*, 4(3), 233-244.
- Alpert, S. M., & Ducoste, J. J. (2008). *Model Parameter Sensitivity for CFD Modeling of the UV/Hydrogen Peroxide Advanced Oxidation Process*. Manuscript in preparation.
- Bali, U., Catalkaya, E. C., & Sengul, F. (2003). Photochemical Degradation and Mineralization of Phenol: A Comparative Study. *Journal of Environmental Science and Health, Part A-Toxic/Hazardous Substances & Environmental Engineering*, A38(10), 2259-2275.
- Blatchley, E. R., III. (1997). Numerical Modelling of UV Intensity: Application to Collimated-Beam Reactors and Continuous-Flow Systems. *Water Research*, 31(9), 2205-2218.
- Crittenden, J. C., Hu, S., Hand, D. W., & Green, S. A. (1999). A Kinetic Model for H<sub>2</sub>O<sub>2</sub>/UV Process in a Completely Mixed Batch Reactor. *Wat. Res.*, 33(10), 2315-2328.
- Devlin, H. R., & Harris, I. J. (1984). Mechanism of the Oxidation of Aqueous Phenol with Dissolved Oxygen. *Ind. Eng. Chem. Fundam.*, 23(4), 387-392.
- Ducoste, J., Liu, D., & Linden, K. G. (2005). Alternative Approaches to Modeling Fluence Distribution and Microbial Inactivation in Ultraviolet Reactors: Lagrangian versus Eulerian. *Journal of Environmental Engineering*, 1393-1403.

- Klassen, N. V., Marchington, D., & McGowan, H. C. E. (1994). H<sub>2</sub>O<sub>2</sub> Determination by the I<sub>3</sub><sup>-</sup> Method and by KMnO<sub>4</sub> Titration. *Analytical Chemistry*, 66(18), 2921-2925.
- Labas, M. D., Zalazar, C. S., Brandi, R. J., Martin, C. A., & Cassano, A. E. (2002). Scaling Up of a Photoreactor for Formic Acid Degradation Employing Hydrogen Peroxide and UV Radiation. *Helvetica Chimica Acta*, 85, 82-95.
- Liu, D., Ducoste, J., Jin, S., & Linden, K. G. (2004). Evaluation of Alternative Fluence Rate Distribution Models. *Journal of Water Supply: Research and Technology - AQUA*, 53(6), 391-408.
- Martin, C. A., Brandi, R. J., Alfano, O. M., & Cassano, A. E. (2002). Homogeneous Photoreactions for AOTs: Reactor Analysis and Design. *J. Adv. Oxid. Technol.*, 5(2), 164-174.
- Mohseni, M., & Taghipour, F. (2004). Experimental and CFD Analysis of Photocatalytic Gas Phase Vinyl Chloride (VC) Oxidation. *Chemical Engineering Science*, 59, 1601-1609.
- Pareek, V. K., Cox, S. J., Brungs, M. P., Young, B., & Adesina, A. A. (2003). Computational Fluid Dynamic (CFD) Simulation of a Pilot-Scale Annular Bubble Column Photocatalytic Reactor. *Chemical Engineering Science*, 58, 859-865.
- Rosenfeldt, E. J., & Linden, K. G. (2004). Degradation of Endocrine Disrupting Chemicals Bisphenol A, Ethinyl Estradiol, and Estradiol during IV Photolysis and Advanced Oxidation Processes. *Environ. Sci. Technol.*, 38(20), 5476-5483.

- Scheck, C. K., & Frimmel, F. H. (1995). Degradation of Phenol and Salicylic Acid by Ultraviolet Radiation/Hydrogen Peroxide/Oxygen. *Water Research*, 29(10), 2346-2352.
- Sharpless, C. M., & Linden, K. G. (2003). Experimental and Model Comparisons of Low- and Medium-Pressure Hg Lamps for the Direct and H<sub>2</sub>O<sub>2</sub> Assisted UV Photodegradation of N-Nitrosodimethylamine in Simulated Drinking Water. *Environ. Sci. Technol.*, 37(9), 1933-1940.
- Shirolkar, J., Coimbra, C., & McQuay, M. (1996). Fundamental aspects of modeling turbulent particle dispersion in dilute flows. *Progress In Energy and Combustion Science*, 22(4), 363-399.
- Stefan, M. I., Hoy, A. R., & Bolton, J. R. (1996). Kinetics and Mechanism of the Degradation and Mineralization of Acetone in Dilute Aqueous Solution Sensitized by the UV Photolysis of Hydrogen Peroxide. *Environ. Sci. Technol.*, 30, 2382-2390.
- Stefan, M. I., Mack, J., & Bolton, J. R. (2000). Degradation Pathways during the Treatment of Methyl tert-Butyl Ether by the UV/H<sub>2</sub>O<sub>2</sub> Process. *Environ. Sci. Technol.*, 34(4), 650-658.
- Wright, H. B., & Lawryshyn, Y. A. (2000). An Assessment of the Bioassay Concept for UV Reactor Validation: Water Environment Federation.
- Zalazar, C. S., Labas, M. D., Martin, C. A., Brandi, R. J., & Cassano, A. E. (2004). Reactor Scale-Up in AOPs: From Laboratory to Commercial Scale. *Water Science and Technology*, 49(4), 13-18.

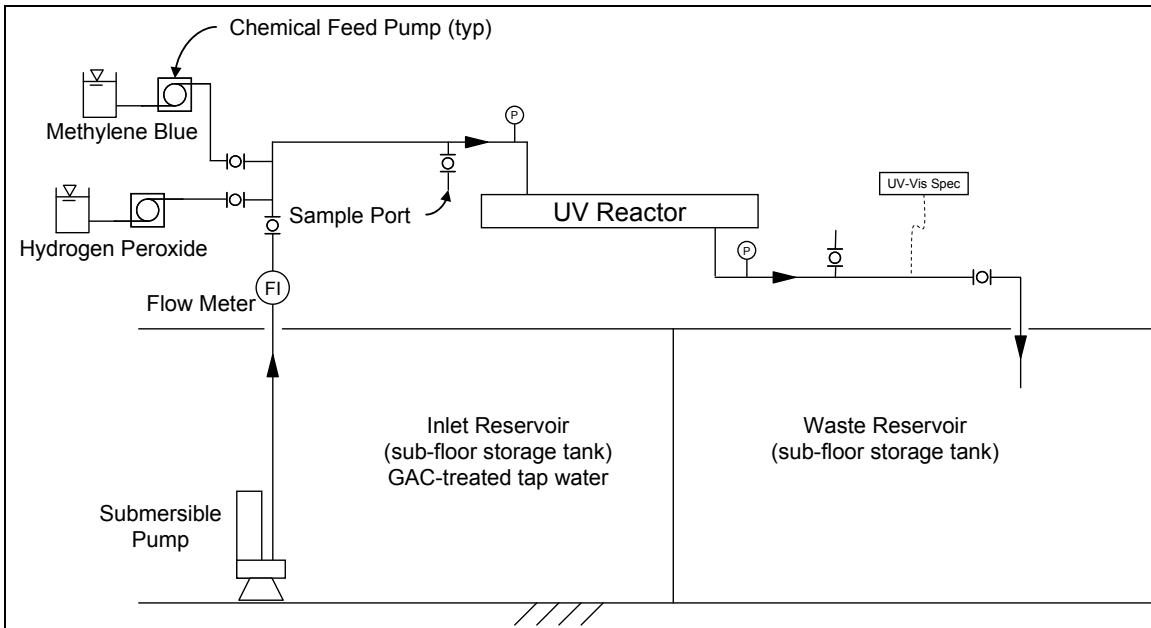


**Figure 1: Low-Pressure UV Pilot System Schematic (NTS)**

**Table 1: CFD Model Boundary Conditions**

Condition	Value
Inlet Velocity (normal to inlet plane)	0.128 – 0.384 m s <sup>-1</sup> (10 – 30 gal min <sup>-1</sup> ) All tangential velocities set to zero.
Outlet Velocity	No external velocity restriction <sup>(1)</sup>
Outlet (External) Pressure	100,000 Pa (Zero Gauge)
Inlet Turbulence Condition (I)	5% <sup>(2)</sup>
Inlet Methylene Blue (MB) Concentration	1.563 x 10 <sup>-6</sup> M
Inlet Hydrogen Peroxide Concentration	(150 * Inlet [MB]) M

<sup>(1)</sup> For the outlet, the gradients of all variables are zero in the flow direction with the exception of pressure.

<sup>(2)</sup> The turbulent kinetic energy and energy dissipation rate inlet conditions are defined as  $k_{inlet} = (I \times U)^2$  and  $\varepsilon_{inlet} = (k_{inlet})^{1.5} (0.1 \times D)^{-1}$  where  $U$  is the normal average inlet velocity and  $D$  is the pipe diameter.

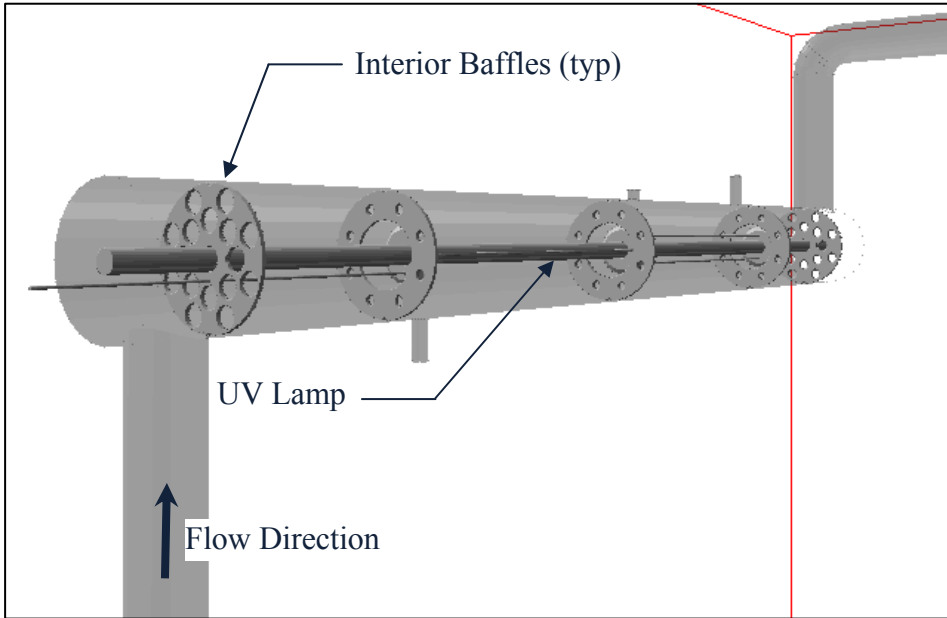


**Figure 2: Reactor Geometry within PHOENICS**

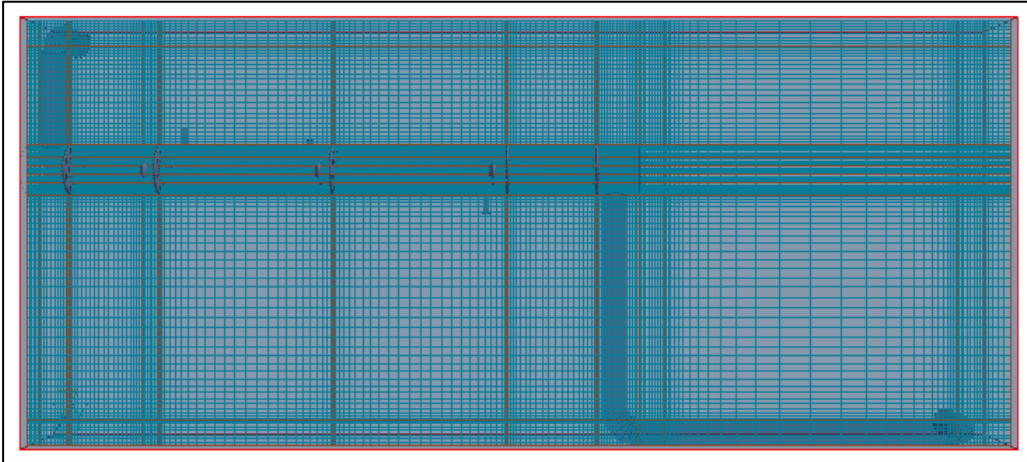


**Figure 3: CFD Grid Spacing in Y-Z Plane**

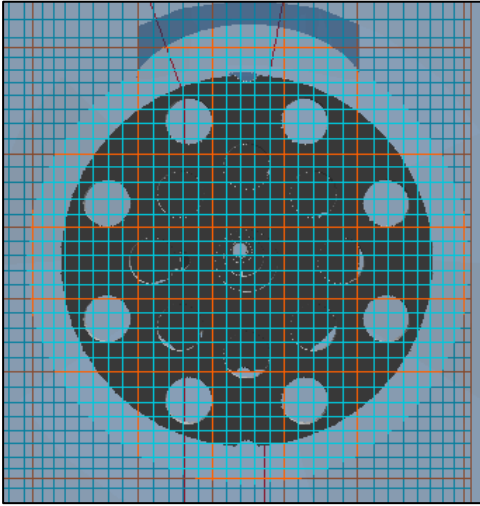


**Figure 4: CFD Grid Spacing in X-Z Plane**

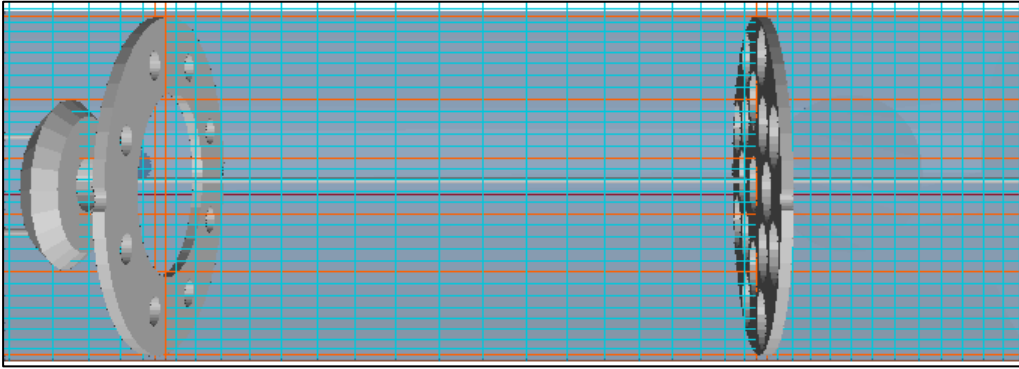


**Figure 5: CFD Grid Among Internal Baffles and Wiper Mechanism**

**Table 2: Variables in Turbulence Closure Sub-models**

Symbol	Definition
$\nu_T$	kinematic eddy viscosity
$k$	turbulent kinetic energy
$\varepsilon$	turbulent energy dissipation
$\tau_{ij}$	Reynolds stress tensor
$\nu$	kinematic molecular viscosity

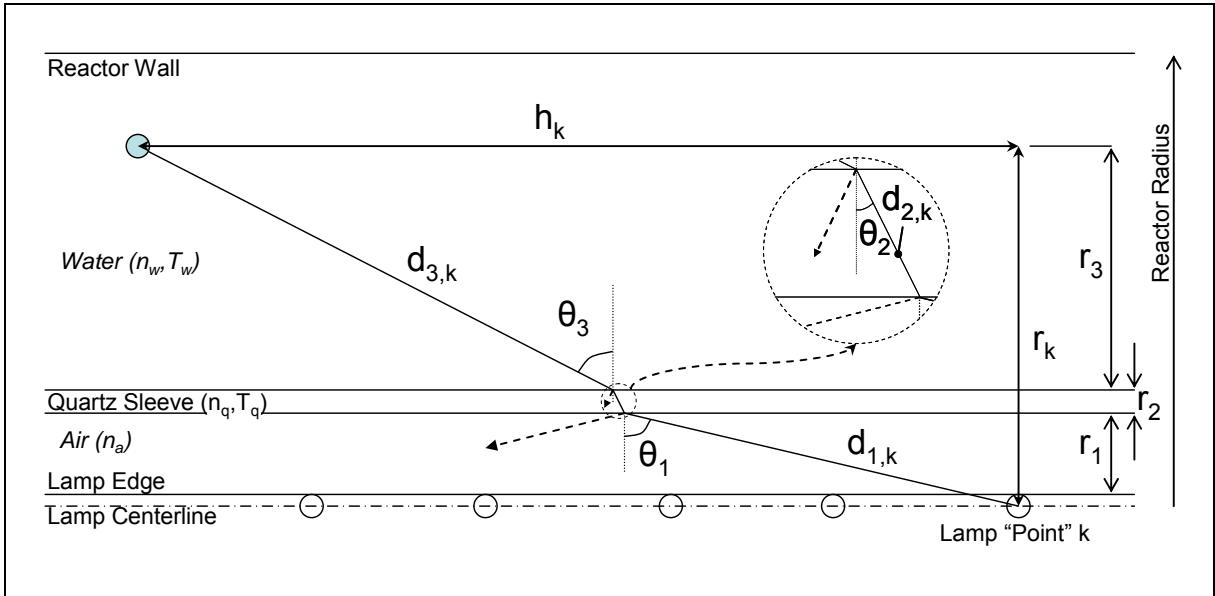


**Figure 6:** Angle Geometry of Attenuation Factor in RAD-LSI Model

**Table 3: Rate Equations for Radical Production and Methylene Blue Degradation**

Reaction System	Equations	Constants (References)
1	$H_2O_2 + hv \rightarrow 2 \cdot OH$ $r_{UV} = 2\Phi_{H_2O_2} E'_{CFD} \varepsilon_{H_2O_2} [H_2O_2]$ $E'_{CFD} = \frac{I_{UV} (W m^{-2}) \times 100 (cm m^{-1})}{U_{254} (J Ein^{-1}) \times 1000 (L m^{-3})}$	$\Phi_{H_2O_2} = 0.5$ $\varepsilon_{H_2O_2} = 19.6 M^{-1} cm^{-1}$ $U_{254} = 471,528 J Ein^{-1}$
2	$H_2O_2 + \cdot OH \rightarrow H_2O + HO_2 \cdot (\rightarrow H^+ + \cdot O_2^-)$ $\frac{d[H_2O_2]}{dt} = -k_1 [H_2O_2] [\cdot OH]$ $\frac{d[\cdot OH]}{dt} = -k_1 [H_2O_2] [\cdot OH]$ $\frac{d[\cdot O_2^-]}{dt} = k_1 [H_2O_2] [\cdot OH]$	$k_1 = 2.7 \times 10^7 M^{-1} s^{-1}$ <p>(Buxton et al., 1988)</p>
3	$H_2O_2 + \cdot O_2^- \rightarrow \cdot OH + O_2 + OH^-$ $\frac{d[H_2O_2]}{dt} = -k_2 [H_2O_2] [\cdot O_2^-]$ $\frac{d[\cdot O_2^-]}{dt} = -k_2 [H_2O_2] [\cdot O_2^-]$ $\frac{d[\cdot OH]}{dt} = k_2 [H_2O_2] [\cdot O_2^-]$	$k_2 = 0.13 M^{-1} s^{-1}$ <p>(Weinstein et al., 1979)</p>
4	$\cdot OH + \cdot OH \rightarrow H_2O_2$ $\frac{d[\cdot OH]}{dt} = -k_3 [\cdot OH] [\cdot OH]$ $\frac{d[H_2O_2]}{dt} = k_3 [\cdot OH] [\cdot OH]$	$k_3 = 5.5 \times 10^9 M^{-1} s^{-1}$ <p>(Buxton et al., 1988)</p>
5	$\cdot OH + \cdot O_2^- \rightarrow O_2 + OH^-$ $\frac{d[\cdot OH]}{dt} = -k_4 [\cdot OH] [\cdot O_2^-]$ $\frac{d[\cdot O_2^-]}{dt} = -k_4 [\cdot OH] [\cdot O_2^-]$	$k_4 = 7.0 \times 10^9 M^{-1} s^{-1}$ <p>(Beck, 1969 as cited in Crittenden, et. al, 1999)</p>

**Table 3 Continued**

Reaction System	Equations	Constants (References)
6	$\bullet OH + MB \rightarrow \text{Unknowns}$ $\frac{d[\bullet OH]}{dt} = -k_{MB,\bullet OH} [\bullet OH][MB]$ $\frac{d[MB]}{dt} = -k_{MB,\bullet OH} [\bullet OH][MB]$	$k_{MB,\bullet OH} = 6.9 \times 10^9 \text{ M}^{-1} \text{ s}^{-1}$

**Table 4: Rate Equations for Radical Scavengers**

Reaction System	Equations	Constants (References)
7	$\frac{d[\cdot OH]}{dt} = -k_{DOC,\cdot OH} [\cdot OH](DOC)$	$k_{DOC,\cdot OH} = 2.5 \times 10^4 \left( \frac{mg}{L} \right)^{-1} s^{-1}$ (Larson and Zepp, 1988)
8	$\frac{d[\cdot OH]}{dt} = -k_{HCO_3^-, \cdot OH} [HCO_3^-][\cdot OH]$	$k_{HCO_3^-, \cdot OH} = 8.5 \times 10^6 M^{-1} s^{-1}$ (Buxton et al., 1988)
9	$\frac{d[\cdot OH]}{dt} = -k_{NH_2Cl, \cdot OH} [NH_2Cl][\cdot OH]$	$k_{NH_2Cl, \cdot OH} = (2.8 \pm 0.2) \times 10^9 M^{-1} s^{-1}$ (Johnson et al., 2002)

**Table 5: Normalized Variables**

Normalized Variable	Variable Meaning	Substitution in Rate Equations
$[H_2O_2]^*$	$\frac{[H_2O_2]}{[H_2O_2]_0}$	$[H_2O_2] = [H_2O_2]^* \times [H_2O_2]_0$
$[MB]^*$	$\frac{[MB]}{[MB]_0}$	$[MB] = [MB]^* \times [MB]_0$
$[\cdot OH]^*$	$\frac{[\cdot OH]}{[H_2O_2]_0}$	$[\cdot OH] = [\cdot OH]^* \times [H_2O_2]_0$
$[\cdot O_2^-]^*$	$\frac{[\cdot O_2^-]}{[H_2O_2]_0}$	$[\cdot O_2^-] = [\cdot O_2^-]^* \times [H_2O_2]_0$

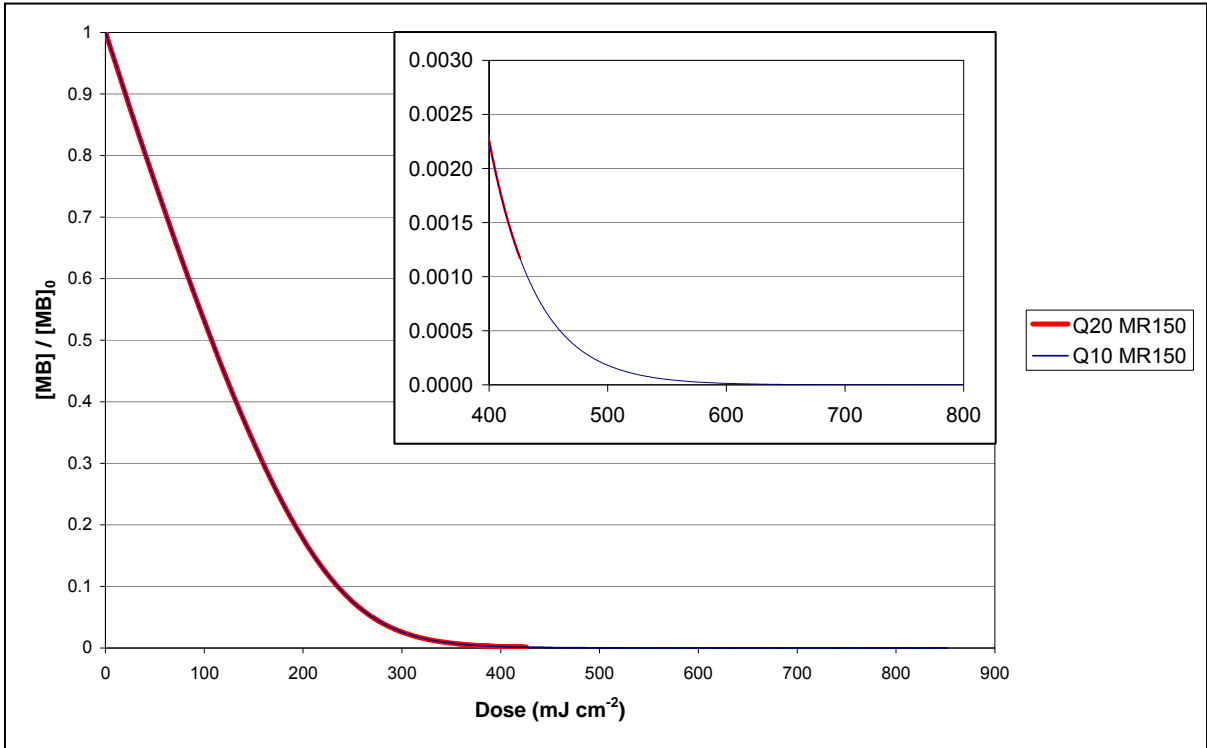


**Figure 7: Dose-Response Curves for Methylene Blue Degradation**

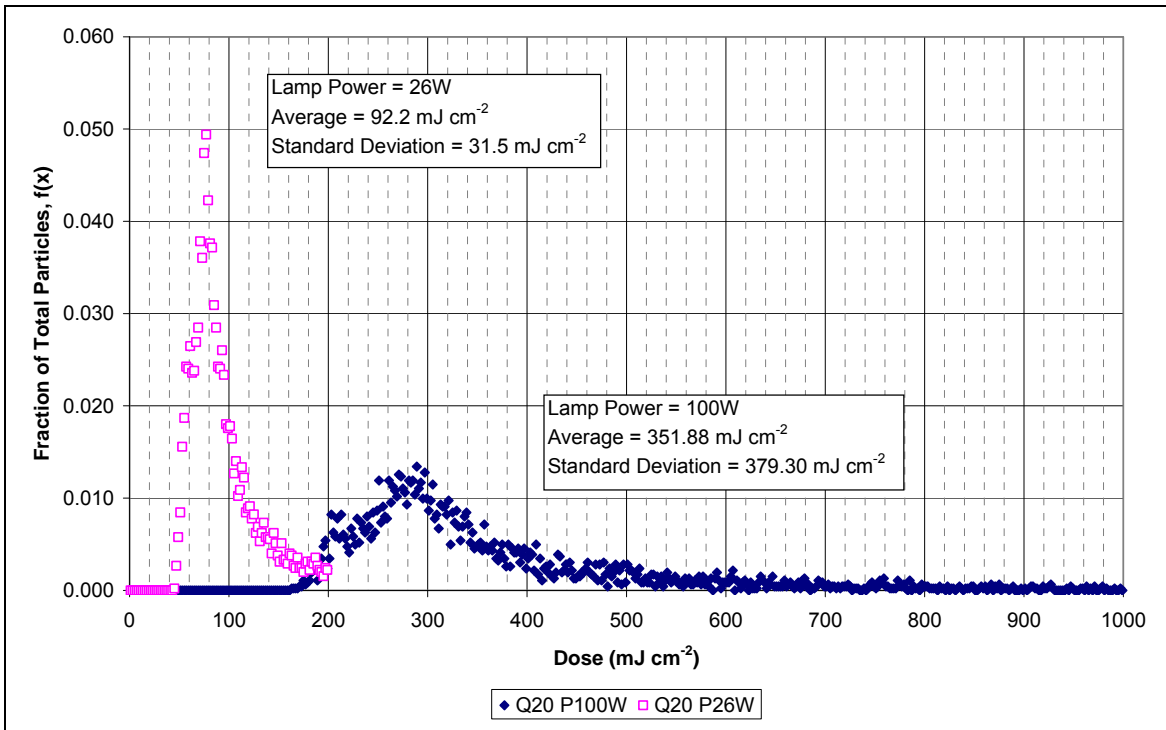


**Figure 8: Dose Distribution for 26.5 and 100 W Output Power at 20 GPM**

**Table 6: Summary of Numerical Solution Results**

Numerical Solution Technique	Percent Removal at P = 26.5 W <sup>1</sup>	Percent Removal at P = 100 W <sup>1</sup>
MATLAB Ideal Hydraulics with Volumetric Average Irradiance	52.26%	99.88%
CFD/MATLAB/Lagrangian (Average Dose)	43.43%	99.25%
CFD/MATLAB/Lagrangian (Segregated Dose Summation)	42.86%	95.78%
CFD/Eulerian	45.85%	97.43%
CFD/Eulerian with Power and UVT Adjusted to Match Pilot Sensor Fluence Rate	47.08%	N/A
Pilot Results	57.7% ± 0.7%	N/A

<sup>1</sup> Lamp Output Power at 254 nm.

Flow Conditions: Q = 20 GPM, Molar Ratio (H<sub>2</sub>O<sub>2</sub>:MB) = 150, k<sub>MB,OH</sub> = 6.9E10 M<sup>-1</sup> s<sup>-1</sup>, DOC = 0.57 mg L<sup>-1</sup>, ALK = 22.7 mg L<sup>-1</sup> as CaCO<sub>3</sub>, pH = 7.3, Combined Chlorine = 0.05 mg L<sup>-1</sup> as Cl<sub>2</sub>

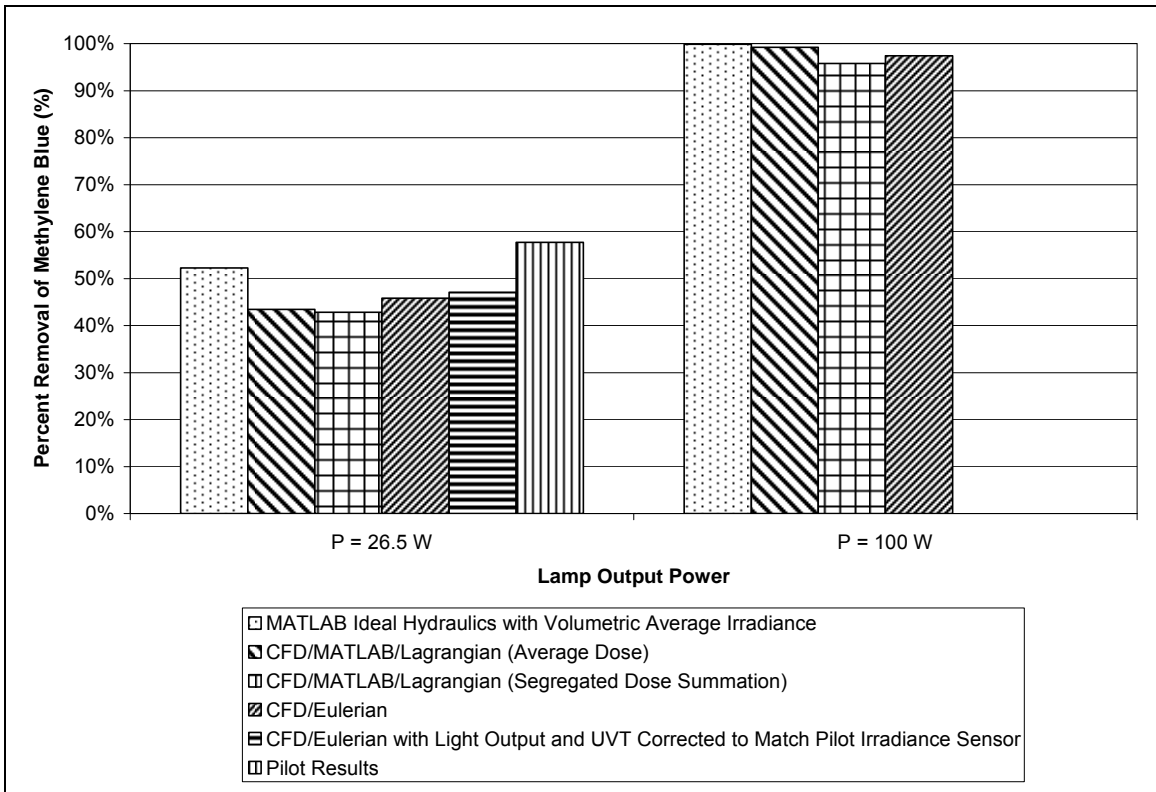


**Figure 9: Comparison of Numerical Models for Methylene Blue Removal**

**Table 7: Example of Model Effect on Regulatory Requirements**

Numerical Model	Predicted Removal (%)	Influent Concentration ( $\mu\text{g L}^{-1}$ )	Effluent Concentration ( $\mu\text{g L}^{-1}$ )	Meets MCL of $3 \mu\text{g L}^{-1}$	Log Removal
MATLAB Ideal Hydraulics	99.88	10	0.01	Yes	2.92
CFD/MATLAB/Lagrangian	95.78	10	0.42	Yes	1.37
CFD/Eulerian	97.43	10	0.26	Yes	1.59

**Table 8: Summary of Input and Output of Three Numerical Models**

Ideal Hydraulics		CFD/Eulerian		CFD/Lagrangian	
Input	Output	Input	Output	Input	Output
Average UV fluence rate	Effluent concentration of target contaminant	System Geometry	Effluent concentration of all tracked species	System Geometry	UV fluence (dose) distribution indicating reactor departure from ideal plug flow
Reaction mechanism with rate constants		Flow Rate		Flow Rate	
Inlet contaminant and hydrogen peroxide concentrations		Inlet contaminant and hydrogen peroxide concentrations	Spatial distribution of all species within reactor	Inlet contaminant and hydrogen peroxide concentrations	Effluent concentration of target contaminant
Theoretical hydraulic residence time of reactor		Lamp arrangement, lamp number, lamp output power at UV wavelength(s) of interest	Spatial distribution of UV light within reactor	Lamp arrangement, lamp number, lamp output power at UV wavelength(s) of interest	
		Turbulence model	Velocity and pressure distribution within reactor	Turbulence model	
		Fluence rate model	Headloss across reactor	Fluence rate model	
		Reaction mechanism with rate constants		Reaction mechanism with rate constants	
				Inlet particle number and distribution	
				UV dose – response curve for contaminant destruction at specific hydrogen peroxide concentration	

## 7. LIST OF REFERENCES

- Alfano, O. M., Brandi, R. J., & Cassano, A. E. (2001). Degradation Kinetics of 2,4-D in Water Employing Hydrogen Peroxide and UV Radiation. *Chemical Engineering Journal*, 82, 209-218.
- Alnaizy, R., & Akgerman, A. (2000). Advanced Oxidation of Phenolic Compounds. *Advances in Environmental Research*, 4(3), 233-244.
- American Public Health Association, American Water Works Association, & Water Environment Federation. (1995). *Standard Methods for the Examination of Water and Wastewater, 19th Edition* (19th ed.). Washington, DC: American Public Health Association.
- Baeza, C., & Knappe, D.R.U. (2005). *UV/H<sub>2</sub>O<sub>2</sub> Oxidation of Antimicrobial Compounds: Biochemical Activity and Biodegradability of Oxidation Intermediates*. Manuscript in preparation.
- Bakker, A., Haidari, A. H., & Oshinowo, L. M. (2001). Realize Greater Benefits from CFD. *Chemical Engineering Progress*, 97(3), 45-53.
- Baldyga, J., & Bourne, J. R. (1989). Simplification of Micromixing Calculations. I. Derivation and Application of New Model. *The Chemical Engineering Journal*, 42, 83-92.
- Baldyga, J., & Bourne, J. R. (1990). Comparison of the Engulfment and the Interaction-by-Exchange-with-the-Mean Micromixing Models. *The Chemical Engineering Journal*, 45, 25-31.

- Baldyga, J., & Bourne, J. R. (1992). Interactions Between Mixing on Various Scales in Stirred Tank Reactors. *Chemical Engineering Science*, 47(8), 1839-1848.
- Baldyga, J., & Bourne, J. R. (1999). *Turbulent Mixing and Chemical Reactions*. Chichester, England: John Wiley & Sons Ltd.
- Baldyga, J., & Pohorecki, R. (1995). Turbulent Micromixing in Chemical Reactors - A Review. *The Chemical Engineering Journal*, 58, 183-195.
- Baldyga, J., & Rohani, S. (1987). Micromixing Described in Terms of Inertial-Convective Disintegration of Large Eddies and Viscous-Convective Interactions Among Small Eddies - I. General Development and Batch Systems. *Chemical Engineering Science*, 42(11), 2597-2610.
- Bali, U., Catalkaya, E. C., & Sengul, F. (2003). Photochemical Degradation and Mineralization of Phenol: A Comparative Study. *Journal of Environmental Science and Health, Part A-Toxic/Hazardous Substances & Environmental Engineering*, A38(10), 2259-2275.
- Banat, F., Al-Asheh, S., Al-Rawashdeh, M. m., & Nusair, M. (2005). Photodegradation of Methylene Blue Dye by the UV/H<sub>2</sub>O<sub>2</sub> and UV/Acetone Oxidation Processes. *Desalination*, 181, 225-232.
- Behnajady, M. A., & Modirshahla, N. (2006). Kinetic Modeling on Photooxidative Degradation of C.I. Acid Orange 7 in a Tubular Continuous-Flow Photoreactor. *Chemosphere*, 62, 1543-1548.

- Behnajady, M. A., Modirshahla, N., & Shokri, M. (2004). Photodestruction of Acid Orange 7 (AO7) in Aqueous Solutions by UV/H<sub>2</sub>O<sub>2</sub>: Influence of Operational Parameters. *Chemosphere*, 55, 129-134.
- Blatchley, E. R., III. (1997). Numerical Modelling of UV Intensity: Application to Collimated-Beam Reactors and Continuous-Flow Systems. *Water Research*, 31(9), 2205-2218.
- Bolton, J. R. (2000). Calculation of Ultraviolet Fluence Rate Distributions in an Annular Reactor: Significance of Refraction and Reflection. *Water Research*, 34(13), 3315-3324.
- Bolton, J. R. (2001). *Ultraviolet Applications Handbook* (Second ed.). Ayr, ON, Canada: Bolton Photosciences, Inc.
- Bolton, J. R., Bircher, K. G., Tumas, W., & Tolman, C. A. (2001). Figures-of-Merit for the Technical Development and Application of Advanced Oxidation Technologies for Both Electric- and Solar-Driven Systems. *Pure Appl. Chem.*, 73(4), 627-637.
- Bolton, J. R., & Linden, K. G. (2003). Standardization of Methods for Fluence (UV Dose) Determination in Bench-Scale UV Experiments. *Journal of Environmental Engineering*, 209-215.
- Boreen, A. L., Arnold, W. A., & McNeill, K. (2004). Photochemical Fate of Sulfa Drugs in the Aquatic Environment: Sulfa Drugs Containing Five-Membered Heterocyclic Groups. *Environ. Sci. Technol.*, 38(14), 3933-3940.
- Braun, A. M., Maurette, M.-T., & Oliveros, E. (1991). *Photochemical Technology* (D. F. Ollis & N. Serpone, Trans.). Chichester: John Wiley & Sons.

- Buxton, G. V., Greenstock, C. L., Helman, W. P., & Ross, A. B. (1988). Critical Review of Rate Constants for Reactions of Hydrated Electrons, Hydrogen Atoms and Hydroxyl Radicals (OH/O<sup>-</sup>) in Aqueous Solution. *J. Phys. Chem. Ref. Data*, 17(2), 513-886.
- Buxton, G. V., & Subhani, M. S. (1972). Radiation Chemistry and Photochemistry of Oxychlorine Ions, Part 1.-Radiolysis of Aqueous Solutions of Hypochlorite and Chlorite Ions. *Journal of the Chemical Society, Faraday Transactions 1: Physical Chemistry in Condensed Phases* 68, 947-957.
- Canonica, S., Meunier, L., & Von Gunten, U. (2008). Phototransformation of selected pharmaceuticals during UV treatment of drinking water. *Water Research*, 42, 121-128.
- Cater, S. R., Stefan, M. I., Bolton, J. R., & Safarzadeh-Amiri, A. (2000). UV/H<sub>2</sub>O<sub>2</sub> Treatment of Methyl tert-Butyl Ether in Contaminated Waters. *Environ. Sci. Technol.*, 34(4), 659-662.
- Clark, M. M. (1996). *Transport Modeling for Environmental Engineers and Scientists*. New York: John Wiley & Sons.
- Crittenden, J. C., Hu, S., Hand, D. W., & Green, S. A. (1999). A Kinetic Model for H<sub>2</sub>O<sub>2</sub>/UV Process in a Completely Mixed Batch Reactor. *Wat. Res.*, 33(10), 2315-2328.
- Devlin, H. R., & Harris, I. J. (1984). Mechanism of the Oxidation of Aqueous Phenol with Dissolved Oxygen. *Ind. Eng. Chem. Fundam.*, 23(4), 387-392.
- Ding, Z.-Y., Aki, S. N. V. K., & Abraham, M. A. (1995). Catalytic Supercritical Water Oxidation: Phenol Conversion and Product Selectivity. *Environ. Sci. Technol.*, 29(11), 2748-2753.

- Ducoste, J., & Linden, K. G. (2005). *Hydrodynamic Characterization of UV Reactors*. Denver: Awwa Research Foundation.
- Ducoste, J., Liu, D., & Linden, K. G. (2005). Alternative Approaches to Modeling Fluence Distribution and Microbial Inactivation in Ultraviolet Reactors: Lagrangian versus Eulerian. *Journal of Environmental Engineering*, 1393-1403.
- El-Dein, A. M., Libra, J. A., & Wiesmann, U. (2001). Kinetics of Decolorization and Mineralization of the Azo Dye Reactive Black 5 by Hydrogen Peroxide and UV Light. *Water Science and Technology*, 44(5), 295-301.
- Elliot, A. J., & Buxton, G. V. (1992). Temperature Dependence of the Reactions  $\text{OH} + \text{O}_2^-$  and  $\text{OH} + \text{HO}_2$  in Water up to 200 °C. *J. Chem. Soc. Faraday Trans.*, 88(17), 2465-2470.
- Feng, Y., Smith, D. W., & Bolton, J. R. (2007). Photolysis of Aqueous Free Chlorine Species ( $\text{HOCl}$  and  $\text{OCl}^-$ ) with 254 nm Ultraviolet Light. *J. Environ. Eng. Sci.*, 6, 277-284.
- Fiveland, W. A. (1984). Discrete-Ordinates Solutions of the Radiative Transport Equation for Rectangular Enclosures. *Journal of Heat Transfer*, 106, 699-705.
- Forney, L. J., & Nafia, N. (1998). Turbulent Jet Reactors: Mixing Time Scales. *Trans IChemE*, 76(A), 728-736.
- Galindo, C., P. Jacques, et al. (2000). Photodegradation of the Aminoazobenzene Acid Orange 52 by Three Advanced Oxidation Processes: UV/H<sub>2</sub>O<sub>2</sub>, UV/TiO<sub>2</sub> and VIS/TiO<sub>2</sub> Comparative Mechanistic and Kinetic Investigations. *Journal of Photochemistry and Photobiology A: Chemistry*, 130, 35-47.

- Gultekin, I., & Ince, N. H. (2004). Degradation of Reactive Azo Dyes by UV/H<sub>2</sub>O<sub>2</sub>: Impact of Radical Scavengers. *Journal of Environmental Science and Health: Part A - Toxic/Hazardous Substances and Environmental Engineering*, *A39*(4), 1069-1081.
- Gupta, B. L., & Hart, E., J. (1971). Radiation Chemistry of Some Sulfonephthalein Dyes. *Radiation Research*, *48*, 8-19.
- Hjertager, L. K., B. H. Hjertager, et al. (2002). CFD modelling of fast chemical reactions in turbulent liquid flows. *Computers and Chemical Engineering*, *26*, 507-515.
- Hu, L., Flanders, P. M., Miller, P. L., & Strathmann, T. J. (2007). Oxidation of Sulfamethoxazole and Related Antimicrobial Agents by TiO<sub>2</sub> Photocatalysis. *Water Research*, *41*, 2612-2626.
- Huber, M. M., Canonica, S., Park, G.-Y., & Von Gunten, U. (2003). Oxidation of Pharmaceuticals during Ozonation and Advanced Oxidation Processes. *Environ. Sci. Technol.*, *37*(5), 1016-1024.
- Jacob, S. M., & Dranoff, J. S. (1970). Light Intensity Profiles in a Perfectly Mixed Photoreactor. *AIChE Journal*, *16*(3), 359-363.
- Johnson, H. D., Cooper, W. J., Mezyk, S. P., & Bartels, D. M. (2002). Free Radical Reactions of Monochloramine and Hydroxylamine in Aqueous Solution. *Radiation Physics and Chemistry*, *65*, 317-326.
- Klassen, N. V., Marchington, D., & McGowan, H. C. E. (1994). H<sub>2</sub>O<sub>2</sub> Determination by the I<sub>3</sub><sup>-</sup> Method and by KMnO<sub>4</sub> Titration. *Analytical Chemistry*, *66*(18), 2921-2925.
- Kolpin, D. W., Furlong, E. T., Meyer, M. T., Thurman, E. M., Zaugg, S. D., Barber, L. B., et al. (2002). Pharmaceuticals, Hormones, and Other Organic Wastewater Contaminants

- in U.S. Streams, 1999-2000: A National Reconnaissance. *Environ. Sci. Technol.*, 36(6), 1202-1211.
- Labas, M. D., Zalazar, C. S., Brandi, R. J., Martin, C. A., & Cassano, A. E. (2002). Scaling Up of a Photoreactor for Formic Acid Degradation Employing Hydrogen Peroxide and UV Radiation. *Helvetica Chimica Acta*, 85, 82-95.
- Larson, R. A., & Zepp, R. G. (1988). Reactivity of the Carbonate Radical with Aniline Derivatives. *Environmental Toxicology and Chemistry*, 7, 265-274.
- Linden, K. G., Sharpless, C. M., Andrews, S. A., Atasi, K. Z., Korategere, V., Stefan, M. I., et al. (2004). *Innovative UV Technologies to Oxidize Organic and Organoleptic Chemicals*: Awwa Research Foundation.
- Liou, B. T., & Wu, C. Y. (1996). Radiative transfer in a multi-layer medium with Fresnel interfaces. *Heat and Mass Transfer*, 32(1-2), 103-107.
- Liu, W., Andrews, S. A., Stefan, M. I., & Bolton, J. R. (2003). Optimal Methods for Quenching H<sub>2</sub>O<sub>2</sub> Residuals Prior to UFC Testing. *Water Research*, 37, 3697-3703.
- Liu, Y., & Ducoste, J. (2006). Numerical Simulation of Chloramines Formation in Turbulent Flow Using a Multi-Fluid Micromixing Model. *Environmental Modelling & Software*, 21, 1198-1213.
- Liu, D., Ducoste, J., Jin, S., & Linden, K. G. (2004). Evaluation of Alternative Fluence Rate Distribution Models. *Journal of Water Supply: Research and Technology - AQUA*, 53(6), 391-408.

- Liu, D., Ducoste, J., Wu, C., & Linden, K. G. (2007). Numerical Simulation of UV Disinfection Reactors: Evaluation of Alternative Turbulence Models. *Applied Mathematical Modeling*, 31, 1753-1769.
- Marchisio, D. L., & Barresi, A. A. (2003). CFD Simulation of Mixing and Reaction: The Relevance of the Micro-mixing Model. *Chemical Engineering Science*, 58, 3579-3587.
- Martin, C. A., Brandi, R. J., Alfano, O. M., & Cassano, A. E. (2002). Homogeneous Photoreactions for AOTs: Reactor Analysis and Design. *J. Adv. Oxid. Technol.*, 5(2), 164-174.
- Modirshahla, N., & Behnajady, M. A. (2006). Photooxidative Degradation of Malachite Green (MG) by UV/H<sub>2</sub>O<sub>2</sub>: Influence of Operational Parameters and Kinetic Modeling. *Dyes and Pigments*, 70, 54-59.
- Mohseni, M., & Taghipour, F. (2004). Experimental and CFD Analysis of Photocatalytic Gas Phase Vinyl Chloride (VC) Oxidation. *Chemical Engineering Science*, 59, 1601-1609.
- Moore, D. E., & Zhou, W. (1994). Photodegradation of Sulfamethoxazole: A Chemical System Capable of Monitoring Seasonal Changes in UVB Intensity. *Photochemistry and Photobiology*, 59(5), 497-502.
- Muller, J.-P., Gottschalk, C., & Jekel, M. (2001). Comparison of Advanced Oxidation Processes in Flow-through Pilot Plants (Part II). *Water Science and Technology*, 44(5), 311-315.

- Muller, J.-P., & Jekel, M. (2001). Comparison of Advanced Oxidation Processes in Flow-through Pilot Plants (Part I). *Water Science and Technology*, 44(5), 303-309.
- Ollis, D. F. (2003). Class Notes - Photochemical Engineering (CHE 760). North Carolina State University.
- Pareek, V. K., Cox, S. J., Brungs, M. P., Young, B., & Adesina, A. A. (2003). Computational Fluid Dynamic (CFD) Simulation of a Pilot-Scale Annular Bubble Column Photocatalytic Reactor. *Chemical Engineering Science*, 58, 859-865.
- Radiation Chemistry Data Center at the Notre Dame Radiation Laboratory. *Hydroxyl radical reaction rates: Methylene blue cation*. Retrieved October 31, 2008, from <http://www.rcdc.nd.edu/compilations/Hydroxyl/OH1254.HTM>
- Rahn, R. O. (1997). Potassium Iodide as a Chemical Actinometer for 254 nm Radiation: Use of Iodate as an Electron Scavenger. *Photochemistry and Photobiology*, 66(4), 450-455.
- Rahn, R. O., Bolton, J. R., & Stefan, M. I. (2006). The Iodide/Iodate Actinometer in UV Disinfection: Determination of the Fluence Rate Distribution in UV Reactors. *Photochemistry and Photobiology*, 82, 611-615.
- Rohani, S., & Baldyga, J. (1987). Micromixing Described in Terms of Inertial-Convective Disintegration of Large Eddies and Viscous-Convective Interactions Among Small Eddies - II. Semi-Batch and Continuous Stirred Tank Reactors. *Chemical Engineering Science*, 42(11), 2611-2619.

- Rosenfeldt, E. J., & Linden, K. G. (2004). Degradation of Endocrine Disrupting Chemicals Bisphenol A, Ethinyl Estradiol, and Estradiol during UV Photolysis and Advanced Oxidation Processes. *Environ. Sci. Technol.*, 38(20), 5476-5483.
- Rossner Campos, A. A. (2008). Sulfamethoxazole HPLC Calibration Data. Unpublished Excel Spreadsheet. North Carolina State University.
- Scheck, C. K., & Frimmel, F. H. (1995). Degradation of Phenol and Salicylic Acid by Ultraviolet Radiation/Hydrogen Peroxide/Oxygen. *Water Research*, 29(10), 2346-2352.
- Schwarzenbach, R. P., Escher, B. I., Fenner, K., Hofstetter, T. B., Johnson, C. A., von Gunten, U., et al. (2006). The Challenge of Micropollutants in Aquatic Systems. *Science*, 313, 1072-1077.
- Sharpless, C. M., & Linden, K. G. (2003). Experimental and Model Comparisons of Low- and Medium-Pressure Hg Lamps for the Direct and H<sub>2</sub>O<sub>2</sub> Assisted UV Photodegradation of N-Nitrosodimethylamine in Simulated Drinking Water. *Environ. Sci. Technol.*, 37(9), 1933-1940.
- Shirolkar, J., Coimbra, C., & McQuay, M. (1996). Fundamental aspects of modeling turbulent particle dispersion in dilute flows. *Progress In Energy and Combustion Science*, 22(4), 363-399.
- Spalding, B. (1998). *Turbulent Mixing and Chemical Reaction; the Multi-Fluid Approach (A Lecture)*, from [http://www.simuserve.com/phoenics/d\\_polis/d\\_lecs/mfm.mfm0.htm](http://www.simuserve.com/phoenics/d_polis/d_lecs/mfm.mfm0.htm)

- Stamnes, K., Tsay, S.-C., Wiscombe, W., & Jayaweera, K. (1988). Numerically Stable Algorithm for Discrete-Ordinate-Method for Radiative Transfer in Multiple Scattering and Emitting Layered Media. *Applied Optics*, 27(12), 2502-2509.
- Stefan, M. I., & Bolton, J. R. (2002). UV Direct Photolysis of N-Nitrosodimethylamine (NDMA): Kinetic and Product Study. *Helvetica Chimica Acta*, 85, 1416-1426.
- Stefan, M. I., Hoy, A. R., & Bolton, J. R. (1996). Kinetics and Mechanism of the Degradation and Mineralization of Acetone in Dilute Aqueous Solution Sensitized by the UV Photolysis of Hydrogen Peroxide. *Environ. Sci. Technol.*, 30, 2382-2390.
- Stefan, M. I., Mack, J., & Bolton, J. R. (2000). Degradation Pathways during the Treatment of Methyl tert-Butyl Ether by the UV/H<sub>2</sub>O<sub>2</sub> Process. *Environ. Sci. Technol.*, 34(4), 650-658.
- Watts, M. J., Rosenfeldt, E. J., & Linden, K. G. (2007). Comparative OH Radical Oxidation Using UV-Cl<sub>2</sub> and UV-H<sub>2</sub>O<sub>2</sub> Processes. *Journal of Water Supply: Research and Technology - AQUA*, 56(8), 469-477.
- Weinstein, J., & Bielski, B. H. J. (1979). Kinetics of the Interaction of HO<sub>2</sub> and O<sub>2</sub><sup>-</sup> Radicals with Hydrogen Peroxide. The Haber-Weiss Reaction. *Journal of the American Chemical Society*, 101(1), 58-62.
- Wilcox, D. C. (2004). *Turbulence Modeling for CFD* (Second ed.). La Canada, California: DCW Industries, Inc.
- Wright, H. B., & Lawryshyn, Y. A. (2000). An Assessment of the Bioassay Concept for UV Reactor Validation: Water Environment Federation.

Yakhot, V., & Orszag, S. A. (1986). Renormalization-Group Analysis of Turbulence.

*Physical Review Letters*, 57(14), 1722-1724.

Zalazar, C. S., Labas, M. D., Martin, C. A., Brandi, R. J., & Cassano, A. E. (2004). Reactor

Scale-Up in AOPs: From Laboratory to Commercial Scale. *Water Science and*

*Technology*, 49(4), 13-18.

Zhou, W., & Moore, D. E. (1997). Photosensitizing Activity of the Anti-Bacterial Drugs

Sulfamethoxazole and Trimethoprim. *Journal of Photochemistry and Photobiology*

*B: Biology*, 39, 63-72.

8. APPENDIX

## 8.1 Appendix A – Sample CFD Codes for Pressure/Velocity, Light, and Kinetics

## Sample CFD Q1 Code – Pressure/Velocity (Research Condition No. 5)

```
<html><head><title>Q1</title>
<link rel="stylesheet" type="text/css"
href="/phoenics/d_polis/polstyle.css">
</head><body><pre><strong>
TALK=T;RUN( 1, 1)

*****
  Q1 created by VDI menu, Version 2006, Date 21/09/06
  CPVNAM=VDI;SPPNAM=Core
  *****
  IRUNN =    1 ;LIBREF =    0
  *****
  Group 1. Run Title
  TEXT(LP3D 20 GPM PV Rev A          )
  *****
  Group 2. Transience
  STEADY = T
  *****
  Groups 3, 4, 5 Grid Information
  * Overall number of cells, RSET(M,NX,NY,NZ,tolerance)
  RSET(M,43,185,108)
  *****
  Group 6. Body-Fitted coordinates
  *****
  Group 7. Variables: STOREd,SOLVEd,NAMED
  ONEPHS = T
  * Non-default variable names
  NAME(147)=EPKE ; NAME(148)=DEN1
  NAME(149)=EL1 ; NAME(150)=ENUT
  * Solved variables list
  SOLVE(P1 ,U1 ,V1 ,W1 )
  * Stored variables list
  STORE(ENUT,EL1 ,DEN1,EPKE)
  * Additional solver options
  TURMOD(KEMODL)

  *****
  Group 8. Terms & Devices
  *****
  Group 9. Properties
  PRESS0 = 1.000000E+05 ;TEMP0 = 2.730000E+02
  * Domain material index is 67 signifying:
  * WATER at 20. deg C
  SETPRPS(1, 67)
  DVO1DT = 1.180000E-04
  PRT (EP )= 1.314000E+00
  *****
  Group 10. Inter-Phase Transfer Processes
  *****
  Group 11. Initialise Var/Porosity Fields
```

No PATCHes used for this Group

INIADD = F

\*\*\*\*\*

Group 12. Convection and diffusion adjustments

No PATCHes used for this Group

\*\*\*\*\*

Group 13. Boundary & Special Sources

No PATCHes used for this Group

EGWF = T

\*\*\*\*\*

Group 14. Downstream Pressure For PARAB

\*\*\*\*\*

Group 15. Terminate Sweeps

LSWEEP = 10000

RESFAC = 1.000000E-03

\*\*\*\*\*

Group 16. Terminate Iterations

LITER (P1 )= 200

\*\*\*\*\*

Group 17. Relaxation

RELAX(P1 ,LINRLX, 2.000000E-01)

RELAX(U1 ,FALSDT, 7.000000E-01)

RELAX(V1 ,FALSDT, 7.000000E-01)

RELAX(W1 ,FALSDT, 7.000000E-01)

RELAX(KE ,LINRLX, 1.000000E-01)

RELAX(EP ,LINRLX, 1.000000E-01)

KELIN = 3

\*\*\*\*\*

Group 18. Limits

VARMAX(U1 ) = 1.000000E+02 ;VARMIN(U1 ) = -1.000000E+02

VARMAX(V1 ) = 1.000000E+02 ;VARMIN(V1 ) = -1.000000E+02

VARMAX(W1 ) = 1.000000E+02 ;VARMIN(W1 ) = -1.000000E+02

\*\*\*\*\*

Group 19. EARTH Calls To GROUND Station

USEGRD = T ;USEGRX = T

ASAP = T

PARSOL = T

CONWIZ = T

\*\*\*\*\*

Group 20. Preliminary Printout

ECHO = T

\*\*\*\*\*

Group 21. Print-out of Variables

\*\*\*\*\*

Group 22. Monitor Print-Out

IXMON = 21 ;IYMON = 11 ;IZMON = 67

NPRMON = 100000

NPRMNT = 1

TSTSWP = -1  
\*\*\*\*\*

Group 23.Field Print-Out & Plot Control  
NPRINT = 100000  
ISWPRF = 1 ;ISWPRL = 100000  
No PATCHes used for this Group  
\*\*\*\*\*

Group 24. Dumps For Restarts  
  
GVIEW(P,1.000000E+00,0.000000E+00,0.000000E+00)  
GVIEW(UP,0.000000E+00,0.000000E+00,1.000000E+00)

> DOM, SIZE, 2.389910E-01, 2.934530E+00, 1.268010E+00  
> DOM, MONIT, 1.460730E-01, 6.842660E-02, 9.341280E-01  
> DOM, SCALE, 1.000000E+00, 1.000000E+00, 1.000000E+00  
> DOM, SNAPSIZ, 1.000000E-02  
> GRID, RSET\_X\_1, 11,-1.380000E+00  
> GRID, RSET\_X\_2, 8, 1.200000E+00  
> GRID, RSET\_X\_3, -5, 1.000000E+00,G  
> GRID, RSET\_X\_4, 5, 1.000000E+00,G  
> GRID, RSET\_X\_5, -5, 1.000000E+00,G  
> GRID, RSET\_X\_6, 8,-1.200000E+00  
> GRID, RSET\_X\_7, 1, 1.000000E+00  
> GRID, RSET\_Y\_1, -6, 1.120000E+00  
> GRID, RSET\_Y\_2, -9, 1.320000E+00  
> GRID, RSET\_Y\_3, 2, 1.000000E+00  
> GRID, RSET\_Y\_4, 1, 1.000000E+00  
> GRID, RSET\_Y\_5, -19, 1.350000E+00  
> GRID, RSET\_Y\_6, -8, 1.180000E+00  
> GRID, RSET\_Y\_7, 1, 1.000000E+00  
> GRID, RSET\_Y\_8, -24, 1.580000E+00  
> GRID, RSET\_Y\_9, 1, 1.000000E+00  
> GRID, RSET\_Y\_10, -24, 1.580000E+00  
> GRID, RSET\_Y\_11, 1, 1.000000E+00  
> GRID, RSET\_Y\_12, -19, 1.450000E+00  
> GRID, RSET\_Y\_13, 1, 1.000000E+00  
> GRID, RSET\_Y\_14, -15, 1.270000E+00  
> GRID, RSET\_Y\_15, -10, 1.230000E+00  
> GRID, RSET\_Y\_16, -28, 1.250000E+00,G  
> GRID, RSET\_Y\_17, -10, 1.220000E+00,G  
> GRID, RSET\_Y\_18, 6, 1.550000E+00  
> GRID, RSET\_Z\_1, -9, 1.500000E+00  
> GRID, RSET\_Z\_2, -34, 1.600000E+00  
> GRID, RSET\_Z\_3, 8, 1.150000E+00  
> GRID, RSET\_Z\_4, -5, 1.000000E+00  
> GRID, RSET\_Z\_5, -5, 1.000000E+00,G  
> GRID, RSET\_Z\_6, -5, 1.100000E+00,G  
> GRID, RSET\_Z\_7, 8,-1.150000E+00  
> GRID, RSET\_Z\_8, -24, 1.500000E+00  
> GRID, RSET\_Z\_9, -10, 1.500000E+00

> OBJ, NAME, REACTOR3  
> OBJ, POSITION, 0.000000E+00, 0.000000E+00, 0.000000E+00

```

> OBJ, SIZE, 2.389905E-01, 2.934527E+00, 1.268006E+00
> OBJ, GEOMETRY, reactor3drev2
> OBJ, ROTATION24, 1
> OBJ, TYPE, BLOCKAGE
> OBJ, COLOR-MODE, USER
> OBJ, COLOR-VAL, 142
> OBJ, OPAQUE, 50
> OBJ, MATERIAL, 198,Solid with smooth-wall friction

> OBJ, NAME, INLET3DR
> OBJ, POSITION, 0.000000E+00, 2.776573E+00, 0.000000E+00
> OBJ, SIZE, 0.000000E+00, 7.930350E-02, 7.923202E-02
> OBJ, GEOMETRY, inlet3drev2
> OBJ, ROTATION24, 1
> OBJ, TYPE, INLET
> OBJ, PRESSURE, 0.000000E+00
> OBJ, VELOCITY, 2.555047E-01, 0.000000E+00, 0.000000E+00
> OBJ, TEMPERATURE, 0.000000E+00
> OBJ, TURB-INTENS, 5.000000E+00

> OBJ, NAME, OUTLET3D
> OBJ, POSITION, 0.000000E+00, 3.496076E-02, 1.188632E+00
> OBJ, SIZE, 0.000000E+00, 7.930348E-02, 7.923210E-02
> OBJ, GEOMETRY, outlet3drev2
> OBJ, ROTATION24, 1
> OBJ, TYPE, OUTLET
> OBJ, PRESSURE, 0.000000E+00
> OBJ, TEMPERATURE, SAME
> OBJ, COEFFICIENT, 1.000000E+03
> OBJ, TURBULENCE, SAME , SAME

> OBJ, NAME, LAMP3DRE
> OBJ, POSITION, 1.492971E-01, 0.000000E+00, 8.084253E-01
> OBJ, SIZE, 2.460623E-02, 1.825625E+00, 2.460623E-02
> OBJ, GEOMETRY, lamp3drev2
> OBJ, ROTATION24, 1
> OBJ, VISIBLE, NO
> OBJ, TYPE, BLOCKAGE
> OBJ, MATERIAL, 198,Solid with smooth-wall friction

> OBJ, NAME, WIPER3DR
> OBJ, POSITION, 1.235021E-01, 3.397250E-01, 7.826303E-01
> OBJ, SIZE, 7.619619E-02, 1.562100E+00, 7.619625E-02
> OBJ, GEOMETRY, wiper3drev2
> OBJ, ROTATION24, 1
> OBJ, TYPE, BLOCKAGE
> OBJ, MATERIAL, 198,Solid with smooth-wall friction

> OBJ, NAME, BAFFLE13
> OBJ, POSITION, 8.678560E-02, 1.697037E+00, 7.458405E-01
> OBJ, SIZE, 1.496291E-01, 4.762530E-03, 1.497757E-01
> OBJ, GEOMETRY, baffle13drev2
> OBJ, ROTATION24, 1

```

```
> OBJ, TYPE, BLOCKAGE
> OBJ, MATERIAL, 198,Solid with smooth-wall friction

> OBJ, NAME, BAFFLE23
> OBJ, POSITION, 8.678405E-02, 1.430338E+00, 7.458678E-01
> OBJ, SIZE, 1.496322E-01, 4.762411E-03, 1.497211E-01
> OBJ, GEOMETRY, baffle23drev2
> OBJ, ROTATION24, 1
> OBJ, TYPE, BLOCKAGE
> OBJ, MATERIAL, 198,Solid with smooth-wall friction

> OBJ, NAME, BAFFLE33
> OBJ, POSITION, 8.678405E-02, 9.096375E-01, 7.458678E-01
> OBJ, SIZE, 1.496322E-01, 4.762471E-03, 1.497211E-01
> OBJ, GEOMETRY, baffle33drev2
> OBJ, ROTATION24, 1
> OBJ, TYPE, BLOCKAGE
> OBJ, MATERIAL, 198,Solid with smooth-wall friction

> OBJ, NAME, BAFFLE43
> OBJ, POSITION, 8.678405E-02, 3.905250E-01, 7.458678E-01
> OBJ, SIZE, 1.496322E-01, 4.762501E-03, 1.497211E-01
> OBJ, GEOMETRY, baffle43drev2
> OBJ, ROTATION24, 1
> OBJ, TYPE, BLOCKAGE
> OBJ, MATERIAL, 198,Solid with smooth-wall friction

> OBJ, NAME, BAFFLE53
> OBJ, POSITION, 8.678405E-02, 1.238250E-01, 7.458678E-01
> OBJ, SIZE, 1.496322E-01, 4.762501E-03, 1.497211E-01
> OBJ, GEOMETRY, baffle53drev2
> OBJ, ROTATION24, 1
> OBJ, TYPE, BLOCKAGE
> OBJ, MATERIAL, 198,Solid with smooth-wall friction
STOP
</strong></pre></body></html>
```

## Sample CFD Q1 Code – Fluence Rate (Research Condition No. 5)

```
<html><head><title>Q1</title>
<link rel="stylesheet" type="text/css"
href="/phoenics/d_polis/polstyle.css">
</head><body><pre><strong>
TALK=T;RUN( 1, 1)

*****
  Q1 created by VDI menu, Version 2006, Date 21/09/06
  CPVNAM=VDI;SPPNAM=Core
*****
  IRUNN =    1 ;LIBREF =    0
*****
  Group 1. Run Title
  TEXT(LP3D 20 GPM Light57 92.9 5B k-e Rev F )
*****
  Group 2. Transience
  STEADY = T
*****
  Groups 3, 4, 5 Grid Information
  * Overall number of cells, RSET(M,NX,NY,NZ,tolerance)
  RSET(M,43,185,108)
*****
  Group 6. Body-Fitted coordinates
*****
  Group 7. Variables: STOREd,SOLVEd,NAMED
  ONEPHS = T
  * Non-default variable names
  NAME(139)=AVGA ; NAME(140)=DXX3
  NAME(141)=DYY3 ; NAME(142)=VOL3
  NAME(143)=FR12 ; NAME(144)=FR11
  NAME(145)=HH1  ; NAME(146)=RR1
  NAME(147)=EPKE ; NAME(148)=DEN1
  NAME(149)=EL1  ; NAME(150)=ENUT
  * Solved variables list
  SOLVE(C3 )
  * Stored variables list
  STORE(ENUT,EL1 ,DEN1,EPKE,RR1 ,HH1 ,FR11,FR12)
  STORE(DYY3,DXX3)
  STORE(AVGA)
  STORE(EP ,KE ,U1 ,W1 ,V1 ,P1 )
  STORE(VOL3)
  * Additional solver options
  SOLUTN(C3 ,Y,Y,Y,N,N,Y)
  TURMOD(KEMODL)
  STORE(KE,EP)

*****
  Group 8. Terms & Devices
  TERMS (C3 ,Y,N,N,N,Y,N)
*****
```

```

Group 9. Properties
PRESS0 = 1.000000E+05 ;TEMP0 = 2.730000E+02
* Domain material index is 67 signifying:
* WATER at 20. deg C
SETPRPS(1, 67)
DVOIDT = 1.180000E-04
PRT (EP ) = 1.314000E+00
*****

Group 10. Inter-Phase Transfer Processes
Echo PLANT settings
PLANTBEGIN
NAMSAT=MOSG

* C3 is the UV fluence rate in W/m^2
PATCH(IRR1,VOLUME,10,43,1,133,15,106,1,LSTEP)
<SORC46> VAL=AMIN1(RG(4)/(4.*RG(81)*RG(10)*RR1)*(ATAN((RG(10)/2.+$
HH1)/RR1)+ATAN((RG(10)/2.-HH1)/RR1)),RG(4)/(2.*RG(81)$
*RG(10)*RR1))*(FR12+TINY)/(FR11+TINY)
COVAL(IRR1,C3,FIXVAL,GRND)

PLANTEND

*****

Group 11. Initialise Var/Porosity Fields
No PATCHes used for this Group

FIINIT(P1)= READFI; FIINIT(U1)= READFI
FIINIT(V1)= READFI; FIINIT(W1)= READFI
FIINIT(KE)= READFI; FIINIT(EP)= READFI
FIINIT(ENUT)= READFI; FIINIT(EL1)= READFI
FIINIT(DEN1)= READFI; FIINIT(EPKE)=READFI
INIADD = F
*****

Group 12. Convection and diffusion adjustments
No PATCHes used for this Group
*****

Group 13. Boundary & Special Sources
No PATCHes used for this Group

EGWF = T
*****

Group 14. Downstream Pressure For PARAB
*****

Group 15. Terminate Sweeps
LSWEEP = 1000

SELREF = F
*****

Group 16. Terminate Iterations

*****

Group 17. Relaxation
RELAX(C3 ,FALSDT, 1.000000E+03)

```

```

KELIN = 3
*****
Group 18. Limits
VARMAX(C3 ) = 1.000000E+10 ;VARMIN(C3 ) = 1.000000E-10
*****
Group 19. EARTH Calls To GROUND Station
USEGRD = T ;USEGRX = T
NAMSAT =MOSG
GENK = T
ASAP = T
PARSOL = T
CONWIZ = T

* RG(1) = x-direction centerline of lamp
RG( 1) = 1.616000E-01

* RG(2) = z-direction centerline of lamp
RG( 2) = 8.207280E-01

* RG(4) = lamp power, W
RG( 4) = 5.200000E+01*0.57

* RG(9) = y-dir, midpt of lamp (to match old code)
RG( 9) = 9.128130E-01

* RG(10) = length of lamp (L) (to match old code)
RG( 10) = 1.825625E+00

* RG(11) = radius of sleeve, m
RG( 11) = 1.230300E-02

* RG(12) = refractive index of water (nw)
RG( 12) = 1.380000E+00

* RG(13) = refractive index of quartz (nq)
RG( 13) = 1.520000E+00

* RG(19) = convergence factor for iteration completion
RG( 19) = 1.000000E-03

* RG(21) = transmittance (10 mm) in water (Tw)
RG( 21) = 9.290000E-01

* RG(41) = constant for code expansion MP spectrum
RG( 41) = 1.000000E+00

* RG(61) = constant for code expansion MP spectrum
RG( 61) = 1.000000E+00

* RG(81) = pi
RG( 81) = 3.141593E+00

* RG(82) = refractive index of air (na)

```

RG( 82) = 1.000000E+00

\* RG(83) = thickness of quartz sleeve, m  
RG( 83) = 1.500000E-03

\* RG(85) = transmittance (10 mm) in quartz (Tq)  
RG( 85) = 8.850000E-01

\* Energy of one einstein for 254 nm in J/Einstein  
RG( 86) = 4.715280E+05

\* convergence factor iteration number  
RG( 92) = 5.000000E+02

\*\*\*\*\*

Group 20. Preliminary Printout

ECHO = T

\*\*\*\*\*

Group 21. Print-out of Variables

\*\*\*\*\*

Group 22. Monitor Print-Out

IXMON = 21 ;IYMON = 11 ;IZMON = 67

NPRMON = 100000

NPRMNT = 1

TSTSWP = -1

\*\*\*\*\*

Group 23. Field Print-Out & Plot Control

NPRINT = 100000

ISWPRF = 1 ;ISWPRL = 100000

No PATCHes used for this Group

\*\*\*\*\*

Group 24. Dumps For Restarts

GVIEW(P,1.000000E+00,0.000000E+00,0.000000E+00)

GVIEW(UP,0.000000E+00,0.000000E+00,1.000000E+00)

> DOM, SIZE, 2.389910E-01, 2.934530E+00, 1.268010E+00  
> DOM, MONIT, 1.460730E-01, 6.842660E-02, 9.341280E-01  
> DOM, SCALE, 1.000000E+00, 1.000000E+00, 1.000000E+00  
> DOM, SNAPSIZ, 1.000000E-02  
> GRID, RSET\_X\_1, 11, -1.380000E+00  
> GRID, RSET\_X\_2, 8, 1.200000E+00  
> GRID, RSET\_X\_3, -5, 1.000000E+00, G  
> GRID, RSET\_X\_4, 5, 1.000000E+00, G  
> GRID, RSET\_X\_5, -5, 1.000000E+00, G  
> GRID, RSET\_X\_6, 8, -1.200000E+00  
> GRID, RSET\_X\_7, 1, 1.000000E+00  
> GRID, RSET\_Y\_1, -6, 1.120000E+00  
> GRID, RSET\_Y\_2, -9, 1.320000E+00  
> GRID, RSET\_Y\_3, 2, 1.000000E+00  
> GRID, RSET\_Y\_4, 1, 1.000000E+00  
> GRID, RSET\_Y\_5, -19, 1.350000E+00  
> GRID, RSET\_Y\_6, -8, 1.180000E+00

```

> GRID, RSET_Y_7, 1, 1.000000E+00
> GRID, RSET_Y_8, -24, 1.580000E+00
> GRID, RSET_Y_9, 1, 1.000000E+00
> GRID, RSET_Y_10, -24, 1.580000E+00
> GRID, RSET_Y_11, 1, 1.000000E+00
> GRID, RSET_Y_12, -19, 1.450000E+00
> GRID, RSET_Y_13, 1, 1.000000E+00
> GRID, RSET_Y_14, -15, 1.270000E+00
> GRID, RSET_Y_15, -10, 1.230000E+00
> GRID, RSET_Y_16, -28, 1.250000E+00,G
> GRID, RSET_Y_17, -10, 1.220000E+00,G
> GRID, RSET_Y_18, 6, 1.550000E+00
> GRID, RSET_Z_1, -9, 1.500000E+00
> GRID, RSET_Z_2, -34, 1.600000E+00
> GRID, RSET_Z_3, 8, 1.150000E+00
> GRID, RSET_Z_4, -5, 1.000000E+00
> GRID, RSET_Z_5, -5, 1.000000E+00,G
> GRID, RSET_Z_6, -5, 1.100000E+00,G
> GRID, RSET_Z_7, 8,-1.150000E+00
> GRID, RSET_Z_8, -24, 1.500000E+00
> GRID, RSET_Z_9, -10, 1.500000E+00

> OBJ, NAME, REACTOR3
> OBJ, POSITION, 0.000000E+00, 0.000000E+00, 0.000000E+00
> OBJ, SIZE, 2.389905E-01, 2.934527E+00, 1.268006E+00
> OBJ, GEOMETRY, reactor3drev2
> OBJ, ROTATION24, 1
> OBJ, TYPE, BLOCKAGE
> OBJ, COLOR-MODE, USER
> OBJ, COLOR-VAL, 142
> OBJ, OPAQUE, 50
> OBJ, MATERIAL, 198,Solid with smooth-wall friction

> OBJ, NAME, INLET3DR
> OBJ, POSITION, 0.000000E+00, 2.776573E+00, 0.000000E+00
> OBJ, SIZE, 0.000000E+00, 7.930350E-02, 7.923202E-02
> OBJ, GEOMETRY, inlet3drev2
> OBJ, ROTATION24, 1
> OBJ, TYPE, INLET
> OBJ, PRESSURE, 0.000000E+00
> OBJ, VELOCITY, 2.555047E-01, 0.000000E+00, 0.000000E+00
> OBJ, TEMPERATURE, 0.000000E+00
> OBJ, TURB-INTENS, 5.000000E+00

> OBJ, NAME, OUTLET3D
> OBJ, POSITION, 0.000000E+00, 3.496076E-02, 1.188632E+00
> OBJ, SIZE, 0.000000E+00, 7.930348E-02, 7.923210E-02
> OBJ, GEOMETRY, outlet3drev2
> OBJ, ROTATION24, 1
> OBJ, TYPE, OUTLET
> OBJ, PRESSURE, 0.000000E+00
> OBJ, TEMPERATURE, SAME
> OBJ, COEFFICIENT, 1.000000E+03

```

```

> OBJ, TURBULENCE, SAME , SAME

> OBJ, NAME, LAMP3DRE
> OBJ, POSITION, 1.492971E-01, 0.000000E+00, 8.084253E-01
> OBJ, SIZE, 2.460623E-02, 1.825625E+00, 2.460623E-02
> OBJ, GEOMETRY, lamp3drev2
> OBJ, ROTATION24, 1
> OBJ, VISIBLE, NO
> OBJ, TYPE, BLOCKAGE
> OBJ, MATERIAL, 198,Solid with smooth-wall friction

> OBJ, NAME, WIPER3DR
> OBJ, POSITION, 1.235021E-01, 3.397250E-01, 7.826303E-01
> OBJ, SIZE, 7.619619E-02, 1.562100E+00, 7.619625E-02
> OBJ, GEOMETRY, wiper3drev2
> OBJ, ROTATION24, 1
> OBJ, TYPE, BLOCKAGE
> OBJ, MATERIAL, 198,Solid with smooth-wall friction

> OBJ, NAME, BAFFLE13
> OBJ, POSITION, 8.678560E-02, 1.697037E+00, 7.458405E-01
> OBJ, SIZE, 1.496291E-01, 4.762530E-03, 1.497757E-01
> OBJ, GEOMETRY, baffle13drev2
> OBJ, ROTATION24, 1
> OBJ, TYPE, BLOCKAGE
> OBJ, MATERIAL, 198,Solid with smooth-wall friction

> OBJ, NAME, BAFFLE23
> OBJ, POSITION, 8.678405E-02, 1.430338E+00, 7.458678E-01
> OBJ, SIZE, 1.496322E-01, 4.762411E-03, 1.497211E-01
> OBJ, GEOMETRY, baffle23drev2
> OBJ, ROTATION24, 1
> OBJ, TYPE, BLOCKAGE
> OBJ, MATERIAL, 198,Solid with smooth-wall friction

> OBJ, NAME, BAFFLE33
> OBJ, POSITION, 8.678405E-02, 9.096375E-01, 7.458678E-01
> OBJ, SIZE, 1.496322E-01, 4.762471E-03, 1.497211E-01
> OBJ, GEOMETRY, baffle33drev2
> OBJ, ROTATION24, 1
> OBJ, TYPE, BLOCKAGE
> OBJ, MATERIAL, 198,Solid with smooth-wall friction

> OBJ, NAME, BAFFLE43
> OBJ, POSITION, 8.678405E-02, 3.905250E-01, 7.458678E-01
> OBJ, SIZE, 1.496322E-01, 4.762501E-03, 1.497211E-01
> OBJ, GEOMETRY, baffle43drev2
> OBJ, ROTATION24, 1
> OBJ, TYPE, BLOCKAGE
> OBJ, MATERIAL, 198,Solid with smooth-wall friction

> OBJ, NAME, BAFFLE53
> OBJ, POSITION, 8.678405E-02, 1.238250E-01, 7.458678E-01

```

```
> OBJ, SIZE, 1.496322E-01, 4.762501E-03, 1.497211E-01
> OBJ, GEOMETRY, baffle53drev2
> OBJ, ROTATION24, 1
> OBJ, TYPE, BLOCKAGE
> OBJ, MATERIAL, 198,Solid with smooth-wall friction
STOP
</strong></pre></body></html>
```



```

c
  IXL=IABS(IXL)
  IF(IGR.EQ.13) GO TO 13
  IF(IGR.EQ.19) GO TO 19
  GO TO (1,2,3,4,5,6,25,8,9,10,11,12,13,14,25,25,25,25,19,20,25,
  121,23,24),IGR
  25 CONTINUE
  RETURN
C*****
C
C--- GROUP 1. Run title and other preliminaries
C
  1 GO TO (1001,1002,1003),ISC
C
1001 CONTINUE
  CALL MAKE(XG2D )
  CALL MAKE(YG2D )
  CALL MAKE(DXG2D )
  CALL MAKE(DYG2D )
  CALL MAKE(VOL )
  CALL MAKE(ZGNZ )

C * -----GROUP 1 SECTION 3 -----
C--- Use this group to create storage via MAKE, GXMAKE etc which it is
C essential to dump to PHI (or PHIDA) for restarts
C User may here change message transmitted to the VDU screen
  IF(.NOT.NULLPR.AND.IDVCGR.EQ.0)
  1 CALL WRYT40('GROUND file is GROUND.F of: 240802 ')
C
  RETURN
C * -----GROUP 1 SECTION 3 -----
C--- Use this group to create storage via GXMAKE which it is not
C necessary to dump to PHI (or PHIDA) for restarts
C
1003 CONTINUE
  GO TO 25
1002 CONTINUE
  RETURN
C*****
C
C--- GROUP 2. Transience; time-step specification
C
  2 CONTINUE
  RETURN
C*****
C
C--- GROUP 3. X-direction grid specification
C
  3 CONTINUE
  RETURN
C*****
C
C--- GROUP 4. Y-direction grid specification

```

```

C
  4 CONTINUE
  RETURN
C*****
C
C--- GROUP 5. Z-direction grid specification
C
  5 CONTINUE
  RETURN
C*****
C
C--- GROUP 6. Body-fitted coordinates or grid distortion
C
  6 CONTINUE
  RETURN
C*****
C * Make changes for this group only in group 19.
C--- GROUP 7. Variables stored, solved & named
C*****
C
C--- GROUP 8. Terms (in differential equations) & devices
C
  8 GO TO (81,82,83,84,85,86,87,88,89,810,811,812,813,814,815,816)
  1,ISC
  81 CONTINUE
C * ----- SECTION 1 -----
C For U1AD.LE.GRND--- phase 1 additional velocity. Index VELAD
  RETURN
  82 CONTINUE
C * ----- SECTION 2 -----
C For U2AD.LE.GRND--- phase 2 additional velocity. Index VELAD
  RETURN
  83 CONTINUE
C * ----- SECTION 3 -----
C For V1AD.LE.GRND--- phase 1 additional velocity. Index VELAD
  RETURN
  84 CONTINUE
C * ----- SECTION 4 -----
C For V2AD.LE.GRND--- phase 2 additional velocity. Index VELAD
  RETURN
  85 CONTINUE
C * ----- SECTION 5 -----
C For W1AD.LE.GRND--- phase 1 additional velocity. Index VELAD
  RETURN
  86 CONTINUE
C * ----- SECTION 6 -----
C For W2AD.LE.GRND--- phase 2 additional velocity. Index VELAD
  RETURN
  87 CONTINUE
C * ----- SECTION 7 ---- Volumetric source for gala
  RETURN
  88 CONTINUE
C * ----- SECTION 8 ---- Convection fluxes

```

```

C--- Entered when UCONV =.TRUE.; block-location indices are:
C  LD11 for east and north (accessible at the same time),
C  LD12 for west and south (accessible at the same time),
C  LD2  for high (which becomes low for the next slab).
C  User should provide INDVAR and NDIREC IF's as appropriate.
  RETURN
89 CONTINUE
C * ----- SECTION 9 ---- Diffusion coefficients
C--- Entered when UDIFF =.TRUE.; block-location indices are LAE
C  for east, LAW for west, LAN for north, LAS for
C  south, LD11 for high, and LD11 for low.
C  User should provide INDVAR and NDIREC IF's as above.
C  EARTH will apply the DIFCUT and GP12 modifications after the user
C  has made his settings.
C
  RETURN
810 CONTINUE
C * ----- SECTION 10 --- Convection neighbors
  RETURN
811 CONTINUE
C * ----- SECTION 11 --- Diffusion neighbors
  RETURN
812 CONTINUE
C * ----- SECTION 12 --- Linearised sources
  RETURN
813 CONTINUE
C * ----- SECTION 13 --- Correction coefficients
  RETURN
814 CONTINUE
C * ----- SECTION 14 --- User's own solver
  RETURN
815 CONTINUE
C * ----- SECTION 15 --- Change solution
  RETURN
816 CONTINUE
C * ----- SECTION 16 --- Change DVEL/DPs
  RETURN
C
C * See the equivalent section in GREX for the indices to be
C  used in sections 7 - 16
C
C * Make all other group-8 changes in GROUP 19.
C*****
C
C--- GROUP 9. Properties of the medium (or media)
C
C  The sections in this group are arranged sequentially in their
C  order of calling from EARTH. Thus, as can be seen from below,
C  the temperature sections (10 and 11) precede the density
C  sections (1 and 3); so, density formulae can refer to
C  temperature stores already set.
  9 GO TO (91,92,93,94,95,96,97,98,99,900,901,902,903,904,905),ISC
C*****

```

```

900 CONTINUE
C * ----- SECTION 10 -----
C For TMP1.LE.GRND----- phase-1 temperature Index TEMP1
  RETURN
901 CONTINUE
C * ----- SECTION 11 -----
C For TMP2.LE.GRND----- phase-2 temperature Index TEMP2
  RETURN
902 CONTINUE
C * ----- SECTION 12 -----
C For EL1.LE.GRND----- phase-1 length scale Index LEN1
  RETURN
903 CONTINUE
C * ----- SECTION 13 -----
C For EL2.LE.GRND----- phase-2 length scale Index LEN2
  RETURN
904 CONTINUE
C * ----- SECTION 14 -----
C For SOLVE(TEM1)----- phase-1 specific heat
  RETURN
905 CONTINUE
C * ----- SECTION 15 -----
C For SOLVE(TEM2)----- phase-2 specific heat
  RETURN
91 CONTINUE
C * ----- SECTION 1 -----
C For RHO1.LE.GRND--- density for phase 1   Index DEN1
  RETURN
92 CONTINUE
C * ----- SECTION 2 -----
C For DRH1DP.LE.GRND--- D(LN(DEN))/DP for phase 1
C                               Index D1DP
  RETURN
93 CONTINUE
C * ----- SECTION 3 -----
C For RHO2.LE.GRND--- density for phase 2   Index DEN2
  RETURN
94 CONTINUE
C * ----- SECTION 4 -----
C For DRH2DP.LE.GRND--- D(LN(DEN))/DP for phase 2
C                               Index D2DP
  RETURN
95 CONTINUE
C * ----- SECTION 5 -----
C For ENUT.LE.GRND--- reference turbulent kinematic viscosity
C                               Index VIST
  RETURN
96 CONTINUE
C * ----- SECTION 6 -----
C For ENUL.LE.GRND--- reference laminar kinematic viscosity
C                               Index VISL
  RETURN
97 CONTINUE

```

```

C * ----- SECTION 7 -----
C For PRNDTL().LE.GRND--- laminar PRANDTL nos., or diffusivity
C                               Index LAMPR
  RETURN
98 CONTINUE
C * ----- SECTION 8 -----
C For PHINT().LE.GRND--- interface value of first phase
C                               Index FII1
  RETURN
99 CONTINUE
C * ----- SECTION 9 -----
C For PHINT().LE.GRND--- interface value of second phase
C                               Index FII2
  RETURN
C*****
C
C--- GROUP 10. Inter-phase-transfer processes and properties
C
  10 GO TO (101,102,103,104,105),ISC
  101 CONTINUE
C * ----- SECTION 1 -----
C For CFIPS.LE.GRND--- inter-phase friction coeff.
C                               Index INTFRC
  RETURN
c<a name="10.2"></a>
  102 CONTINUE
C * ----- SECTION 2 -----
C For CMDOT.EQ.GRND- inter-phase mass transfer Index INTMDT
  RETURN
  103 CONTINUE
C * ----- SECTION 3 -----
C For CINT().EQ.GRND--- phase1-to-interface transfer coefficients
C                               Index COI1
  RETURN
  104 CONTINUE
C * ----- SECTION 4 -----
C For CINT().EQ.GRND--- phase2-to-interface transfer coefficients
C                               Index COI2
  RETURN
  105 CONTINUE
C * ----- SECTION 5 -----
C For CVM.EQ.GRND--- virtual mass coefficient
C                               Index LD12
  RETURN
C*****
C
C--- GROUP 11. Initialization of variable or porosity fields
C                               Index VAL
  11 CONTINUE
  RETURN
C*****
C
C--- GROUP 12. Convection and diffusion adjustments

```

```

C
  12 CONTINUE
  RETURN
C*****
C
C--- GROUP 13. Boundary conditions and special sources
C          Index for Coefficient - CO
C          Index for Value    - VAL
  13 CONTINUE
  GO TO (130,131,132,133,134,135,136,137,138,139,1310,
        11311,1312,1313,1314,1315,1316,1317,1318,1319,1320,1321),ISC
  130 CONTINUE
C----- SECTION 1 ----- coefficient = GRND
  RETURN
  131 CONTINUE
C----- SECTION 2 ----- coefficient = GRND1
  RETURN
  132 CONTINUE
C----- SECTION 3 ----- coefficient = GRND2
  RETURN
  133 CONTINUE
C----- SECTION 4 ----- coefficient = GRND3
  RETURN
  134 CONTINUE
C----- SECTION 5 ----- coefficient = GRND4
  RETURN
  135 CONTINUE
C----- SECTION 6 ----- coefficient = GRND5
  RETURN
  136 CONTINUE
C----- SECTION 7 ----- coefficient = GRND6
  RETURN
  137 CONTINUE
C----- SECTION 8 ----- coefficient = GRND7
  RETURN
  138 CONTINUE
C----- SECTION 9 ----- coefficient = GRND8
  RETURN
  139 CONTINUE
C----- SECTION 10 ----- coefficient = GRND9
  RETURN
  1310 CONTINUE
C----- SECTION 11 ----- coefficient = GRND10
  RETURN
  1311 CONTINUE
C----- SECTION 12 ----- value = GRND
C   Source name: SORC46
  IF(INDVAR.EQ.INAME('C3  ').AND.NPATCH.EQ.'IRR1  ') THEN
    LFVAL =L0F(VAL)
    LFRR1 =L0F(INAME('RR1  '))
    LFHH1 =L0F(INAME('HH1  '))
    LFFR12 =L0F(INAME('FR12  '))
    LFFR11 =L0F(INAME('FR11  '))

```

```

DO 13845 IX=IXF ,IXL
IADD=NY*(IX-1)
DO 13845 IY=IYF ,IYL
I=IY+IADD
L0RR1 =LFRR1 +I
L0HH1 =LFHH1 +I
L0FR12 =LFFR12 +I
L0FR11 =LFFR11 +I
13845 F(LFVAL+I)=AMIN1(RG(4)/(4.*RG(81)*RG(10)*F(L0RR1))
1*(ATAN((RG(10)/2.+F(L0HH1))/F(L0RR1))+ATAN((RG(10)/2.
1-F(L0HH1 ))/F(L0RR1))),RG(4)/(2.*RG(81)*RG(10)
1*F(L0RR1 )))*(F(L0FR12)+TINY)/(F(L0FR11)+TINY)
ENDIF
RETURN
1312 CONTINUE
C----- SECTION 13 ----- value = GRND1
RETURN
1313 CONTINUE
C----- SECTION 14 ----- value = GRND2
RETURN
1314 CONTINUE
C----- SECTION 15 ----- value = GRND3
RETURN
1315 CONTINUE
C----- SECTION 16 ----- value = GRND4
RETURN
1316 CONTINUE
C----- SECTION 17 ----- value = GRND5
RETURN
1317 CONTINUE
C----- SECTION 18 ----- value = GRND6
RETURN
1318 CONTINUE
C----- SECTION 19 ----- value = GRND7
RETURN
1319 CONTINUE
C----- SECTION 20 ----- value = GRND8
RETURN
1320 CONTINUE
C----- SECTION 21 ----- value = GRND9
RETURN
1321 CONTINUE
C----- SECTION 22 ----- value = GRND10
RETURN
C*****
C
C--- GROUP 14. Downstream pressure for PARAB=.TRUE.
C
14 CONTINUE
RETURN
C*****
C* Make changes to data for GROUPS 15, 16, 17, 18 GROUP 19.
C*****

```

```

C
C--- GROUP 19. Special calls to GROUND from EARTH
C
  19 GO TO (191,192,193,194,195,196,197,198,199,1910,1911),ISC
  191 CONTINUE
C * ----- SECTION 1 ---- Start of time step.
  RETURN
  192 CONTINUE
C * ----- SECTION 2 ---- Start of sweep.
  RETURN
  193 CONTINUE
C * ----- SECTION 3 ---- Start of iz slab.
  RETURN
  194 CONTINUE
C * ----- SECTION 4 ---- Start of iterations over slab.
  RETURN
  1911 CONTINUE
C * ----- SECTION 11---- After calculation of convection
C           fluxes for scalars, and of volume
C           fractions, but before calculation of
C           scalars or velocities
  RETURN
  199 CONTINUE
C * ----- SECTION 9 ---- Start of solution sequence for
C           a variable
  CALL FN0(LBNAME('DXX3'),DXG2D)
  CALL FN0(LBNAME('DYY3'),DYG2D)
  CALL FN0(LBNAME('VOL3'),VOL)

C  Grid Dimensions for Entire Reactor Block
C  YYF=FIRST Y DIRECTION (BEGIN), YYL=LAST Y DIRECTION (END)

  XXF=10
  XXL=43
  YYF=1
  YYL=133
  ZZF=15
  ZZL=106
C*****
C  Special calls name: SC10
C  Special calls name: SC1001
  IF(ISTEP.GE.1 .AND.ISTEP.LE.LSTEP ) THEN
  IF(IZ.GE.ZZF .AND.IZ.LE.ZZL ) THEN
  LFRR1 =L0F(INAME('RR1 '))
  LFXG2D=L0F(XG2D )
  L0ZGNZ=L0F(ZGNZ )+IZ
  DO 19901 IX=XXF ,XXL
  IADD=NY*(IX-1)
  DO 19901 IY=YYF ,YYL
  I=IY+IADD
  L0RR1 =LFRR1 +I
  L0XG2D=LFXG2D+I
  19901 F(L0RR1 )=(F(L0XG2D)-RG(1))**2.+(F(L0ZGNZ)-RG(2))**2

```

```

1.)*0.5+TINY
ENDIF
ENDIF
C*****
C   Special calls name: SC10
C   Special calls name: SC1002
IF(ISTEP.GE.1 .AND.ISTEP.LE.LSTEP ) THEN
IF(IZ.GE.ZZF .AND.IZ.LE.ZZL ) THEN
LFHH1 =L0F(INAME('HH1 '))
LFYG2D=L0F(YG2D )
DO 19902 IX=XXF ,XXL
IADD=NY*(IX-1)
DO 19902 IY=YYF ,YYL
I=IY+IADD
L0HH1 =LFHH1 +I
L0YG2D=LFYG2D+I
19902 F(L0HH1 )=-(F(L0YG2D)-RG(9)+TINY)
ENDIF
ENDIF
C*****
C   Special calls name: SC10
C   Special calls name: SC1011
IF(ISTEP.GE.1 .AND.ISTEP.LE.LSTEP ) THEN
IF(IZ.GE.ZZF .AND.IZ.LE.ZZL ) THEN
LFFR11 =L0F(INAME('FR11 '))
LFRR1 =L0F(INAME('RR1 '))
LFHH1 =L0F(INAME('HH1 '))
DO 19911 IX=XXF ,XXL
IADD=NY*(IX-1)
DO 19911 IY=YYF ,YYL
I=IY+IADD
L0FR11 =LFFR11 +I
L0RR1 =LFRR1 +I
L0HH1 =LFHH1 +I
19911 F(L0FR11 )=1.0/(F(L0RR1)**2+(RG(10)/2-F(L0HH1)-1*RG(
110)/60)**2+TINY)+1.0/(F(L0RR1)**2+(RG(10)/2-F(L0HH1)-
13*RG(10)/60)**2+TINY)+1.0/(F(L0RR1)**2+(RG(10)/2-F(L0HH1)-
15*RG(10)/60)**2+TINY)+1.0/(F(L0RR1)**2+(RG(10)/2-F(L0HH1)-
17*RG(10)/60)**2+TINY)+1.0/(F(L0RR1)**2+(RG(10)/2-F(L0HH1)-
19*RG(10)/60)**2+TINY)+1.0/(F(L0RR1)**2+(RG(10)/2-F(L0HH1)-
111*RG(10)/60)**2+TINY)+1.0/(F(L0RR1)**2+(RG(10)/2-F(L0HH1)-
113*RG(10)/60)**2+TINY)+1.0/(F(L0RR1)**2+(RG(10)/2-F(L0HH1)-
115*RG(10)/60)**2+TINY)+1.0/(F(L0RR1)**2+(RG(10)/2-F(L0HH1)-
117*RG(10)/60)**2+TINY)+1.0/(F(L0RR1)**2+(RG(10)/2-F(L0HH1)-
119*RG(10)/60)**2+TINY)+1.0/(F(L0RR1)**2+(RG(10)/2-F(L0HH1)-
121*RG(10)/60)**2+TINY)+1.0/(F(L0RR1)**2+(RG(10)/2-F(L0HH1)-
123*RG(10)/60)**2+TINY)+1.0/(F(L0RR1)**2+(RG(10)/2-F(L0HH1)-
125*RG(10)/60)**2+TINY)+1.0/(F(L0RR1)**2+(RG(10)/2-F(L0HH1)-
127*RG(10)/60)**2+TINY)+1.0/(F(L0RR1)**2+(RG(10)/2-F(L0HH1)-
129*RG(10)/60)**2+TINY)+1.0/(F(L0RR1)**2+(RG(10)/2-F(L0HH1)-
131*RG(10)/60)**2+TINY)+1.0/(F(L0RR1)**2+(RG(10)/2-F(L0HH1)-
133*RG(10)/60)**2+TINY)+1.0/(F(L0RR1)**2+(RG(10)/2-F(L0HH1)-
135*RG(10)/60)**2+TINY)+1.0/(F(L0RR1)**2+(RG(10)/2-F(L0HH1)-

```

```

137*RG(10)/60)**2+TINY)+1.0/(F(L0RR1)**2+(RG(10)/2-F(L0HH1)-
139*RG(10)/60)**2+TINY)+1.0/(F(L0RR1)**2+(RG(10)/2-F(L0HH1)-
141*RG(10)/60)**2+TINY)+1.0/(F(L0RR1)**2+(RG(10)/2-F(L0HH1)-
143*RG(10)/60)**2+TINY)+1.0/(F(L0RR1)**2+(RG(10)/2-F(L0HH1)-
145*RG(10)/60)**2+TINY)+1.0/(F(L0RR1)**2+(RG(10)/2-F(L0HH1)-
147*RG(10)/60)**2+TINY)+1.0/(F(L0RR1)**2+(RG(10)/2-F(L0HH1)-
149*RG(10)/60)**2+TINY)+1.0/(F(L0RR1)**2+(RG(10)/2-F(L0HH1)-
151*RG(10)/60)**2+TINY)+1.0/(F(L0RR1)**2+(RG(10)/2-F(L0HH1)-
153*RG(10)/60)**2+TINY)+1.0/(F(L0RR1)**2+(RG(10)/2-F(L0HH1)-
155*RG(10)/60)**2+TINY)+1.0/(F(L0RR1)**2+(RG(10)/2-F(L0HH1)-
157*RG(10)/60)**2+TINY)+1.0/(F(L0RR1)**2+(RG(10)/2-F(L0HH1)-
159*RG(10)/60)**2+TINY)
ENDIF
ENDIF

```

C\*\*\*\*\*

C Special calls name: SC10

C Special calls name: SC1019

```

IF(ISTEP.GE.1 .AND.ISTEP.LE.LSTEP ) THEN
IF(IZ.GE.ZZF .AND.IZ.LE.ZZL ) THEN
LFFR12 =L0F(INAME('FR12 '))
LFRR1 =L0F(INAME('RR1 '))
LFHH1 =L0F(INAME('HH1 '))
DO 19919 IX=XXF ,XXL
IADD=NY*(IX-1)
DO 19919 IY=YYF ,YYL
I=IY+IADD
L0FR12 =LFFR12 +I
L0RR1 =LFRR1 +I
L0HH1 =LFHH1 +I
F(L0FR12 )=0.0
DO 39919 J=1,30
AN1=RG(12)
AN2=RG(13)
AN3=RG(82)
AD1=ABS(F(L0RR1)-RG(11))
AD2=RG(83)
AD3=RG(11)-RG(83)
AD=ABS(RG(10)/2.-F(L0HH1)-(2*J-1)*RG(10)/60.)
ACF=RG(19)
ACFEND=RG(92)
ANG2=CALANG(AN1,AN2,AN3,AD1,AD2,AD3,AD,ACF,ACFEND)
ANG1=ASIN(SIN(ANG2)*AN2/AN1)
ANG3=ASIN(SIN(ANG2)*AN2/AN3)
ARV1=(AN3*COS(ANG3)-AN2*COS(ANG2))/(AN3*COS(ANG3)+AN2*COS(ANG2))
ARH1=(AN2*COS(ANG3)-AN3*COS(ANG2))/(AN3*COS(ANG2)+AN2*COS(ANG3))
AR1=0.5*(ARV1**2+ARH1**2)
IF(AR1>1.0) THEN
AR1=1.0
ENDIF
ARV2=(AN2*COS(ANG2)-AN1*COS(ANG1))/(AN2*COS(ANG2)+AN1*COS(ANG1))
ARH2=(AN1*COS(ANG2)-AN2*COS(ANG1))/(AN2*COS(ANG1)+AN1*COS(ANG2))
AR2=0.5*(ARV2**2+ARH2**2)
IF(AR2>1.0) THEN

```

```

    AR2=1.0
    ENDIF
    DO 49919 K=1,1
C   * RG(21) = transmittance (10 mm) in water (Tw)
      ATR1=RG(K+20)
C   * RG(85) = transmittance (10 mm) in quartz (Tq)
      ATR2=RG(K+84)
      APF=RG(K+40)
      AGF=RG(K+60)
    ARAD=CALRAD(AD1,AD2,AD3,ANG1,ANG2,ANG3,ATR1,ATR2,APF,AGF)
      F(L0FR12 )=F(L0FR12 )+ARAD

49919 CONTINUE
39919 CONTINUE
19919 CONTINUE
    ENDIF
    ENDIF

    RETURN
1910 CONTINUE
C * ----- SECTION 10---- Finish of solution sequence for
C                               a variable
    RETURN
195 CONTINUE
C * ----- SECTION 5 ---- Finish of iterations over slab.
    RETURN
196 CONTINUE
C * ----- SECTION 6 ---- Finish of iz slab.
    RETURN
197 CONTINUE
C * ----- SECTION 7 ---- Finish of sweep.
    RETURN
198 CONTINUE
C * ----- SECTION 8 ---- Finish of time step.
C
    RETURN
C*****
C
C--- GROUP 20. Preliminary print-out
C
20 CONTINUE
    RETURN
C*****
C--- GROUP 21. Special print-out to screen
21 CONTINUE
    GO TO 25
C*****
C* Make changes to data for GROUP 22 only in GROUP 19.
C*****
C
C--- GROUP 23. Field print-out and plot control
23 CONTINUE
    RETURN

```

```

C*****
C
C--- GROUP 24. Dumps for restarts
C
  24 CONTINUE
    CONTAINS
      FUNCTION CALANG(N1,N2,N3,D1,D2,D3,D,CF,CFEND) RESULT(CALANG_RESULT)
      REAL N1,N2,N3,D1,D2,D3,D,CF,CALANG_RESULT,CFEND
      REAL ANG1,ANG2,ANG3
      ANG1=0.0
      ANG2=ASIN(N3/N2)
      ANG3=(ANG1+ANG2)/2.0
      countcf=0
      countcf2=0
30650 IF (D1*TAN(ASIN(SIN(ANG3)*N2/N1))+D2*TAN(ANG3)+D3*TAN(ASIN(
C SIN(ANG3)*N2/N3))-D.GT.CF) THEN
      ANG2=ANG3
      ANG3=(ANG1+ANG2)/2.0
      countcf=countcf+1
      if(countcf.gt.CFEND) goto 30651
      GOTO 30650
    endif
30651 continue
      IF(D1*TAN(ASIN(SIN(ANG3)*N2/N1))+D2*TAN(ANG3)+D3*TAN(ASIN(
C SIN(ANG3)*N2/N3))-D.LT.-CF) THEN
      ANG1=ANG3
      ANG3=(ANG1+ANG2)/2.0
      countcf2=countcf2+1
      if(countcf2.gt.CFEND) goto 30652
      GOTO 30650
    END IF
30652 continue
      CALANG_RESULT=ANG3
      END FUNCTION CALANG

      FUNCTION CALRAD(D1,D2,D3,ANG1,ANG2,ANG3,TR1,TR2,PF,GF)
      C RESULT(CALRAD_RESULT)
      REAL D1,D2,D3,ANG1,ANG2,ANG3,TR1,TR2,PF,GF
      REAL CALRAD_RESULT
      CALRAD_RESULT=TR1**(100*D1/COS(ANG1))*TR2**(100*D2/COS(ANG2))/
C (D1/COS(ANG1)+D2/COS(ANG2)+D3/COS(ANG3))**2.*PF*GF
      END FUNCTION CALRAD

      END
c</pre></strong></body></html>

```

## Sample CFD Q1 Code – Kinetics (Research Condition No. 5)

```
<html><head><title>Q1</title>
<link rel="stylesheet" type="text/css"
href="/phoenics/d_polis/polstyle.css">
</head><body><pre><strong>
TALK=T;RUN( 1, 1)

*****
Q1 created by VDI menu, Version 2006, Date 21/09/06
CPVNAM=VDI;SPPNAM=Core
*****
IRUNN = 1 ;LIBREF = 0
*****
Group 1. Run Title
TEXT(LP3DR5 MR200 Q20 L51 5B Kinetics Rev B )
*****
Group 2. Transience
STEADY = T
*****
Groups 3, 4, 5 Grid Information
* Overall number of cells, RSET(M,NX,NY,NZ,tolerance)
RSET(M,43,185,108)
*****
Group 6. Body-Fitted coordinates
*****
Group 7. Variables: STOREd,SOLVEd,NAMED
ONEPHS = T
* Non-default variable names
NAME(147)=EPKE ; NAME(148)=DEN1
NAME(149)=EL1 ; NAME(150)=ENUT
* Solved variables list
SOLVE(C1 ,C2 ,C5 ,C6 )
SOLVE(C9 ,C10 )
* Stored variables list
STORE(ENUT,EL1 ,DEN1,EPKE)
STORE(U1 ,V1 ,W1 ,P1 )
STORE(C3 ,OHSS,O2SS)
* Additional solver options
TURMOD(KEMODL)
STORE(KE,EP)

*****
Group 8. Terms & Devices
**SCHEME(SMART ,ALL)
*****
Group 9. Properties
PRESS0 = 1.000000E+05 ;TEMP0 = 2.730000E+02
* Domain material index is 67 signifying:
* WATER at 20. deg C
SETPRPS(1, 67)
DVO1DT = 1.180000E-04
```

PRT (EP ) = 1.314000E+00

\*\*\*\*\*

Group 10.Inter-Phase Transfer Processes

Echo PLANT settings

PLANTBEGIN

NAMSAT=MOSG

\* Convert C1,C2 from velocity file to non-dim variables C5,C6

PATCH(INIT,INIVAL,1,NX,1,NY,1,NZ,1,1)

<INIT01> VAL=RG(90)

INIT(INIT,C1,0.0,GRND)

<INIT02> VAL=RG(88)

INIT(INIT,C2,0.0,GRND)

<INIT03> VAL=C1/RG(90)

INIT(INIT,C5,0.0,GRND)

<INIT04> VAL=C2/RG(88)

INIT(INIT,C6,0.0,GRND)

<INIT05> VAL=C1/RG(90)

INIT(INIT,C9,0.0,GRND)

<INIT06> VAL=C2/RG(88)

INIT(INIT,C10,0.0,GRND)

\* OHSS is normalized SS Hydroxyl Radical Concentration, [•OH]/[H2O2]0

<SC0905> OHSS=(((-RG(24)\*C5\*RG(90))-RG(30)\*O2SS\*RG(90))-RG(\$  
31)\*C6\*RG(88))-RG(33)-(RG(34)\*RG(35))-(RG(37)\*RG(38)\$  
)-(RG(39)\*RG(40))-(RG(71)\*RG(59))-(RG(72)\*RG(58))-(RG(74)\*RG(73\$  
)))-(((((-RG(24)\*C5\*RG(90))-RG(30)\*O2SS\*RG(90))-(\$  
RG(31)\*C6\*RG(88))-RG(33)-(RG(34)\*RG(35))-(RG(37)\*RG(38))-(RG(39\$  
) \*RG(40))-(RG(71)\*RG(59))-(RG(72)\*RG(58))-(RG(74)\*RG\$  
(73))\*\*2)-(4.\*(-RG(26)\*RG(90))\*(2.\*RG(22)\*RG(89)\*C5\*((C3\*100)\$  
/(RG(86)\*1000)))+(RG(32)\*C5\*O2SS\*RG(90))))+TINY)\*\*0\$  
.5)/(2.\*(-RG(26)\*RG(90))+TINY)

\* O2SS is normalized SS radical concentration, [•O2-]/[H2O2]0

<SC0906> O2SS=(RG(24)\*C5\*OHSS)/((RG(30)\*OHSS)+(RG(32)\*C5)+TINY)

\* C5 is normalized peroxide concentration, [H2O2]/[H2O2]0

PATCH(PLSR1,PHASEM,10,43,1,133,15,106,1,LSTEP)

<SORC57> VAL=(-1.\*RG(22)\*RG(89)\*C5\*((C3\*100)/(RG(86)\*1000)))-(R\$  
G(24)\*C5\*OHSS\*RG(90))-(RG(32)\*C5\*O2SS\*RG(90))+(RG(26\$  
) \*OHSS\*OHSS\*RG(90))

COVAL(PLSR1,C5,FIXFLU,GRND)

\* C6 is normalized contaminant concentration, [MB]/[MB]0

PATCH(PLSR2,PHASEM,10,43,1,133,15,106,1,LSTEP)

<SORC58> VAL=(-RG(31)\*C6\*OHSS\*RG(90))-RG(84)\*RG(87)\*C6\*((C3\*10\$  
0)/(RG(86)\*1000))

COVAL(PLSR2,C6,FIXFLU,GRND)

PLANTEND

\*\*\*\*\*

Group 11.Initialise Var/Porosity Fields

No PATCHes used for this Group

```
FIINIT(U1 )= READFI ;FIINIT(V1 )= READFI
FIINIT(W1 )= READFI ;FIINIT(KE )= READFI
FIINIT(EP )= READFI ;FIINIT(C3 )= READFI
FIINIT(P1 )= READFI
FIINIT(EPKE)= READFI ;FIINIT(DEN1)= READFI
FIINIT(EL1 )= READFI ;FIINIT(ENUT)= READFI
```

INIADD = F

\*\*\*\*\*

Group 12. Convection and diffusion adjustments

No PATCHes used for this Group

\*\*\*\*\*

Group 13. Boundary & Special Sources

No PATCHes used for this Group

EGWF = T

\*\*\*\*\*

Group 14. Downstream Pressure For PARAB

\*\*\*\*\*

Group 15. Terminate Sweeps

LSWEEP = 80000

SELREF = F

\*\*\*\*\*

Group 16. Terminate Iterations

\*\*\*\*\*

Group 17. Relaxation

```
RELAX(C1 ,FALSDT, 1.000000E-01)
RELAX(C2 ,FALSDT, 1.000000E-01)
RELAX(C5 ,FALSDT, 1.000000E-03)
RELAX(C6 ,FALSDT, 1.000000E-03)
RELAX(C9 ,FALSDT, 1.000000E-03)
RELAX(C10 ,FALSDT, 1.000000E-03)
```

KELIN = 3

\*\*\*\*\*

Group 18. Limits

```
VARMAX(C1 )= 1.000000E+02 ;VARMIN(C1 )= 1.000000E-20
VARMAX(C2 )= 1.000000E+02 ;VARMIN(C2 )= 1.000000E-20
VARMAX(C5 )= 1.000000E+02 ;VARMIN(C5 )= 1.000000E-20
VARMAX(C6 )= 1.000000E+02 ;VARMIN(C6 )= 1.000000E-20
VARMAX(C9 )= 1.000000E+02 ;VARMIN(C9 )= 0.000000E+00
VARMAX(C10 )= 1.000000E+02 ;VARMIN(C10 )= 0.000000E+00
*****
```

Group 19. EARTH Calls To GROUND Station

```
USEGRD = T ;USEGRX = T
NAMSAT =MOSG
GENK = T
ASAP = T
PARSOL = T
```

CONWIZ = T

\* RG(22) = quantum yield of hydrogen peroxide  
RG( 22) = 5.000000E-01

\* RG(24) = k2 (per Crittenden et al.), M-1 s-1  
RG( 24) = 2.700000E+07

\* RG(25) = k4 (per Crittenden et al.), M-1 s-1  
RG( 25) = 3.000000E+00

\* RG(26) = k13 (per Crittenden et al.), M-1 s-1  
RG( 26) = 5.500000E+09

\* RG(27) = k14 (per Crittenden et al.), M-1 s-1  
RG( 27) = 6.600000E+09

\* RG(28) = k15 (per Crittenden et al.), M-1 s-1  
RG( 28) = 8.300000E+05

\* RG(29) = k16 (per Crittenden et al.), M-1 s-1  
RG( 29) = 9.700000E+07

\* RG(30) = k17 (per Crittenden et al.), M-1 s-1  
RG( 30) = 7.000000E+09

\*\*\* RG(31) = 2nd order rate constant for MB+OH, M-1 s-1  
RG( 31) = 6.900000E+10

\* RG(32) = k5 (per Crittenden et al.), M-1 s-1  
RG( 32) = 1.300000E-01

\*\*\* RG(33) = First Order Radical Scavenger, ks, s-1  
RG( 33) = 0.000000E+00

\* RG(34) = 2nd Order DOC Radical Scavenger, kDOC, L mg-1 s-1  
RG( 34) = 2.500000E+04

\*\*\* RG(35) = DOC Concentration, DOC, mg L-1  
RG( 35) = 5.700000E-01

\*\*\* RG(36) = Total Alkalinity ALK, mg L-1 as CaCO3  
RG( 36) = 2.220000E+01

\* RG(37) = 2nd Order HCO3- Radical Scavenger, kHCO3-, M-1 s-1  
RG( 37) = 8.500000E+06

\* RG(38) = HCO3- Concentration, M (Assume neutral pH)  
RG( 38) = RG(36)\*(1/100)\*(1/1000)\*2

\* RG(39) = 2nd Order CO3- Radical Scavenger, kCO3-, M-1 s-1  
RG( 39) = 3.900000E+08

\*\*\* RG(40) = CO<sub>3</sub>- Concentration, M (Assume neutral pH)  
 RG( 40) = 0.000000E+00

\* RG(41) = constant for code expansion MP spectrum  
 RG( 41) = 1.000000E+00

\*\*\* RG(51) = pH  
 RG( 51) = 7.230000E+00

\*\*\* RG(52) = Free Chlorine Concentration, mg L-1 as Cl<sub>2</sub>  
 RG( 52) = 0.000000E+00

\*\*\* RG(53) = Combined Chlorine Concentration, mg L-1 as Cl<sub>2</sub>  
 RG( 53) = 0.013000E+00

\* RG(54) = Proton Concentration, M  
 RG( 54) = 10\*\*(-1\*RG(51))

\* RG(55) = Free Chlorine Concentration, M  
 RG( 55) = RG(52)/(7.090000E+04)

\* RG(56) = Equilibrium Constant HOCl/OCl<sup>-</sup>, K<sub>a</sub>  
 RG( 56) = 3.162278E-08

\* RG(57) = Fraction of Free Cl that is HOCl  
 RG( 57) = 1/(1+(RG(56)/RG(54)))

\* RG(58) = HOCl Concentration, M  
 RG( 58) = RG(57)\*RG(55)

\* RG(59) = OCl<sup>-</sup> Concentration, M  
 RG( 59) = (1-RG(57))\*RG(55)

\* RG(61) = constant for code expansion MP spectrum  
 RG( 61) = 1.000000E+00

\* RG(71) = 2nd Order OCl<sup>-</sup> Radical Scavenger, kOCl<sup>-</sup>, M-1 s-1  
 RG( 71) = 8.800000E+09

\* RG(72) = 2nd Order HOCl Radical Scavenger, kHOCl, M-1 s-1  
 RG( 72) = 8.500000E+04

\* RG(73) = Monochloramine Concentration, M (Assume no di- or tri-)  
 RG( 73) = RG(53)/(7.090000E+04)

\* RG(74) = 2nd Order NH<sub>2</sub>Cl Radical Scavenger, kNH<sub>2</sub>Cl, M-1 s-1  
 RG( 74) = 2.800000E+09

\* RG(81) = pi  
 RG( 81) = 3.141593E+00

\*\*\* RG(84) = Quantum Yield of Direct Photolysis of Contaminant (MB)  
 RG( 84) = 0.000000E+00

\* Energy of one einstein for 254 nm in J/Einstein  
RG( 86) = 4.715280E+05

\*\*\* Contaminant (MB) molar absorptivity (M<sup>-1</sup> cm<sup>-1</sup>)  
RG( 87) = 1.900000E+01

\* Peroxide molar absorptivity (M<sup>-1</sup> cm<sup>-1</sup>)  
RG( 89) = 1.960000E+01

\*\*\* Background absorbance (1/cm)  
RG( 91) = 0.000000E+00

\* convergence factor iteration number  
RG( 92) = 5.000000E+02

\*\*\* Main inlet velocity (m/s);should match geometry attrib  
RG( 93) = 2.555047E-01

\*\*\* Main inlet area (m<sup>2</sup>);should match geometry  
RG( 94) = (7.937503E-02\*7.937503E-02)\*(3.14159/4)

\* Total Flow (m<sup>3</sup>/s);should match geometry attrib  
RG(101) = RG(93)\*RG(94)

\*\*\* Peroxide C1 initial concentration into reactor (mol/L)  
RG( 90) = 199.7\*1.563230E-06

\*\*\* Contaminant C2 initial concentration into reactor (mol/L)  
RG( 88) = 1.563230E-06

\*\*\*\*\*

Group 20. Preliminary Printout  
ECHO = T

\*\*\*\*\*

Group 21. Print-out of Variables

\*\*\*\*\*

Group 22. Monitor Print-Out

IXMON = 21 ;IYMON = 11 ;IZMON = 67

NPRMON = 100000

NPRMNT = 1

TSTSWP = -1

\*\*\*\*\*

Group 23. Field Print-Out & Plot Control

NPRINT = 100000

ISWPRF = 1 ;ISWPRL = 100000

No PATCHes used for this Group

\*\*\*\*\*

Group 24. Dumps For Restarts

GVIEW(P,1.000000E+00,0.000000E+00,0.000000E+00)

GVIEW(UP,0.000000E+00,0.000000E+00,1.000000E+00)

```

> DOM, SIZE, 2.389910E-01, 2.934530E+00, 1.268010E+00
> DOM, MONIT, 1.460730E-01, 6.842660E-02, 9.341280E-01
> DOM, SCALE, 1.000000E+00, 1.000000E+00, 1.000000E+00
> DOM, SNAPSIZ, 1.000000E-02
> GRID, RSET_X_1, 11, -1.380000E+00
> GRID, RSET_X_2, 8, 1.200000E+00
> GRID, RSET_X_3, -5, 1.000000E+00,G
> GRID, RSET_X_4, 5, 1.000000E+00,G
> GRID, RSET_X_5, -5, 1.000000E+00,G
> GRID, RSET_X_6, 8, -1.200000E+00
> GRID, RSET_X_7, 1, 1.000000E+00
> GRID, RSET_Y_1, -6, 1.120000E+00
> GRID, RSET_Y_2, -9, 1.320000E+00
> GRID, RSET_Y_3, 2, 1.000000E+00
> GRID, RSET_Y_4, 1, 1.000000E+00
> GRID, RSET_Y_5, -19, 1.350000E+00
> GRID, RSET_Y_6, -8, 1.180000E+00
> GRID, RSET_Y_7, 1, 1.000000E+00
> GRID, RSET_Y_8, -24, 1.580000E+00
> GRID, RSET_Y_9, 1, 1.000000E+00
> GRID, RSET_Y_10, -24, 1.580000E+00
> GRID, RSET_Y_11, 1, 1.000000E+00
> GRID, RSET_Y_12, -19, 1.450000E+00
> GRID, RSET_Y_13, 1, 1.000000E+00
> GRID, RSET_Y_14, -15, 1.270000E+00
> GRID, RSET_Y_15, -10, 1.230000E+00
> GRID, RSET_Y_16, -28, 1.250000E+00,G
> GRID, RSET_Y_17, -10, 1.220000E+00,G
> GRID, RSET_Y_18, 6, 1.550000E+00
> GRID, RSET_Z_1, -9, 1.500000E+00
> GRID, RSET_Z_2, -34, 1.600000E+00
> GRID, RSET_Z_3, 8, 1.150000E+00
> GRID, RSET_Z_4, -5, 1.000000E+00
> GRID, RSET_Z_5, -5, 1.000000E+00,G
> GRID, RSET_Z_6, -5, 1.100000E+00,G
> GRID, RSET_Z_7, 8, -1.150000E+00
> GRID, RSET_Z_8, -24, 1.500000E+00
> GRID, RSET_Z_9, -10, 1.500000E+00

> OBJ, NAME, REACTOR3
> OBJ, POSITION, 0.000000E+00, 0.000000E+00, 0.000000E+00
> OBJ, SIZE, 2.389905E-01, 2.934527E+00, 1.268006E+00
> OBJ, GEOMETRY, reactor3drev2
> OBJ, ROTATION24, 1
> OBJ, TYPE, BLOCKAGE
> OBJ, COLOR-MODE, USER
> OBJ, COLOR-VAL, 142
> OBJ, OPAQUE, 50
> OBJ, MATERIAL, 198, Solid with smooth-wall friction

> OBJ, NAME, INLET3DR
> OBJ, POSITION, 0.000000E+00, 2.776573E+00, 0.000000E+00
> OBJ, SIZE, 0.000000E+00, 7.930350E-02, 7.923202E-02

```

```

> OBJ, GEOMETRY, inlet3drev2
> OBJ, ROTATION24, 1
> OBJ, TYPE, INLET
> OBJ, PRESSURE, 0.000000E+00
> OBJ, VELOCITY, 2.555047E-01, 0.000000E+00, 0.000000E+00
> OBJ, TEMPERATURE, 0.000000E+00
> OBJ, TURB-INTENS, 5.000000E+00

> OBJ, NAME, OUTLET3D
> OBJ, POSITION, 0.000000E+00, 3.496076E-02, 1.188632E+00
> OBJ, SIZE, 0.000000E+00, 7.930348E-02, 7.923210E-02
> OBJ, GEOMETRY, outlet3drev2
> OBJ, ROTATION24, 1
> OBJ, TYPE, OUTLET
> OBJ, PRESSURE, 0.000000E+00
> OBJ, TEMPERATURE, SAME
> OBJ, COEFFICIENT, 1.000000E+03
> OBJ, TURBULENCE, SAME, SAME

> OBJ, NAME, LAMP3DRE
> OBJ, POSITION, 1.492971E-01, 0.000000E+00, 8.084253E-01
> OBJ, SIZE, 2.460623E-02, 1.825625E+00, 2.460623E-02
> OBJ, GEOMETRY, lamp3drev2
> OBJ, ROTATION24, 1
> OBJ, VISIBLE, NO
> OBJ, TYPE, BLOCKAGE
> OBJ, MATERIAL, 198,Solid with smooth-wall friction

> OBJ, NAME, WIPER3DR
> OBJ, POSITION, 1.235021E-01, 3.397250E-01, 7.826303E-01
> OBJ, SIZE, 7.619619E-02, 1.562100E+00, 7.619625E-02
> OBJ, GEOMETRY, wiper3drev2
> OBJ, ROTATION24, 1
> OBJ, TYPE, BLOCKAGE
> OBJ, MATERIAL, 198,Solid with smooth-wall friction

> OBJ, NAME, BAFFLE13
> OBJ, POSITION, 8.678560E-02, 1.697037E+00, 7.458405E-01
> OBJ, SIZE, 1.496291E-01, 4.762530E-03, 1.497757E-01
> OBJ, GEOMETRY, baffle13drev2
> OBJ, ROTATION24, 1
> OBJ, TYPE, BLOCKAGE
> OBJ, MATERIAL, 198,Solid with smooth-wall friction

> OBJ, NAME, BAFFLE23
> OBJ, POSITION, 8.678405E-02, 1.430338E+00, 7.458678E-01
> OBJ, SIZE, 1.496322E-01, 4.762411E-03, 1.497211E-01
> OBJ, GEOMETRY, baffle23drev2
> OBJ, ROTATION24, 1
> OBJ, TYPE, BLOCKAGE
> OBJ, MATERIAL, 198,Solid with smooth-wall friction

> OBJ, NAME, BAFFLE33

```

```
> OBJ, POSITION, 8.678405E-02, 9.096375E-01, 7.458678E-01
> OBJ, SIZE, 1.496322E-01, 4.762471E-03, 1.497211E-01
> OBJ, GEOMETRY, baffle33drev2
> OBJ, ROTATION24, 1
> OBJ, TYPE, BLOCKAGE
> OBJ, MATERIAL, 198,Solid with smooth-wall friction

> OBJ, NAME, BAFFLE43
> OBJ, POSITION, 8.678405E-02, 3.905250E-01, 7.458678E-01
> OBJ, SIZE, 1.496322E-01, 4.762501E-03, 1.497211E-01
> OBJ, GEOMETRY, baffle43drev2
> OBJ, ROTATION24, 1
> OBJ, TYPE, BLOCKAGE
> OBJ, MATERIAL, 198,Solid with smooth-wall friction

> OBJ, NAME, BAFFLE53
> OBJ, POSITION, 8.678405E-02, 1.238250E-01, 7.458678E-01
> OBJ, SIZE, 1.496322E-01, 4.762501E-03, 1.497211E-01
> OBJ, GEOMETRY, baffle53drev2
> OBJ, ROTATION24, 1
> OBJ, TYPE, BLOCKAGE
> OBJ, MATERIAL, 198,Solid with smooth-wall friction
STOP
</strong></pre></body></html>
```



```

c
  IXL=IABS(IXL)
  IF(IGR.EQ.13) GO TO 13
  IF(IGR.EQ.19) GO TO 19
  GO TO (1,2,3,4,5,6,25,8,9,10,11,12,13,14,25,25,25,25,19,20,25,
  121,23,24),IGR
  25 CONTINUE
  RETURN
C*****
C
C--- GROUP 1. Run title and other preliminaries
C
  1 GO TO (1001,1002,1003),ISC
C
  1001 CONTINUE

C * -----GROUP 1 SECTION 3 -----
C--- Use this group to create storage via MAKE, GXMAKE etc which it is
C essential to dump to PHI (or PHIDA) for restarts
C User may here change message transmitted to the VDU screen
  IF(.NOT.NULLPR.AND.IDVCGR.EQ.0)
  1 CALL WRYT40('GROUND file is GROUND.F of: 240802 ')
C
  RETURN
C * -----GROUP 1 SECTION 3 -----
C--- Use this group to create storage via GXMAKE which it is not
C necessary to dump to PHI (or PHIDA) for restarts
C
  1003 CONTINUE
  GO TO 25
  1002 CONTINUE
  RETURN
C*****
C
C--- GROUP 2. Transience; time-step specification
C
  2 CONTINUE
  RETURN
C*****
C
C--- GROUP 3. X-direction grid specification
C
  3 CONTINUE
  RETURN
C*****
C
C--- GROUP 4. Y-direction grid specification
C
  4 CONTINUE
  RETURN
C*****
C

```

```

C--- GROUP 5. Z-direction grid specification
C
  5 CONTINUE
  RETURN
C*****
C
C--- GROUP 6. Body-fitted coordinates or grid distortion
C
  6 CONTINUE
  RETURN
C*****
C * Make changes for this group only in group 19.
C--- GROUP 7. Variables stored, solved & named
C*****
C
C--- GROUP 8. Terms (in differential equations) & devices
C
  8 GO TO (81,82,83,84,85,86,87,88,89,810,811,812,813,814,815,816)
  1,ISC
  81 CONTINUE
C * ----- SECTION 1 -----
C For U1AD.LE.GRND--- phase 1 additional velocity. Index VELAD
  RETURN
  82 CONTINUE
C * ----- SECTION 2 -----
C For U2AD.LE.GRND--- phase 2 additional velocity. Index VELAD
  RETURN
  83 CONTINUE
C * ----- SECTION 3 -----
C For V1AD.LE.GRND--- phase 1 additional velocity. Index VELAD
  RETURN
  84 CONTINUE
C * ----- SECTION 4 -----
C For V2AD.LE.GRND--- phase 2 additional velocity. Index VELAD
  RETURN
  85 CONTINUE
C * ----- SECTION 5 -----
C For W1AD.LE.GRND--- phase 1 additional velocity. Index VELAD
  RETURN
  86 CONTINUE
C * ----- SECTION 6 -----
C For W2AD.LE.GRND--- phase 2 additional velocity. Index VELAD
  RETURN
  87 CONTINUE
C * ----- SECTION 7 ---- Volumetric source for gala
  RETURN
  88 CONTINUE
C * ----- SECTION 8 ---- Convection fluxes
C--- Entered when UCONV =.TRUE.; block-location indices are:
C LD11 for east and north (accessible at the same time),
C LD12 for west and south (accessible at the same time),
C LD2 for high (which becomes low for the next slab).
C User should provide INDVAR and NDIREC IF's as appropriate.

```

```

RETURN
89 CONTINUE
C * ----- SECTION 9 ---- Diffusion coefficients
C--- Entered when UDIFF =.TRUE.; block-location indices are LAE
C for east, LAW for west, LAN for north, LAS for
C south, LD11 for high, and LD11 for low.
C User should provide INDVAR and NDIREC IF's as above.
C EARTH will apply the DIFCUT and GP12 modifications after the user
C has made his settings.
C
RETURN
810 CONTINUE
C * ----- SECTION 10 --- Convection neighbors
RETURN
811 CONTINUE
C * ----- SECTION 11 --- Diffusion neighbors
RETURN
812 CONTINUE
C * ----- SECTION 12 --- Linearised sources
RETURN
813 CONTINUE
C * ----- SECTION 13 --- Correction coefficients
RETURN
814 CONTINUE
C * ----- SECTION 14 --- User's own solver
RETURN
815 CONTINUE
C * ----- SECTION 15 --- Change solution
RETURN
816 CONTINUE
C * ----- SECTION 16 --- Change DVEL/DPs
RETURN
C
C * See the equivalent section in GREX for the indices to be
C used in sections 7 - 16
C
C * Make all other group-8 changes in GROUP 19.
C*****
C--- GROUP 9. Properties of the medium (or media)
C
C The sections in this group are arranged sequentially in their
C order of calling from EARTH. Thus, as can be seen from below,
C the temperature sections (10 and 11) precede the density
C sections (1 and 3); so, density formulae can refer to
C temperature stores already set.
9 GO TO (91,92,93,94,95,96,97,98,99,900,901,902,903,904,905),ISC
C*****
900 CONTINUE
C * ----- SECTION 10 -----
C For TMP1.LE.GRND----- phase-1 temperature Index TEMP1
RETURN
901 CONTINUE

```

```

C * ----- SECTION 11 -----
C For TMP2.LE.GRND----- phase-2 temperature Index TEMP2
  RETURN
902 CONTINUE
C * ----- SECTION 12 -----
C For EL1.LE.GRND----- phase-1 length scale Index LEN1
  RETURN
903 CONTINUE
C * ----- SECTION 13 -----
C For EL2.LE.GRND----- phase-2 length scale Index LEN2
  RETURN
904 CONTINUE
C * ----- SECTION 14 -----
C For SOLVE(TEM1)----- phase-1 specific heat
  RETURN
905 CONTINUE
C * ----- SECTION 15 -----
C For SOLVE(TEM2)----- phase-2 specific heat
  RETURN
91 CONTINUE
C * ----- SECTION 1 -----
C For RHO1.LE.GRND--- density for phase 1    Index DEN1
  RETURN
92 CONTINUE
C * ----- SECTION 2 -----
C For DRH1DP.LE.GRND--- D(LN(DEN))/DP for phase 1
C                               Index D1DP
  RETURN
93 CONTINUE
C * ----- SECTION 3 -----
C For RHO2.LE.GRND--- density for phase 2    Index DEN2
  RETURN
94 CONTINUE
C * ----- SECTION 4 -----
C For DRH2DP.LE.GRND--- D(LN(DEN))/DP for phase 2
C                               Index D2DP
  RETURN
95 CONTINUE
C * ----- SECTION 5 -----
C For ENUT.LE.GRND--- reference turbulent kinematic viscosity
C                               Index VIST
  RETURN
96 CONTINUE
C * ----- SECTION 6 -----
C For ENUL.LE.GRND--- reference laminar kinematic viscosity
C                               Index VISL
  RETURN
97 CONTINUE
C * ----- SECTION 7 -----
C For PRNDTL().LE.GRND--- laminar PRANDTL nos., or diffusivity
C                               Index LAMPR
  RETURN
98 CONTINUE

```

```

C * ----- SECTION 8 -----
C For PHINT().LE.GRND--- interface value of first phase
C                               Index FII1
  RETURN
99 CONTINUE
C * ----- SECTION 9 -----
C For PHINT().LE.GRND--- interface value of second phase
C                               Index FII2
  RETURN
C*****
C
C--- GROUP 10. Inter-phase-transfer processes and properties
C
10 GO TO (101,102,103,104,105),ISC
101 CONTINUE
C * ----- SECTION 1 -----
C For CFIPS.LE.GRND--- inter-phase friction coeff.
C                               Index INTFRC
  RETURN
c<a name="10.2"></a>
102 CONTINUE
C * ----- SECTION 2 -----
C For CMDOT.EQ.GRND- inter-phase mass transfer Index INTMDT
  RETURN
103 CONTINUE
C * ----- SECTION 3 -----
C For CINT().EQ.GRND--- phase1-to-interface transfer coefficients
C                               Index COI1
  RETURN
104 CONTINUE
C * ----- SECTION 4 -----
C For CINT().EQ.GRND--- phase2-to-interface transfer coefficients
C                               Index COI2
  RETURN
105 CONTINUE
C * ----- SECTION 5 -----
C For CVM.EQ.GRND--- virtual mass coefficient
C                               Index LD12
  RETURN
C*****
C
C--- GROUP 11. Initialization of variable or porosity fields
C                               Index VAL
11 CONTINUE
C*****
C Initial fields name: INIT01 *** Defines C1 Initial H2O2
IF(INDVAR.EQ.INAME('C1 ').AND.NPATCH.EQ.'INIT ') THEN
  LFVAL =L0F(VAL )
  DO 11001 IX=IXF ,IXL
    IADD=NY*(IX-1)
  DO 11001 IY=IYF ,IYL
    I=IY+IADD
  LOVAL =LFVAL +I

```

```

11001 F(L0VAL )=RG(90)
  ENDIF
C*****
C*****
C   Initial fields name: INIT02 *** Defines C2 Initial MB
  IF(INDVAR.EQ.INAME('C2 ').AND.NPATCH.EQ.'INIT ') THEN
    LFVAL =L0F(VAL )
    DO 11002 IX=IXF ,IXL
      IADD=NY*(IX-1)
    DO 11002 IY=IYF ,IYL
      I=IY+IADD
    L0VAL =LFVAL +I
11002 F(L0VAL )=RG(88)
  ENDIF
C*****
C*****
C   Initial fields name: INIT03 *** Converts C1 into normalized form
  IF(INDVAR.EQ.INAME('C5 ').AND.NPATCH.EQ.'INIT ') THEN
    LFVAL =L0F(VAL )
    LFC1 =L0F(C1 )
    DO 11003 IX=IXF ,IXL
      IADD=NY*(IX-1)
    DO 11003 IY=IYF ,IYL
      I=IY+IADD
    L0VAL =LFVAL +I
    L0C1 =LFC1 +I
11003 F(L0VAL )=F(L0C1)/RG(90)
  ENDIF
C*****
C   Initial fields name: INIT04 *** Converts C2 into normalized form
  IF(INDVAR.EQ.INAME('C6 ').AND.NPATCH.EQ.'INIT ') THEN
    LFVAL =L0F(VAL )
    LFC2 =L0F(C2 )
    DO 11004 IX=IXF ,IXL
      IADD=NY*(IX-1)
    DO 11004 IY=IYF ,IYL
      I=IY+IADD
    L0VAL =LFVAL +I
    L0C2 =LFC2 +I
11004 F(L0VAL )=F(L0C2)/RG(88)
  ENDIF
C*****
C   Initial fields name: INIT05 *** C9 is normalized tracer for C1 (peroxide)
  IF(INDVAR.EQ.INAME('C9 ').AND.NPATCH.EQ.'INIT ') THEN
    LFVAL =L0F(VAL )
    LFC1 =L0F(C1 )
    DO 11005 IX=IXF ,IXL
      IADD=NY*(IX-1)
    DO 11005 IY=IYF ,IYL
      I=IY+IADD
    L0VAL =LFVAL +I
    L0C1 =LFC1 +I
11005 F(L0VAL )=F(L0C1)/RG(90)

```

```

ENDIF
C*****
C   Initial fields name: INIT06 *** C10 is normalized tracer for C2 (MB)
IF(INDVAR.EQ.INAME('C10 ').AND.NPATCH.EQ.'INIT ') THEN
  LFVAL =L0F(VAL )
  LFC2 =L0F(C2 )
  DO 11006 IX=IXF ,IXL
    IADD=NY*(IX-1)
  DO 11006 IY=IYF ,IYL
    I=IY+IADD
    L0VAL =LFVAL +I
    L0C2 =LFC2 +I
11006 F(L0VAL )=F(L0C2)/RG(88)
  ENDF
  RETURN
C*****
C
C--- GROUP 12. Convection and diffusion adjustments
C
  12 CONTINUE
  RETURN
C*****
C
C--- GROUP 13. Boundary conditions and special sources
C           Index for Coefficient - CO
C           Index for Value      - VAL
  13 CONTINUE
  GO TO (130,131,132,133,134,135,136,137,138,139,1310,
    11311,1312,1313,1314,1315,1316,1317,1318,1319,1320,1321),ISC
  130 CONTINUE
C----- SECTION 1 ----- coefficient = GRND
  RETURN
  131 CONTINUE
C----- SECTION 2 ----- coefficient = GRND1
  RETURN
  132 CONTINUE
C----- SECTION 3 ----- coefficient = GRND2
  RETURN
  133 CONTINUE
C----- SECTION 4 ----- coefficient = GRND3
  RETURN
  134 CONTINUE
C----- SECTION 5 ----- coefficient = GRND4
  RETURN
  135 CONTINUE
C----- SECTION 6 ----- coefficient = GRND5
  RETURN
  136 CONTINUE
C----- SECTION 7 ----- coefficient = GRND6
  RETURN
  137 CONTINUE
C----- SECTION 8 ----- coefficient = GRND7
  RETURN

```

```

138 CONTINUE
C----- SECTION 9 ----- coefficient = GRND8
  RETURN
139 CONTINUE
C----- SECTION 10 ----- coefficient = GRND9
  RETURN
1310 CONTINUE
C----- SECTION 11 ----- coefficient = GRND10
  RETURN
1311 CONTINUE
C----- SECTION 12 ----- value = GRND
C*****
C   Source name: SORC57 C5 is normalized peroxide concentration, [H2O2]/[H2O2]0
  IF(INDVAR.EQ.INAME('C5 ').AND.NPATCH.EQ.'PLSR1 ') THEN
    LFVAL =L0F(VAL)
    LFC3 =L0F(C3 )
    LFC5 =L0F(C5 )
    LFC6 =L0F(C6 )
    LFOHSS =L0F(INAME('OHSS '))
    LFO2SS =L0F(INAME('O2SS '))
    DO 13801 IX=IXF ,IXL
      IADD=NY*(IX-1)
    DO 13801 IY=IYF ,IYL
      I=IY+IADD
      L0C3 =LFC3 +I
      L0C5 =LFC5 +I
      L0C6 =LFC6 +I
      L0OHSS =LFOHSS +I
      L0O2SS =LFO2SS +I
13801 F(LFVAL+I)=(-1.*RG(22)*RG(89)*F(L0C5)*((F(L0C3)*100)/
1(RG(86)*1000)))-(RG(24)*F(L0C5)*F(L0OHSS)*RG(90))-(RG(32)
1*F(L0C5)*F(L0O2SS)*RG(90))+(RG(26)*F(L0OHSS)*F(L0OHSS)*RG(90))
    ENDIF
C*****
C   Source name: SORC58 C6 is normalized contaminant concentration, [MB]/[MB]0
  IF(INDVAR.EQ.INAME('C6 ').AND.NPATCH.EQ.'PLSR2 ') THEN
    LFVAL =L0F(VAL)
    LFC3 =L0F(C3 )
    LFC6 =L0F(C6 )
    LFOHSS =L0F(INAME('OHSS '))
    DO 13802 IX=IXF ,IXL
      IADD=NY*(IX-1)
    DO 13802 IY=IYF ,IYL
      I=IY+IADD
      L0C3 =LFC3 +I
      L0C6 =LFC6 +I
      L0OHSS =LFOHSS +I
13802 F(LFVAL+I)=(-RG(31)*F(L0C6)*F(L0OHSS)*RG(90))-(RG(84)*RG(87)*
1F(L0C6)*((F(L0C3)*100)/(RG(86)*1000))
    ENDIF
  RETURN
1312 CONTINUE
C----- SECTION 13 ----- value = GRND1

```

```

RETURN
1313 CONTINUE
C----- SECTION 14 ----- value = GRND2
RETURN
1314 CONTINUE
C----- SECTION 15 ----- value = GRND3
RETURN
1315 CONTINUE
C----- SECTION 16 ----- value = GRND4
RETURN
1316 CONTINUE
C----- SECTION 17 ----- value = GRND5
RETURN
1317 CONTINUE
C----- SECTION 18 ----- value = GRND6
RETURN
1318 CONTINUE
C----- SECTION 19 ----- value = GRND7
RETURN
1319 CONTINUE
C----- SECTION 20 ----- value = GRND8
RETURN
1320 CONTINUE
C----- SECTION 21 ----- value = GRND9
RETURN
1321 CONTINUE
C----- SECTION 22 ----- value = GRND10
RETURN
C*****
C
C--- GROUP 14. Downstream pressure for PARAB=.TRUE.
C
14 CONTINUE
RETURN
C*****
C* Make changes to data for GROUPS 15, 16, 17, 18 GROUP 19.
C*****
C
C--- GROUP 19. Special calls to GROUND from EARTH
C
19 GO TO (191,192,193,194,195,196,197,198,199,1910,1911),ISC
191 CONTINUE
C * ----- SECTION 1 ---- Start of time step.
RETURN
192 CONTINUE
C * ----- SECTION 2 ---- Start of sweep.
RETURN
193 CONTINUE
C * ----- SECTION 3 ---- Start of iz slab.
RETURN
194 CONTINUE
C * ----- SECTION 4 ---- Start of iterations over slab.
RETURN

```

```

1911 CONTINUE
C * ----- SECTION 11---- After calculation of convection
C           fluxes for scalars, and of volume
C           fractions, but before calculation of
C           scalars or velocities
      RETURN
199 CONTINUE
C * ----- SECTION 9 ---- Start of solution sequence for

C  Grid Dimensions for Entire Reactor Block
C  YYF=FIRST Y DIRECTION (BEGIN), YYL=LAST Y DIRECTION (END)

      XXF=10
      XXL=43
      YYF=1
      YYL=133
      ZZF=15
      ZZL=106

C*****
C  Special calls name: SC0905 OHSS is normalized SS Hydroxyl Radical Concentration, [OH]/[H2O2]0
IF(ISTEP.GE.1 .AND.ISTEP.LE.LSTEP ) THEN
IF(IZ.GE.ZZF .AND.IZ.LE.ZZL ) THEN
  LFC3 =L0F(C3 )
  LFC5 =L0F(C5 )
  LFC6 =L0F(C6 )
  LFOHSS =L0F(INAME('OHSS '))
  LFO2SS =L0F(INAME('O2SS '))
  DO 19907 IX=XXF ,XXL
    IADD=NY*(IX-1)
    DO 19907 IY=YYF ,YYL
      I=IY+IADD
      L0C3 =LFC3 +I
      L0C5 =LFC5 +I
      L0C6 =LFC6 +I
      L0OHSS =LFOHSS +I
      L0O2SS =LFO2SS +I
19907 F(L0OHSS )=(((-RG(24)*F(L0C5)*RG(90))-RG(30)*F(L0O2SS))*
1RG(90))-RG(31)*F(L0C6)*RG(88))-RG(33)-(RG(34)*RG(35))-
1(RG(37)*RG(38))-(RG(39)*RG(40))-(RG(71)*RG(59))-(RG(72)*RG(58))
1-(RG(74)*RG(73)))-(((((-RG(24)*F(L0C5)*RG(90))-RG(30)*
IF(L0O2SS)*RG(90))-RG(31)*F(L0C6)*RG(88))-RG(33)-(RG(34)*RG(35))
1-(RG(37)*RG(38))-(RG(39)*RG(40))-(RG(71)*RG(59))-(RG(72)*RG(58))
1-(RG(74)*RG(73)))**2)-(4.*(-RG(26)*RG(90))*(2.*RG(22)*RG(89)*
1F(L0C5)*((F(L0C3)*100)/(RG(86)*1000)))+(RG(32)*F(L0C5)*F(L0O2SS)
1*RG(90))))+TINY)**0.5)/((2.*(-RG(26)*RG(90)))+TINY)
  ENDIF
  ENDIF
C*****
C  Special calls name: SC0906 O2SS is normalized SS radical Concentration, [O2-]/[H2O2]0
IF(ISTEP.GE.1 .AND.ISTEP.LE.LSTEP ) THEN
IF(IZ.GE.ZZF .AND.IZ.LE.ZZL ) THEN
  LFC5 =L0F(C5 )

```

```

LFC6 =L0F(C6 )
LFOHSS =L0F(INAME('OHSS '))
  LFO2SS =L0F(INAME('O2SS '))
DO 19908 IX=XXF ,XXL
  IADD=NY*(IX-1)
DO 19908 IY=YYP ,YYL
  I=IY+IADD
L0C5 =LFC5 +I
L0C6 =LFC6 +I
L0OHSS =LFOHSS +I
  L0O2SS =LFO2SS +I
19908 F(L0O2SS )=(RG(24)*F(L0C5)*F(L0OHSS))/
  1((RG(30)*F(L0OHSS))+RG(32)*F(L0C5))+TINY)
ENDIF
ENDIF
C*****
  RETURN
1910 CONTINUE
C * ----- SECTION 10---- Finish of solution sequence for
C                               a variable
  RETURN
195 CONTINUE
C * ----- SECTION 5 ---- Finish of iterations over slab.
  RETURN
196 CONTINUE
C * ----- SECTION 6 ---- Finish of iz slab.
  RETURN
197 CONTINUE
C * ----- SECTION 7 ---- Finish of sweep.
  RETURN
198 CONTINUE
C * ----- SECTION 8 ---- Finish of time step.
C
  RETURN
C*****
C
C--- GROUP 20. Preliminary print-out
C
  20 CONTINUE
  RETURN
C*****
C--- GROUP 21. Special print-out to screen
  21 CONTINUE
  GO TO 25
C*****
C* Make changes to data for GROUP 22 only in GROUP 19.
C*****
C
C--- GROUP 23. Field print-out and plot control
  23 CONTINUE
  RETURN
C*****
C

```

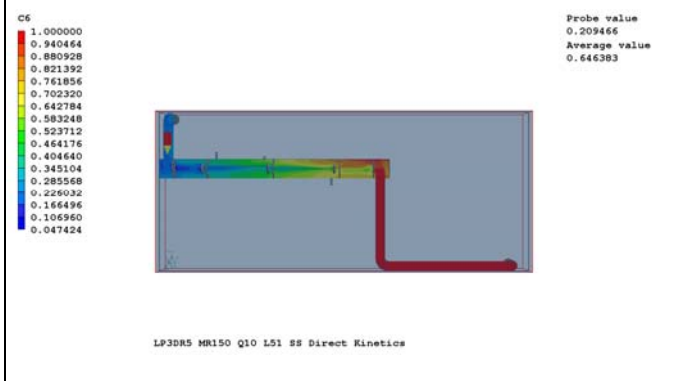
```
C--- GROUP 24. Dumps for restarts
C
  24 CONTINUE
  END
c</pre></strong></body></html>
```

## 8.2 Appendix B – CFD Result Summaries

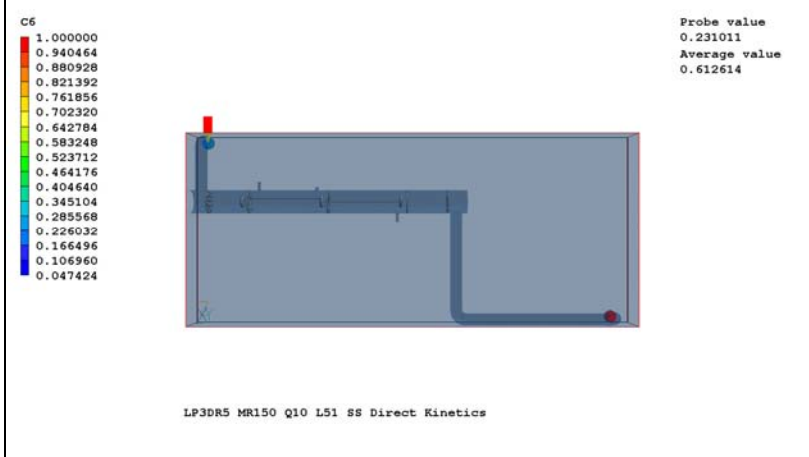
### Research Condition (Model) 1

Filename	C:\Documents and Settings\smalpert\My Documents\Phoenics\LP3D Rev 5 Expanded Scavengers\GPM10_Light51Percent\Five Baffles\Average Density\Kinetics150Light51\LP3DR5_MR150_SS_DirectKinetics_RevBRS
Flowrate (GPM) & Turbulence Model	10, k-eps
MB In (M)	1.563230E-06
Molar Ratio (H2O2:MB)	150.3
Lamp Power (W)	5.200000E+01*0.51
C3 at x=0.156679, y=0.834382, z=0.899000	18.032
UV254 Transmittance (%)	9.490000E-01
MB Rate Constant ( $M^{-1} s^{-1}$ )	6.900000E+10
Alkalinity (mg/L as $CaCO_3$ )	2.300000E+01 (assume all as $HCO_3^-$ )
pH	7.24
DOC (mg/L)	0.57
Combined Chlorine (mg/L as $Cl_2$ )	0.05
Model Run Time (hrs)	
Computer	

I=	24	J=	10	K=	79
----	----	----	----	----	----

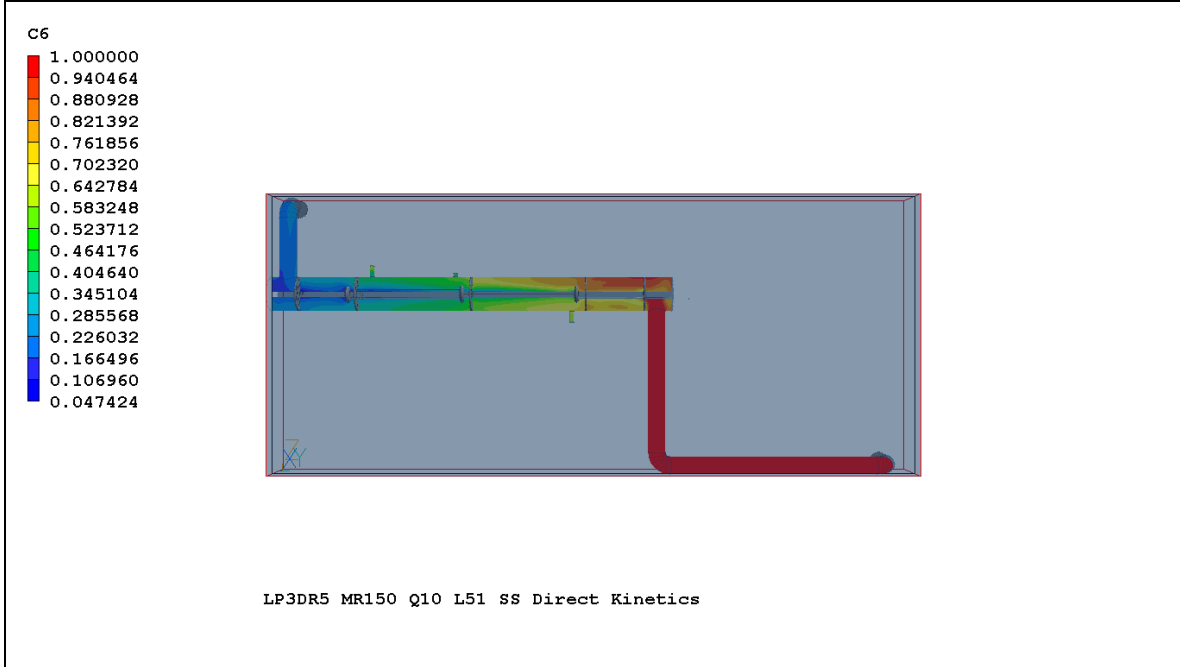


I=	2	J=	11	K=	103
----	---	----	----	----	-----



%R = 76.9
-----------

I=	27	J=	11	K=	103
----	----	----	----	----	-----



From Phi Reader: Average over i=2:

Average 2.19E-01

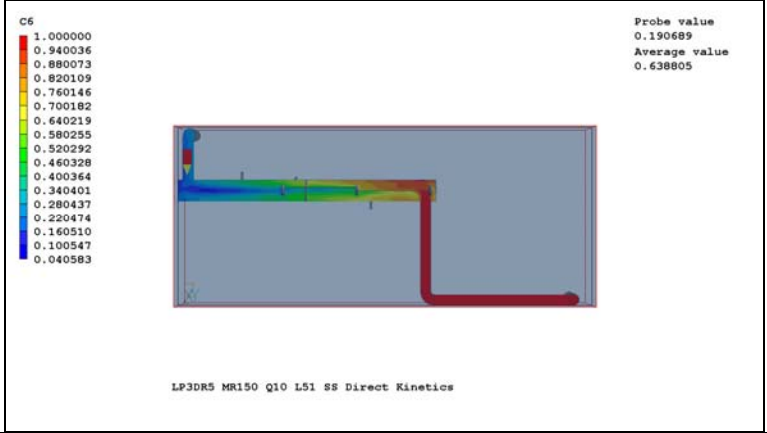
C/C0 = 0.218550

%R = 0.781450

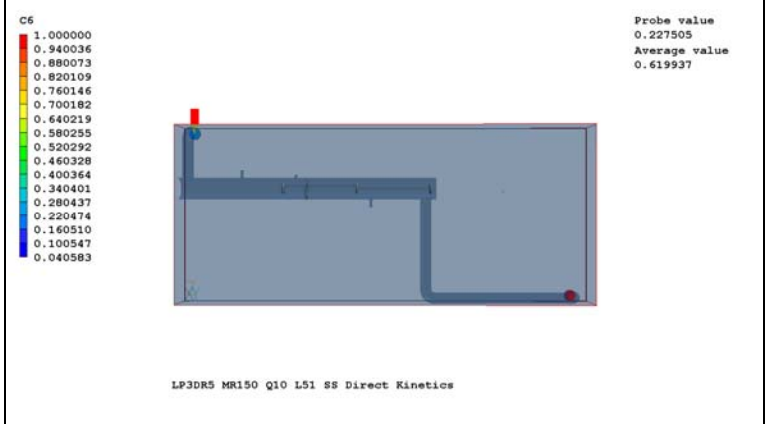
### Research Condition (Model) 2

Filename	C:\Documents and Settings\smalpert\My Documents\Phoenix\LP3D Rev 5 Expanded Scavengers\GPM10_Light51Percent\One Baffle\Average Density\Kinetics150Light51B1\LP3DR5_MR150_SS_DirectKinetics_RevBRS
Flowrate (GPM) & Turbulence Model	10, k-eps
MB In (M)	1.563230E-06
Molar Ratio (H2O2:MB)	149.3
Lamp Power (W)	5.200000E+01*0.51; RAD-LSI
C3 at x=0.156679, y=0.834382, z=0.899000	17.34
UV254 Transmittance (%)	9.460000E-01
MB Rate Constant ( $M^{-1} s^{-1}$ )	6.900000E+10
Alkalinity (mg/L as $CaCO_3$ )	20.8 (assume all as $HCO_3^-$ )
pH	7.250000E+00
DOC (mg/L)	0.57
Combined Chlorine (mg/L as $Cl_2$ )	0.04
Model Run Time (hrs)	
Computer	

I=	24	J=	10	K=	79
----	----	----	----	----	----

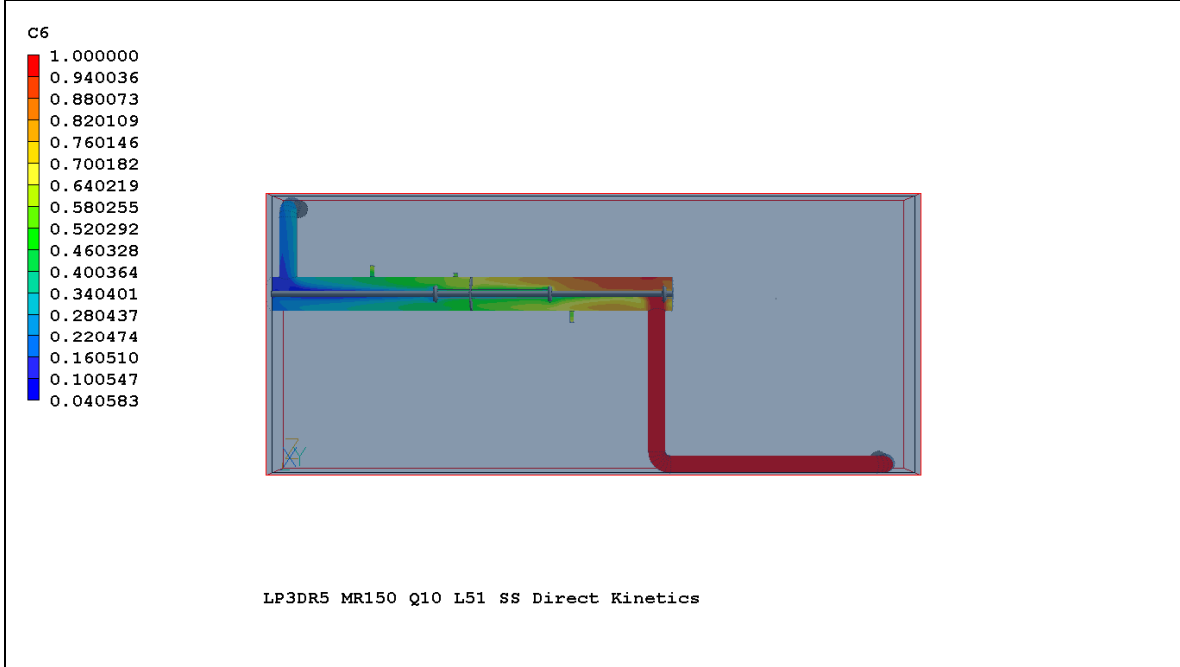


I=	2	J=	11	K=	103
----	---	----	----	----	-----



%R = 77.3

I=	27	J=	11	K=	103
----	----	----	----	----	-----



From Phi Reader, average over i=2:

Average 2.27E-01

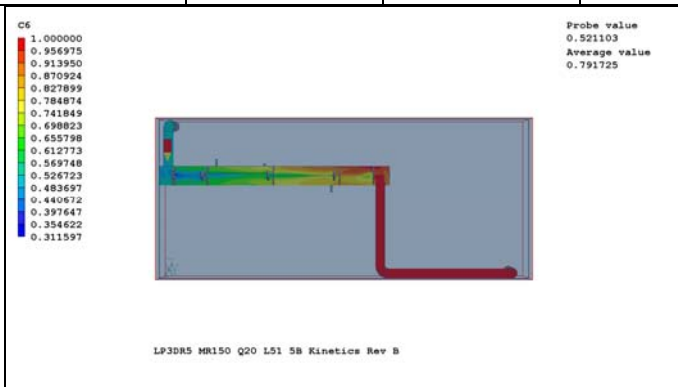
C/C0 = 0.226696

%R = 0.773304

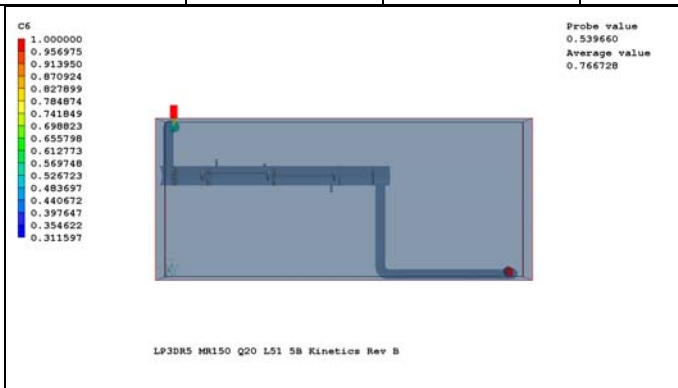
### Research Condition (Model) 3

Filename	C:\Documents and Settings\smalpert\My Documents\Phoenix\LP3D Rev 5 Expanded Scavengers\GPM20_Light51Percent\Five Baffles\Average Density\k-eps\Kinetics150_51_5B_20GPM_ke_RADLSI\LP3DR5_MR150_20_5B_ke_DK_RevBRS
Flowrate (GPM) & Turbulence Model	20, k-eps
MB In (M)	1.563230E-06
Molar Ratio (H2O2:MB)	150
Lamp Power (W)	5.200000E+01*0.575 = 29.9
C3 at x=0.156679, y=0.834382, z=0.899000	16.799, RADLSI
UV254 Transmittance (%)	92.7
MB Rate Constant ( $M^{-1} s^{-1}$ )	6.900000E+10
Alkalinity (mg/L as $CaCO_3$ )	22.7 (assume all as $HCO_3^-$ )
pH	7.30
DOC (mg/L)	0.57
Combined Chlorine (mg/L as $Cl_2$ )	0.05
Model Run Time (hrs)	
Computer	

I=	24	J=	10	K=	79
----	----	----	----	----	----

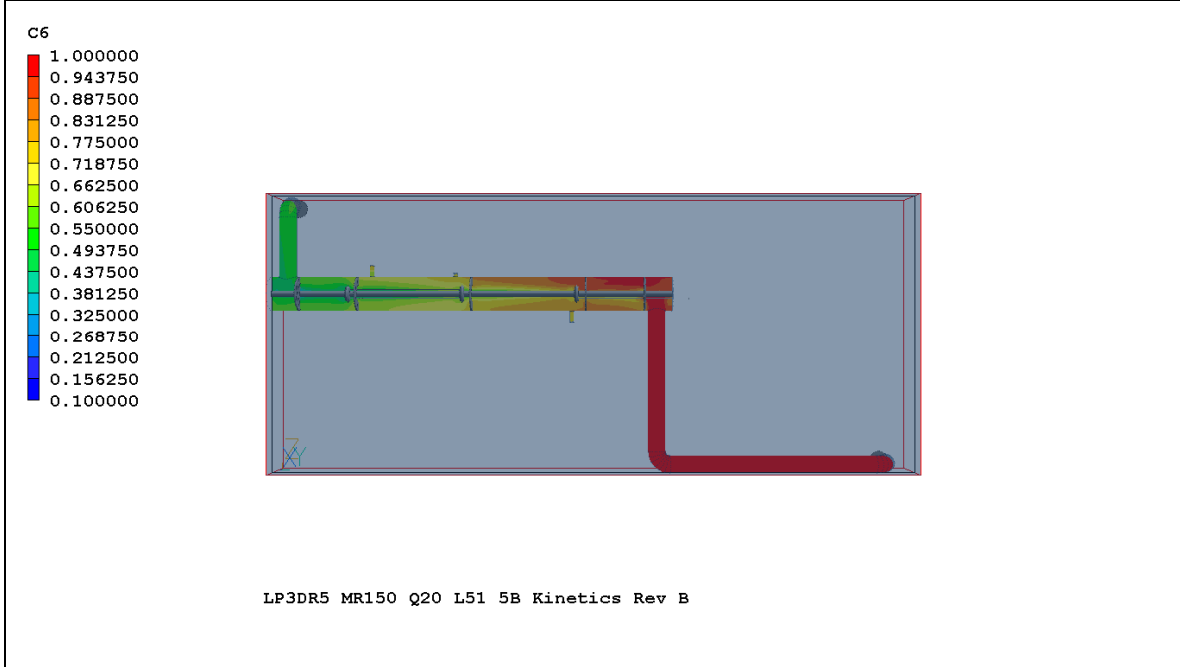


I=	2	J=	11	K=	103
----	---	----	----	----	-----



%R = 46.0
-----------

I=	27	J=	11	K=	103
----	----	----	----	----	-----



From Phi Reader: Average over i=2:

Average 5.29E-01

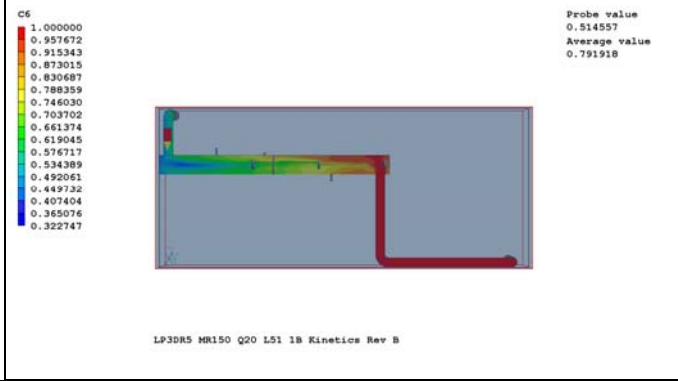
C/C0 = 0.529158

%R = 0.470842

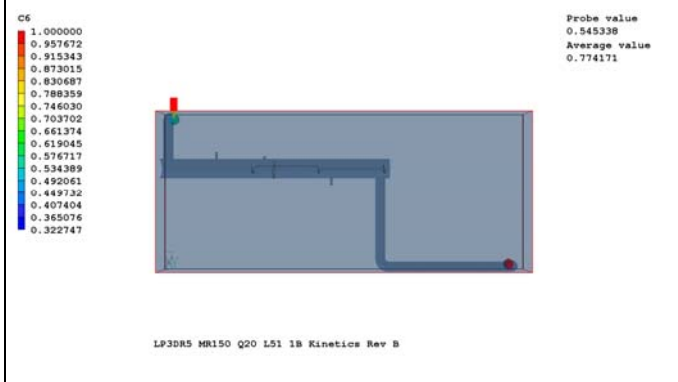
### Research Condition (Model) 4

Filename	C:\Documents and Settings\smalpert\My Documents\Phoenix\LP3D Rev 5 Expanded Scavengers\GPM20_Light51Percent\One Baffle\Average Density\Kinetics150Light51B1\LP3DR5_MR150_20_1B_ke_DK_RevBRS2
Flowrate (GPM) & Turbulence Model	20, k-eps
MB In (M)	1.531968E-06 (0.49 mg/L)
Molar Ratio (H2O2:MB)	149.3
Lamp Power (W)	5.200000E+01*0.51 (26.5)
C3 at x=0.156679, y=0.834382, z=0.899000	17.802
UV254 Transmittance (%)	94.9
MB Rate Constant ( $M^{-1} s^{-1}$ )	6.9e10
Alkalinity (mg/L as $CaCO_3$ )	21.1 (assume all as $HCO_3^-$ )
pH	7.24
DOC (mg/L)	0.57
Combined Chlorine (mg/L as $Cl_2$ )	0.04
Model Run Time (hrs)	
Computer	

I=	24	J=	10	K=	79
----	----	----	----	----	----

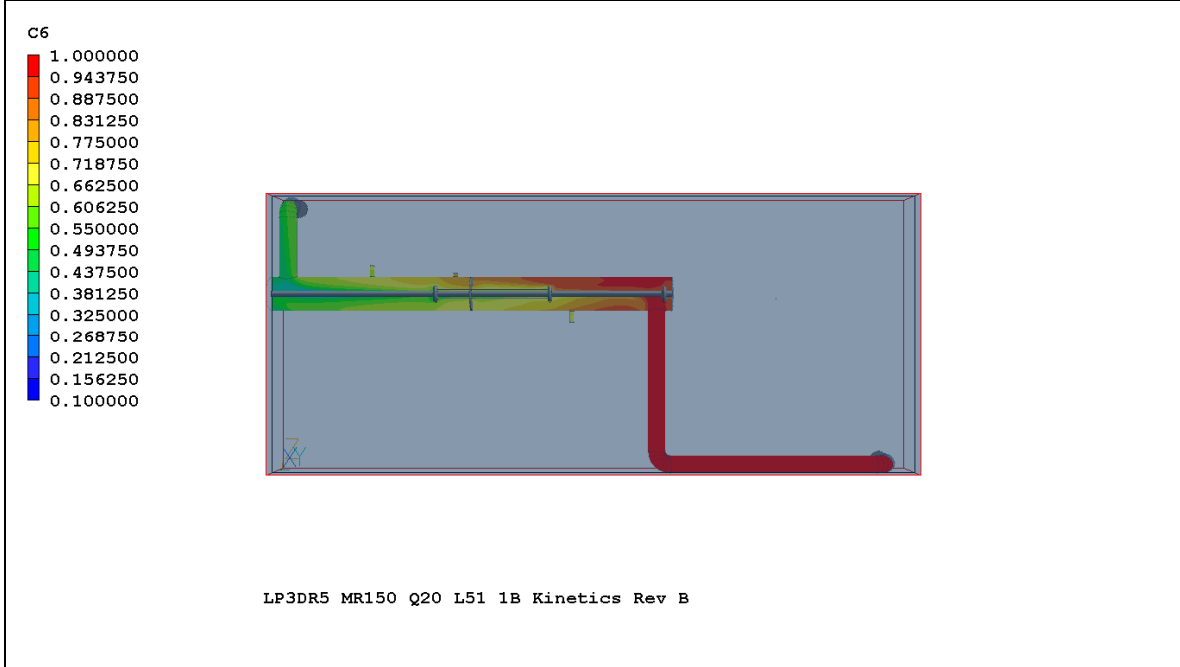


I=	2	J=	11	K=	103
----	---	----	----	----	-----



%R = 45.5

I=	27	J=	11	K=	103
----	----	----	----	----	-----



From Phi Reader, average over i=2:

Average 5.40E-01

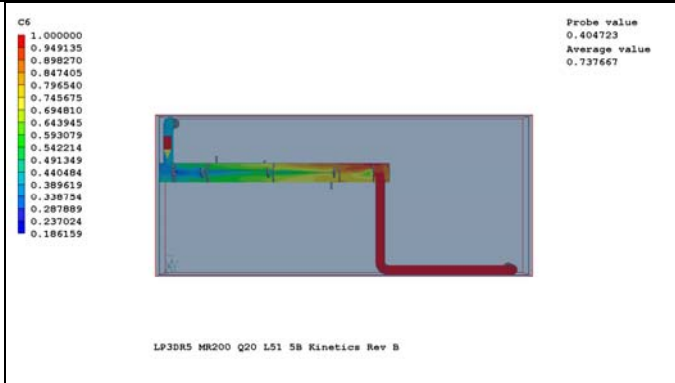
C/C0 = 0.540460

%R = 0.459540

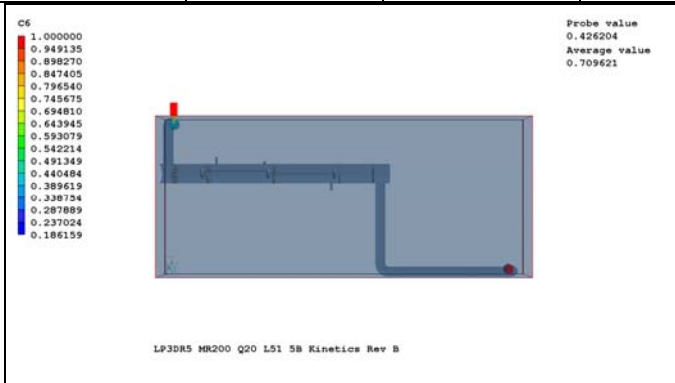
### Research Condition (Model) 5

Filename	C:\Documents and Settings\smalper\My Documents\Phoenics\LP3D Rev 5 Expanded Scavengers\GPM20_Light51Percent\Five Baffles\Average Density\k-eps\Kinetics200_51_5B_20GPM_ke_Radlsi\LP3DR5_MR200_20_5B_ke_DK_RevBRS
Flowrate (GPM) & Turbulence Model	20, k-eps
MB In (M)	1.563230E-06
Molar Ratio (H2O2:MB)	199.7
Lamp Power (W)	5.200000E+01*057 (29.64)
C3 at x=0.156679, y=0.834382, z=0.899000	16.947, RADLSI
UV254 Transmittance (%)	92.9
MB Rate Constant ( $M^{-1} s^{-1}$ )	6.9e10
Alkalinity (mg/L as $CaCO_3$ )	22.2 (assume all as $HCO_3^-$ )
pH	7.23
DOC (mg/L)	0.57
Combined Chlorine (mg/L as $Cl_2$ )	0.013
Model Run Time (hrs)	
Computer	

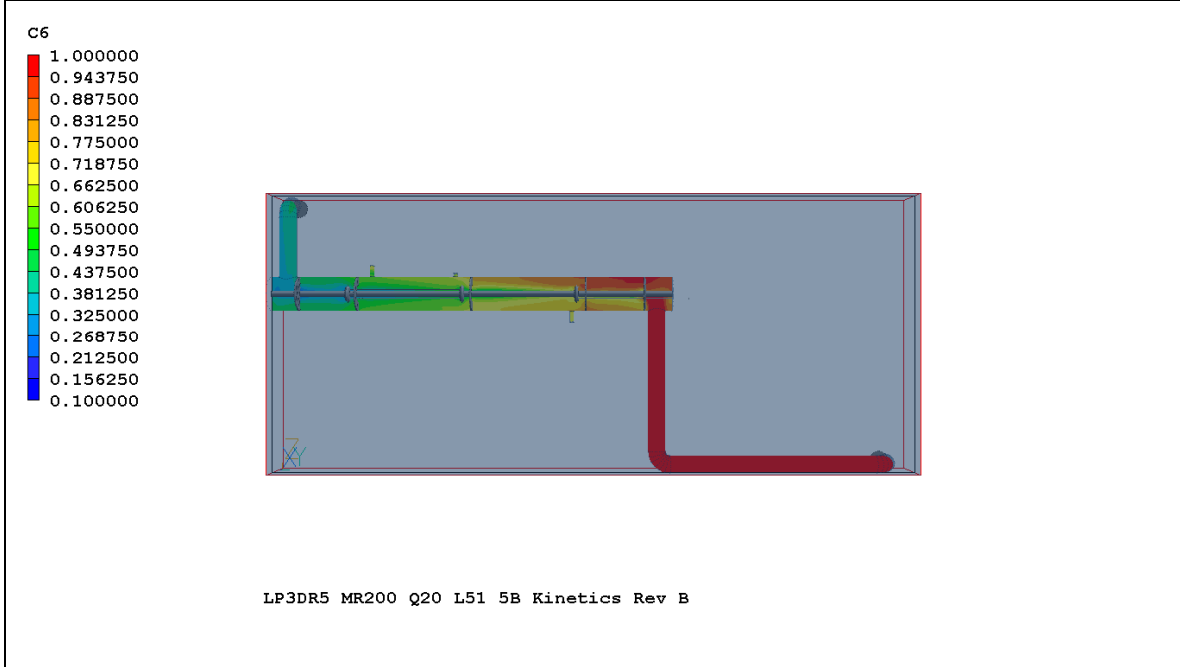
I=	24	J=	10	K=	79
----	----	----	----	----	----



I=	2	J=	11	K=	103
----	---	----	----	----	-----



I=	27	J=	11	K=	103
----	----	----	----	----	-----



From Phi Reader, average over i=2:

Average 4.14E-01

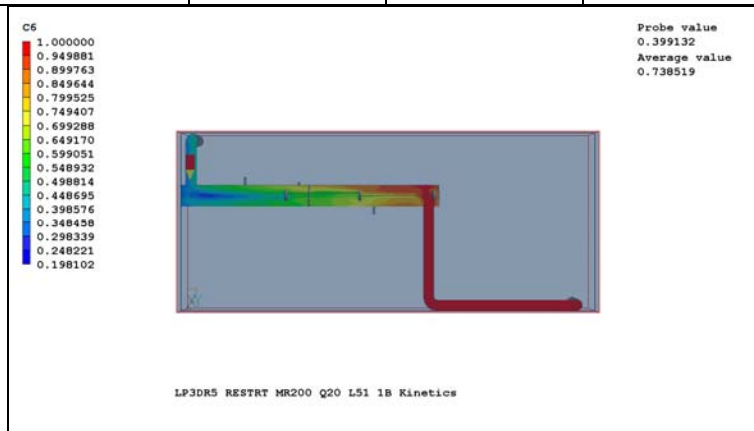
C/C0 = 0.413959

%R = 0.586041

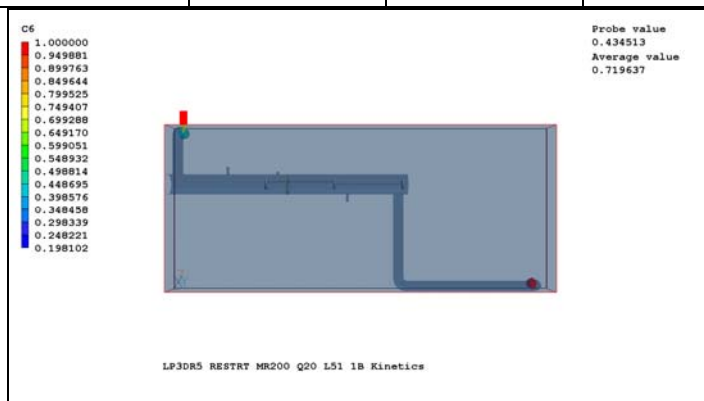
### Research Condition (Model) 6

Filename	C:\Documents and Settings\smlpert\My Documents\Phoenics\LP3D Rev 5 Expanded Scavengers\GPM20_Light51Percent\One Baffle\Average Density\Kinetics200_51_1B_20GPM\LP3DR5_MR200_20_1B_ke_D K_RevBRS
Flowrate (GPM) & Turbulence Model	20, k-eps
MB In (M)	1.563230E-06
Molar Ratio (H2O2:MB)	200.3
Lamp Power (W)	5.200000E+01*0.52 (26.52)
C3 at x=0.156679, y=0.834382, z=0.899000	17.802, RADLSI
UV254 Transmittance (%)	94.9
MB Rate Constant ( $M^{-1} s^{-1}$ )	6.9e10
Alkalinity (mg/L as $CaCO_3$ )	21.8 (assume all as $HCO_3^-$ )
pH	7.25
DOC (mg/L)	0.57
Combined Chlorine (mg/L as $Cl_2$ )	0.04
Model Run Time (hrs)	150 hrs
Computer	Mike

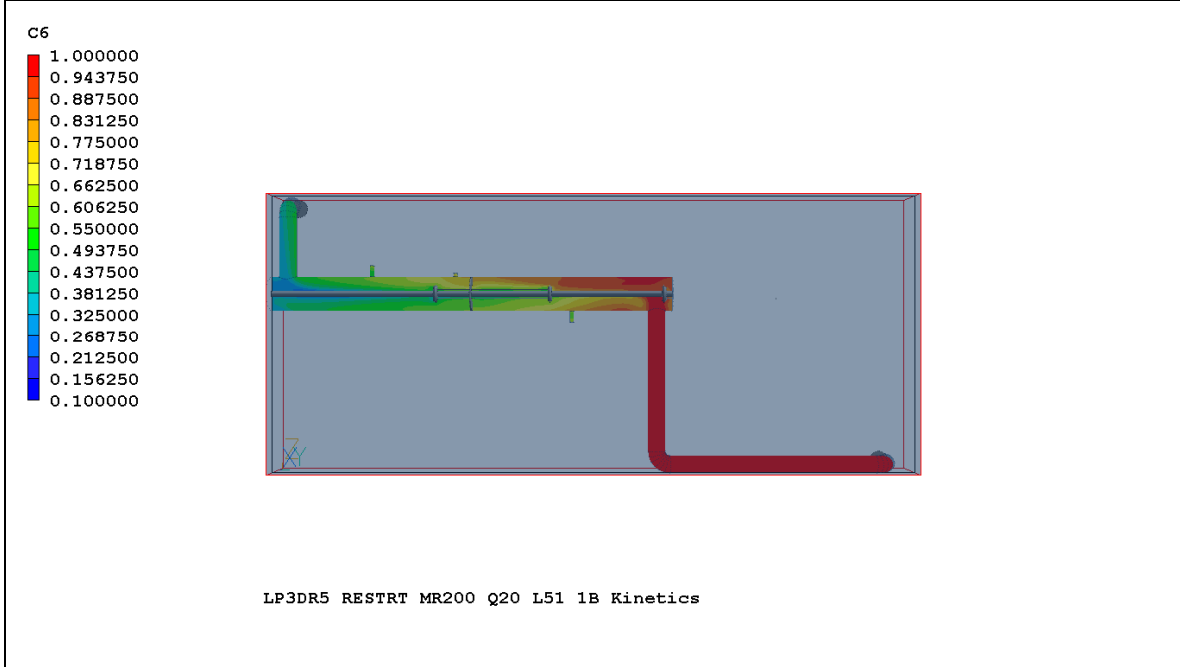
I=	24	J=	10	K=	79
----	----	----	----	----	----



I=	2	J=	11	K=	103
----	---	----	----	----	-----



I=	27	J=	11	K=	103
----	----	----	----	----	-----



From Phi Reader, average over i=2:

Average 4.29E-01

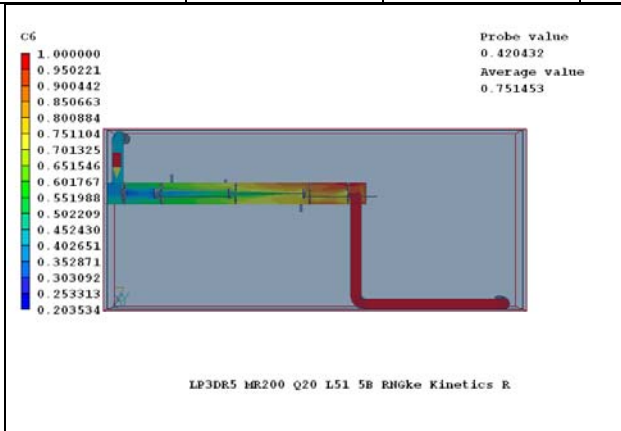
C/C0 = 0.429438

%R = 0.570562

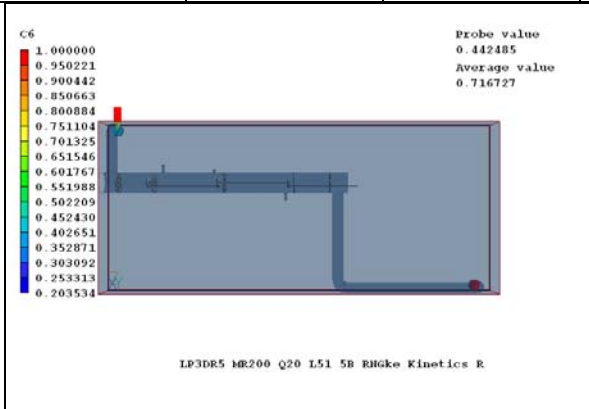
### Research Condition (Model) 7

Filename	C:\Documents and Settings\smlpert\My Documents\Phoenix\LP3D Rev 5 Expanded Scavengers\GPM20_Light5 1Percent\Five Baffles\Average Density\RNG-k-eps\Kinetics200_51_5B_20GPM_RNGke_Radlsi\LP3DR5_MR200_20_5B_RNGke_DK_RevARS
Flowrate (GPM) & Turbulence Model	20, RNG k-eps
MB In (M)	1.563230E-06
Molar Ratio (H2O2:MB)	199.25 (to match pilot)
Lamp Power (W)	5.200000E+01*051
C3 at x=0.156679, y=0.834382, z=0.899000	18.032, RADLSI
UV254 Transmittance (%)	94.9
MB Rate Constant ( $M^{-1} s^{-1}$ )	6.9e10
Alkalinity (mg/L as $CaCO_3$ )	22.2 (assume all as $HCO_3^-$ )
pH	7.24
DOC (mg/L)	0.57
Combined Chlorine (mg/L as $Cl_2$ )	0.013
Model Run Time (hrs)	
Computer	

I=	24	J=	10	K=	79
----	----	----	----	----	----



I=	2	J=	11	K=	103
----	---	----	----	----	-----

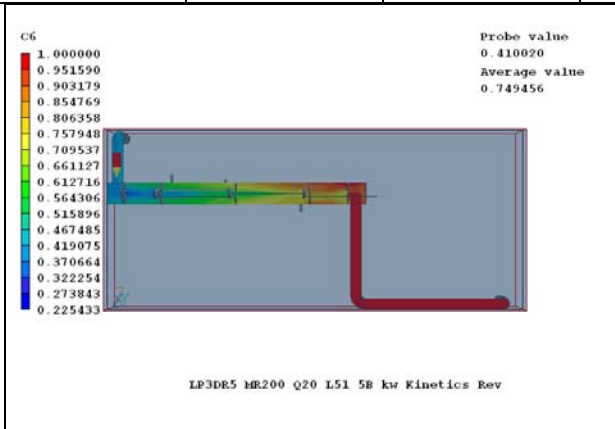


%R = 55.8

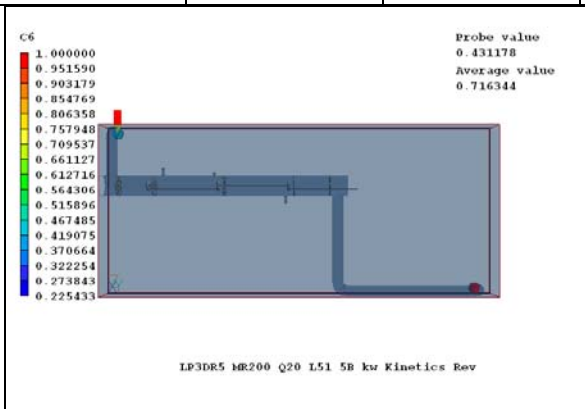
### Research Condition (Model) 8

Filename	C:\Documents and Settings\smlpert\My Documents\Phoenics\LP3D Rev 5 Expanded Scavengers\GPM20_Light5 1Percent\Five Baffles\Average Density\k-omega\Kinetics200_51_5B_20GPM_kw_Radlsi\LP3DR5_MR200_20_5B_kw_DK_RevARS
Flowrate (GPM) & Turbulence Model	20, k-omega
MB In (M)	1.563230E-06
Molar Ratio (H2O2:MB)	199.25 (to match pilot)
Lamp Power (W)	5.200000E+01*051
C3 at x=0.156679, y=0.834382, z=0.899000	18.032, RADLSI
UV254 Transmittance (%)	94.9
MB Rate Constant ( $M^{-1} s^{-1}$ )	6.9e10
Alkalinity (mg/L as $CaCO_3$ )	22.2 (assume all as $HCO_3^-$ )
pH	7.24
DOC (mg/L)	0.57
Combined Chlorine (mg/L as $Cl_2$ )	0.013
Model Run Time (hrs)	
Computer	

I=	24	J=	10	K=	79
----	----	----	----	----	----



I=	2	J=	11	K=	103
----	---	----	----	----	-----

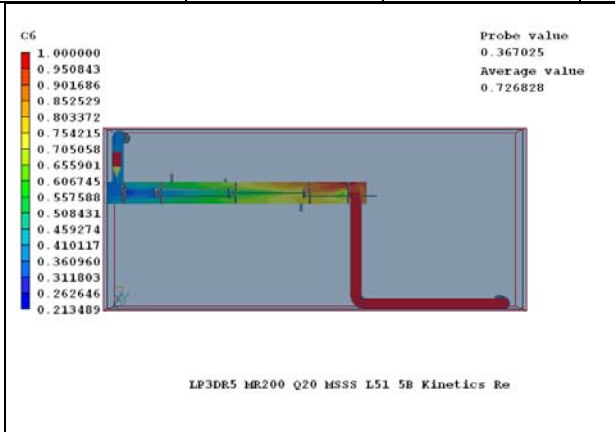


%R = 56.9

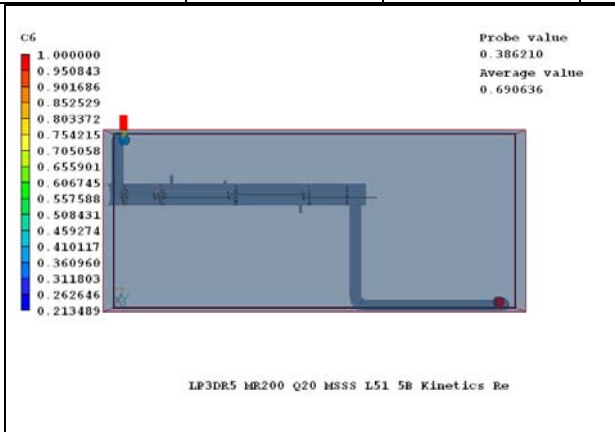
### Research Condition (Model) 9

Filename	C:\Documents and Settings\smalpert\My Documents\Phoenics\LP3D Rev 5 Expanded Scavengers\GPM20_Light51Percent\Five Baffles\Average Density\k-eps\Kinetics200_51_5B_20GPM_ke_MSSS\LP3DR5_MR200_20_5B_ke_MSSS_RevARS
Flowrate (GPM) & Turbulence Model	20, k-eps
MB In (M)	1.563230E-06
Molar Ratio (H2O2:MB)	199.25
Lamp Power (W)	5.200000E+01*0.51, MSSS
C3 at x=0.156679, y=0.834382, z=0.899000	23.988, MSSS
UV254 Transmittance (%)	9.490000E-01
MB Rate Constant ( $M^{-1} s^{-1}$ )	6.900000E+10
Alkalinity (mg/L as $CaCO_3$ )	22.2 (assume all as $HCO_3^-$ )
pH	7.24
DOC (mg/L)	0.57
Combined Chlorine (mg/L as $Cl_2$ )	0.013
Model Run Time (hrs)	
Computer	

I=	24	J=	10	K=	79
----	----	----	----	----	----



I=	2	J=	11	K=	103
----	---	----	----	----	-----

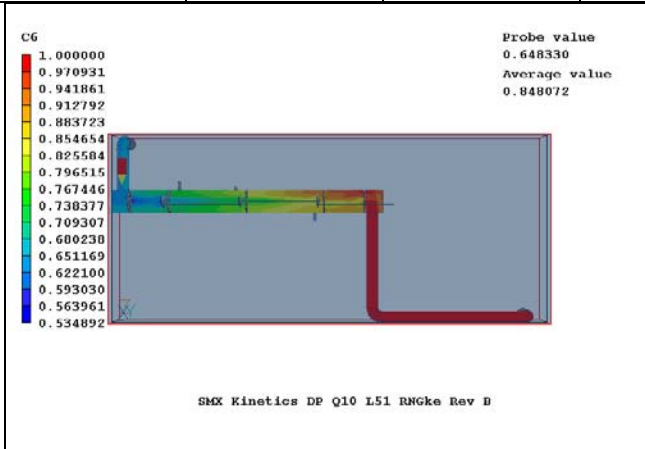


%R = 61.4

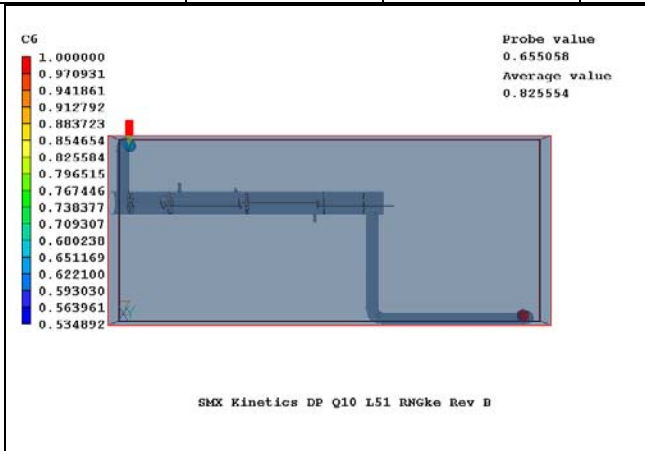
### Research Condition (Model) 10a

Filename	C:\phoenics\d_priv1\Scott\SMX\GPM_10\ RNG k_eps\SMXKinetics_51_10GPM_RNGke_Radlsi\SMXKinetics_DP_200_10_RNGke_RevBRS (Note: Files On New Computer)
Flowrate (GPM) & Turbulence Model	10, RNG k-eps
SMX In (M)	3.948215E-08 (10 µg/L)
Molar Ratio (H2O2:MB)	0 – Direct Photolysis
Lamp Power (W)	52*0.57 = 29.64; RADLSI
C3 at x=0.156679, y=0.834382, z=0.899000	26.210
UV254 Transmittance (%)	98.0
SMX Rate Constant (M <sup>-1</sup> s <sup>-1</sup> )	5.600000E+09
Alkalinity (mg/L as CaCO <sub>3</sub> )	19.5 (assume all as HCO <sub>3</sub> <sup>-</sup> )
pH	7.63
DOC (mg/L)	0.57
Combined Chlorine (mg/L as Cl <sub>2</sub> )	0.16
Model Run Time (hrs)	
Computer	New

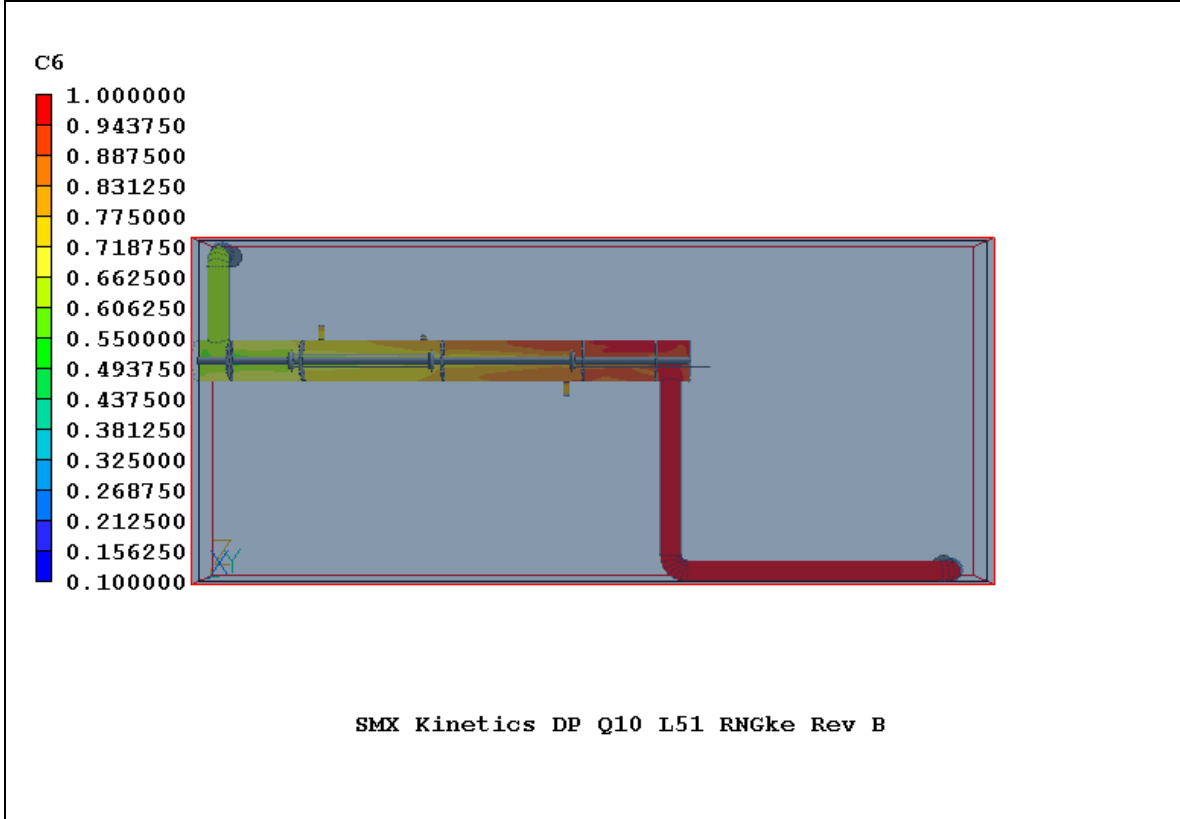
I=	24	J=	10	K=	79
----	----	----	----	----	----



I=	2	J=	11	K=	103
----	---	----	----	----	-----



I=	27	J=	11	K=	103
----	----	----	----	----	-----



From Phi Reader: Average over i=2:

Average      6.48E-01

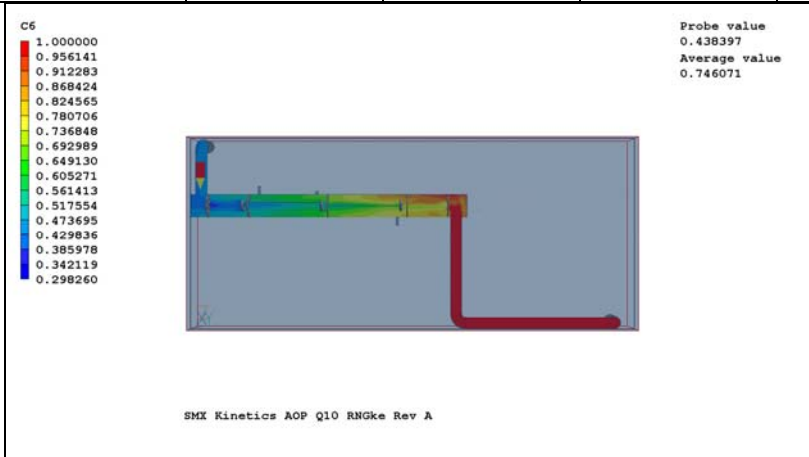
C/CO          0.647704

% Removal    35.230%

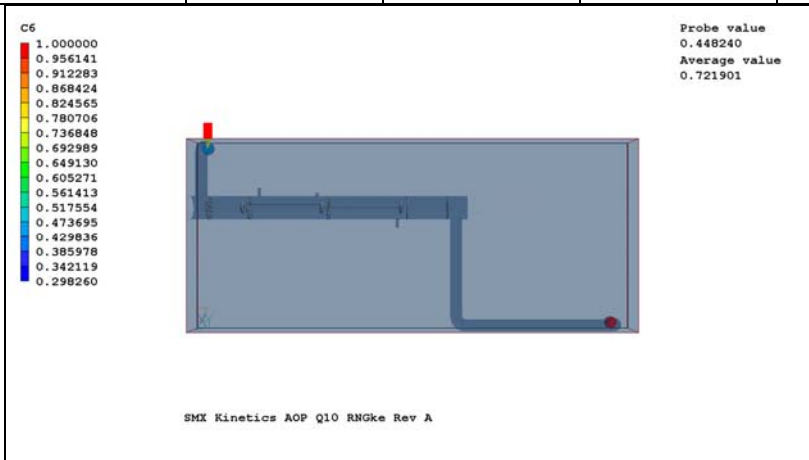
### Research Condition (Model) 10b

Filename	C:\phoenics\d_priv1\Scott\SMX\GPM_10\ RNG k_eps\SMXKinetics_51_10GPM_RNGke_Radlsi\SMXKinetics_AOP_10_RNGke_RevARS (Note: Files On New Computer)
Flowrate (GPM) & Turbulence Model	10, RNG k-eps
SMX In (M)	3.948215E-08 (10.0 µg/L)
H2O2 Concentration (M)	2.98E-04 (10.13 mg/L)
Lamp Power (W)	52*0.57 = 29.64; RADLSI
C3 at x=0.156679, y=0.834382, z=0.899000	23.895
UV254 Transmittance (%)	96.9
SMX Rate Constant (M <sup>-1</sup> s <sup>-1</sup> )	5.600000E+09
Alkalinity (mg/L as CaCO <sub>3</sub> )	19.5 (assume all as HCO <sub>3</sub> <sup>-</sup> )
pH	7.74
DOC (mg/L)	0.57
Combined Chlorine (mg/L as Cl <sub>2</sub> )	0.16
Model Run Time (hrs)	70
Computer	New Computer

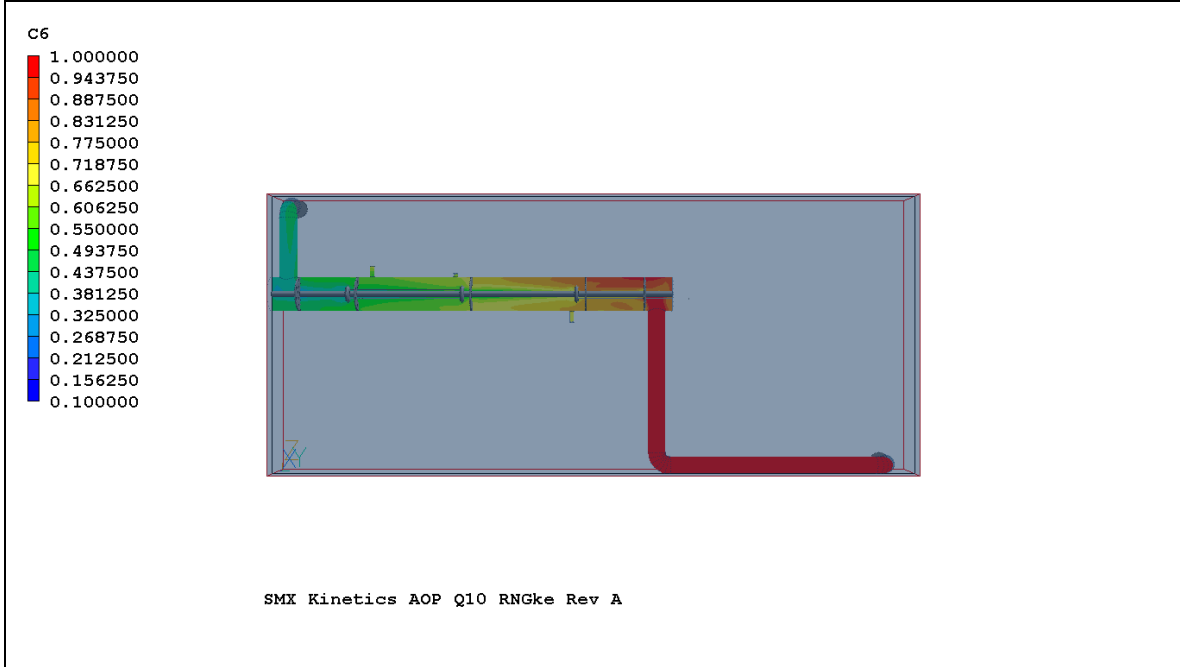
I=	24	J=	10	K=	79
----	----	----	----	----	----



I=	2	J=	11	K=	103
----	---	----	----	----	-----



I=	27	J=	11	K=	103
----	----	----	----	----	-----



From Phi Reader: Average over i=2:

Average      4.39E-01

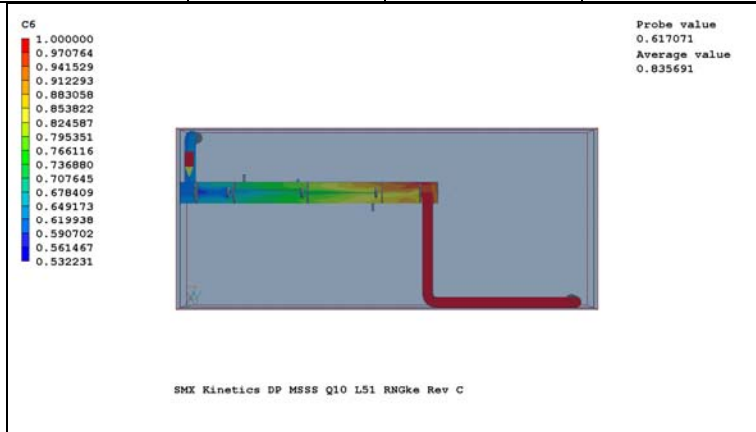
C/C0          0.438576

% Removal    56.142%

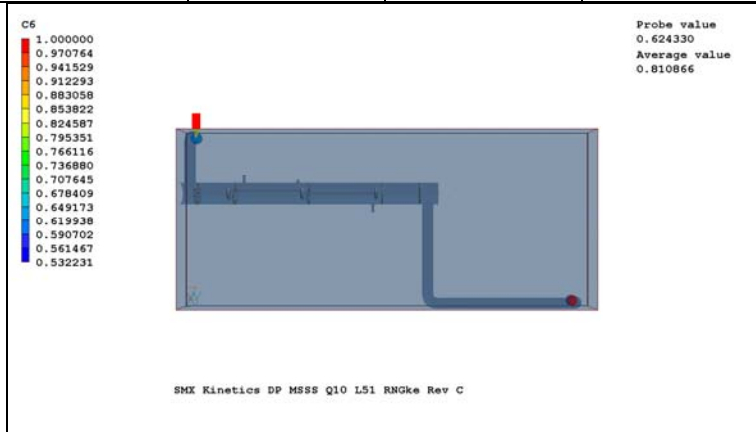
### Research Condition (Model) 11a

Filename	C:\phoenics\d_priv1\Scott\SMX\GPM_10\ RNG k_eps\SMXKinetics_51_10GPM_RNGke_MSSS\SMXKinetics_DP_MSSS_10_RNGke_RevCRS (Note: Files On New Computer)
Flowrate (GPM) & Turbulence Model	10, RNG k-eps
SMX In (M)	3.722405E-08 (9.43 µg/L)
Molar Ratio (H2O2:MB)	0 – Direct Photolysis
Lamp Power (W)	52*0.57 = 29.64; MSSS
C3 at x=0.156679, y=0.834382, z=0.899000	33.874
UV254 Transmittance (%)	98.0
SMX Rate Constant (M <sup>-1</sup> s <sup>-1</sup> )	5.600000E+09
Alkalinity (mg/L as CaCO <sub>3</sub> )	19.5 (assume all as HCO <sub>3</sub> <sup>-</sup> )
pH	7.63
DOC (mg/L)	0.57
Combined Chlorine (mg/L as Cl <sub>2</sub> )	0.16
Model Run Time (hrs)	70
Computer	New Computer

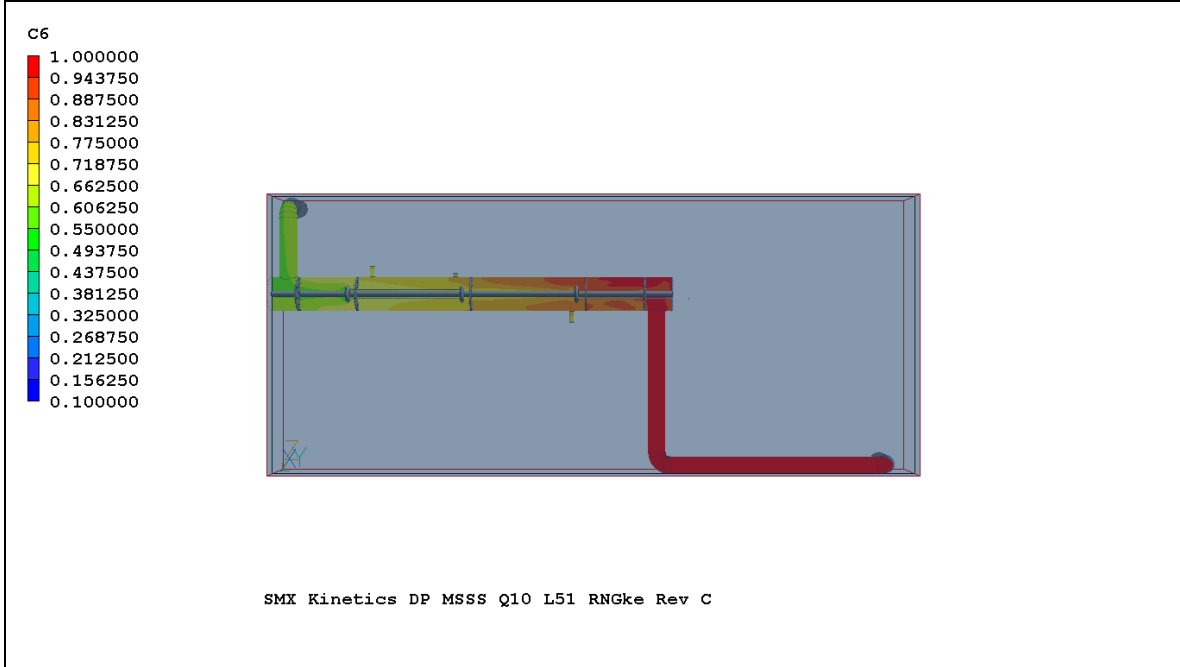
I=	24	J=	10	K=	79
----	----	----	----	----	----



I=	2	J=	11	K=	103
----	---	----	----	----	-----



I=	27	J=	11	K=	103
----	----	----	----	----	-----



From Phi Reader: Average over i=2:

Average      6.18E-01

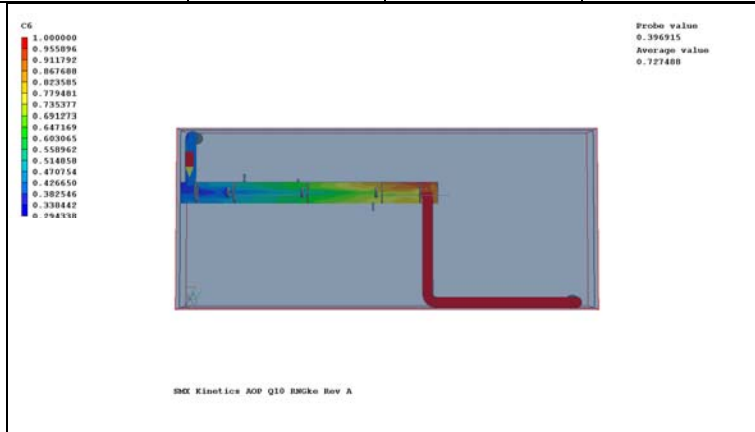
C/C0          0.618232

% Removal    38.177%

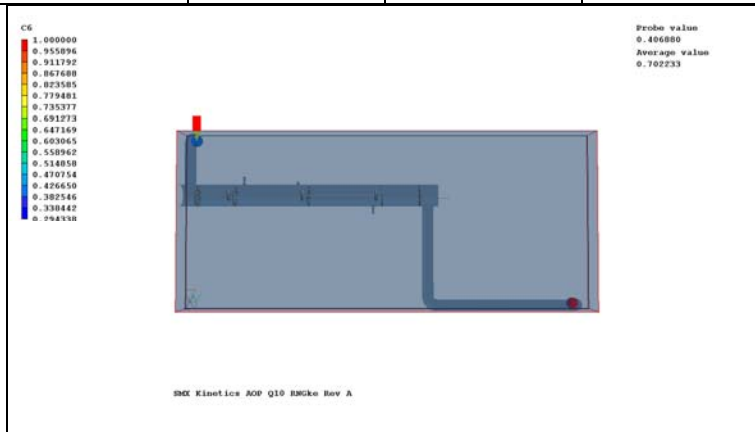
### Research Condition (Model) 11b

Filename	C:\phoenics\d_priv1\Scott\SMX\GPM_10\ RNG k_eps\SMXKinetics_51_10GPM_RNGke_MSSS\SMXKineticsMSSS_AOP_10_RNGke_RevARS (Note: Files On New Computer)
Flowrate (GPM) & Turbulence Model	10, RNG k-eps
SMX In (M)	3.948215E-08 (10.0 µg/L)
Molar Ratio (H2O2:MB)	2.980000E-04 (10.13 mg/L)
Lamp Power (W)	52*0.57 = 29.64; MSSS
C3 at x=0.156679, y=0.834382, z=0.899000	31.202
UV254 Transmittance (%)	96.9
SMX Rate Constant (M <sup>-1</sup> s <sup>-1</sup> )	5.600000E+09
Alkalinity (mg/L as CaCO <sub>3</sub> )	19.5 (assume all as HCO <sub>3</sub> <sup>-</sup> )
pH	7.74
DOC (mg/L)	0.57
Combined Chlorine (mg/L as Cl <sub>2</sub> )	0.16
Model Run Time (hrs)	70
Computer	New Computer

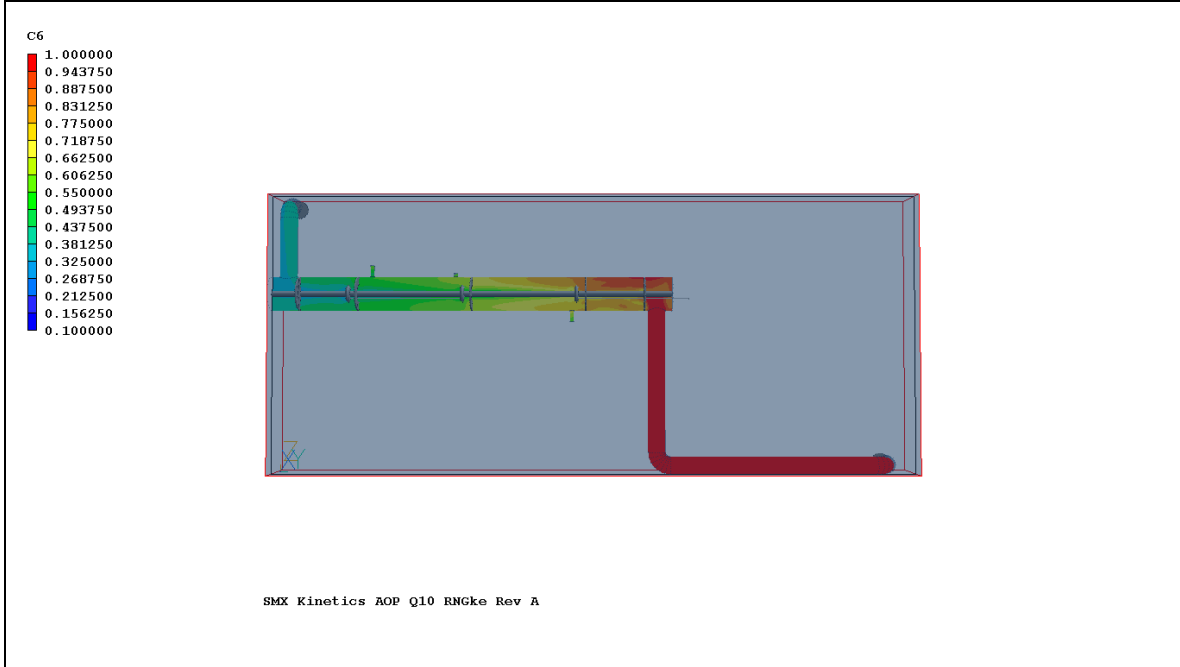
I=	24	J=	10	K=	79
----	----	----	----	----	----



I=	2	J=	11	K=	103
----	---	----	----	----	-----



I=	27	J=	11	K=	103
----	----	----	----	----	-----



From Phi Reader: Average over i=2:

Average 3.99E-01

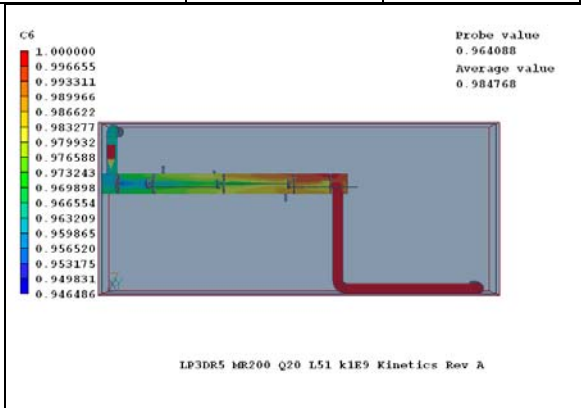
C/C0 0.399128

% Removal 60.087%

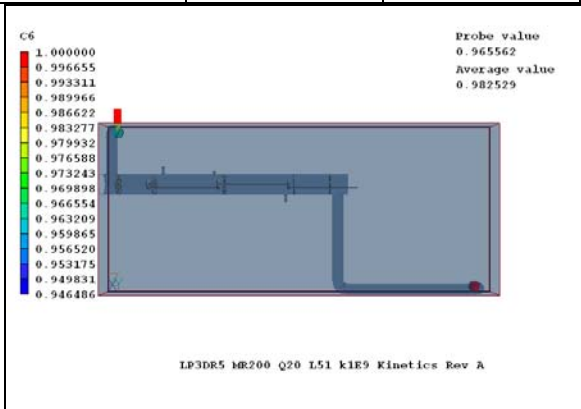
### Research Condition (Model) 15

Filename	C:\Documents and Settings\smalpert\My Documents\Phoenix\LP3D Rev 5 Expanded Scavengers\GPM20_Light51Percent\Five Baffles\Average Density\k-eps\Rate Constant Dependence\Kinetics200_51_20_k1e9\LP3DR5_MR200_20_5B_k1e9_RevARS
Flowrate (GPM) & Turbulence Model	20, k-eps
MB In (M)	1.563230E-06
Molar Ratio (H2O2:MB)	199.25
Lamp Power (W)	5.200000E+01*0.51, RADLSI
C3 at x=0.156679, y=0.834382, z=0.899000	18.032, RADLSI
UV254 Transmittance (%)	9.490000E-01
MB Rate Constant ( $M^{-1} s^{-1}$ )	1.000000E+09
Alkalinity (mg/L as $CaCO_3$ )	22.2 (assume all as $HCO_3^-$ )
pH	7.24
DOC (mg/L)	0.57
Combined Chlorine (mg/L as $Cl_2$ )	0.013
Model Run Time (hrs)	
Computer	

I=	24	J=	10	K=	79
----	----	----	----	----	----



I=	2	J=	11	K=	103
----	---	----	----	----	-----

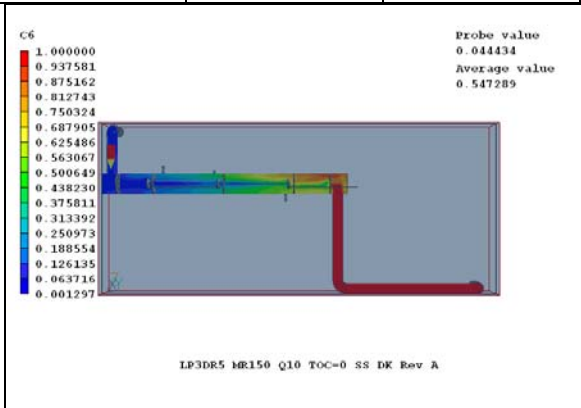


%R = 3.4
----------

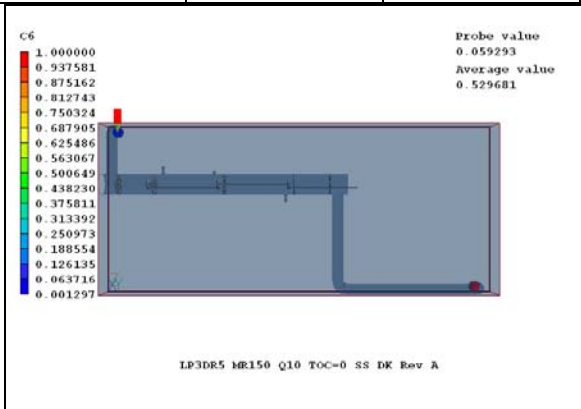
### Research Condition (Model) 18

Filename	C:\Documents and Settings\smlpert\My Documents\Phoenics\LP3D Rev 5 Expanded Scavengers\GPM10_Light60Percent\Five Baffles\Average Density\Kinetics150TOC_0\LP3DR5_MR150_SS_TOC0_DK_RevA RS
Flowrate (GPM) & Turbulence Model	10, k-eps
MB In (M)	1.563230E-06
Molar Ratio (H2O2:MB)	150
Lamp Power (W)	5.200000E+01*0.608
C3 at x=0.156679, y=0.834382, z=0.899000	21.496
UV254 Transmittance (%)	94.9
MB Rate Constant ( $M^{-1} s^{-1}$ )	6.9e10
Alkalinity (mg/L as $CaCO_3$ )	23 (assume all as $HCO_3^-$ )
pH	7.25
DOC (mg/L)	0.0
Combined Chlorine (mg/L as $Cl_2$ )	0.00
Model Run Time (hrs)	150
Computer	Cindy

I=		J=		K=	
----	--	----	--	----	--



I=	2	J=	11	K=	103
----	---	----	----	----	-----

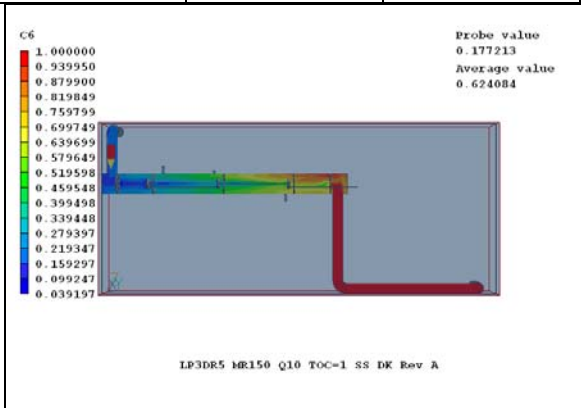


%R = 94.1

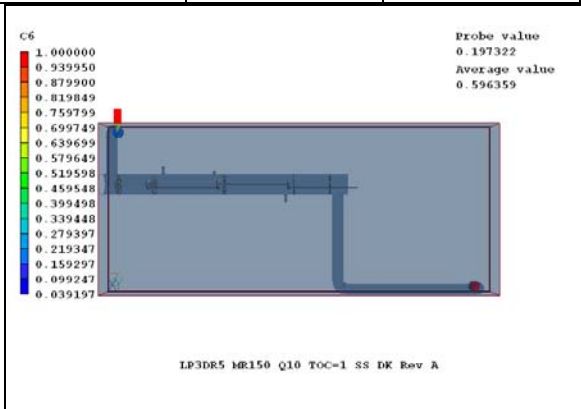
Research Condition (Model) 19

Filename	C:\Documents and Settings\smalpert\My Documents\Phoenics\LP3D Rev 5 Expanded Scavengers\GPM10_Light60Percent\Five Baffles\Average Density\Kinetics150TOC_1\LP3DR5_MR150_SS_TOC1_DK_RevA RS
Flowrate (GPM) & Turbulence Model	10, k-eps
MB In (M)	1.563230E-06
Molar Ratio (H2O2:MB)	150
Lamp Power (W)	5.200000E+01*0.608
C3 at x=0.156679, y=0.834382, z=0.899000	21.496
UV254 Transmittance (%)	94.9
MB Rate Constant ( $M^{-1} s^{-1}$ )	6.9e10
Alkalinity (mg/L as $CaCO_3$ )	23 (assume all as $HCO_3^-$ )
pH	7.25
DOC (mg/L)	1.0
Combined Chlorine (mg/L as $Cl_2$ )	0.00
Model Run Time (hrs)	150
Computer	Cindy

I=	24	J=	10	K=	79
----	----	----	----	----	----



I=	2	J=	11	K=	103
----	---	----	----	----	-----

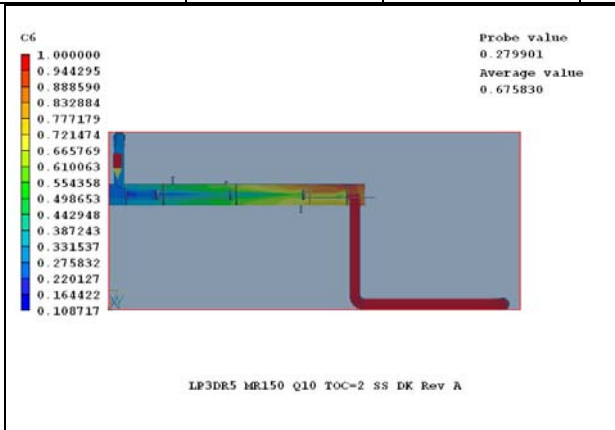


%R = 80.3

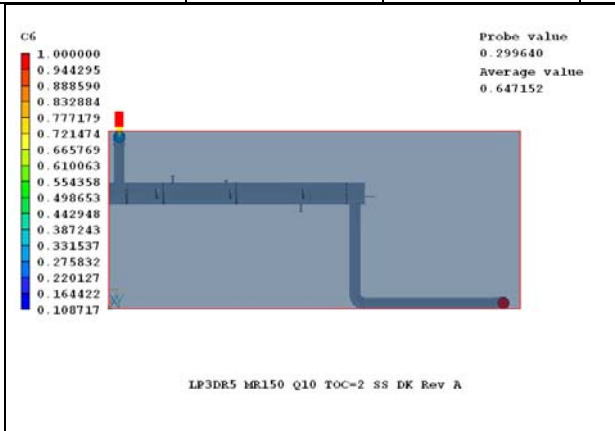
Research Condition (Model) 20

Filename	C:\...\Light_60Percent\Kinetics150TOC_2\LP3DR5_MR150_SS_TOC2_D K_RevARS
Flowrate (GPM) & Turbulence Model	10, k-eps
MB In (M)	1.563230E-06
Molar Ratio (H2O2:MB)	150
Lamp Power (W)	5.200000E+01*0.608
C3 at x=0.156679, y=0.834382, z=0.899000	21.496
UV254 Transmittance (%)	94.9
MB Rate Constant (M <sup>-1</sup> s <sup>-1</sup> )	6.9e10
Alkalinity (mg/L as CaCO <sub>3</sub> )	23 (assume all as HCO <sub>3</sub> <sup>-</sup> )
pH	7.25
DOC (mg/L)	2.0
Combined Chlorine (mg/L as Cl <sub>2</sub> )	0.00
Model Run Time (hrs)	150
Computer	Cindy

I=	24	J=	10	K=	79
----	----	----	----	----	----



I=	2	J=	11	K=	103
----	---	----	----	----	-----

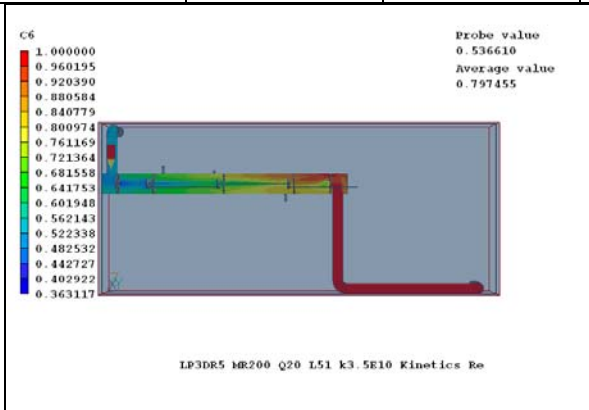


%R = 70.0

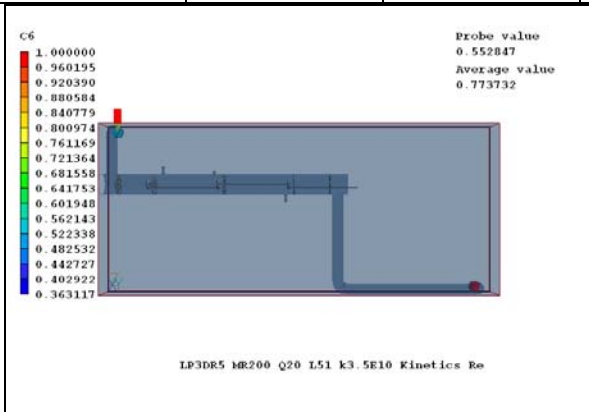
### Research Condition (Model) 23

Filename	C:\Documents and Settings\smlpert\My Documents\Phoenix\LP3D Rev 5 Expanded Scavengers\GPM20_Light51Percent\Five Baffles\Average Density\k-eps\Rate Constant Dependence\Kinetics200_51_20_35e10\LP3DR5_MR200_20_5B_k35e10_RevARS
Flowrate (GPM) & Turbulence Model	20, k-eps
MB In (M)	1.563230E-06
Molar Ratio (H2O2:MB)	199.25
Lamp Power (W)	5.200000E+01*0.51, RADLSI
C3 at x=0.156679, y=0.834382, z=0.899000	18.032, RADLSI
UV254 Transmittance (%)	9.490000E-01
MB Rate Constant ( $M^{-1} s^{-1}$ )	3.500000E+10
Alkalinity (mg/L as $CaCO_3$ )	22.2 (assume all as $HCO_3^-$ )
pH	7.24
DOC (mg/L)	0.57
Combined Chlorine (mg/L as $Cl_2$ )	0.013
Model Run Time (hrs)	
Computer	

I=	24	J=	10	K=	79
----	----	----	----	----	----



I=	2	J=	11	K=	103
----	---	----	----	----	-----

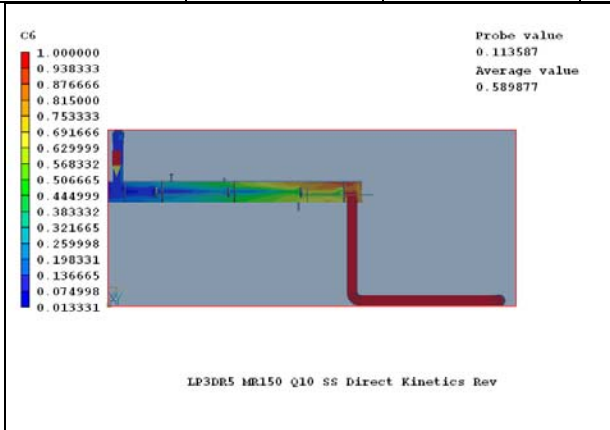


%R = 44.7

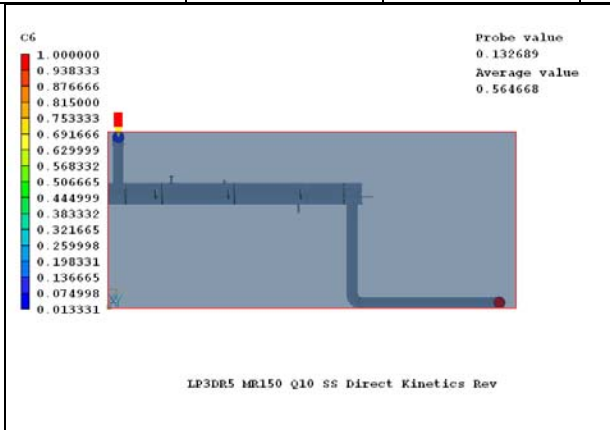
### Research Condition (Model) 28

Filename	C:\Documents and Settings\smlpert\My Documents\Phoenics\LP3D Rev 5 Expanded Scavengers\GPM10_Light60Percent\Five Baffles\Average Density\Kinetics150\LP3DR5_MR150_SS_DirectKinetics_RevA RS
Flowrate (GPM) & Turbulence Model	10, k-eps
MB In (M)	1.563230E-06
Molar Ratio (H2O2:MB)	150
Lamp Power (W)	5.200000E+01*0.608
C3 at x=0.156679, y=0.834382, z=0.899000	21.496
UV254 Transmittance (%)	94.9
MB Rate Constant ( $M^{-1} s^{-1}$ )	6.9e10
Alkalinity (mg/L as $CaCO_3$ )	23 (assume all as $HCO_3^-$ )
pH	7.25
DOC (mg/L)	0.5
Combined Chlorine (mg/L as $Cl_2$ )	0.00
Model Run Time (hrs)	71
Computer	Kiseok

I=		J=		K=	
----	--	----	--	----	--



I=	2	J=	11	K=	103
----	---	----	----	----	-----

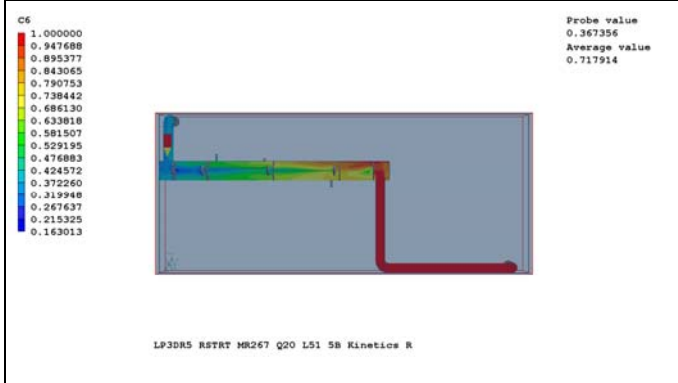


%R = 86.7

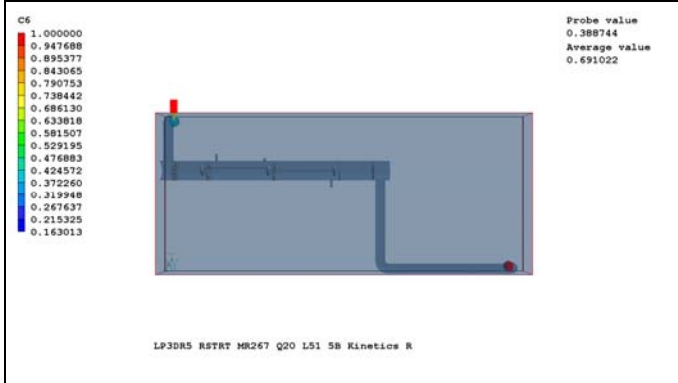
### Research Condition (Model) 29

Filename	C:\Documents and Settings\smalpert\My Documents\Phoenix\LP3D Rev 5 Expanded Scavengers\GPM20_Light51Percent\Five Baffles\Average Density\k-eps\Kinetics267_51_5B_20GPM_ke_Radlsi\LP3DR5_MR267_20_5B_ke_DK_RevARS
Flowrate (GPM) & Turbulence Model	20, k-eps
MB In (M)	1.563230E-06
Molar Ratio (H2O2:MB)	266.4
Lamp Power (W)	5.200000E+01*0.51
C3 at x=0.156679, y=0.834382, z=0.899000	15.57
UV254 Transmittance (%)	93.2
MB Rate Constant ( $M^{-1} s^{-1}$ )	6.900000E+10
Alkalinity (mg/L as $CaCO_3$ )	23.8 (assume all as $HCO_3^-$ )
pH	7.37
DOC (mg/L)	0.57
Combined Chlorine (mg/L as $Cl_2$ )	0.16
Model Run Time (hrs)	
Computer	

I=	24	J=	10	K=	79
----	----	----	----	----	----

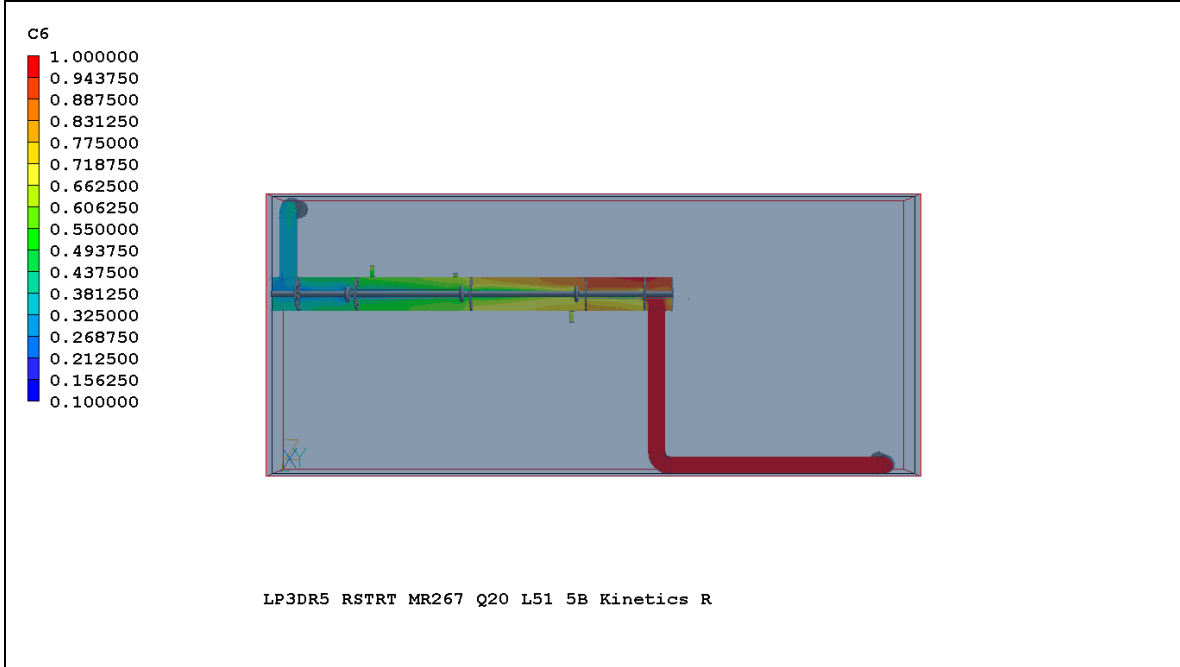


I=	2	J=	11	K=	103
----	---	----	----	----	-----



%R = 61.1

I=	27	J=	11	K=	103
----	----	----	----	----	-----



From Phi Reader: Average over i=2:

Average 3.76E-01

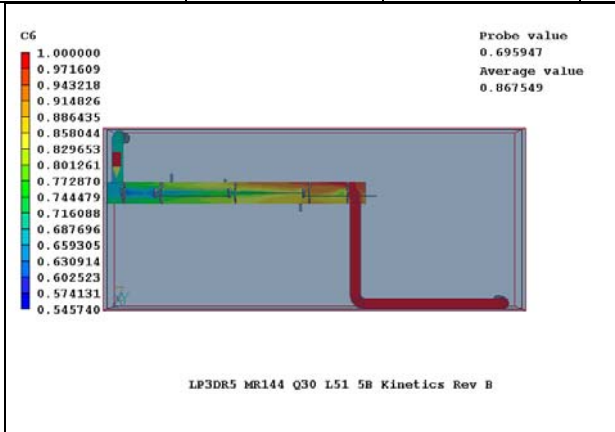
C/C0 = 0.376480

%R = 0.623520

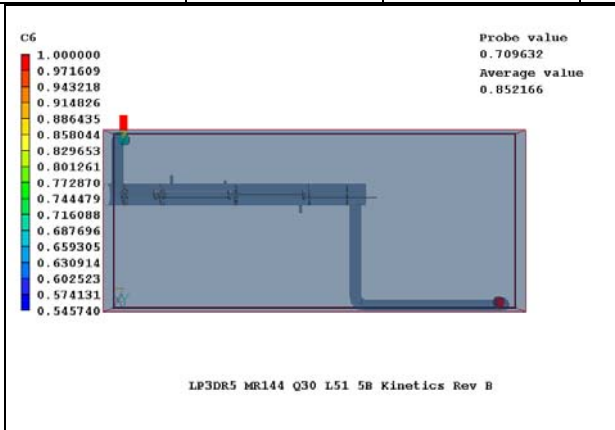
### Research Condition (Model) 30

Filename	C:\Documents and Settings\smlpert\My Documents\Phoenix\LP3D Rev 5 Expanded Scavengers\GPM30_Light51Percent\Five Baffles\Average Density\k-eps\Kinetics150_5B_30GPM_ke_Radlsi\LP3DR5_MR144_30_5B_ke_DK_RevBRS
Flowrate (GPM) & Turbulence Model	30, k-eps
MB In (M)	1.563230E-06 (0.50 mg/L)
Molar Ratio (H2O2:MB)	144.2
Lamp Power (W)	52*0.58 (30.16)
C3 at x=0.156679, y=0.834382, z=0.899000	15.794
UV254 Transmittance (%)	91.9
MB Rate Constant ( $M^{-1} s^{-1}$ )	6.900000E+10
Alkalinity (mg/L as $CaCO_3$ )	28.05 (assume all as $HCO_3^-$ )
pH	7.49
DOC (mg/L)	0.57
Combined Chlorine (mg/L as $Cl_2$ )	0.14
Model Run Time (hrs)	50 hrs
Computer	KiSeok

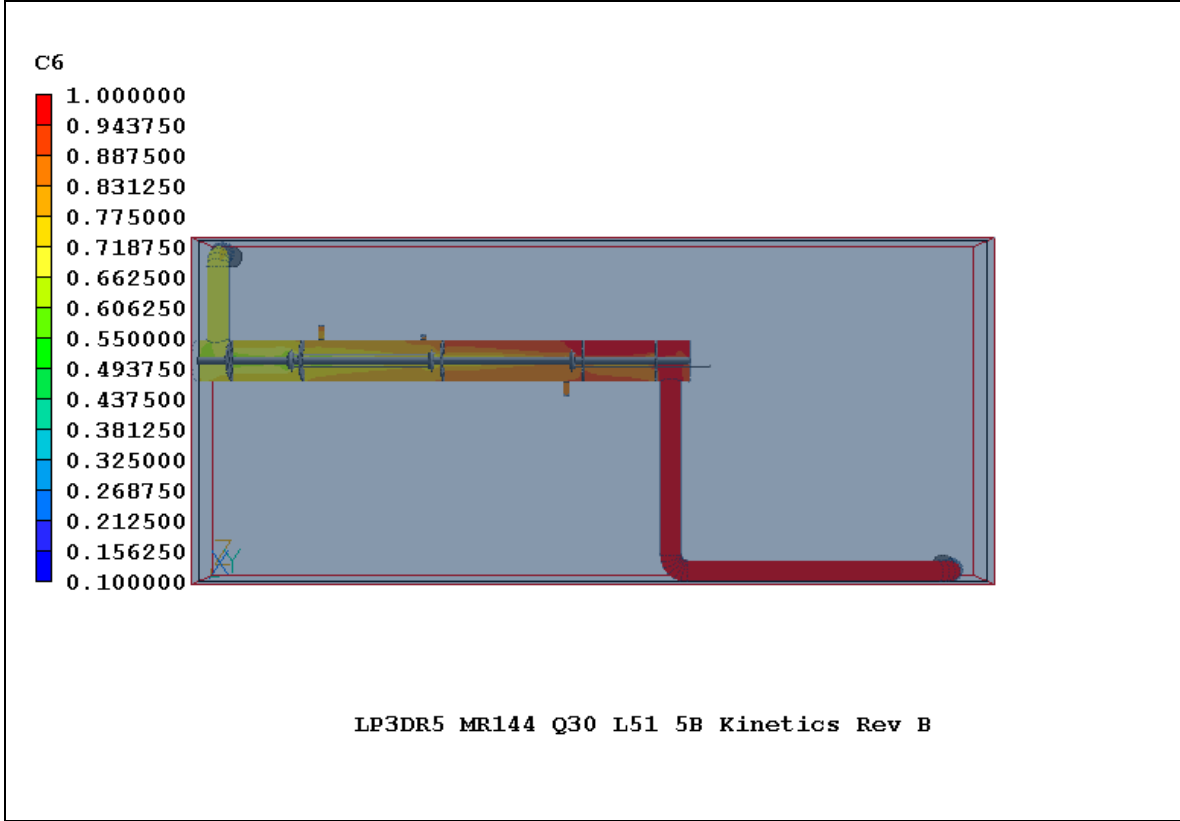
I=	24	J=	10	K=	79
----	----	----	----	----	----



I=	2	J=	11	K=	103
----	---	----	----	----	-----



I=	27	J=	11	K=	103
----	----	----	----	----	-----



From Phi Reader: Average over i=2:

Average 7.01E-01

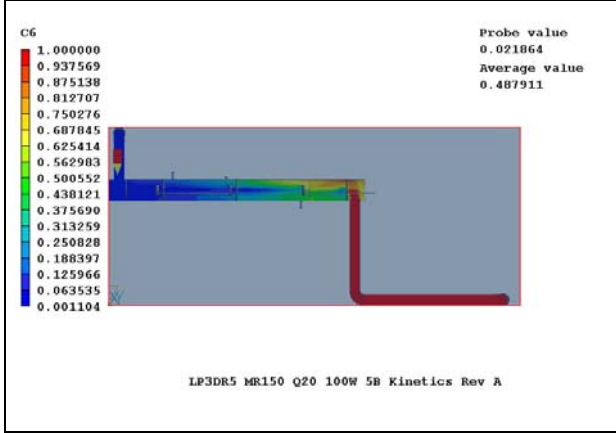
C/C0 = 0.701462

%R = 0.298538

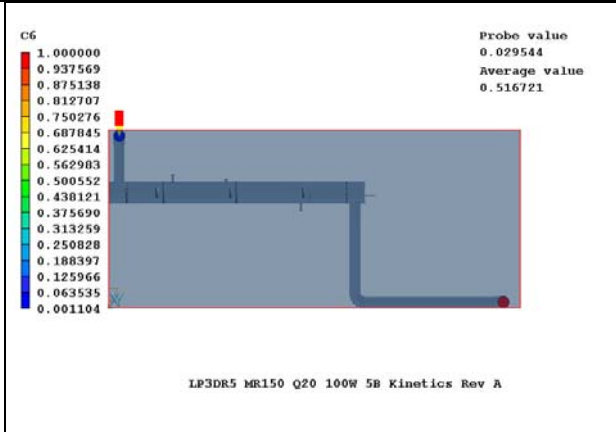
Research Condition (Model) 31

Filename	C:\phoenics\d_priv1\Scott\Kinetics100W\LP3DR5_MR150_20_100W_5B_ke_RevARS (Note: Files On Kiseok Computer)
Flowrate (GPM) & Turbulence Model	20, k-eps
Methylene Blue In (M)	1.563230E-06 (0.5 mg/L)
Molar Ratio (H2O2:MB)	150
Lamp Power (W)	100; RADLSI
C3 at x=0.156679, y=0.834382, z=0.899000	67.412
UV254 Transmittance (%)	94.8
k(MB,OH) Rate Constant ( $M^{-1} s^{-1}$ )	6.9E10
Alkalinity (mg/L as $CaCO_3$ )	22.7 (assume all as $HCO_3^-$ )
pH	7.30
DOC (mg/L)	0.57
Combined Chlorine (mg/L as $Cl_2$ )	0.05
Model Run Time (hrs)	70
Computer	Kiseok

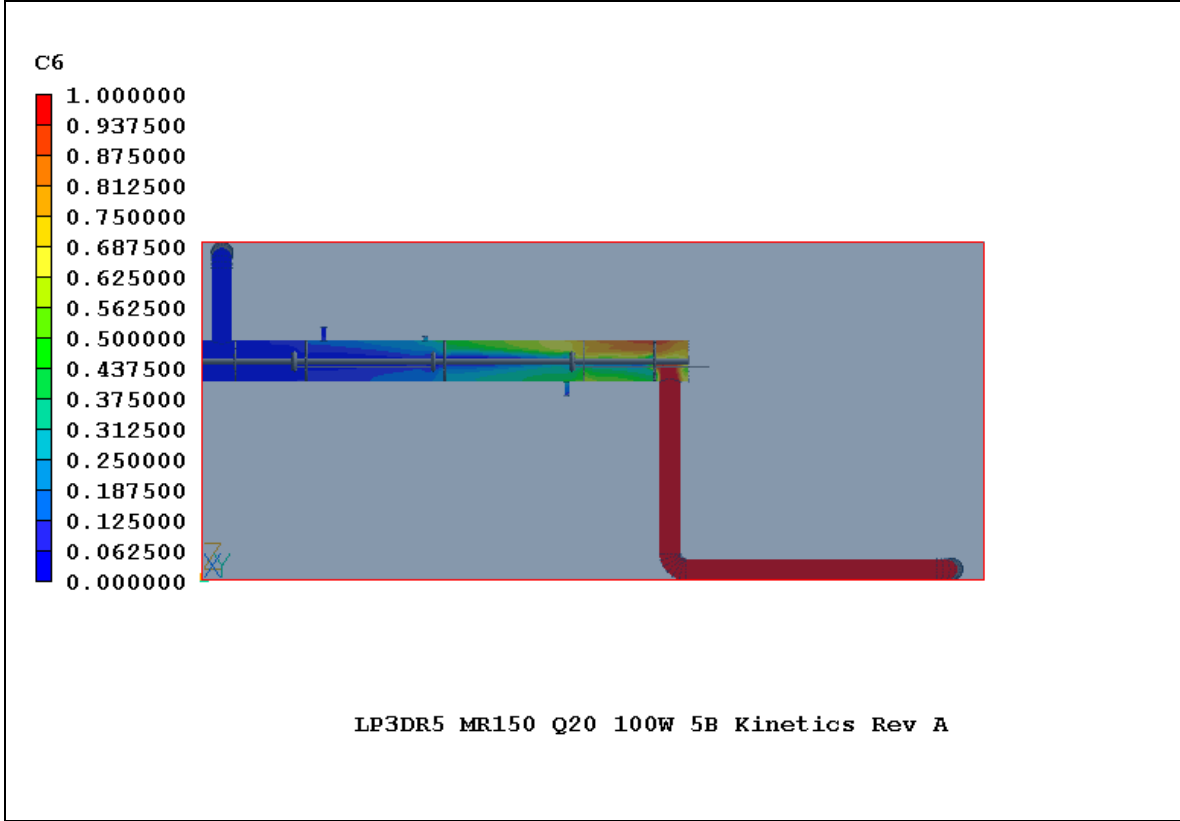
I=	24	J=	10	K=	79
----	----	----	----	----	----



I=	2	J=	11	K=	103
----	---	----	----	----	-----



I=	27	J=	11	K=	103
----	----	----	----	----	-----



From Phi Reader: Average over i=2:

Average            2.57E-02

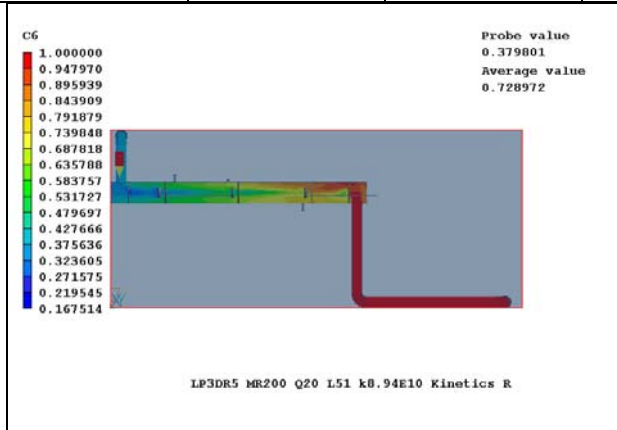
C/C0                0.025715

Percent Removal    97.43%

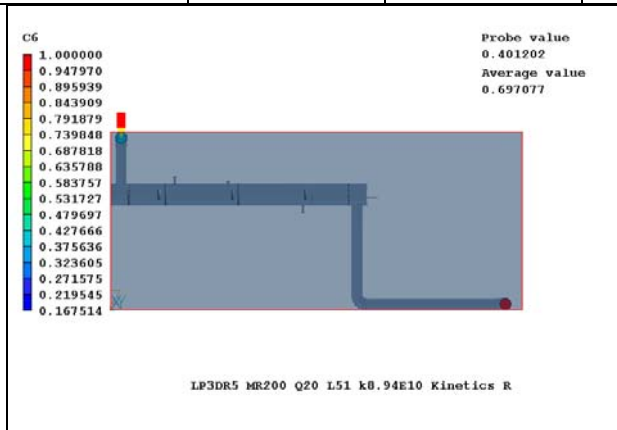
### Research Condition (Model) 32

Filename	C:\phoenics\d_priv1\Scott\Kinetics200_51_20_k894e10\LP3DR5_MR200_20_5B_k894e10_RevARS (Note: Files On Kiseok Computer)
Flowrate (GPM) & Turbulence Model	20, k-eps
Methylene Blue In (M)	1.563230E-06 (0.5 mg/L)
Molar Ratio (H2O2:MB)	199.25
Lamp Power (W)	26.5; RADLSI
C3 at x=0.156679, y=0.834382, z=0.899000	18.032
UV254 Transmittance (%)	94.9
k(MB,OH) Rate Constant ( $M^{-1} s^{-1}$ )	8.94E10
Alkalinity (mg/L as $CaCO_3$ )	22.2 (assume all as $HCO_3^-$ )
pH	7.24
DOC (mg/L)	0.57
Combined Chlorine (mg/L as $Cl_2$ )	0.013
Model Run Time (hrs)	70
Computer	Kiseok

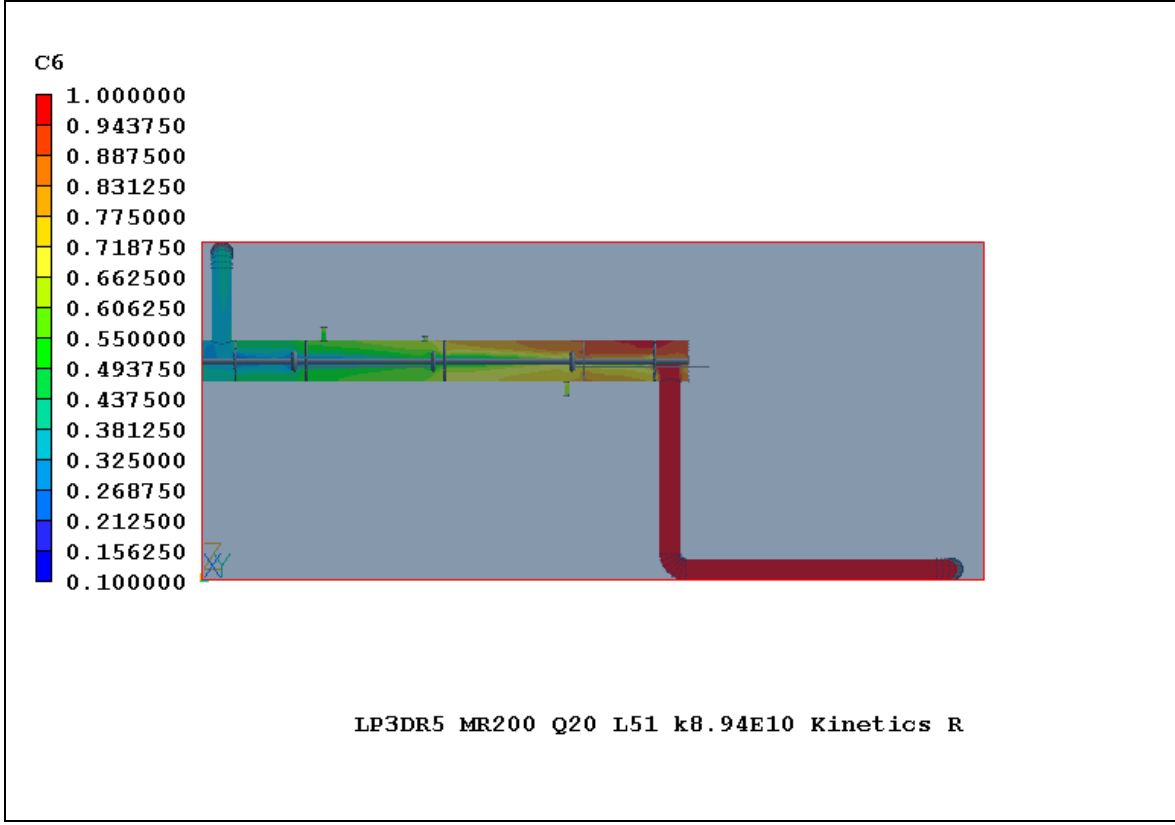
I=	24	J=	10	K=	79
----	----	----	----	----	----



I=	2	J=	11	K=	103
----	---	----	----	----	-----



I=	27	J=	11	K=	103
----	----	----	----	----	-----



From Phi Reader: Average over i=2:

Average            3.89E-01

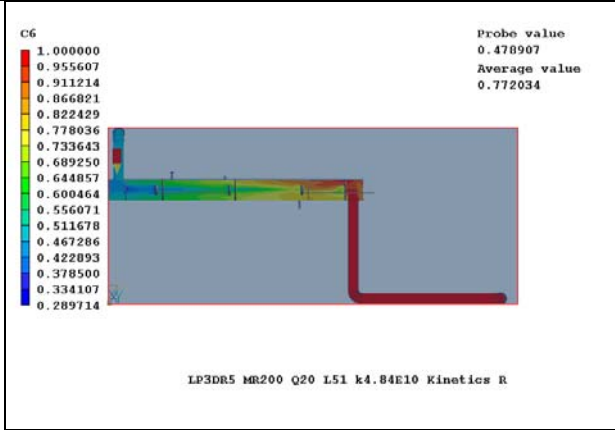
C/C0                0.388677

Percent Removal    61.13%

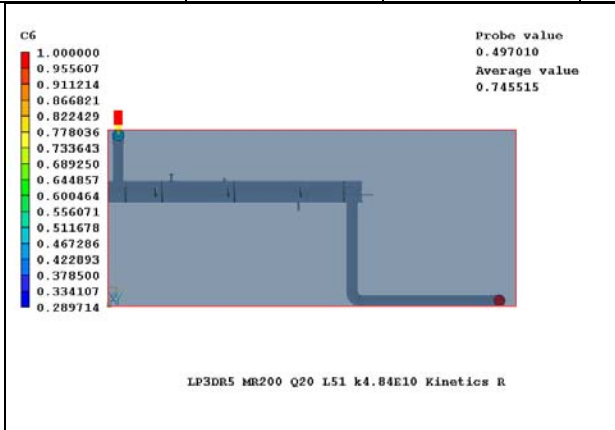
### Research Condition (Model) 33

Filename	C:\phoenics\d_priv1\Scott\Kinetics200_51_20_k484e10\LP3DR5_MR200_20_5B_k484e10_RevARS (Note: Files On Kiseok Computer)
Flowrate (GPM) & Turbulence Model	20, k-eps
Methylene Blue In (M)	1.563230E-06 (0.5 mg/L)
Molar Ratio (H2O2:MB)	199.25
Lamp Power (W)	26.5; RADLSI
C3 at x=0.156679, y=0.834382, z=0.899000	18.032
UV254 Transmittance (%)	94.9
k(MB,OH) Rate Constant (M <sup>-1</sup> s <sup>-1</sup> )	4.84E10
Alkalinity (mg/L as CaCO <sub>3</sub> )	22.2 (assume all as HCO <sub>3</sub> <sup>-</sup> )
pH	7.24
DOC (mg/L)	0.57
Combined Chlorine (mg/L as Cl <sub>2</sub> )	0.013
Model Run Time (hrs)	70
Computer	Kiseok

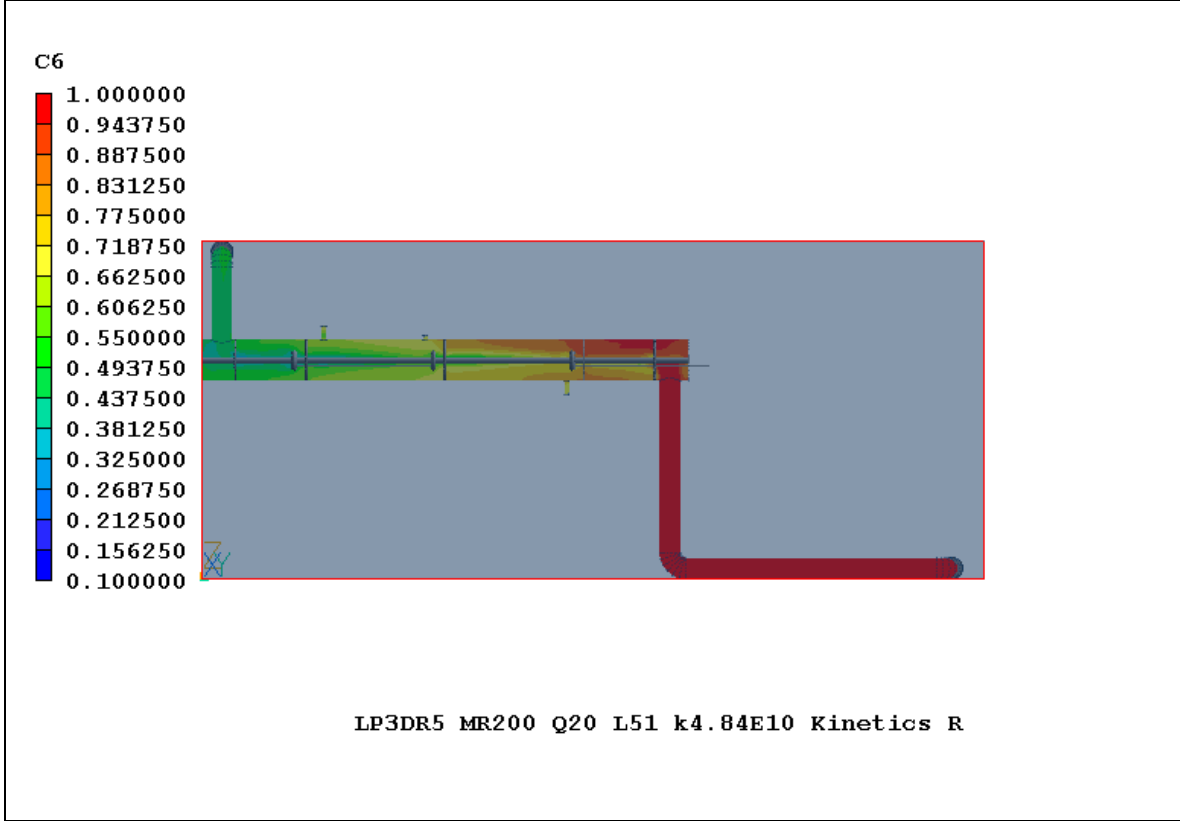
I=	24	J=	10	K=	79
----	----	----	----	----	----



I=	2	J=	11	K=	103
----	---	----	----	----	-----



I=	27	J=	11	K=	103
----	----	----	----	----	-----



From Phi Reader: Average over i=2:

Average                    4.86E-01

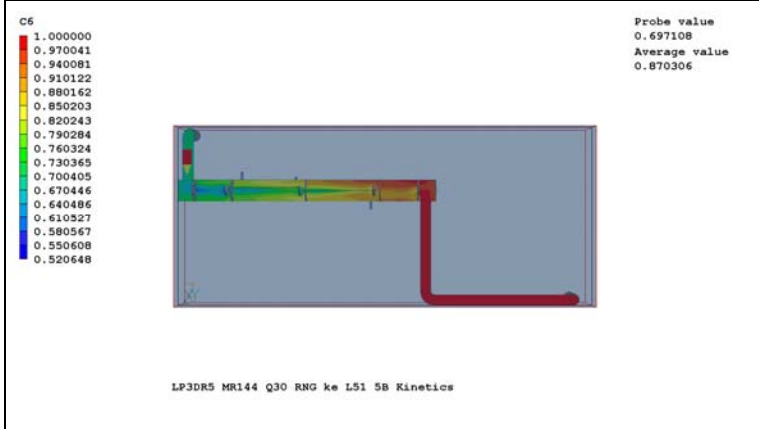
C/C0                        0.486421

Percent Removal        51.36%

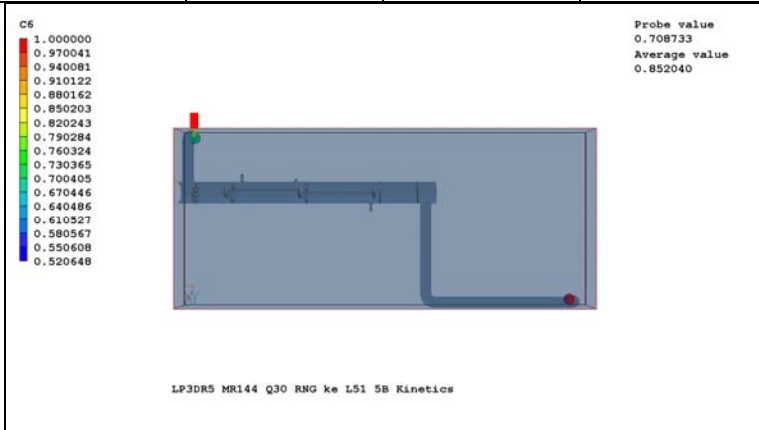
### Research Condition (Model) 34

Filename	C:\Documents and Settings\smalpert\My Documents\Phoenix\LP3D Rev 5 Expanded Scavengers\GPM30_Light51Percent\Five Baffles\Average Density\ RNG_ke\Kinetics\LP3DR5_MR144_30_5B_RNGke_DK_RevBRS
Flowrate (GPM) & Turbulence Model	30, RNG k-eps
MB In (M)	1.563230E-06 (0.50 mg/L)
Molar Ratio (H2O2:MB)	144.2
Lamp Power (W)	52*0.58 (30.16)
C3 at x=0.156679, y=0.834382, z=0.899000	15.794
UV254 Transmittance (%)	91.9
MB Rate Constant ( $M^{-1} s^{-1}$ )	6.900000E+10
Alkalinity (mg/L as $CaCO_3$ )	28.05 (assume all as $HCO_3^-$ )
pH	7.49
DOC (mg/L)	0.57
Combined Chlorine (mg/L as $Cl_2$ )	0.14
Model Run Time (hrs)	150 hrs
Computer	Mike

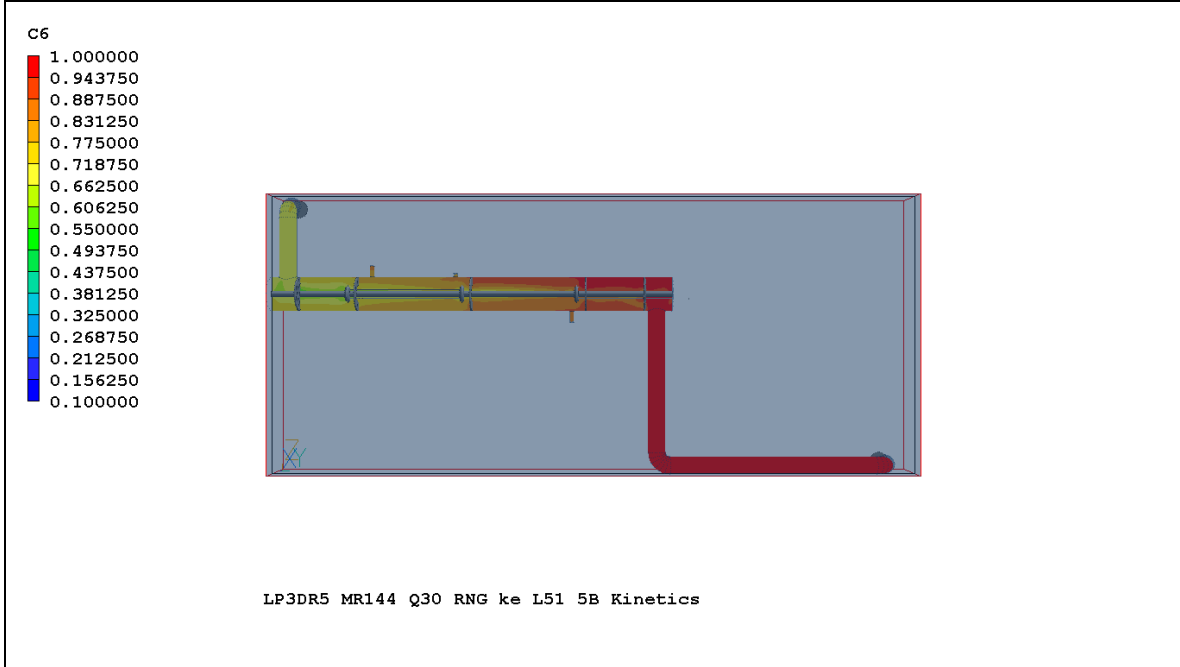
I=	24	J=	10	K=	79
----	----	----	----	----	----



I=	2	J=	11	K=	103
----	---	----	----	----	-----



I=	27	J=	11	K=	103
----	----	----	----	----	-----



From Phi Reader: Average over i=2:

Average 7.01E-01

C/C0 = 0.700859

%R = 0.299141

### 8.3 Appendix C – Sample MATLAB Code

## MATLAB Code

```
function []=MBAOPReactorDoseRev3
% Solves system of ODEs to evaluate degradation of methylene blue by UV/peroxide AOP
global Vact x y0
P=100; % Lamp output power at 254 nm (W)
%%%%%%%%%%%%%%%%%%%%%%%%%%%%%%%%%%%%%%%%%%%%%%%%%%%%%%%%%%%%%%%%%%%%%%%%
% First Calls ode23s to solve UV chemical degradation equations, Stiff system of ODEs
Q=20; % Reactor flow rate (gpm)
L=182.88; % length of cylinder (cm)
d=15.24; % diameter of cylinder (cm)
R=d/2; % radius of cylinder (cm)
rq=1.27; % radius of quartz (cm)
Vact=pi*L*((R^2)-(rq^2)); % Reactor Volume (cm^3)
Vactg=(pi*((L*0.393701)/12)*(((R*0.393701)/12)^2)...
    -(((rq*0.393701)/12)^2))*7.48; % Reactor Volume (gal)
MB = 0.5; % Initial MB Concentration (mg/L)
MBMW = 319.85; % MB Molecular Weight (g/mol)
MBinit=(MB/1000)/MBMW; % Initial concentration of MB, M
Phinit=MBinit/MBinit; %1.56e-6; % Initial normalized concentration of MB, M
Ratio=150; % Ratio of peroxide to MB
Peinit=(Ratio*MBinit)/(Ratio*MBinit); % Initial normalized concentration of peroxide, M
y0 = [Phinit; Peinit; 0; 0]; %Initial Conditions (1)=[MB]init, (8)=[Peroxide]init
x0 = 0; %First point
xn = (Vactg/Q)*60; %Last point, theoretical detention time in seconds
N = 1000; %100; %Number of points between first and last point
x = linspace(x0,xn,N+2); %Range of values over which to solve system of ODE's
Phinit=y0(1);
[X,Y] = ode23s(@function_name,x,y0,[],P,Phinit,Peinit,MBinit,Ratio);
%%%%%%%%%%%%%%%%%%%%%%%%%%%%%%%%%%%%%%%%%%%%%%%%%%%%%%%%%%%%%%%%%%%%%%%%
% Plot concentrations versus time
figure(1);
[EavgF]=feval(@EcalcF,P,Phinit,Peinit,MBinit,Ratio);
I=EavgF % W/m^2
plot(X*I*0.1,Y(:,1),'r');
legend(['MB']);
title('Photochemical Degradation of Methylene Blue');
str8=num2str(Ratio);
str9=num2str(Phinit);
str10=num2str(Peinit);
strf1=['H2O2/MB Ratio=' str8];
xtex=60;
text(xtex,7e-4,strf1);
strf2=['Init MB (mol/L)=' str9];
text(xtex,6e-4,strf2);
strf3=['Init H2O2 (mol/L)=' str10];
text(xtex,5e-4,strf3);
xlabel('UV Dose (mJ/cm^2)');
ylabel('Normalized Concentration');
hold off;
%%%%%%%%%%%%%%%%%%%%%%%%%%%%%%%%%%%%%%%%%%%%%%%%%%%%%%%%%%%%%%%%%%%%%%%%
```

```

% Opens external file for exporting of data points defined below.
fid = fopen('data100W_MR150_Q20.txt','w');
% Formats data to write to text file
YY=[X*I*0.1,Y(:,1)];
% fprintf(fid,'%6.2f %6.10f\n',YY); % Writes data to text file
fprintf(fid,'%6.10f\n',YY); % Writes data to text file
% Closes external text file
fclose(fid);
%%%%%%%%%%%%%%%%%%%%%%%%%%%%%%%%%%%%%%%%%%%%%%%%%%%%%%%%%%%%%%%%%%%%%%%%
return

```

```

function [dydt] = function_name(x,y,P,Phinit,Peinit,MBinit,Ratio)
% Hardcode system of ODEs
dydt=zeros(4,1);
%%%%%%%%%%%%%%%%%%%%%%%%%%%%%%%%%%%%%%%%%%%%%%%%%%%%%%%%%%%%%%%%%%%%%%%%
% Assign variables
% y(1)= Methylene Blue (Normalized)
% y(2)= Hydrogen Peroxide (Normalized)
% y(3)= OH Radical (Normalized)
% y(4)= Superoxide Radical (Normalized)
%%%%%%%%%%%%%%%%%%%%%%%%%%%%%%%%%%%%%%%%%%%%%%%%%%%%%%%%%%%%%%%%%%%%%%%%
% Assign rate constants
% * RG(24) = k2 (per Crittenden paper), M-1 s-1
k2 = 2.70e7;
% * RG(25) = k4 (per Crittenden paper), M-1 s-1
k4 = 3.00;
% * RG(26) = k13 (per Crittenden paper), M-1 s-1
k13 = 5.50e9;
% * RG(27) = k14 (per Crittenden paper), M-1 s-1
k14 = 6.60e9;
% * RG(28) = k15 (per Crittenden paper), M-1 s-1
k15 = 8.30e5;
% * RG(29) = k16 (per Crittenden paper), M-1 s-1
k16 = 9.70e7;
% * RG(30) = k17 (per Crittenden paper), M-1 s-1
k17 = 7.00e9;
% *** RG(31) = 2nd order rate constant for MB+OH, M-1 s-1
kmb = 6.9e10;
% * RG(32) = k5 (per Crittenden paper), M-1 s-1
k5 = 0.13;
% *** RG(33) = First Order Radical Scavenger, ks, s-1
ks = 0.00;
% * RG(34) = 2nd Order DOC Radical Scavenger, kDOC, L mg-1 s-1
kdoc = 2.50e4;
% *** RG(35) = DOC Concentration, DOC, mg L-1
DOC = 0.57;
% *** RG(36) = Total Alkalinity ALK, mg L-1 as CaCO3
ALK = 22.70;
% * RG(37) = 2nd Order HCO3- Radical Scavenger, kHCO3-, M-1 s-1
khco = 8.50e6;
% * RG(38) = HCO3- Concentration, M (Assume neutral pH)
HCO = ALK*(1/100)*(1/1000)*2;
% * RG(39) = 2nd Order CO3- Radical Scavenger, kCO3-, M-1 s-1

```

```

kco = 3.90e8;
% *** RG(40) = CO3- Concentration, M (Assume neutral pH)
CO3 = 0.00;
% *** RG(51) = pH
ph = 7.3;
% *** RG(52) = Free Chlorine Concentration, mg L-1 as Cl2
fcl = 0.00;
% *** RG(53) = Combined Chlorine Concentration, mg L-1 as Cl2
ccl = 0.05;
% * RG(54) = Proton Concentration, M
pro = 10^(-1*ph);
% * RG(55) = Free Chlorine Concentration, M
fclm = fcl/(70900);
% * RG(56) = Equilibrium Constant HOCl/OCl-, Ka
ka = 3.162278e-8;
% * RG(57) = Fraction of Free Cl that is HOCl
fra = 1/(1+(ka/pro));
% * RG(58) = HOCl Concentration, M
hocl = fra*fclm;
% * RG(59) = OCl- Concentration, M
ocl = (1-fra)*fclm;
% * RG(71) = 2nd Order OCl- Radical Scavenger, kOCl-, M-1 s-1
kocl = 8.80e9;
% * RG(72) = 2nd Order HOCl Radical Scavenger, kHOCl, M-1 s-1
khocl = 8.50e4;
% * RG(73) = Monochloramine Concentration, M (Assume no di- or tri-)
nhcl = ccl/(70900);
% * RG(74) = 2nd Order NH2Cl Radical Scavenger, kNH2Cl, M-1 s-1
knhcl = 2.80e9;
% * RG(81) = pi
pi = 3.141593;
% *** RG(84) = Quantum Yield of Direct Photolysis of Contaminant (MB)
phidp = 0.000000E+00;
% * Energy of one einstein for 254 nm in J/Einstein
U = 4.715280E+05;
%%%%%%%%%%%%%%%%%%%%%%%%%%%%%%%%%%%%%%%%%%%%%%%%%%%%%%%%%%%%%%%%%%%%%%%%
% Reactor Characteristics
[EavgF]=feval(@EcalcF,P,Phinit,Peinit,MBinit,Ratio);
I=EavgF; % W/m^2
%%%%%%%%%%%%%%%%%%%%%%%%%%%%%%%%%%%%%%%%%%%%%%%%%%%%%%%%%%%%%%%%%%%%%%%%
% Assign reaction equations
phi=0.5; % quantum yield for peroxide
epsmb=19; % molar absorptivity of phenol, M^-1 cm^-1 (assume decadic)
epsperoxide=19.6; % molar absorptivity of peroxide, M^-1 cm^-1 (assume decadic)
% Concentration of OH radicals (pseudo-steady-state)
y(3)=((-((-k2*y(2)*MBinit*Ratio)-(k17*y(4)*MBinit*Ratio)-(kmb*y(1)*MBinit)...
-k*(kdoc*DOC)-(khco*HCO)-(kco*CO3)-(kocl*ocl)-(khocl*hocl)...
-(knhcl*nhcl))-(((((-k2*y(2)*MBinit*Ratio)-(k17*y(4)*MBinit*Ratio)...
-(kmb*y(1)*MBinit)-k*(kdoc*DOC)-(khco*HCO)-(kco*CO3)-(kocl*ocl)...
-(khocl*hocl)-(knhcl*nhcl))^2)-(4.*(k13*MBinit*Ratio)...
*(2.*phi*epsperoxide*y(2)*((I*100)/(U*1000))))...
+(k5*y(2)*y(4)*MBinit*Ratio))))^0.5)/((2.*(-k13*MBinit*Ratio)));
OHSS=y(3)*MBinit*Ratio;

```

```

% Concentration of O2- radicals (pseudo-steady-state)
y(4)=(k2*y(2)*y(3))/((k17*y(3))+k5*y(2));
%%%%%%%%%%%%%%%%%%%%%%%%%%%%%%%%%%%%%%%%%%%%%%%%%%%%%%%%%%%%%%%%%%%%%%%%
% Differential Equations
dydt(1)=(-kmb*y(1)*y(3)*MBinit*Ratio)-(phidp*epsmb*y(1)*((I*100)/(U*1000)));
dydt(2)=(-1.*phi*epsperoxide*y(2)*((I*100)/(U*1000)))...
-(k2*y(2)*y(3)*MBinit*Ratio)-(k5*y(2)*y(4)*MBinit*Ratio)...
+(k13*y(3)*y(3)*MBinit*Ratio);
return

function [EavgF]=EcalcF(P,Phinit,Peinit,MBinit,Ratio)
% Calculates the average irradiance of the fraction of absorbed light that is absorbed by peroxide
L=182.88; % length of cylinder (cm)
tx=1;
d=15.24; % diameter of cylinder (cm)
R=d/2;
rq=1.27; % radius of quartz (cm)
nL=100; % number of length segments
nr=100; % number of radial segments
deltal=L/nL;
deltar=(R-rq)/nr;
epsmb=19; % molar absorptivity of MB, M^-1 cm^-1 (assume decadic)
epsperoxide=19.6; % molar absorptivity of peroxide, M^-1 cm^-1 (assume decadic)
aback = 0.0184845; % background water absorbance, cm^-1
abstotal = (epsmb*MBinit)+(epsperoxide*MBinit*Ratio)+aback; % total absorbance, cm^-1
UVT=10^-abstotal
%%%%%%%%%%%%%%%%%%%%%%%%%%%%%%%%%%%%%%%%%%%%%%%%%%%%%%%%%%%%%%%%%%%%%%%%
for x=1:nL % Changed from nL+1 to look at length in center of volume
    for y=1:nr % Changed from nr+1 to look at radii in center of volume
        r=(rq+(0.5*deltar))+deltar*(y-1); %Changed from rq+(deltar*(y-1)); to look at radii in center of
volume
        l=(0.5*deltal)+(deltal*(x-1)); %Changed from deltal*(x-1); to look at length in center of volume
        H=abs((L/2)-l);
        a1=(10^(-1*abstotal*(r-rq))); % Attenuation Constant for light transmittance
        f1=(epsperoxide*MBinit*Ratio)/abstotal;
        f2=1-(10^(-1*abstotal*(r-rq))); % Correct according to Linden
        I1=P/(2*pi*(L/100)*(r/100)); % Radial Model Fluence rate (W/m^2) at a point with a normal distance R
from lamp
        I2=(P/(4*pi*(L/100)*(r/100)))*(atan(((L/2)+H)/r)+atan(((L/2)-H)/r)); % RAD-LSI fluence rate (W/m^2)
        I3=[I1 I2];
        Ir(y,x)=min(I3);
        Irad(y,x)=Ir(y,x)*a1; % Attenuated light transmitted
        V(y,x)=(pi*((r+(0.5*deltar))^2)*deltal)-(pi*((r-(0.5*deltar))^2)*deltal); % Volume of concentric
elemental slice of reactor (cm^3)
    end
end
%%%%%%%%%%%%%%%%%%%%%%%%%%%%%%%%%%%%%%%%%%%%%%%%%%%%%%%%%%%%%%%%%%%%%%%%
TotalV=0;
TotalIrad=0;
clear x y
for x=1:nL %Changed from nL+1 to look at length in center of volume
    for y=1:nr %Changed from nr+1 to look at radii in center of volume
        TotalIrad=TotalIrad+(Irad(y,x)*V(y,x));
    end
end

```

```
    TotalV=TotalV+V(y,x); % Calculates total volume of reactor
end
end
Iradavg=TotalIrad/TotalV;
EavgF=Iradavg;
tx=tx+1;
return
```